



Ollscoil Chathair  
Bhaile Átha Cliath  
Dublin City University

# **Development of a BEM-AD model for optimisation of Horizontal Axis Tidal Current Turbine Arrays**

A thesis submitted to  
School of Engineering  
Dundalk Institute of Technology

For the degree of  
**Doctor of Philosophy**

By  
**Chee Meng Pang M.Sc. B.Eng. (Hons)**

Supervised by **Dr. Fergal O'Rourke**  
Co-supervised by **Prof. David M. Kennedy (TU Dublin)**

August 2024



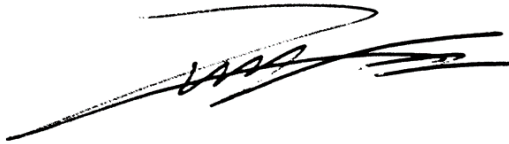
## Declaration

We, the undersigned declare that this thesis entitled Development of BEM-AD model for optimisation of Horizontal Axis Tidal Current Turbine Arrays is entirely the author's own work and has not been taken from the work of others, except as cited and acknowledged within the text.

The thesis has been prepared according to the regulations of Dundalk Institute of Technology and has not been submitted in whole or in part for an award in this or any other institution.

**Author Name:** Chee Meng Pang

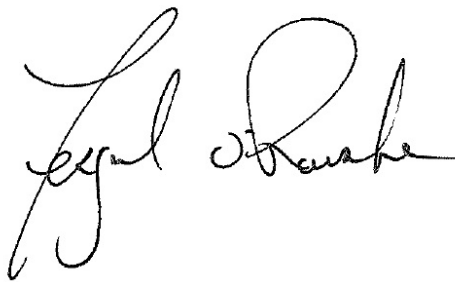
**Author Signature:**



**Date:** 20 August 2024

**Supervisor Name:** Fergal O'Rourke

**Supervisor Signature:**



**Date:** 20 August 2024

PGF014

Declaration by Author & Supervisor

## Declaration

I hereby certify that this material, which I now submit for assessment on the programme of study leading to the award of the degree of PhD is entirely my own work, and that I have exercised reasonable care to ensure that the work is original, and does not to the best of my knowledge breach any law of copyright, and has not been taken from the work of others save and to the extent that such work has been cited and acknowledged within the text of my work.

**Signed:**

A handwritten signature in black ink, appearing to read 'Chee Meng Pang', written over a horizontal line.

**(Chee Meng Pang)**

**ID No.:** D00161875

**Date:** 20 August 2024

## **Acknowledgements**

First and foremost, I would like to express my deepest appreciation to my family, especially my father. I would have never gotten this far without their constant love, encouragement and support despite being far from home. I would like to gratefully thank my colleagues and friends especially Eng Jet Yeo and Qui Ren See for all their support, brainstorming and company.

I would like to express my sincere gratitude and appreciation to my supervisors Dr. Fergal O'Rourke and Prof. David Kennedy for their patience and guidance during my PhD study. I cannot keep my research work in the right direction without their invaluable experience, support and encouragement. Also, many thanks to all the engineering staff for helping me through my studies.

Lastly, I would like to acknowledge the Centre for Renewable Energy (CREDIT) and Dundalk Institute of Technology (DKIT) for providing me with a bursary and the opportunity to carry out this research.

## **Abstract**

### **Development of a BEM-AD model for optimisation of Horizontal Axis Tidal Current Turbine Arrays**

**Chee Meng Pang**

Advancement and improvement of new and efficient techniques to meet the ever-increasing energy demand for economic and social development are of significant interest. Renewable energy technologies offer an appealing option to supply this growing electricity demand, while also assisting with the European Union's policy on sustainability. Ireland has excellent tidal energy resources which can be utilised to meet future energy goals. However, significant research and development is still needed to realise Ireland's tidal energy potential. tidal current turbines (TCTs) are at an early stage of development, particularly the deployment of devices in arrays, thus more studies and investigations are required on wake interactions between turbines to optimise array performance via numerical modelling. Computational Fluid Dynamics (CFD) is a very suitable numerical method to study TCT arrays, but high computational cost is needed to obtain high-accuracy results. For that reason, the development of low computational cost numerical models with suitable accuracy is paramount.

In this work, a numerical model was developed to predict the wake effects of a tidal current turbine for array optimisation with a focus on downstream velocity, turbulence intensity and energetic predictions. The first stage of the work focused on developing and enhancing a single-turbine model by coupling Actuator Disk (AD) theory and Blade Element Momentum (BEM) theory to model turbine wake effects known as BEM-AD model. Variations and hybrid models were developed to further improve prediction of downstream wake effects. In the second stage of the work, a multiple turbine wake interaction study was performed to evaluate hydrodynamically, the array spacing, array arrangement, effects of turbine sizes and the placement of turbines at different depths in the water column. For the third stage of the work, an optimised TCT array model was developed and evaluation was conducted for a range of different domain conditions. Finally, a case study on the Shannon Estuary was conducted to assess the tidal current turbine array model's energetic performance in a pseudo-transient state

# Contents

<b>1</b>	<b>Introduction</b>	<b>1</b>
1.1	Introduction . . . . .	1
1.2	Tidal Energy . . . . .	1
1.3	Numerical modelling . . . . .	3
1.4	Project Scope . . . . .	4
1.5	Aims and Objectives . . . . .	5
1.6	Report Structure . . . . .	6
1.7	Original Contributions . . . . .	8
1.8	Publications . . . . .	9
<b>2</b>	<b>Literature Review</b>	<b>11</b>
2.1	Introduction . . . . .	11
2.2	Tide and Tidal Current . . . . .	13
2.3	Tidal Current Technologies . . . . .	14
2.4	Tidal Resource in Ireland . . . . .	20
2.4.1	Shannon Estuary . . . . .	22
2.5	Turbine wake . . . . .	24
2.6	Experimental modelling . . . . .	30
2.7	Turbine representations . . . . .	33
2.8	Numerical Modelling . . . . .	39
2.8.1	Blade Element Momentum (BEM) Theory . . . . .	40
2.8.2	Computational fluid dynamics (CFD) . . . . .	41
2.8.3	Reynolds-averaged Navier-Stokes (RANS) . . . . .	43
2.8.4	Large-eddy simulation (LES) . . . . .	46
2.8.5	Numerical modelling of Tidal Current turbine . . . . .	48
2.9	Numerical modelling of TCT array . . . . .	51
2.10	Conclusions . . . . .	53

---

<b>3</b>	<b>Theory</b>	<b>56</b>
3.1	Introduction . . . . .	56
3.2	Basic rotor definitions . . . . .	57
3.3	Actuator Disk (AD) Theory . . . . .	60
3.3.1	Betz Limit . . . . .	62
3.4	Blade Element Momentum (BEM) Theory . . . . .	64
3.4.1	Momentum Theory . . . . .	64
3.4.2	Blade Element Theory . . . . .	66
3.4.3	Blade element momentum (BEM) theory . . . . .	67
3.4.4	Prandtl's loss correction . . . . .	69
3.4.5	Turbulent wake state correction model . . . . .	70
3.5	Computational Fluid Dynamics (CFD) . . . . .	74
3.5.1	Reynolds-Averaged Navier-Stokes (Reynolds Averaged Navier Stokes (RANS)) . . . . .	75
3.5.2	$k - \omega$ shear stress transport (shear stress transport (SST)) . .	77
3.5.3	Near wall region . . . . .	79
3.5.4	Discretisation . . . . .	82
3.5.5	ANSYS software . . . . .	85
3.6	Summary . . . . .	86
<b>4</b>	<b>Methodology</b>	<b>89</b>
4.1	Introduction . . . . .	89
4.2	Single Turbine model . . . . .	89
4.2.1	Actuator disk (AD) model . . . . .	90
4.2.2	Numerical BEM turbine model . . . . .	95
4.2.3	Velocity and radial variations . . . . .	98
4.2.4	Hybrid Modification . . . . .	102
4.2.5	CFD Meshing . . . . .	107
4.2.6	Summary . . . . .	110
4.3	Array Turbine model . . . . .	111
4.3.1	Optimised blade profile . . . . .	111
4.3.2	Optimised Modified BEM-AD model . . . . .	114
4.3.3	Aligned and Staggered Array Layout: Ideal Channel . . . .	119
4.3.4	Aligned and Staggered Array Layout: Ideal Channel . . . .	121
4.3.5	Shannon Estuary . . . . .	127



---

4.3.6	Shannon Estuary psuedo-transient simulation . . . . .	130
4.3.7	Summary . . . . .	132
<b>5</b>	<b>Results and discussion</b>	<b>133</b>
5.1	Introduction . . . . .	133
5.2	Single Turbine model . . . . .	133
5.2.1	AD model study: 2-dimensional vs 3-dimensional model . . . . .	134
5.2.2	AD model study: ANSYS-CFX vs ANSYS-Fluent . . . . .	138
5.2.3	Modified BEM-AD model: Velocity Variation . . . . .	143
5.2.4	Modified BEM-AD model: Radial Variation . . . . .	146
5.2.5	Modified BEM-AD model: Hybrid model . . . . .	149
5.2.6	Modified BEM-AD model: Overall Discussion . . . . .	152
5.3	Multiple Turbine Model . . . . .	159
5.3.1	Turbine Lateral Spacing – Two turbines . . . . .	159
5.3.2	Turbine Lateral Spacing – Three turbines . . . . .	163
5.3.3	Turbines Staggered Layout – downstream spacing . . . . .	168
5.3.4	Turbine Size and Depth Investigation . . . . .	171
5.3.5	Summary . . . . .	179
5.4	Array Turbine Model . . . . .	181
5.4.1	Array Configuration: Aligned vs Staggered . . . . .	181
5.4.2	Idealised Tidal Channel: Headland (location and yaw) . . . . .	186
5.4.3	Idealised Tidal Channel: Headland and Island . . . . .	196
5.4.4	Case Study: Shannon Estuary . . . . .	200
5.4.5	Overall Summary . . . . .	208
<b>6</b>	<b>Conclusions</b>	<b>211</b>
6.1	Summaries and conclusions . . . . .	211
6.2	Further work . . . . .	216

# List of Figures

1.1	Demonstration of thesis scope and stages. . . . .	5
2.1	Eleven viable tidal energy site locations identified in Ireland (SEI 2004). . . . .	21
2.2	Measured tidal-current speed at mid-depth of the water column over a lunar month for a site in the Shannon Estuary (O’Rourke et al. 2014). . . . .	24
2.3	Tidal rises of measured tidal-current data over a lunar month at a site in Shannon Estuary for depth of 2m, 4m, 6m, 8m and 10m (O’Rourke et al. 2014). . . . .	25
2.4	Potential area with high exploitable tidal energy resources in Shannon Estuary (Fouz et al. 2022). . . . .	26
2.5	Near wake and far wake regions downstream of a turbine. . . . .	27
2.6	Types of rotors used in laboratory studies, (a) mesh disk rotor simulator (Myers & Bahaj 2010) and (b) 0.8-m-diameter scaled rotor (Myers & Bahaj 2009). . . . .	30
2.7	Downstream longitudinal centreline velocity deficit of different laboratory scaled rotor (Chamorro et al. 2013, Stallard et al. 2013, Myers & Bahaj 2010, 2009, Bahaj, Myers, Thomson & Jorge 2007, Hachmann et al. 2020). . . . .	34
2.8	Centreline normalised velocity profile of a range of different ADM. (MacLeod et al. 2002, Gant & Stallard 2008, Batten et al. 2013, Sun et al. 2008, Harrison et al. 2010, Roc et al. 2010). . . . .	39
2.9	The procedure of solving a typical CFD problem. . . . .	42
2.10	RANS turbulence closure models in increasing level of complexity. . . . .	44
2.11	Comparison of velocity and turbulence intensity along the downstream centreline of experimental and numerical results of different RANS turbulence model (Nguyen et al. 2016). . . . .	47

---

2.12	Velocity contour of (a) regular staggered and (b) modified staggered array arrangement and (c) power outputs for the two arrangements (Malki et al. 2014). . . . .	53
3.1	Section blade element diagram with angles, forces and velocities. . . . .	58
3.2	Actuator disk model of a rotor turbine. . . . .	61
3.3	Power coefficient and thrust coefficient as a function of axial induction factor, $a$ , for an ideal horizontal TCT. . . . .	63
3.4	Comparison between experimental and numerical thrust coefficient at different axial induction factor (Zhang 2018). . . . .	69
3.5	Sub-divisions of near-wall region in turbulent flow condition (Ansys 2009). . . . .	80
3.6	Difference in grid resolution using a wall function. (Kalitzin et al. 2005) . . . . .	82
4.1	ANSYS CFX. Setup for actuator disk model. . . . .	91
4.2	ANSYS CFX set-up branches outline. . . . .	92
4.3	Geometry of the fluid domain. . . . .	92
4.4	Velocity profile (a) and turbulence intensity profile (b) at the inlet comparing numerical and experimental inlet conditions. . . . .	94
4.5	Lift coefficients (a) and drag coefficients (b) at angle of attack between -10 degrees to 60 degrees. . . . .	96
4.6	Comparison of numerical predicted power coefficients (a) and thrust coefficients (b) with experimental measurements (Batten et al. 2007) for a range of tip speed ratios . . . . .	97
4.7	Porosity (a) and resistance coefficients (b) of the actuator disk domain at different tip speed ratios. . . . .	98
4.8	Porosity (a) and resistance coefficients (b) of the actuator disk domain at different normalised velocity. . . . .	99
4.9	Numerical and empirical calculation of Porosity (a) and resistance coefficients (b) of the actuator disk domain at different normalised velocities. . . . .	99
4.10	Porosity (a) and resistance coefficients (b) of the actuator disk domain at different normalised radii. . . . .	101

---

4.11	Numerical and empirical calculations of Porosity (a) and resistance coefficients (b) of the actuator disk domain at different normalised radius locations. . . . .	101
4.12	The disk domain seperated into three regions. . . . .	102
4.13	Porosity (a) and resistance coefficients (b) of the actuator disk domain at the different normalised radius and normalised velocity excluding base and tip regions. . . . .	103
4.14	Numerical (dots) and empirical (contours) calculation of Porosity (a) and resistance coefficients (b) of the actuator disk domain's body region at different normalised radius locations and normalised velocity. . . . .	104
4.15	Numerical and empirical calculation of Porosity (a) and resistance coefficients (b) of the actuator disk domain's base region at different normalised velocities. . . . .	105
4.16	Numerical and empirical calculation of Porosity (a) and resistance coefficients (b) of the actuator disk domain's tip region at different normalised velocities. . . . .	106
4.17	An isometric sectional view of the concentrated mesh fluid domain. . . . .	108
4.18	Vertical water column comparison between normal mesh (a) and concentrated mesh (b) fluid domains in terms of downstream velocity and turbulence intensity at 5D downstream from the actuator disk. . . . .	109
4.19	Lift coefficients(a) and drag coefficients (b) of NACA-6415 at angle of attack between -15 degrees to 20 degrees. . . . .	112
4.20	Comparison of numerical predicted power coefficients (a) and thrust coefficients (b) with the Yeo et al. model (Yeo et al. 2022) for a range of tip speed ratios. . . . .	113
4.21	Porosity (a) and resistance coefficient (b) of the actuator disk domain at different normalised radial locations and normalised velocities excluding base and tip regions for the optimised tidal current turbine blade. . . . .	115
4.22	Numerical (dots) and empirical (contours) calculation of porosity (a) and resistance coefficient (b) of the actuator disk domain's body region at different normalised radial locations and normalised velocities for the optimised tidal current turbine blade. . . . .	116

4.23	Numerical and empirical calculation of porosity (a) and resistance coefficient (b) for the actuator disk domain's base region at different normalised velocity for the optimised tidal current turbine blade. . .	118
4.24	Numerical and empirical calculation of porosity (a) and resistance coefficient (b) for the actuator disk domain's tip region at different normalised velocities for the optimised tidal current turbine blade. . .	118
4.25	An ideal channel with tidal current turbine deployed area (turbine deployed area (TDA)) located in the centre of the channel at mid-depth, shown from the top view. . . . .	119
4.26	Aligned layout array (a) and staggered layout array (b) in the TDA at mid-depth, shown from the top view. . . . .	120
4.27	Mesh of turbine deployed area (TDA) for aligned layout array at mid-depth, shown from the top view. . . . .	121
4.28	An ideal channel with headland located in the centre left-side (as seen from the inlet) of the channel at mid-depth, shown from top view. . . . .	121
4.29	An ideal channel with headland located in the centre left-side (as seen from the inlet) of the channel at mid-depth, shown from the top view. . . . .	122
4.30	Geometry (a) and mesh (b) of an ideal headland channel with turbine deployed area (TDA) located in the centre of the channel at mid-depth, shown from the top view. . . . .	123
4.31	An ideal channel with headland and island at mid-depth, shown from the top view. . . . .	124
4.32	Velocity contour of an ideal channel with headland and island at mid-depth, shown from the top view. . . . .	125
4.33	Geometry (a) and mesh (b) of the TDA located in between the headland and the island in the channel at mid-depth, shown from top view.	126
4.34	The Shannon Estuary at mid-depth, shown from the top view. . . . .	127
4.35	The bathymetry of Shannon Estuary at mid-depth, shown from the top view. . . . .	127
4.36	The velocity profile comparison of numerical and measured values (O'Rourke et al. 2014) at the probe in Shannon Estuary during spring tide (a) and neap tide (b). . . . .	128
4.37	Mesh of the Shannon Estuary at mid-depth, shown from top view. . .	129

---

4.38	Velocity contour during flooding (a) and ebbing (b) in the Shannon Estuary at mid-depth, shown from top view during spring tide. . . .	129
4.39	Tide velocity at mid-depth in the Shannon Estuary in a day during spring tide (a) and neap tide (b). . . . .	131
4.40	Tidal flow velocity at mid-depth in the Shannon estuary over a lunar month (28 days). . . . .	132
5.1	Comparison of downstream centreline normalised velocity (a) and turbulence intensity (b) of the 2-dimensional AD model and the 3-dimensional AD model with experimental measurements (Batten et al. 2013). . . . .	135
5.2	Comparison of vertical normalised velocity and vertical turbulence intensity of 2-dimensional and 3-dimensional AD models with experimental measurements (Batten et al. 2013) at downstream distances of 5D(a), 8D(b) and 10D(c). . . . .	136
5.3	Velocity contour of the 2-dimensional AD model (a) and the 3-dimensional AD model (b). . . . .	137
5.4	Turbulence intensity contour of the 2-dimensional AD model (a) and the 3-dimensional AD model (b). . . . .	138
5.5	Comparison of predicted downstream centreline velocity (a) and turbulence intensity (b) for the ANSYS-CFX AD model and the ANSYS-Fluent AD model and compared with experimental measurements (Batten et al. 2013). . . . .	140
5.6	Comparison of vertical normalised velocity and vertical turbulence intensity of ANSYS-CFX and ANSYS-Fluent AD models with experimental measurements (Batten et al. 2013) at downstream distances of 5D(a), 8D(b) and 10D(c). . . . .	141
5.7	Comparison of vertical normalised velocity and vertical turbulence intensity of ANSYS-CFX and ANSYS-Fluent AD models with experimental measurements (Batten et al. 2013) at downstream distances of 5D(a), 8D(b) and 10D(c). . . . .	142
5.8	Comparison of downstream centreline velocity (a) and turbulence intensity (b) of the velocity variation bem-AD model against experimental measurements (Batten et al. 2013). . . . .	143

---

5.9	Comparison of vertical normalised velocity and vertical turbulence intensity of the velocity variation BEM-AD model with experimental measurements (Batten et al. 2013) at downstream distances of 5D, 8D and 10D. . . . .	145
5.10	Comparison of downstream centreline velocity (a) and turbulence intensity (b) of the radial variation bem-AD model against experimental measurements (Batten et al. 2013). . . . .	146
5.11	Comparison of vertical velocity and vertical turbulence intensity of the radial variation BEM-AD model with experimental measurements (Batten et al. 2013) at downstream distances of 5D, 8D and 10D. . . . .	148
5.12	Comparison of downstream centreline velocity (a) and turbulence intensity (b) of the modified hybrid BEM-AD model against experimental measurements (Batten et al. 2013). . . . .	149
5.13	Comparison of vertical velocity and vertical turbulence intensity of the modified hybrid BEM-AD model with experimental measurements (Batten et al. 2013) at downstream distances of 5D, 8D and 10D. . . . .	151
5.14	Comparison of downstream centreline velocity (a) and turbulence intensity (b) for the velocity variation model, radial variation model and hybrid modification model against experimental measurements (Batten et al. 2013). . . . .	152
5.15	Comparison of downstream velocity profile and turbulence intensity profile for the velocity variation model, radial variation model and hybrid modification model against experimental measurements (Batten et al. 2013) at a downstream distance of 5D. . . . .	154
5.16	Velocity side-view contour of velocity variation model (a), radial variation model (b) and hybrid modification model (c). . . . .	156
5.17	Turbulence intensity side-view contour of velocity variation model (a), radial variation model (b) and hybrid modification model (c). . . . .	156
5.18	Power density contour of the actuator disk from front view for the velocity variation model (a), radial variation model (b) and the hybrid modification model (c). . . . .	157

5.19	Comparison of centreline downstream velocity of the two turbine model with experimental measurements of the lateral distance of 0.5D (a), 1.0D (b) and 1.5D (c). . . . .	159
5.20	Comparison of velocity profile at downstream distance of 3D for the two turbines model at the lateral distance of 0.5D (a), 1.0D (b) and 1.5D (c) against experimental measurements. . . . .	160
5.21	Velocity side-view contours of the two turbines model at the lateral distance of 0.5D (a), 1.0D (b) and 1.5D (c). . . . .	161
5.22	Comparison of velocity profile for the two turbines model at a downstream distance of 5D (a), 7D (b) and 9D (c) against experimental measurements. . . . .	163
5.23	Comparison of velocity profile for the three turbines model at a downstream distance of 5D (left), 7D (centre) and 9D (right) against experimental measurements. . . . .	164
5.24	Comparison of velocity profile for the three turbines model at a downstream distance of 5D (left), 7D (centre) and 9D (right) against experimental measurements. . . . .	164
5.25	Velocity contour from side view of the two turbines model (a) and three turbines model (b). . . . .	165
5.26	Power density front-view contour of the actuator disks of the two turbines model (a) and three turbines model (b). . . . .	166
5.27	Thrust coefficient (a) and power coefficient (b) of the second row turbine at a range of downstream spacing settings. . . . .	168
5.28	The centreline downstream velocity after the second row turbine at downstream spacing scenarios of 3D, 5D, 10D and 15D. . . . .	169
5.29	The centreline downstream velocity after the second row turbine at downstream spacing scenarios of 3D (a), 5D (b), 8D (c), 10D (d) and 15D (e). . . . .	170
5.30	Velocity profile at 5D downstream distance after second row turbine for downstream spacing scenarios of 3D, 5D, 10D and 15D. . . . .	171
5.31	Thrust coefficient (a) and power coefficient (b) of the three turbines in the staggered layout for diameter ranging from 5m to 12m. . . . .	172
5.32	Centreline downstream velocity of Turbine 3 (second row) at mid-depth for turbine size of 5m, 8m and 12m. . . . .	173



---

5.33	Lateral velocity profile at mid-depth at downstream distances of 5D (a), 7D (b), 9D (c) and 25D (d) for turbine diameter of 5m, 8m, and 12m. . . . .	174
5.34	Velocity top-view contour of turbine diameter size: 5m (a), 8m (b) and 12m (c). . . . .	176
5.35	Thrust coefficient (a) and power coefficient (b) of all three turbines in a staggered layout at different depth placements. . . . .	176
5.36	Centreline downstream velocity of Turbine 3 (second row) at mid-depth for turbine size of 5m, 8m and 12m. . . . .	177
5.37	Velocity top-view contour of turbines at normalised depths: 0.25H (a), 0.50H (b) and 0.75H (c). . . . .	178
5.38	Centreline velocity side-view contour of turbine at normalised depths: 0.25H (a), 0.50H (b) and 0.75H (c). . . . .	179
5.39	Mid-depth velocity top-view contour of aligned (a) and staggered (b) array layout. . . . .	182
5.40	Direction of the incoming flow from horizontal when interacting with the array of tidal current turbines for aligned (a) and staggered (b) array layout. . . . .	183
5.41	Mid-depth velocity top-view contour of aligned array layout without yaw (a) and yaw (b). . . . .	184
5.42	Mid-depth velocity top-view contour of aligned staggered layout without yaw (a) and yaw (b). . . . .	185
5.43	The velocity top-view contour of aligned layout array (a) and staggered layout array (b) in an idealised channel with headland at mid-depth. . . . .	186
5.44	The velocity top-view contour of aligned (a, c and e) and staggered (b, d and f) layout array at mid-depth of various gap distance between TDA and headland: 100m (a and b), 200m (c and d) and 400m (e and f). . . . .	189
5.45	The velocity top-view contour of aligned (a, c and e) and staggered (b, d and f) layout array at mid-depth at different TDA and headland alignments scenarios: front (a and b), centre (c and d) and back (e and f). . . . .	191

---

5.46	The velocity contour of aligned layout array without yaw (a) and with yaw (b); and the velocity contour of staggered layout array without yaw (c) and with yaw (d). . . . .	195
5.47	The velocity contour of the aligned (a) and the staggered (b) array layouts in an idealised channel with a headland and island at mid-depth. . . . .	196
5.48	The velocity contour of the aligned array layout without yaw (a) and with yaw (b) between a headland and an island in an idealised channel. . . . .	198
5.49	The velocity contour of the staggered array layout without yaw (a) and with yaw (b) between a headland and an island in an idealised channel. . . . .	198
5.50	The velocity top-view contour of turbine array layout deployed in the Shannon Estuary at peak spring tide during flooding (a) and ebbing (b) at mid-depth. . . . .	200
5.51	The velocity top-view contour of a yaw-aligned array at peak spring tide during flooding (a) and ebbing (b) at mid-depth. . . . .	201
5.52	The velocity top-view contour of a turbine array layout deployed in Shannon Estuary at peak spring tide during flooding (a) and ebbing (b) from top view at mid-depth. . . . .	201
5.53	The tidal current turbine array power (a) and tidal current turbine array energy output, calculated in 10-minute intervals, (b) for aligned and staggered array layouts for a day during spring tide. . . . .	205
5.54	The tidal current turbine array power (a) and tidal current turbine array energy output, calculated in 10-minute intervals, (b) for aligned and staggered array layouts for a day during neap tide. . . . .	206
5.55	The tidal current turbine array power in a lunar month for the aligned array layout (a) and the staggered array layout (b). . . . .	207
5.56	Cumulative energy outputted in a day during spring tide (a) and neap tide (b) for aligned and staggered array layouts. . . . .	208
5.57	Cumulative energy outputted in a lunar month for an aligned array layout and a staggered array layout. . . . .	209

# List of Tables

2.1	Tidal current development protocol. TRL refers to technology readiness levels (Nachtane et al. 2020) . . . . .	17
2.2	Tidal turbine devices summarisation (Sleiti 2017) . . . . .	18
2.3	A summary of the hydrokinetic characterises of the seven potential exploitable area. . . . .	23
2.4	A summary of the laboratory studies. . . . .	32
2.5	Description of various TCT rotor representation techniques. . . . .	35
2.6	Summary of different TCT representation techniques . . . . .	38
2.7	Summary of findings of different models in terms of blade and wake performance among single turbine and multiple turbine arrays. . . . .	49
4.1	summary of boundaries parameters . . . . .	94
4.2	Geometry parameter of the blade (Batten et al. 2007) . . . . .	95
4.3	Total number of elements of 5 different mesh setup. . . . .	109
4.4	Summary of mesh study for different mesh setups, detailing number of elements, normalised velocity at point location P2 and P3 and convergence time. . . . .	110
4.5	Geometry parameters of the Yeo et al. optimised blade (Yeo et al. 2022). . . . .	112
4.6	Comparative analysis of power and thrust coefficients for the current model against the Yeo et al. model (Yeo et al. 2022). . . . .	113
4.7	Summarised parameters of all boundaries in an ideal channel fluid domain. . . . .	120
4.8	Summarised parameters of all boundaries in an ideal channel fluid domain containing headland. . . . .	122
4.9	Summarised parameters of all boundaries in an ideal channel fluid domain containing headland and island. . . . .	125

---

4.10	Summarised parameters of all boundaries in an ideal channel fluid domain containing headland and island. . . . .	128
4.11	Statistical analysis of the numerical velocity against experimental measurements during spring tide and neap tide (O'Rourke et al. 2014)	131
5.1	Statistical analysis of 2-dimensional and 3-dimensional AD models against experimental measurements (Batten et al. 2013) for centre-line downstream velocity and turbulence intensity. . . . .	135
5.2	Statistical analysis of ANSYS-CFX and ANSYS-Fluent AD models against experimental measurements (Batten et al. 2013) for centre-line downstream velocity and turbulence intensity. . . . .	139
5.3	Statistical analysis each of the three modified BEM-AD models against experimental measurements (Batten et al. 2013) for downstream centreline velocity and turbulence intensity. . . . .	153
5.4	Statistical analysis for each of the three modified BEM-AD models against experimental measurements (Batten et al. 2013) in terms of downstream velocity profile and turbulence intensity profile at a downstream distance of 5D. . . . .	155
5.5	Comparative analysis of thrust coefficient and power coefficient of velocity variation, radial variation and hybrid modification against BEM numerical value. . . . .	158
5.6	Comparative analysis of thrust coefficient and power coefficient for the two turbines model at the lateral distance of 0.5D against BEM numerical value. . . . .	162
5.7	Comparative analysis of thrust coefficient and power coefficient for the two turbines model at the lateral distance of 1.0D against BEM numerical value. . . . .	162
5.8	Comparative analysis of thrust coefficient and power coefficient for the two turbines model at the lateral distance of 1.5D against BEM numerical value. . . . .	162
5.9	Comparative analysis of thrust coefficient and power coefficient for the two turbine model against BEM numerical value. . . . .	167
5.10	Comparative analysis of thrust coefficient and power coefficient for the three turbines model against BEM numerical value. . . . .	167

5.11	Power and average power coefficient of each row of turbines in the aligned and the staggered layout. . . . .	182
5.12	Yaw angle from the horizontal of each turbine in the aligned array layout. . . . .	184
5.13	Yaw angle from the horizontal of each turbine in the staggered array layout. . . . .	184
5.14	Power and average power coefficient of each row of turbines in aligned layout without yaw and with yaw. . . . .	185
5.15	Power and average power coefficient of each row of turbines in aligned layout without yaw and with yaw. . . . .	185
5.16	Total power of each row of turbines in the aligned and staggered layout in an idealised channel with headland. . . . .	187
5.17	Total power of each row of turbines in the aligned layout at various gap distances between the TDA and the headland. . . . .	189
5.18	Total power of each row of turbines in the staggered layout at various gap distances between the TDA and the headland. . . . .	190
5.19	Total power of each row of turbines in the aligned layout at different alignments scenarios of the TDA with the headland. . . . .	192
5.20	Total power of each row of turbines in the staggered layout at different alignments scenarios of the TDA with the headland. . . . .	192
5.21	Total power of each row of turbines in the aligned array without yaw and with yaw. . . . .	195
5.22	Total power of each row of turbines in the staggered array without yaw and with yaw. . . . .	195
5.23	Total power of each row of turbines in the aligned and the staggered array layouts between the headland and the island in an idealised channel. . . . .	197
5.24	Total power of each row of turbines in the aligned array layout without yaw and with yaw between a headland and an island in an idealised channel. . . . .	199
5.25	Total power of each row of turbines in the staggered array layout without yaw and with yaw between a headland and an island in an idealised channel. . . . .	199
5.26	Total power of each row of turbines in the aligned and staggered array layouts at peak spring tide during flood and ebb. . . . .	203

---

5.27	Total power of each row of turbines in the aligned array layout at peak spring tide during flood and ebb for the actuator disk model, modified disk model, and yaw-modified disk model. . . . .	203
5.28	Total power of each row of turbines in the staggered array layout at peak spring tide during flood and ebb for the actuator disk model, modified disk model, and yaw-modified disk model. . . . .	204
5.29	Total array energy in a day during spring and neap tide for the aligned and the staggered array layouts. . . . .	207
5.30	Total energy outputted by the tidal current turbine array, for a half lunar month, a lunar month, and a year, for the aligned and the staggered array layouts. . . . .	208

## Abbreviation and acronyms

<b>AD</b>	Actuator Disk
<b>ALM</b>	Actuator Line Model
<b>BE</b>	Blade Element
<b>BEM</b>	Blade Element Momentum
<b>BRM</b>	Bed Roughness Model
<b>CFD</b>	Computational Fluid Dynamics
<b>DNS</b>	Direct numerical simulation
<b>EMEC</b>	European Marine Energy Centre
<b>FDM</b>	Finite Difference Method
<b>FEA</b>	Finite Element Analysis
<b>FEM</b>	Finite Element Method
<b>FVM</b>	Finite Volume Method
<b>HAT</b>	Horizontal-axis turbine
<b>LES</b>	Large Eddy Simulation
<b>MAE</b>	mean absolute error
<b>MAPE</b>	mean absolute percentage error
<b>MCT</b>	Marine Current Turbine
<b>MSM</b>	Momentum Sink Model
<b>MT</b>	Momentum theory
<b>NS</b>	Navier-Stokes
<b>RANS</b>	Reynolds Averaged Navier Stokes
<b>Re</b>	Reynolds number
<b>RITE</b>	Roosevelt Island Tidal Energy
<b>RMSE</b>	root mean square error
<b>RNG</b>	renormalisation group
<b>RRF</b>	Rotating Reference Frame
<b>RSM</b>	Reynolds stress model
<b>SMM</b>	Sliding Mesh Model
<b>SST</b>	shear stress transport
<b>TCT</b>	tidal current turbine
<b>TDA</b>	turbine deployed area
<b>TI</b>	turbulence intensity
<b>TSR</b>	tip speed ratio

<b>TRL</b>	Technology readiness levels
<b>TSE</b>	tidal current exploitability
<b>VAT</b>	Vertical-axis turbine
<b>VM</b>	vortex methods

## Nomenclature

### Greek Notations

$\alpha$	Angle of attack
$\alpha_e$	Effective angle of attack
$\alpha_i$	Downwash angle
$\varepsilon$	Dissipation per unit mass
$\gamma$	twist angle
$\kappa$	von Kármán constant
$\lambda$	Tip speed ratio
$\lambda_r$	Local tip speed ratio
$\mu$	Dynamics viscosity
$\mu_T$	Eddy-viscosity
$\nu$	Kinematic viscosity
$\nabla^2$	Laplacian operator
$\omega$	Specific dissipation rate
$\Omega$	Rotational angular velocity
$\phi$	Relative angle
$\rho$	Fluid density
$\sigma$	local blade solidity
$\theta$	Porosity of porous domain
$\theta_p$	pitch angle
$\alpha^{\omega\varepsilon}$	closure coefficients 1
$\beta^{\omega\varepsilon}$	closure coefficients 2
$\sigma^{\omega\varepsilon}$	closure coefficients 3
$\sigma_2^{\omega\varepsilon}$	closure coefficients 4
$\alpha^{SST}$	SST closure coefficients 1
$\beta_1^{SST}$	SST closure coefficients 2



$\beta_2^{SST}$	SST closure coefficients 3
$\sigma_1^{SST}$	SST closure coefficients 4
$\sigma_2^{SST}$	SST closure coefficients 5

### Roman Notations

$a'$	Angular induction factor
$A$	Area of turbine
$a$	Axial induction factor
$A_d$	Area of disk
$A_S$	Blade area between the local radial and the blade tip
$B$	Number of blades
$\bar{c}$	Geometric mean chord length
$c$	chord length
$C^+$	empirical parameter for wall function
$C_{Le}$	Lift Coefficient at effective angle of attack
$C_\mu$	constant = 0.09
$C_{TAN}$	Tangential Coefficient
$C_1$	Prescribed matrix 1 in ANSYS-Fluent
$C_2$	Prescribed matrix 2 in ANSYS-Fluent
$C_D$	Drag Coefficient
$C_{De}$	Drag Coefficient at effective angle of attack
$C_L$	Lift Coefficient
$C_N$	Normal Coefficient
$C_P$	Power Coefficient
$C_T$	Thrust Coefficient
$CD_{kw}$	cross-diffusion term
$d$	Channel depth
$D$	Rotor Diameter
$d_t$	Thickness of the disk
$F$	Tip loss correction factor
$F_D$	Drag force
$F_L$	Lift force
$F_N$	Normal force

---

$F_{Shen}$	Shen's correction factor
$F_{tan}$	Tangential force
$F_1$	First blending function
$F_2$	Second blending function
$F_R$	Rotation correction factor
$F_S$	Downwash factor
$g_1$	Shen's $g_1$ parameter
$H$	characteristic length or depth
$I$	Turbulence intensity
$I_{mean}$	Mean turbulence intensity
$K$	resistance coefficient of porous domain
$k$	Specific turbulence kinetic energy
$k_{turb}$	Turbulence kinetic energy
$K_1$	Shen's $K_1$ parameter
$L$	Characteristic length
$\dot{m}_1$	Upstream mass flow rate
$\dot{m}_4$	Downstream mass flow rate
$\dot{m}$	mass flow rate
$m$	curve slope of the linear zone of the hydrofoil lift coefficient profile
$M$	Local torque
$p$	Pressure
$P$	Rotor power
$R$	Blade radius
$r$	Local radius
$S$	Source term
$T$	Thrust force
$t$	Time
$\bar{u}_i$	Mean velocity component
$U$	Freestream velocity
$U^*$	Friction velocity at the wall
$U_\theta$	Tangential velocity
$U_{inlet}$	Inlet velocity
$U_{mean}$	Mean inlet intensity
$U_{rel}$	Relative velocity
$U_1$	Upstream velocity

$U_2$	Velocity at disk
$U_4$	Downstream velocity
$U_z$	Axial velocity
$V$	Velocity vector
$w$	Channel width
$y^+$	dimensionless length distance from wall
$y_s$	Distance to the nearest wall
$z$	Distance from the seabed
$z$	Distance from the seabed

# Chapter 1

## Introduction

### 1.1 Introduction

This section presents an introduction to the current state-of-the-art of tidal energy and the recent development of numerical modelling of (tidal current turbines (TCTs)). The report's structure is detailed, and a number of the original contributions of this work are clearly outlined. A list of publications from this PhD project is then given and finally, some conclusions are detailed.

### 1.2 Tidal Energy

The tidal current energy is a potential source of energy that can contribute greatly to global energy demands. Tidal current energy is a form of kinetic energy from fast moving tidal currents which can be harnessed via tidal current turbines. The island of Ireland has excellent tidal energy potential with an estimated theoretical resource of 230 TWh per annum (SEAI 2008), a horizontal axis tidal current turbine is a popular choice to harness tidal current energy and an ideal tidal current energy site for deployment has been identified as sites with peak tidal current speeds in the range of  $2\text{m/s}$  (SEAI 2008); but most devices would begin power generation at  $0.8\text{m/s}$ . However, the tidal current speed in the open ocean is usually in the order of  $0.1\text{m/s}$  which is below the range required by a tidal current turbine to effectively operate (Wolff 2007). The interaction of tidal current with coastal topography can result in an acceleration of the tidal current speed to above  $2\text{m/s}$ . Some good examples of such coastal topography are headlands, islands and narrow channels between adja-

cent landmasses. Another coastal topography worth mentioning is estuaries. Estuaries typically consist of complex topography that can induce strong tidal current flow. Hence, the most suitable sites tend to be in the coastal area and are typically highly localised in the area. In Ireland, the Shannon Estuary located on the west coast of Ireland is a potential site for tidal energy extraction, with strong tidal currents, with peak current speed ranging between  $2 - 3\text{ m/s}$  and has been identified as a suitable site for tidal current energy deployment (O'Rourke et al. 2014)

Technological advancement has led to an increase in development in the TCT industry. In 2019, there was a 19% growth globally in the marine energy sector (Chowdhury et al. 2021). However, there is still much development and progress needed in order to achieve the sustainable development scenario's (SDS) target set down in the Paris Agreement which is an annual growth of 23% through to 2030 Cozzi et al. (2020). Although there is much development needed in the growth of TCT technology, there are numerous TCT projects already in operation globally. A good example is the MeyGen Project deployed in the Pentland Firth, this project is currently the largest tidal current energy project worldwide (Atlantis Project 2010). Most of the currently active TCT projects utilise horizontal axis TCTs, this design is the most common design to date. So, this research focuses primarily on the modelling of horizontal axis TCTs.

Most of the up-to-date commercially viable TCTs have been tested using single devices or in small arrays, but commercial applications of TCTs will likely be farms containing hundreds of deployed devices. Therefore, the investigation and study into the operation and impacts of large-scale TCT arrays is of significant importance. The viability of TCT technology largely depends on the expected energy capture and the related environmental impacts. In a TCT array deployment, the fluid flow field around the TCT is of great interest, i.e. wake effects. The wake can be categorised into near-field which is the alteration to the flow field within a 5-rotor-diameter distance from the turbine and the far-field wake which is the alteration to the flow field more than a 5-rotor-diameter downstream from the turbine. This alteration to the flow field is known as turbine downstream wake, the deployment of a TCT device will affect the velocities and turbulence of the downstream wake. The downstream wake plays a crucial role in determining large TCT array arrangement. Ergo, understanding and investigating the downstream wake is

paramount in the further development of TCT technology. The aim of this research is to investigate and develop a numerical model capable of accurately predicting the wake development of TCTs in a real tidal current energy site and was utilised to optimise TCT arrays with respect to energy output and environmental impacts. Furthermore, providing crucial inputs to determine the economic viability of proposed TCT arrays.

### 1.3 Numerical modelling

Work on the development of numerical models of coastal waters was first presented around the 1960s/70s. As the industry developed, the accuracy of predicting the fluid flow field has increased as well as the complexity and computational demands of the numerical models presented in the literature. The numerical models vary in their process and parameters of interest, thus selecting and developing the appropriate numerical model is crucial to solving and investigating the hydrodynamic system of interest. Due to the lack of accessibility of commercial-scale tidal current turbine data to date, most numerical models are usually validated against laboratory measured data.

Computational cost is often an important consideration in numerical modelling, for a hydrodynamics model to be economically viable, optimisation of cost is crucial. Computational cost can generally be defined by the simulation duration of the model; thus, reducing the computational time will typically reduce the costs. Nevertheless, an increase in model complexity, to achieve better accuracy, also increases the computational cost, this is mainly due to the inclusion of more investigation parameters. Thus, to reduce computational cost many numerical models have resolved the fluid flow field to a low spatial resolution, such as using a coarser mesh or by using a more simplified geometry. This approach may be computationally less demanding, but it is at the cost of model prediction accuracy. Hence, a balanced approach between computational demand and model accuracy is paramount. This research focuses on developing a numerical model of tidal current turbine wake development with optimal numerical accuracy and computational cost.

## 1.4 Project Scope

According to the above-mentioned content, the motivations of the thesis can be concluded as follows:

- Ireland has excellent tidal energy resource potential which can be utilised to meet future energy goals. However, the tidal energy sector still needs significant research and development to realise Ireland's tidal energy potential.
- TCTs are in the early stages of array commercialisation, thus it is important to carry out in-depth studies and investigations into the wake interactions between turbines to better optimise the array performance via numerical modelling.
- Numerical modelling is a very suitable method to study TCT arrays, but a high computational cost is needed to obtain high accuracy results. Hence, developing a low computational cost numerical model with reasonable accuracy is of high priority.

This research project is divided into three stages as shown in Figure 1.1 which shows the scope of each stage as presented in this thesis. The overview of each stage can be summarised as follows:

- Stage 1: Single turbine model, this stage mainly focuses on the development of a modified hybrid Blade Element Momentum (BEM)-Actuator Disk (AD) model which is a combination of two variations of the BEM-AD models. During this stage, a model study was conducted which included the investigations of 2-dimensional vs 3-dimensional models and ANSYS CFX vs FLUENT. Additionally, a mesh suitability and sensitivity study were conducted to cover the use of a concentrated mesh and to investigate mesh density.
- Stage 2: Multiple turbine model, in this stage a multiple turbine wake interaction study was conducted, which evaluates, hydrodynamically, the array spacing of two turbines, a staggered arrangement of three turbines, different turbine sizes and the placement of turbines at different depth in the water column.
- Stage 3: Turbine array model, in this stage a tidal current turbine array model was developed using an optimised blade for two different array layouts employing a pseudo-transient RANS model. The developed array model was

then used to study and predict energy output for a range of different bathymetry and tidal resources to evaluate model appropriateness.

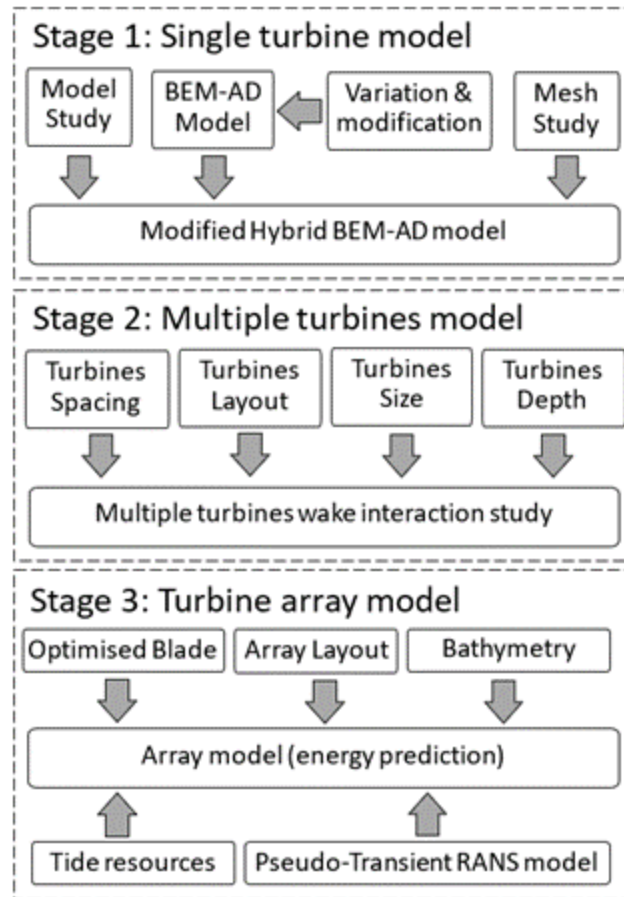


**Figure 1.1:** Demonstration of thesis scope and stages.

## 1.5 Aims and Objectives

The primary aim of this research is the development of a numerical model for predicting tidal current turbine wake effects for the purpose of array optimisation with a particular focus placed on downstream velocity, turbulence intensity, power output and energy predictions. The objectives of this work include the following:

- To construct a basic actuator disk model to predict tidal current turbine wake development in 2-dimensional and 3-dimensional fluid flow.



- To investigate the differences between ANSYS-CFX and ANSYS-Fluent in affecting the predictions of tidal current turbine wake development.
- Development of a methodology to construct a hybrid BEM-AD model to predict tidal current turbine wake effects for typical 3-dimensional fluid flow conditions.
- Compare the developed numerical model with experimental results, such as downstream wake velocity and turbulence intensity.
- Modification of the hybrid BEM-AD model to further improve the accuracy for predicting tidal current turbine wake development.
- Investigate the ability of the modified model to predict the wake interaction of multiple turbines.
- To evaluate the effects of turbine spacing, arrangements, turbine size and depth deployment on the wake interaction of multiple turbines.
- To construct an aligned layout array and staggered layout array models consisting of 12 turbines with an optimised tidal current turbine blade and to evaluate the wake interactions and energetic performance.
- Compare the predicted power for various domain conditions such as: ideal channel, headland and headland & island.
- Modification of the array to include yawing to further improve the power prediction of both the aligned layout and staggered layout arrays.
- Conduct a case study on the Shannon Estuary to predict the energetic performance of both the developed aligned layout and staggered layout arrays.

## 1.6 Report Structure

The report is systematically categorised into a number of main chapters in the following order:

Chapter 2 presents a literature review of the relevant research in the domain of tidal current turbine wake development and turbine representation models. The first

portion of the chapter discusses tidal currents and their behaviour followed by the factors affecting the wake development of tidal current turbines. Then, a review of the tidal current resources in Ireland, with a focus on the Shannon Estuary is presented. A description of the most widely used rotor representations and the type of turbulence models employed in the literature are described. Lastly, the chapter presents details on tidal current turbine array modelling with a focus placed on numerical modelling techniques and methodologies. A conclusion is then given on the key points raised in the chapter.

Chapter 3 presents the theory of tidal current turbine actuator disk modelling and wake development. The first part describes basic rotor theory and the fundamental equations used. A description of actuator disk theory and the Betz limit conditions were included in the second part, followed by a detailed description of blade element momentum theory along with the turbulent wake state correction model. Lastly, a description of the theory behind Computational Fluid Dynamics (CFD) is detailed, i.e. Reynolds Averaged Navier Stokes (RANS) equations, turbulence models, mesh discretisation and also ANSYS CFX and Fluent theory.

Chapter 4 presents the model development undertaken in this research. The chapter has two main sub chapters, the first sub-chapter focuses on the development of a hybrid BEM-AD disk model along with its various variations and modifications. In this sub-chapter, the numerical BEM model of the experimental blade was included along with the actuator disk configurations. Additionally, a mesh sensitivity and independence study were carried out and the results are presented. The second sub-chapter focuses on the development of an aligned layout and staggered layout array models. In this sub-chapter, the numerical BEM model of an optimised blade was included along with the modified actuator disk configurations. Furthermore, this sub-chapter also provides details on the parametric setup to achieve an averaged pseudo-transient model in RANS. The domain setup for an ideal channel, headland and headland & island are also detailed in this chapter. Lastly, the domain setup for the Shannon Estuary is detailed in this sub-chapter along with the validation of some of its inflow conditions.

Chapter 5 presents the results and a discussion of the work presented in this thesis. The chapter is broken down into three main sub-chapters which are the single tur-

bine model, multiple turbine model and the array model. In the single turbine model sub-chapter, the work focuses on the validation of the developed model against experimental measurements and also comparing the wake predictions of various different variations and modifications. The second sub-chapter presents the multiple turbine model sub-chapter which focuses on investigating the effects of spacing, layout, turbine size and depth deployment on the turbine-to-turbine wake interactions. The last sub-chapter focuses on the array model which presents an evaluation of the performance of an aligned and staggered layout array for a range of different domain conditions such as: ideal channel, headland and headland & island. A case study on the energetic performance of deploying the developed aligned and staggered layout array is detailed.

Chapter 6 presents a summary of the research, along with the key conclusions and recommendations for further progression of the research.

## 1.7 Original Contributions

The novel contributions of the research work can be summarised as follows:

- Two new variations of the BEM-AD model were developed which include velocity variations and radial variations to improve the wake prediction capability of the BEM-AD model. Both variations provide a better description of the disk properties (e.g. the porosity and resistance coefficients) in the BEM-AD model.
  - The velocity variation BEM-AD model describes the disk properties using two empirical formulas developed by incorporating the velocity profiles of the incoming current into account.
  - The radial variation BEM-AD model describes the disk properties using two empirical formulas developed by treating the disk as annular elements rather than treating it as an area-averaged value.
- A new meshing methodology was created which focuses on the region of interest known as the ‘concentrated mesh’ region in the single turbine model and known as the ‘turbine deployed area (TDA)’ in the turbine array model.

This approach managed to reduce the computational cost while still maintaining high numerical prediction accuracy.

- The development of an aligned layout and staggered layout tidal current turbine array model in a pseudo-transient RANS simulation. The pseudo-transient state approach was achievable in the RANS simulation by utilising the parametric configuration in ANSYS CFX. In the parametric configuration, the rate of change of tidal conditions (e.g. velocity and height) was treated as a series of instantaneous individual parametric inputs and the rate of change of energy yield of the array as a series of instantaneous parametric outputs.
- An analytical evaluation of the flow and energy predictions of the Shannon Estuary at a selected location for both the aligned layout and staggered layout arrays was developed. The study carried out showcases the energy yield of the arrays under fluctuations of tidal conditions in a year which is important in predicting the annual energy output of the tidal energy site.

## 1.8 Publications

1. C.M. Pang, D. M. Kennedy, and F. O'Rourke, "CFD study of small scale tidal current turbine array in predicting energy extraction in Shannon Estuary", Energy, (Under Review).
2. C.M. Pang, D. M. Kennedy, and F. O'Rourke, "An Investigation on the wake prediction capability of a hybrid modified BEM-AD model using RANS-CFD", Energy, (Under Review).
3. C.M. Pang, D. M. Kennedy, and F. O'Rourke, "A CFD investigation of the wake interaction of various spacing between tidal current turbines using a RANS modified BEM-AD model" in SEEP 2022, Proc. of the 14th International Conference on Sustainable Energy & Environmental Protection, London, UK, Sept 12 – 15, 2022.
4. C.M. Pang, D. M. Kennedy, and F. O'Rourke, "A CFD investigation of the changing disk characteristics on the wake development of tidal current turbine using a modified BEM-AD model" in ECOS 2022, 35th Int. Conf. on Efficiency, Cost, Optimisation, Simulation and Environmental Impact of Energy Systems, Copenhagen, Denmark, July 3 - 7, 2022.

5. C.M. Pang, D. M. Kennedy, and F. O'Rourke, "The Impacts of tidal shear profiles on the wake development of a tidal current turbine using a hybrid BEM-AD model" in SEEP 2021, Proc. of the 13th International Conference on Sustainable Energy & Environmental Protection, Vienna, Austria, Sept 13 – 16, 2021.
6. C.M. Pang, D. M. Kennedy, and F. O'Rourke, in EWTEC 2021, "An investigation of various inflow effects on the wake development of a hybrid BEM-actuator disk model using CFD" in EWTEC 2021, Proc. of the 14th European Wave and Tidal Energy Conference, Plymouth, UK, Sept 5 – 9, 2021.
7. C.M. Pang, D. M. Kennedy, and F. O'Rourke, "An investigation of a hybrid BEM-actuator disk approach in predicting wake development in a RANS-CFD model" in ECOS 2021, 34th Int. Conf. on Efficiency, Cost, Optimisation, Simulation and Environmental Impact of Energy Systems, Taormina, Italy, June 28 - July 2, 2021.
8. C.M. Pang, D. M. Kennedy, and F. O'Rourke, "Comparison of RANS turbulence models in predicting wake development in a 2-dimensional actuator disk model" in ECOS 2020, 33rd Int. Conf. on Efficiency, Cost, Optimisation, Simulation and Environmental Impact of Energy Systems, Osaka, Japan, June 29 - July 3, 2020.
9. C.M. Pang, D. M. Kennedy, and F. O'Rourke, "The Effects of Inflow Turbulence Intensity on predicting wake velocity in a two-dimensional RANS Actuator disc model" in EWTEC 2019, Proc. of the 13th European Wave and Tidal Energy Conference, Naples, Italy, Sept 1 – 6, 2019.

# Chapter 2

## Literature Review

### 2.1 Introduction

The demand for renewable energy is increasing due to international energy policies aiming to reduce the dependence on carbon-intensive fossil fuels to meet energy demand. Recently, the advancement in renewable energy technology has pushed forward the development of horizontal-axis tidal current turbine (TCT) technology, making it more competitive in the renewable energy industry (Chowdhury et al. 2021). The TCT is a machine that converts kinetic energy in water currents into mechanical energy and then electrical energy by submerging turbine in moving body of water such as ocean, rivers and channels (O'Rourke et al. 2010). Tidal energy is an attractive and promising alternative for future electricity generation (Ramírez et al. 2016). Furthermore, a TCT system requires very little investment in terms of construction and unlike its hydro-counterparts, tidal barrage technology and hydropower plants, there isn't a need to construct reservoirs or dams to amass water, reducing some of the environmental concerns (Khan et al. 2008, Nago et al. 2022).

The principle of operation of a TCT is very similar to a wind turbine, however there are fundamental differences in operation, deployment, cost and fluid flow interaction (Lande-Sudall et al. 2018). Furthermore, in comparison to wind energy resources, tidal energy resources have a number of noteworthy advantages. Firstly, tidal energy resources are predictable over large timescales, i.e. the tidal change can be predicted in advance. Moreover, unlike solar and wind energy, it is less dependent on weather conditions making it more reliable, the only exception is any

tidal-wave interaction. Secondly, water is roughly 800 times more dense than air; since power is directly proportional to fluid density, therefore theoretically a TCT can produce more power than a wind turbine of an identical rotor size operating under the same fluid velocity (Ahmed 2012). Lastly, tidal energy resources are abundant in many coastal regions and coincidentally about half of the world's population lives within 200km of the coastline and this number is growing (Council 2016, Creel 2003). Ergo, it is expected that tidal energy, and in particular tidal current energy, will contribute greatly to this growing energy demand. Studies have placed the global potential tidal resource at 3 TW but only 50 GW of this resource is considered feasible for utilisation (Wang & Wang 2019, Rusu & Venugopal 2019, Chen et al. 2018). Many researchers have studied the possibility of deploying TCT in different hydrokinetic environments throughout various parts of the world and concluded that most of the exploitable tidal energy resources are concentrated in regions with huge tidal ranges such as loughs, estuaries and the flow between islands (Wang & Wang 2019, Iglesias et al. 2021, González-Gorbeña et al. 2015, Kabir et al. 2015, O'Rourke et al. 2010). However, to fully utilise TCTs there are still significant challenges to overcome such as technological and economic issues (Kabir et al. 2015, O'Rourke et al. 2010).

The development of TCTs has drawn on the experience and knowledge of the more mature wind turbine industry. However, the overall TCT industry is still underdeveloped and very costly for energy extraction in comparison to the wind industry. Some of the notable technological advancements in the TCT industry are since 2003, the first tidal turbine was deployed by Marine Current Turbines (Marine Current Turbine (MCT)); in 2007, the deployment of the world's first grid-connected tidal array by Verdant Power under the Roosevelt Island Tidal Energy (Roosevelt Island Tidal Energy (RITE) ) project. In the following year, 2008, MCT successfully installed the 1.2MW SeaGen turbine, this was the world's first commercial-scale TCT, and it was deployed in Strangford Lough, Northern Ireland. Furthermore, many other developers have since followed with successful deployment of full-scale devices. These examples show the readiness and progression of the TCT industry towards commercial-scale array deployment. However, despite the readiness of the industry; significant work is still required on array studies and there is a lack of available measured TCT array data due to a limited number of deployments to date and the lack of methodologies to aid the arrangement of TCTs in arrays further hinders the

progression of commercial-scale arrays (Filho et al. 2017). Hence, an understanding and prediction of wake behaviour is paramount in the optimisation of TCT arrays, i.e. in a TCT array the upstream wake will directly influence the performance of downstream turbines such as power output and turbine loading. In array studies, the arrangement and placement of turbines will give rise to complications not seen in single turbine operation, such as wake-to-wake interaction that could greatly affect wake recovery and turbine efficiency (Nishino 2013).

This chapter focuses on reviewing the most relevant existing literature pertaining to the wake modelling of TCTs. In this chapter, an investigation of experimental and numerical wake modelling of both single turbine and arrays is conducted. The chapter also presents a description of the various techniques used in wake modelling, such as the different numerical modelling techniques and the various rotor representation methods utilised. Additionally, the factors affecting wake formation and recovery in both single turbine and arrays are also investigated.

## 2.2 Tide and Tidal Current

Tides are the result of the interaction of the gravitational force of the moon and, to a lesser extent, the sun, on the seas. Tidal cycles can be categorised into one of three basic groups (Greaves & Iglesias 2018):

- Semi-diurnal (half-day) cycle: It is a tide effect caused by the rotation of the earth within the gravitational pull of the moon and occurs every 12 hours.
- Diurnal (daily) tides: This type of tide pattern only consists of one high tide and one low tide in a 24-hour period. An example region where this tidal type occurs is the Gulf of Mexico.
- 14 days cycle: This tidal pattern is caused by the superposition of the gravitational fields of the moon and sun. The sun's gravitational field reinforces that of the moon at new moon and full moon and results in maximum tides or spring tides. At quarter phases of the moon, there is partial cancellation, resulting in minimum or neap tides.

Because of the unique repetitional characteristics of tides, it can be predicted with great accuracy. For that reason, tidal energy is more predictable in comparison



to other forms of renewable energy. Schemes that use tidal energy harness energy from the following: twice-daily tides; on the resultant upstream flows and the downstream ebbs in estuaries; the lower reaches of some rivers; and tidal movement out at the sea. This is an inexhaustible energy source and can be classified as renewable and is utilised to supply electrical energy. However, converting this abundant energy resource into useful electrical energy is difficult and expensive. Tidal energy can be classified into two main types (Charlier & Finkl 2009):

- **Tidal Current.** Tidal current systems use the movement, principally the kinetic energy, of the huge quantities of flowing water, which is approximately 800 times more dense than air, to output energy. Early indications from demonstration sites suggest that tidal current devices can have minimal environmental impact.
- **Tidal Range.** Energy from the tidal range can be captured using a tidal barrage or lagoons, which make use of the difference in tidal height, the potential or head, between high and low tides. Huge civil infrastructure costs, the lack of viable sites and environmental impact have restricted the development of this type of system.

Although the prospects for tidal range energy systems, such as the mature tidal barrage technology, look relatively limited at present, the tidal current energy systems have garnered significant attention. The concept behind tidal current energy systems is very straightforward: it utilises the kinetic energy from tidal currents in the same way a wind turbine extracts the kinetic energy from a moving air mass. To provide optimum energy output in areas where sufficiently rapid tidal flows occur, TCTs need to be constructed in arrays, analogous to wind farms underwater.

### 2.3 Tidal Current Technologies

The concept of harnessing tidal current energy is nothing new. The current systems typically operate on the same principle as a wind turbine, but harness kinetic energy from tidal current instead of from wind to generate electricity (Lande-Sudall et al. 2018). Statistics have shown between the years 2006 to 2013, there is more than 40 novel tidal current systems have been showcased (Mueller & Wallace 2008). One major difference between these systems is the type of turbine being applied. These

technologies can be classified, based on the turbine characteristics, into six different classes as follows:

- **Horizontal-axis turbine (Horizontal-axis turbine (HAT)):** Similar to how wind turbines capture energy from moving air, a horizontal axis tidal current turbine converts the kinetic energy of free-flowing water into rotational energy, which is then transferred into electricity (Khan et al. 2009).
- **Vertical-axis turbine (Vertical-axis turbine (VAT)):** The primary working principle of this type of system is similar to that of horizontal systems, except that the tidal current rotates the rotors around a vertical axis to the current flow direction to generate power (Khan et al. 2009).
- **Oscillating hydrofoil:** A hydrofoil is attached to a swing arm, and as marine currents flow past either side of the hydrofoil, they generate lift. This motion then drives fluid through a hydraulic circuit by means of a motor, and the resulting rotational movement can be converted into electricity (Ma et al. 2017).
- **Ducted Turbine / enclosed tips:** These devices consist primarily of horizontal axis turbines housed within a nozzle, which is designed to accelerate and direct fluid motion. Enclosing the turbines within a nozzle may also reduce turbulence around the turbines and facilitate the alignment of water flow for optimal turbine performance (Maduka & Li 2022).
- **Archimedes' Screw:** The Archimedes screw is a helical system that utilises a change in water level along the helix to generate power by rotating the turbines (Zhang et al. 2022).
- **Tidal kite:** Tidal kite systems involve a small turbine attached to a kite, which is propelled by the flow which increases the relative speed of flow entering the turbine (Andersson et al. 2018).

It should be noted that there may exist other types of turbines beyond those mentioned above, which encompass technologies with unique and distinct system designs, and for which information on the device's features may not be readily available. Generally, a TCT converts the kinetic energy of free-flowing water into electrical energy, and the blades play a crucial role in maximising turbine output and

providing sufficient support to the blade structure. So, designing the hydrofoils correctly is of utmost importance. HATs and VATs systems are some of the more popular designs in the industry and both have seen great improvement and development in recent years (Nachtane et al. 2019, 2020, Touimi et al. 2018, Khan et al. 2009). HATs are highly regarded as one of the most cost-effective technologies for large-scale tidal current turbines with power capacities exceeding 500 kW, and are considered one of the more mature technologies within the diverse field of tidal current energy (Zhou et al. 2017). Some experimental tests have confirmed that the roughness of the blades in a VATs has a negative impact on turbine performance when compared to HATs (Priegue & Stoesser 2017). The main drawbacks of vertical axis turbines include a limited range of suitable current velocities, relatively low self-starting capability, and issues with dynamic stability, which restrict their performance to lower current conditions (Tarfaoui et al. 2019). Although several turbine developments have been reported in research articles and review papers, many of these developments were only at the prototype phase with only a few commercial-scale TCT projects (Sangiuliano 2017).

The development of tidal current energy technology, from conceptualisation to industrial implementation, is typically envisioned to progress through five distinct stages in terms of Technology readiness levels (TRL) as seen in Table 2.1. An investigation in 2017 has shown that the UK and the USA are currently leading the tidal turbine technology industry (Sleiti 2017). The study surveyed 75 developers, with 29 developers from the UK and 16 developers from the USA. Out of the 75 developers investigated, 34 developers have completed the lab-testing stage and are heading on into commercialisation (TRL7 and 8) developers have reached commercialisation (TRL9).

In 2006, OpenHydro made history by becoming the first company to install its tidal turbine prototype at the European Marine Energy Centre (EMEC). The EMEC serves as a test centre for wave and tidal power development, providing developers with the unique opportunity to test full-scale grid-connected prototype devices in unparalleled wave and tidal conditions. The EMEC's efforts have contributed significantly to the development of tidal turbine technology in Europe. Ever since then, there have been numerous TCT projects operating globally. One good example is Verdant Power's RITE project which deployed the first grid-connected tidal

**Table 2.1:** Tidal current development protocol. TRL refers to technology readiness levels (Nachtane et al. 2020)

Stage	Tidal current development protocol
TRL 1–3	Tidal-current energy conversion concept formulated (Scope of Protocol begins here).
TRL 4	Technical analysis (CFD, FEA, Dynamic analysis ...) at intermediate scale.
TRL 5–6	Technical analysis at large scale.
TRL 7–8	Performing prototype-scale tests at sea.
TRL 9	The experimentation of an industrial demonstrator at sea for a prolonged period.

turbine array in 2007 consisting of six units of 5-m-diameter turbines. Since then, the RITE project has moved onto its next stage with the array number increased to 35 units (Verdant Power 2010). Another example is the MeyGen Project deployed in the Pentland Firth, this project is currently the largest tidal current energy project worldwide (Atlantis Project 2010), the project exported 50GWh per annum to the grid in February 2023 (Garanovic 2023). The Magallanes Renovables company successfully installed a grid-connected 2nd generation 2MW tidal platform, ATIR, in April 2021 in Orkney, Scotland, which is a floating platform TCT (NWE Secretariat 2021). Table 2.2. is a summarisation of some tidal turbine devices as of 2017 made by Ahmed (Sleiti 2017), where H is a horizontal-axis turbine, V is a vertical-axis turbine and D is the ducted turbine.

**Table 2.2:** Tidal turbine devices summarisation (Sleiti 2017)

<b>Company</b>	<b>Device name</b>	<b>TRLs</b>	<b>Turbine type</b>	<b>Country</b>
Alstom Hydro	BELUGA 9	TRL7 - 8	HD (bi-symmetrical)	France
Alternative Hydro Solutions	Freestream Darries Water Turbine	TRL9	V	Canada
Aquantis Ecomerit Technology	C-Plane	TRL5	H	USA
Aquascientific	Aquascientific Turbine	Unknown	Others	UK
Atlantis Resources Corp	AK-1000	TRL8 - 9	H (dual-turbines)	UK
Atlantisstorm	Atlantisstorm	TRL6	Others	Germany
Balkee Tide and Wave Electricity Generator	TWPEG	TRL5 - 6	Unconventional	Mauritius
BioPower Systems Pty Ltd	BioStream	TRL1 - 5	Oscillation	Australia
Blue Energy Canada Inc	Vertical Axis Hydro Turbine	TRL6 - 7	V	Canada
Bourne Energy	RiverStar /RS Portable /Tidal-Star	TRL1 - 5	H (dual-turbines)	USA
Cetus Energy	Cetus Turbine	TRL6 - 8	H	Australia
Clean Current Power Systems	Clean Current Turbine	TRL8 - 9	HD (bi-directional)	Canada
Current Power Sweden AB	Current Power	TRL1 - 5	V	Sweden
Current2Current	Current2Current Tidal Turbine	TRL1 - 5	Unconventional	UK
Cyclo Ocean	Subsurface Current Generator	TRL1 - 5	HD	USA
Ecofys	Tidal Wave Rotor	TRL6	V and wave	Netherlands
Firth Tidal Energy	SeaCats	TRL1 - 5	H (unconventional)	UK
Flumill	Flumill Power Tower	TRL1 - 5	Unconventional	UK
Free Flow 69	Osprey	TRL1 - 5	Flipping	USA
Free Flow Power Corporation	SmarTurbine (river)	TRL7 - 9	HD	USA
GCK Technology	Gorlov Helical	TRL9	V (self-start)	USA
Greener Works Limited	Relentless	TRL1 - 5	Unconventional	UK
Hales Energy Ltd	Hales Turbine	TRL5	V (Flip wind Rotor)	UK
Hammerfest Strom	Hammerfest Strom 1000	TRL8 - 9	H (pitch-control)	Norway

<b>Company</b>	<b>Device name</b>	<b>TRLs</b>	<b>Turbine type</b>	<b>Country</b>
Hydra Tidal Energy Tech.	MORILDII	TRL8 - 9	H (dual-turbines)	Norway
Hydro Green Energy	hydrokinetic turbine	TRL5 - 7	HD	USA
Hydro-Gen	Hydro-Gen	TRL5 - 6	H	France
HydroRing	HydroRing Turbine (river)	TRL5 - 6	HD	Netherlands
Hydrovolts Inc	Flipwing Turbine Class I, II and III	TRL5 - 7	V (Flipping Rotor)	USA
Ing Arvid nesheim	WaterTurbine		Wave and current	
Kepler Energy	Kepler Transerse Horizontal Axis	TRL1 - 5	V (self-start)	UK
Lunar Energy	Rotech Tidal Turbine (RTT)	TRL8 - 9	HD (bi-symmetrical)	UK
Magallanes Renovables	Magallanes Project	TRL1 - 5	H	Spain
MCT	SeaGen	TRL9	H (pitch-control)	UK
Minesto	Deep Green	TRL7 - 9	H	Sweden
Natural Currents energy Severices, LLC	Red Hwak Tidal Power Generator	TRL7 - 9	H	USA
Nautricity Ltd	CoRMat	TRL9	H	UK
Neo-Aerodynamic	Hydro Unit	TRL5 - 6	V	USA
Neptune Renewable Energy	Neptune Proteus	TRL7 - 8	VH	UK
New Energy Crop	EnCurrent Power	TRL9	V	Canada
Norwegian Ocean Power	Pulsus	TRL1 - 9	V	Norway
Ocean Flow Energy	Evopod	TRL6	H	UK
Ocean Renewable Power Company	ORPC Power System	TRL8 - 9	V (self-start@1.0m/s)	USA
Offshore Islands Ltd	Current Cather (ocean current)	Limited information	HD	USA
OpenHydro	OCT	TRL9	HD (reverse rotation in opposite flow dir.)	Ireland
Ponte di Archimede	Kobold Turbine	TRL7 - 9	V (self-start)	Italy
Pulse Tidal	Pulse-Stream	TRL7 - 8	Oscillation	UK
Robert Gordon University	Sea Snail	TRL7 - 8	Mooring system	UK
Rugged Renewables	Savonius Turbine		Unconventional	UK

Company	Device name	TRLs	Turbine type	Country
Scotrenewables	Scotrenewable Tidal	TRL8	H (yaw-control)	UK
SMD Hydro	TidEL	TRL1 - 5	H	UK
Sustainable Energy Research Group of University of Southampton	Marine Current Turbine	TRL5 - 6	H	UK
Sustainable Marine Technologies	Plat-O	TRL1 - 5	H	UK
Swan turbines Ltd.	Swan Turbine	TRL6 - 7	H (yaw-control)	UK
The Engineering Business	Oscillation		Oscillation	UK
Tidal Energy Ltd	Delta Stream	TRL6 - 7	H (yaw-control)	UK
Tidal Energy Pty Ltd	DHV Turbine	TRL7 - 9	VH	Australia
Tidal Generation Limited	Deep-gen	TRL8 - 9	H (pitch-control)	UK
Tidal Sail	Tidal Sails	TRL7 - 8	Unconventional	Norway
tidal current	tidal current	TRL5 - 7	H	UK
Tideng	Tideng	TRL5	Unconventional	UK
Tocado International BV	T50/T100/T200/	TRL9	H (bi-symmetrical)	UK
UEK	Underwater Electric Kite	TRL9	HD	USA
Verdant	RITE	TRL8 - 9	H (pivot)	USA
Voith Hydro	Seaturtle Tidal Park	TRL7 - 8	H (bi-symmetrical)	Germany
Woodshed Technologies	Tidal Delay			UK and Australia

## 2.4 Tidal Resource in Ireland

The island of Ireland has a coastline of roughly 7,500km in length with access to several important oceans and seas (Nairn 2005). The Irish Sea has some of the most energetic tidal flows accessible by the island, this flow is a result of ocean currents entering the area from the North Channel and St. George Channel (SEI 2004). However, for effective extraction of energy from tidal current, velocity is a major factor (O'Rourke et al. 2010). Studies have shown that large tidal resources are commonly located adjacent to headlands or between land masses and accelerated flow can be achieved through the funnelling effect when flow passes through narrow straits (Charlier & Finkl 2009, Boyle 2004). A resource assessment has

been carried out by the Sustainable Energy Authority of Ireland and was published in a report entitled “Tidal and Current Energy Resources in Ireland” in 2004 (SEI 2004). The assessment has identified the theoretical tidal energy resources available in Ireland is about 230 TWh/y. However, limitations and constraints from both technology and site availability needed to be taken into account. As a consequence, the practical accessible tidal current energy resource in Ireland is about 2.663 TWh/y. The report further narrowed down the viable tidal current sites by factoring in variables such as costs, scale, grid connection and resource distribution. There were eleven sites identified in the report which met the criteria as shown in Figure 2.1 (SEI 2004).



**Figure 2.1:** Eleven viable tidal energy site locations identified in Ireland (SEI 2004).

Out of the eleven sites identified, six sites have a viable tidal energy resource greater



than 50 GWh/y. Three of the sites located in Northern Ireland are the North East Coast, Copeland Islands and Strangford lough; two sites located on the east coast were the Codling & Arklow Banks and Tuskar Rock & Carnsore Point; and one site located on the west coast is the Shannon Estuary. The literature review focuses on the sites in the Republic of Ireland where the three highest were the Tuskar Rock & Carnsore Point with a viable tidal energy resource of 177GWh/y; Shannon Estuary with a viable tidal energy resource of 111GWh/y; and Codling & Arklow Banks with a viable tidal energy resource of 70GWh/y as shown in Figure 2.1 (SEI 2004).

The Shannon Estuary has the lowest cost among the three highest viable tidal energy resources in the Republic of Ireland. The reason Shannon Estuary site has a lower cost compared to the other two high potential sites is due to foundations and grid connection. It is easier to construct foundations and connect to the grid in an estuary compared to an offshore site. For example, the estimated capital cost of an installation in the Shannon estuary was €1700/kW, while the estimated capital cost of an installation along the Codling & Arklow Bank was €3700/kW (SEI 2004). From the aspect of resource viability and installed cost, the Shannon Estuary would be a location of much focus, and as such an array study is necessary to greatly aid the development of a tidal energy project in the Shannon Estuary.

### 2.4.1 Shannon Estuary

The Shannon Estuary is located on the west coast of Ireland. In recent years, studies and measurements have been carried out to further investigate the tidal energy resources in Shannon Estuary (O'Rourke et al. 2014, Fouz et al. 2022). Figure 2.2 shows the variation of the mid-depth tidal-current speed over a lunar month for Shannon Estuary. The varying tidal current speed with respect to time is crucial as it provides important daily period availability information when harnessing available tidal energy resources. The Shannon Estuary overall has a peak spring-tide speed of 2.02 m/s over the lunar month and an overall mean tidal-current speed of 0.83 m/s over the lunar month (O'Rourke et al. 2014).

The tidal current flow at Shannon Estuary mainly flows from the east and the west-south directions. Figure 2.3 illustrates the tidal rises for the Shannon Estuary over a lunar month at depths of two, four, six, eight and ten metres. It is also shown that

**Table 2.3:** A summary of the hydrokinetic characterises of the seven potential exploitable area.

area	Surface ( $km^2$ )	Mean water depth (m)	Mean TSE	Max TSE
I	6.1	23	2.7	5.7
II	3.3	17.4	3.0	5.5
III	0.4	26.4	1.4	2.5
IV	5.7	18.7	4.4	9.4
V	1.1	30.0	2.5	3.7
VI	0.1	23.3	2.3	2.8
VII	1.0	12.6	1.4	2.1

the directions of the tidal currents do not vary much through different depths over the lunar month. The seabed of Shannon Estuary is a mixture of mud, sand and gravel with a seabed roughness of 0.3mm (O'Rourke et al. 2014).

As flow travels along the estuary, it will experience changes in its current flow speed due to the topography of the estuary. According to a study done by D.M. Fouz (Fouz et al. 2022), there are seven potential exploitable areas in Shannon Estuary as highlighted in Figure 2.4 with details given of the high tidal current exploitability (TSE) index.

Table 2.3 presents a summary of the surface area, mean water depth, mean TSE and max TSE of the seven potential exploitable areas. TSE is an index used to measure the exploitability of tidal current resources at an area, the mean TSE index was identified using mean flow speed, while the max TSE index was identified using max flow speed. Area I, II and IV have the largest surface area of  $6.1 km^2$ ,  $3.3 km^2$  and  $5.7 km^2$  respectively. Also, areas I, II and IV have the largest mean TSE and max TSE. While areas III, V and VI have the deepest mean water depth of 26.4m, 30.0m and 23.3m.

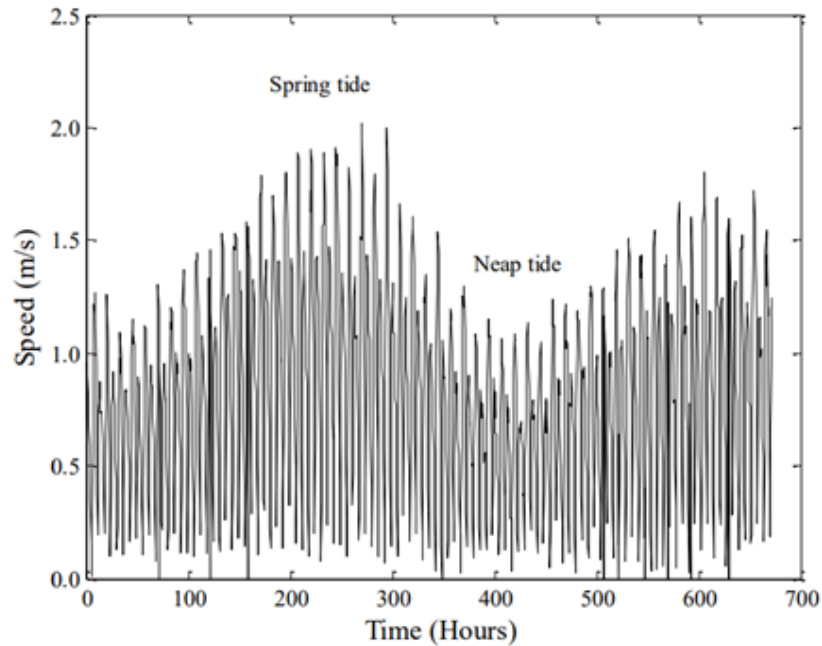


**Figure 2.2:** Measured tidal-current speed at mid-depth of the water column over a lunar month for a site in the Shannon Estuary (O'Rourke et al. 2014).

## 2.5 Turbine wake

The area downstream of a TCT which experiences disturbed flow is known as a wake. The wake is a result of the fluid flow around an object immersed in a fluid, for example, a TCT. A turbine wake can be defined as a formation of spiral fluid motion which occurs after fluid flows through the rotor (Nago et al. 2022). The region within the wake experiences a velocity deficit due to energy loss. For a wake to form, the rotor must experience fluid drag caused by a reduction in initial velocity, intense pressure gradients and vortex structures; these causes can be summarised as a momentum loss. An idealised wake tends to conserve momentum and gradually expand itself in a cone shape (Myers & Bahaj 2010). Investigations have shown that the occurrence of turbulent mixing in the region between the wake and undisturbed flow field brings energy into the wake region that could ease the velocity deficit (Myers & Bahaj 2010, Ivanell et al. 2010). According to Barthelmie, the characteristic of a rotor's wake is mainly affected by two key factors which were the body shape and Reynolds number (Barthelmie et al. 2010). One can generally observe these three phenomenon in a turbine's wake (Chamorro et al. 2013, Kang et al. 2014):

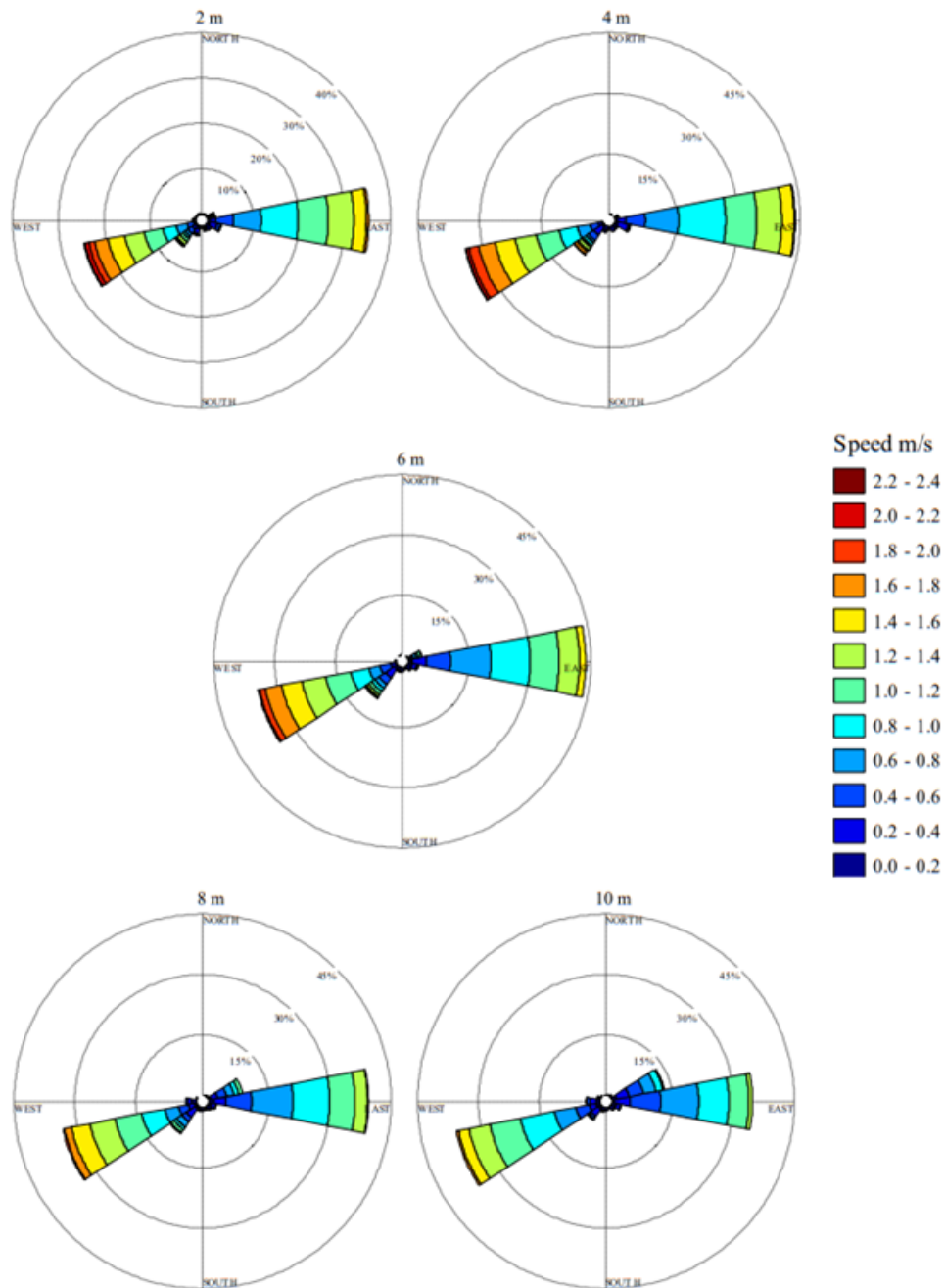


**Figure 2.3:** Tidal rises of measured tidal-current data over a lunar month at a site in Shannon Estuary for depth of 2m, 4m, 6m, 8m and 10m (O'Rourke et al. 2014).

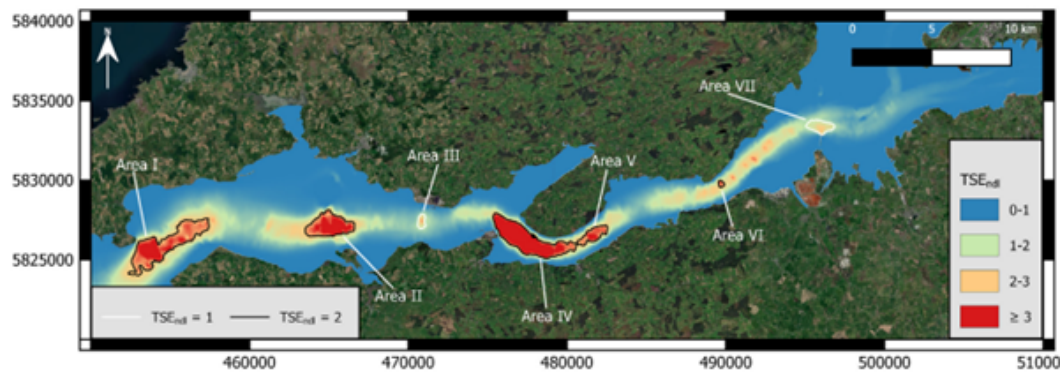


**Figure 2.4:** Potential area with high exploitable tidal energy resources in Shannon Estuary (Fouz et al. 2022).

- Deficit in average flow caused by drag which is generated from the turbine structure and energy loss.
- Change in turbulence due to vortex swirls imposed by the turbine structure and blade.
- Intricate interaction between turbulent structures created by turbines and natural channels.

The fluid in the wake experiences different flow conditions to that of the flow field, such as reduced fluid flow speed, reduction of fluid momentum, increased turbulence and swirl. The flow behaviour in the wake, as illustrated in Figure 2.5, can be classified into the near wake and far wake. The near wake features of the wake are directly shaped by the sharp flow gradient velocity known as velocity deficit and will also experience a peak in turbulence intensity because of complex vortex formations such as wake swirl. Whilst the far wake region experiences a recovery in fluid velocity and a fall in the overall turbulence intensity of the fluid.

As the fluid flow approaches the turbine, the tidal current velocity will decrease, and the pressure will rise. However, once the fluid flows through the turbine, the pressure will drastically decrease to its lowest level, immediately downstream of the turbine. Furthermore, the velocity and pressure field become non-uniform due to the interaction between the flow and the rotating turbine which causes vortex shedding. As the flow continues to move further downstream away from the turbine plane, the influence of the wake expands radially, the velocity of the wake decreases and the

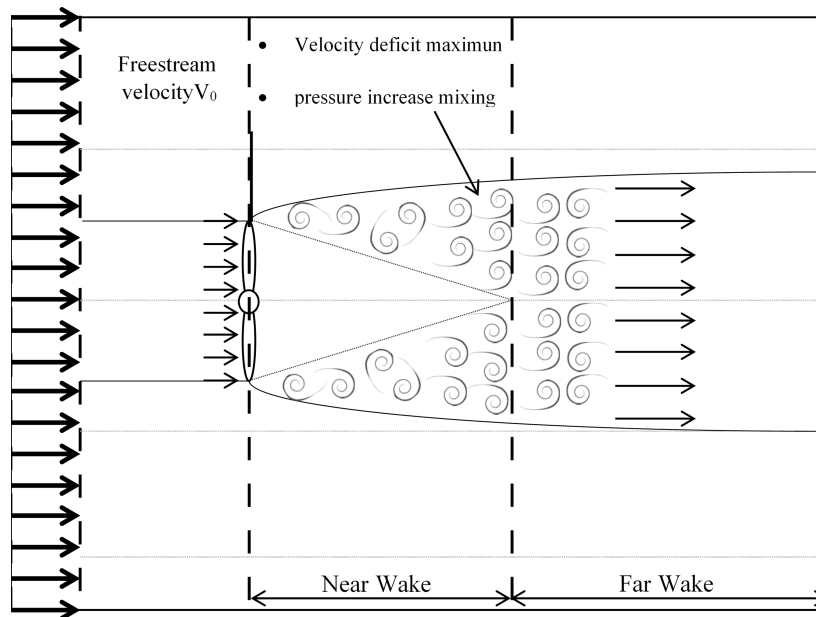


**Figure 2.5:** Near wake and far wake regions downstream of a turbine.

local pressure increases exponentially until reaching the ambient pressure, which marks the end of near wake and the beginning of far wake region usually at around five diameters (rotor diameter distance) downstream. In an idealised wake situation, after a certain distance downstream of the turbine, the wake should almost dissipate and the flow should recover to its original initial state (Myers & Bahaj 2010). However, it is evident that the flow cannot fully recuperate to its initial state due to the extraction of energy from the flow system.

It is important to understand the behaviour of a TCT wake and also the factors influencing wake generation. One of the key features of TCT wake is velocity deficit. Due to the momentum change of the fluid flow caused by the turbine, the flow velocity decreases and accordingly, the flow downstream of the turbine is slower compared to the upstream velocity. Some studies observed that velocity deficits due to wakes can last up to or more than 20 diameters downstream of the TCT (Chen et al. 2017, Masters et al. 2015). Swirling occurs in the wake of a TCT, an opposing rotational torque of equal magnitude to the turbine is generated in the flow by the turbine. A swirl flow is defined as the flow undergoing simultaneous axial and vortex motion. Therefore, the fluid downstream of the turbine rotates in the opposite direction of the turbine blades. A study has shown that swirl effects from a three-

bladed TCT are weak in far wake region (Morris et al. 2016).

The rotation of the turbine blades also causes the formation of tip vortices shedding into the flow downstream of the turbine. A number of studies have investigated this phenomenon using a range of numerical modelling techniques (Jung et al. 2017). There are differences between a TCT wake and a wind turbine wake, with the former considered to be asymmetric and the latter is axisymmetric. This is due to the influence of some physical features, such as the seabed, the free-surface and the tidal turbine support structure, which affect the shape and direction of the wake, these changes are known as meandering (Bahaj et al. 2011, Apsley et al. 2018). Several studies have found that meandering typically begins  $4D$  downstream and has a high mean velocity fluctuation level (Ouro & Stoesser 2019, Chamorro et al. 2013, Kang et al. 2014). Flow recovery is another crucial element in the wake, flow recovery occurs as a result of mixing between the low energy wake region and the ambient flow region of the fluid flow. Momentum is transferred from the ambient fluid flow back into the wake, as the distance increases downstream from the turbine, and as a result the rate of dissipation of the wake increases. Therefore, the velocity recovers with distance downstream from the turbine, with studies showing that turbulence enhances the recovery process (Jump et al. 2019, Pang et al. 2019).

The wake created by a TCT is mainly dependent on the extraction of energy from the fluid flow which requires an understanding of the tidal flow parameters such as speed and direction, to predict turbine power output and the wake characteristics. However, there are other factors that affect and influence the behaviour of the wake such as water depth, blockage effects, turbulence, and waves, to name a few. The depth and bathymetry of a tidal energy site such as the width of a channel will influence the wake formation. The expansion and meandering of the wake can be influenced by the distance between the turbine and the seabed, water surface and channel walls. i.e. blockage effects. Experimental and numerical studies have shown that deeper channels lead to faster wake recovery in comparison to shallow channels for similar fluid flow conditions (Aghsaei & Markfort 2018). The roughness of the seabed will induce friction onto the water flow forming shear profiles. This phenomenon causes the turbine to experience different flow velocities for a TCT blade as it rotates from its lowest position to its highest position. Furthermore, tidal shear will affect the energy extraction of a tidal turbine especially devices deployed close

to the seabed which will lead to changes in wake formation and recovery. Additionally, shear profiles can differ with depth, flow direction and seabed roughness (Guillou & Thiébot 2016).

A number of papers in the literature have described turbulence and how upstream turbulence significantly affects wake formation and recovery. In addition to affecting wake formation, turbulence plays a role in the hydro-structural performance of the turbine such as loading, fatigue, power extraction, etc (Ahmed et al. 2017, Milne et al. 2016). Ambient turbulence is seen to increase wake recovery (Pang et al. 2019, MacLeod et al. 2002), also a large regular structure generates a short life span wake compared to an irregular structure (Gant & Stallard 2008). Experimental studies have shown when observing turbulence (Stallard et al. 2013), turbulence intensity (turbulence intensity (TI)) is highest at the outside of the wake in the near-wake region due to a strong boundary layer. Whilst in the far wake region the TI was much more uniform because of turbulent mixing between the wake and the ambient surrounding fluid. Further studies have also shown that at around 10 diameters (10D) downstream, the turbulence level reached uniformity and after 12D downstream the TI returned to the background TI level (Stallard et al. 2015).

Another factor affecting tidal flow wake is the free surface, especially the influence of surface waves. The operation of a TCT is complex when wave conditions are included, this is because waves cause transient effects in the tidal current flow (Sufian et al. 2017, Zang et al. 2019, Holst et al. 2015). Furthermore, waves also propagate at any given direction either in-line, opposing or at an angle to the tidal current flow direction (Ward et al. 2018). Some studies show that the variation of oscillation of the wave is also affected by the amplitude and frequency of the wave (Draycott et al. 2019). In some cases, it was observed that the wave can increase the magnitude of velocity fluctuation up to two times in the upper region of the wake (Stallard et al. 2013). A number of studies involving numerical modelling have predicted wave influence on wake and its recovery by enhancing the mixing of local turbulence and the fluid flow behind the TCT (Sufian et al. 2017). Incorporation of the free surface is necessary for computational fluid dynamics (CFD) models if wave interaction is to be expected (O'Doherty et al. 2018). Other notable factors influencing wake development are temperature, wind conditions, storm surge, neap-spring tidal cycles, etc.



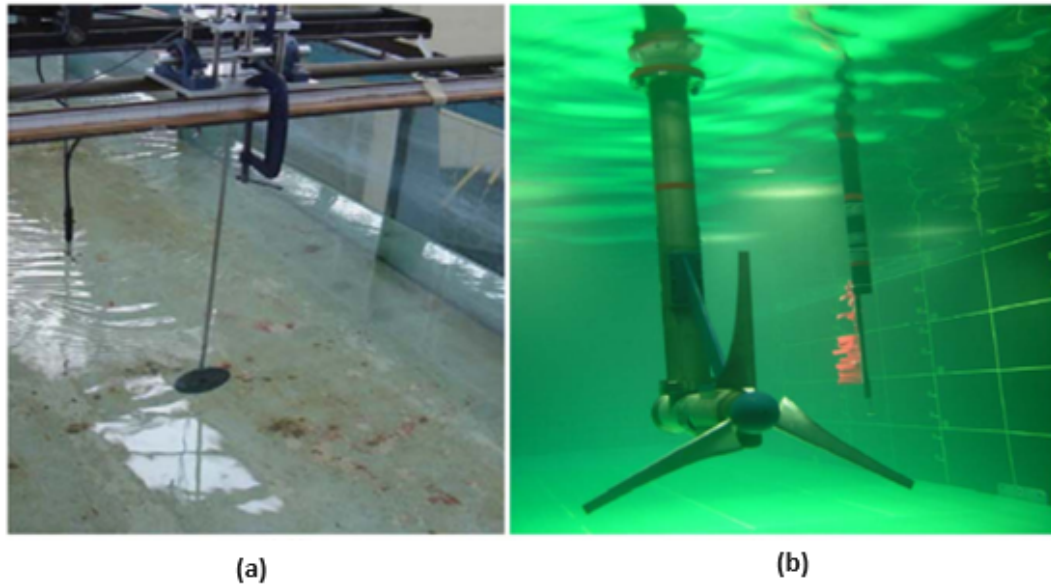


**Figure 2.6:** Types of rotors used in laboratory studies, (a) mesh disk rotor simulator (Myers & Bahaj 2010) and (b) 0.8-m-diameter scaled rotor (Myers & Bahaj 2009).

## 2.6 Experimental modelling

Experimental and laboratory studies of scale tidal current turbines have mainly focused on the assessment of hydrodynamic performance and impacts. Energy removal from the fluid flow is mostly the primary focus of these studies with some studies investigating the static effect of the turbine structure. Due to the dimensional constraints of tank tests, laboratory studies have been mostly limited to a single turbine. However, with developments in scale-model testing, new tanks and testing facilities have been made available for carrying out array study investigations.

Experimental studies can be divided mainly into two major types: scale-model turbine rotors and porous mesh disks known as pseudo-turbines as shown in Figure 2.6. The thrust exerted on the turbine rotor by the fluid causes a change in momentum which results in a reduction in fluid speed downstream of the turbine, this, as described earlier, is known as the turbine wake. Porous mesh disks can generate similar thrust to scale-model rotors by varying the porosity of the disk, this allows both the scale-model rotor and porous disks to be used to study wake effects (Myers & Bahaj 2010). An upside of using porous mesh disks is it can avoid some of the challenges faced in modelling a small-scale turbine (Myers & Bahaj 2009).

One such challenge is turbine scaling, which requires accurately scaling the turbine properties, where any change will drastically affect the downstream fluid flow field (Bahaj, Myers, Thomson & Jorge 2007). Thus, in comparison with a scale-model rotor, a porous disk is much more computationally cost-effective and easily implemented (Nash & Phoenix 2017). However, the porous disk method has limitations, the stationary porous disk cannot create a downstream swirl similar to the rotating turbine, and it does not replicate the tip vorticity of the turbine, but can simulate the turbulence effect in the wake (Bahaj, Myers, Thomson & Jorge 2007). However, it was observed that these limitations in the actuator disk approach have been shown to subside in the near wake region (less than five rotor diameters downstream) when compared with the flow-field generated by a rotor (Nash & Phoenix 2017). According to Bahaj and Myers, accurately scaling the thrust and flow properties is key to obtaining better far wake characteristics that closely match those of a full-scale rotor (Bahaj, Myers, Thomson & Jorge 2007).

A summary of prior laboratory studies on horizontal axis TCTs is provided in Table 2.4. All of these studies were conducted in steady-state fluid flow conditions, in circulating flume tanks and focused on investigating the downstream wake velocity and turbulence intensity. As mentioned previously there are two rotor approaches, which are the scale-model rotor and porous disk approaches. In the studies implementing scale-model rotors, a three-bladed horizontal axis rotor was used. The scale-model rotors were either suspended from above the water or attached to the bottom of the tank and the diameters of the rotors ranged from 0.27m to 0.8m. Whereas, the porous disk approaches were suspended from above the water surface and have a diameter range between 1.0m to 1.15m. Out of all the reviewed laboratory studies, nine focus on investigating the fluid flow through a single rotors/disks. The remaining four studies focus on investigating the flow through multiple rotor/disk for the primary purpose of tidal current turbine array arrangement and spacing.

The reviewed studies in the literature were all conducted in different fluid flow conditions. For example, the channel depth,  $d$ , and channel width,  $w$ , range from 0.16m to 2.0m and 1.2m to 5.0m respectively. The freestream velocity,  $U$ , ranges from 0.25m/s to 1.5m/s. The Reynolds number (Reynolds number (Re)) is one of the most important flow conditions in laboratory studies due to its impact on scaling,

Table 2.4: A summary of the laboratory studies.

Type	No. of turbines	Channel cross-section w x d (m)	Upstream Velocity (m/s)	Reynolds Number	Rotor Diameter (m)	Blockage ratio (%)	Assessed results	Reference	
Mesh Disk	single	1.35 x 0.3	0.61-0.94	1.8-2.8 x 10 <sup>5</sup>	0.1	1.9	Velocity, Turbulence	Bahaj, Myers, Thomson & Jorge (2007)	
		1.35 x 0.3	0.25	7.5 x 10 <sup>4</sup>	0.1	1.9	Velocity, Turbulence	Myers & Bahaj (2010)	
	1.2 x 0.26	0.26	6.9 x 10 <sup>4</sup>	0.15	5.7	Velocity, Turbulence	Abolghasemi et al. (2016)		
	arrays	1.35 x 0.3	-	-	0.1	0.2	Velocity	Myers & Bahaj (2012)	
		2.1 x 0.18	0.248	5.0 x 10 <sup>5</sup>	0.11	12.5	Velocity, Turbulence	Hachmann et al. (2020)	
Three-bladed rotor	single	4.0 x 2.0	0.8	1.6 x 10 <sup>6</sup>	0.8	6.3	Velocity, Turbulence	Myers & Bahaj (2009)	
		4.0 x 2.0	0.5-1.5	1.0-3.0 x 10 <sup>6</sup>	0.7	4.8	Velocity	Hachmann et al. (2020)	
		2.75 x 1.15	0.4	4.6 x 10 <sup>5</sup>	0.5	6.2	Velocity	Chamorro et al. (2013)	
	single		5.0 x 0.45	0.46	2.1 x 10 <sup>5</sup>	0.27	2.5	Velocity, Turbulence	Stallard et al. (2015)
			0.8 x 0.54	0.59	3.2 x 10 <sup>5</sup>	0.3	16.4	Velocity, Turbulence	Chen et al. (2017)
			3.0 x 1.6	0.25-0.8	5.0 x 10 <sup>5</sup>	0.28	1.3	Velocity, Turbulence	Nuernberg & Tao (2018)
	arrays		5.0 x 0.45	0.47	2.1 x 10 <sup>5</sup>	0.27	2.5	Velocity, Turbulence	Stallard et al. (2013)
		3.0 x 1.6	0.25-0.8	5.0 x 10 <sup>5</sup>	0.28	>4	Velocity, Turbulence	Nuernberg & Tao (2018)	

the  $Re$  from all studies is between  $7.5 \times 10^4$  to  $3.0 \times 10^6$ . Blockage ratio is also a key component in experimental studies, it is the ratio of rotor swept area to channel flow cross-sectional area. Due to the limitation of tank size, the blockage ratio in the laboratory can exceed that of a real site deployment, this greatly affects the turbine performance and wake characteristics (Tedds 2014). Hence, there is a recommended blockage ratio of below 20% and it is shown that all of the reviewed studies are below the recommended blockage ratio (Bahaj et al. 2008). A study on the impact of different blockage ratios has found that a higher blockage ratio results in reduced momentum loss through the rotor (Consul et al. 2013). One study has shown the comparison of velocity deficit in the downstream longitudinal turbine centreline of six different laboratory studies of singular scale turbines as shown in Figure 2.7. Although there are differences in the setup of each experiment, the resulting downstream velocity deficit curve from the compared studies is very similar. As observed from Figure 2.7, the deficits are the highest in the regions of the fluid flow nearest to the turbine and decrease with increasing distance downstream of the turbine, as the wake velocity is able to recover to the free-stream velocity. The comparison, Figure 2.7, shows the velocity reduction in the near wake (less than 5D) ranges from 50% to 90%, while the velocity reduction in the far wake (more than 10D) drops to less than 25%. The near wake region seems to be greatly affected by the setup of the experiment, such as tank size, turbine characteristics and inflow conditions. Additionally, the velocity deficits in the far wake region, especially after 15D, seem to be non-affected by the experimental setup. This observation is in line with the understanding that the far-wake is mainly influenced by turbulent mixing and surrounding topography (Myers & Bahaj 2010).

## 2.7 Turbine representations

Simplified representation is a common approach used in numerical modelling of a tidal current turbine to reduce the complexity and computational cost. However, the simplification of the turbine typically results in reduced detail characteristic descriptions of both the tidal current turbine and the wake. In modelling horizontal axis tidal current turbines, near wake and far wake models play a crucial role in deciding the selection of a suitable tidal current turbine representation. Near wake models require fine mesh densities and are solved in a three-dimensional environment. This

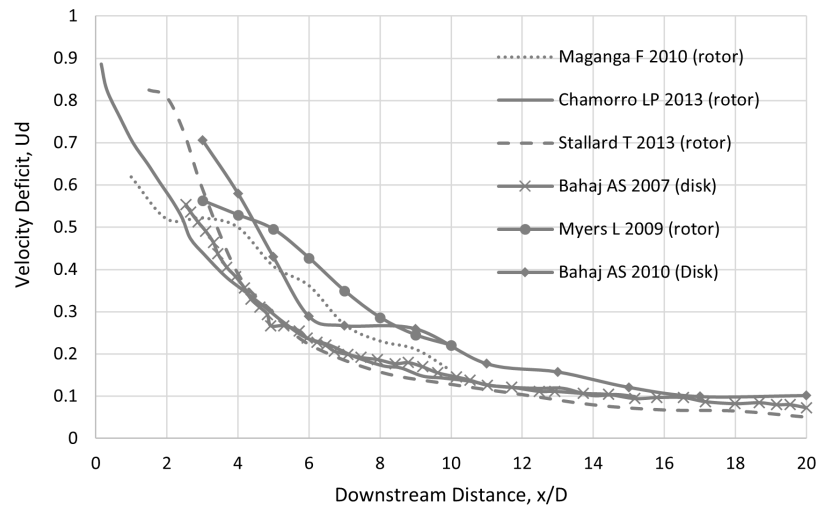


**Figure 2.7:** Downstream longitudinal centreline velocity deficit of different laboratory scaled rotor (Chamorro et al. 2013, Stallard et al. 2013, Myers & Bahaj 2010, 2009, Bahaj, Myers, Thomson & Jorge 2007, Hachmann et al. 2020).

approach accurately captures the fluid flow through and around the rotor, however this is computationally expensive. This approach is mostly employed for single turbine modelling in idealised steady fluid flow conditions. Whereas, far-wake models use much coarser mesh densities and can be solved in either two-dimensional or three-dimensional fluid flow environments. Although far-field models lack the accuracy to capture the full fluid flow field through an individual tidal current turbine rotor, however, it is computationally less expensive. Thus, this approach is much more suitable for modelling large arrays of tidal current turbines. The various approaches used to represent tidal current turbine rotors are briefly summarised in Table 2.5.

For a TCT representation, SMM and RRF are the most accurate in representing the hydrodynamics and flow characteristics of the tidal current turbine, these approaches are sometimes referred to as a blade resolved approach. Comprehensive studies undertaken using these approaches have to account for the fluid flow field to investigate the interaction between the turbine and its support structure and the impact on the fluid flow field (Zhang et al. 2017). The emphasis on blade geometry details increases the complexity of the model, as a result, it is computationally expensive. In recent studies, SMM and RRF approaches were successful in predicting

**Table 2.5:** Description of various TCT rotor representation techniques.

Type	Model	Description	Ref.
Sliding Mesh Model (SMM)	Near-wake	The sliding mesh interface is used to simulate a rotating turbine. This method enables a region of mesh cells to rotate in a large stationary grid which results in a detailed simulation of the rotor motion and complex flows. Hence, it is computationally expensive.	Mcnaughton et al. (2014)
Rotating Reference Frame (RRF)		This method uses detailed blade geometry to simulate rotating flows and hydrodynamics characteristics. The governing equations of fluid flow are solved in a reference frame which rotates at the turbine speed by including Coriolis and centripetal force terms in the momentum equation.	Mozfari (2014)
Actuator Line Model (ALM)		Represents the turbine blades as a set of segments and distributes loads along each blade's axis rather than averaging them over an area. This method includes the effect of non-uniform loading and is a modification of BEM.	Apsley et al. (2018), Churchfield et al. (2013a), Baratchi et al. (2017)
Blade Element (BE)		The time-averaged hydrodynamic effects of the rotating blades are simulated using a momentum source term placed inside a rotor disk fluid zone that depends on the blade parameter and characteristics such as chord length, angle of attack, and lift and drag coefficients for different sections along the turbine blade.	Masters et al. (2015), Chawdhary et al. (2017), Batten et al. (2013), Masters et al. (2013), Turnock et al. (2011)
Actuator DiskAD	Near & Far-wake	The turbine rotor was represented by a substantially thin porous disk where the area is equivalent to the swept area of the turbine. The loss of pressure across the rotor was assumed to be a loss of energy due to work done on the rotor by the fluid flow, this can be incorporated into the momentum equation as a momentum sink over a given area in the streamwise direction. This method is similar to MSM but with a better emphasis on the rotor momentum loss. This theory is also referred to as momentum theory	Churchfield et al. (2013a), Batten et al. (2013), Harrison et al. (2010), Sun et al. (2008)
Momentum Sink Model (MSM)	Far-wake	This method represents the axial thrust and drag induced by both the tidal current turbine and the support structure as a whole as momentum sinks in the momentum equation to simulate momentum loss due to energy extraction from the fluid flow.	Fallon et al. (2014), Fairley et al. (2015), Thiébot et al. (2015), Ramos et al. (2013), Ahmadian & Falconer (2012)
Bed Roughness Model (BRM)		BRM increased the bed roughness to simulate the wake effects of the rotor on the fluid flow field. It is the simplest and cheapest approach, however it ignores the relationship between flow direction and turbine rotor orientation especially in the case of a horizontal axis tidal current turbine.	Funke et al. (2014), Divett et al. (2013)

far-wake development provided the turbulence model was solved using Large Eddy Simulation (LES) (Afgan et al. 2013). Furthermore, the BRM approach was the most computationally efficient approach due to the low level of complexity, however, this approach has shown an inability to accurately simulate the full wake fluid flow conditions. The most common representation approaches, presented in the literature, are the MSM, AD, BE and ALM. From the computational models presented, the MSM and AD approaches use a momentum sink to model momentum loss with MSM focusing on the whole structure and the AD focusing more on the tidal current turbine rotor. Both methods are a good choice for large turbine array modelling, however this approach fails to capture rotational flow, swirl effects and the turbulence induced by the turbine (Liu et al. 2016). MSM is less accurate when predicting the flow through the turbine when compared to AD. From the experimental models, the porosity of the actuator disk (AD) was set up depending on the thrust coefficient of the tidal steam turbine. In recent developments, AD can be tuned to better agree with the downstream wake predictions, but it is very sensitive to inlet turbulence conditions, making it difficult to predict turbulence intensity in the wake (Gant & Stallard 2008).

MSM and AD are popular approaches for modelling far wake effects, while BE and ALM are popular approaches for modelling near-wake fluid flow effects. However, recent studies have seen BE and ALM have been adopted for far-wake models. For example, the use of LES to solve turbulence closure enables ALM to predict far wake and BET was able to predict far wake fluid flow conditions by coupling with AD (Creech et al. 2017, Olczak et al. 2016). BET was established to include effects of non-uniform loading across the turbine rotor swept area which was a drawback with the AD approach. Time-averaged loads were represented as source terms in the Navier-Stokes Equation. The difference between ALM and BE-AD hybrid is the inclusion of the effect of non-uniform loading, in the ALM model, along the rotating line while the BE-AD hybrid method averages the loading over the rotor's swept area.

A comparison of turbine representation methods is shown in Table 2.6, the summarisation mainly focuses on studies undertaken on downstream wake velocity. Overall, 3-dimensional models are suitable for all types of turbine representation, while 2-dimensional models are suitable for turbine representation of medium and

low numerical requirements. Furthermore, Table 2.6 shows that turbine representation approaches which can predict both near and far wake tend to have a higher numerical requirement when compared to turbine representations that can only predict either near or far wake fluid flow effects.

A study has been carried out on comparing the accuracy of different AD tidal current turbine rotors with various other studies in the literature (Batten et al. 2013), the study compares the normalised centreline velocities as shown in Figure 2.8. All of the AD turbine rotors in this comparison have a thrust coefficient of approximately 0.9, apart from the model by Sun (Sun et al. 2008), consequently an assumption could be made that the downstream wake is similar for each model. However, Figure 2.8 shows that the centreline velocities vary significantly especially in the near wake region with the lowest normalised velocities ranging from -0.2 to 0.65. Additionally, the rate of recovery also varies significantly from the tidal current turbine rotor up to 12D downstream with Sun(Sun et al. 2008) having the highest recovery rate and the model by MacLeod showing the longest recovery (MacLeod et al. 2002). The rate of recovery is dependent on ambient turbulence intensity and tidal current turbine induced turbulence (Harrison et al. 2010). The study conducted by Batten (Batten et al. 2013) has demonstrated the accuracy of their model in predicting wake effects and has also validated the numerical findings with experimental measurements (Harrison et al. 2010).



**Table 2.6:** Summary of different TCT representation techniques

Turbine representation	Wake prediction Capacity	Numerical Capacity	Modelling approach	Reference
SMM/RRF	Near & Far Wake	Very High	3D	Mcnaughton et al. (2014), Mozfari (2014), Zhang et al. (2017), Afgan et al. (2013)
	Near Wake	High		
ALM	Near & Far Wake	High	3D	Apsley et al. (2018), Churchfield et al. (2013a), Baratchi et al. (2017), Creech et al. (2017)
	Near Wake	Medium		
BE	Near Wake	Medium	2D/3D	Masters et al. (2015), Chawdhary et al. (2017), Batten et al. (2013), Masters et al. (2013), Turnock et al. (2011)
BE+AD	Near & Far Wake	Medium	2D/3D	Churchfield et al. (2013b), Batten et al. (2013), Harrison et al. (2010), Sun et al. (2008), Gant & Stallard (2008), Liu et al. (2016), Olczak et al. (2016)
AD	Far Wake	Low		
MSM	Far Wake	Low	2D/3D	Fallon et al. (2014), Fairley et al. (2015), Thiébot et al. (2015), Ramos et al. (2013), Ahmadian & Falconer (2012)
BRM	Far Wake	Low	2D/3D	Funke et al. (2014), Divett et al. (2013)

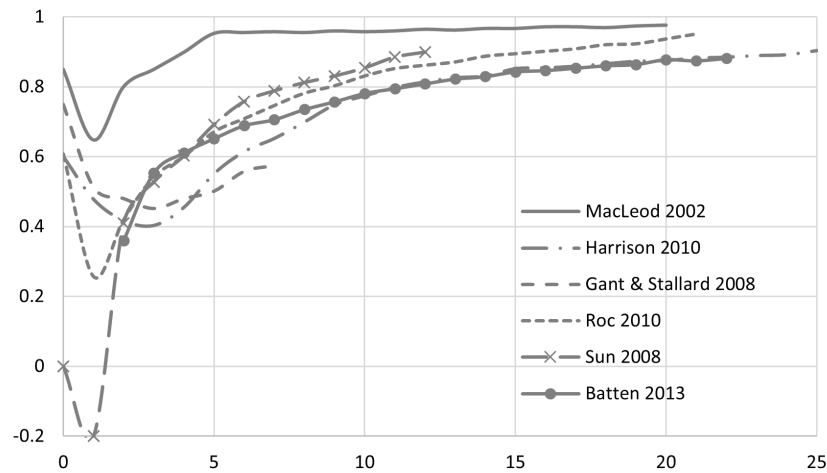


**Figure 2.8:** Centreline normalised velocity profile of a range of different ADM. (MacLeod et al. 2002, Gant & Stallard 2008, Batten et al. 2013, Sun et al. 2008, Harrison et al. 2010, Roc et al. 2010).

## 2.8 Numerical Modelling

Numerical modelling is an excellent and popular approach used to predict and simulate the hydrodynamic performance of a tidal current turbine. There are a range of numerical modelling approaches that can be utilised to determine the performance of a tidal current turbine, such as vortex methods (VM), BEM theory methods and CFD. The key differences between these approaches are typically model complexity, solver accuracy and computational cost. VM models focus more on the vorticity shedding from the airfoil, unlike the other two methods which primarily focus on the velocity and pressure of the fluid within the control volume stream tube (Branlard 2017). VM is useful when tracking the formation of the fluid wake and the time-varying effects of the fluid flow model of a tidal current turbine. Meanwhile, BEM is a combination of BE theory and momentum theory. The use of BEM in predicting the wake performance of a tidal current turbine is popular but this method has limitations in providing sufficient wake information (Lee & Wu 2015). Another popular approach modelling the hydrodynamic performance and wake behaviour of a tidal current turbine is CFD, however this is much more time consuming and computationally demanding when compared to VM and BEM (Masters et al. 2015).

### 2.8.1 Blade Element Momentum (BEM) Theory

BEM theory is a numerical modelling approach that combines momentum theory and blade element theory. The combination of both theories provides a popular, simple and well-tested method to model the hydrodynamic performance of a TCT. The Momentum theory (MT) is applied to an ideal turbine rotor, also known as an actuator disk (AD). The disk creates a discontinuity of pressure as the fluid flows through it. So, MT employs a finite control volume, where the control volume is a stream-tube of the flow with an entrance and exit perpendicular to the flow, the flow is uniform through the disk and in the wake (Sørensen 2011). Moreover, MT provides a good prediction of the tidal current turbine thrust and power performance for a steady incompressible fluid flow. There are limitations to MT such as the assumption of no frictional drag between the turbine and fluid, and no swirl effects from the actuator disk (Sørensen 2011). However, recent studies have shown a modification to include wake rotation in MT (Tedds 2014). This modification has allowed the actuator disk to impart rotation to the flow downstream of the actuator disk. The flow upstream of the actuator disk is not affected by the disk rotation. The rotation in the wake is imparted to the downstream wake in the form of tangential fluid flow by converting the angular rotor velocity to a rotational fluid flow velocity also known as the tangential induction factor (Tedds 2014). The established implementation of MT is to solve the fluid flow field in a steady and unbounded fluid flow; however studies have shown a growing interest in modelling bounded flow conditions for the purpose of tidal current turbines. This bounded flow is due to physical conditions such as the water free-surface, the seabed and the channel walls (Fernandez-Rodriguez 2014). These conditions cause blockage which, in turn, causes an increase in fluid flow velocity through the channel, bypass, estuary, etc., which leads to a greater drop in pressure across the turbine (Fernandez-Rodriguez 2014). When deploying multiple tidal current turbines in an array, higher power efficiencies will result, up to a certain limit before the stagnation of fluid flow occurs (Garrett & Cummins 2007). On that account, the blockage condition may cause the power predicted to exceed the Betz limit for individual turbines (Branlard 2017). When the axial induction factor is greater than approximately 0.5, MT is generally less accurate in predicting the actuator disk behaviour, this is known as a turbulent-wake state and needs experimental input and validation (Zhang et al. 2020).

The other part of the BEM approach is BE, this theory uses the properties of the blade such as lift and drag coefficient to calculate the tidal current turbine rotor force and torque based on flow characteristics like Reynolds number (Chamorro et al. 2012). A velocity equilibrium can be established between rotor rotation and inflow speed by using geometric parameters of the airfoil such as pitch angle and chord to obtain the normal and tangential forces acting on the airfoil. The most common methods of obtaining lift and drag coefficient is through either computational modelling or water/wind tunnel testing. BEM combines blade element theory and momentum theory by subdividing the blades of a tidal current turbine into multiple individual hydrodynamically independent sections of equal length, where the forces from MT and BE are assumed to be equal. Hence, the equations of momentum must balance the requirement of the corresponding component characterised by lift and drag components in the airfoil. BEM is usually written in a numerical coding environment using a standard iteration procedure to obtain a solution, typically for axial and angular induction factors (Fernandez-Rodriguez 2014). BEM is comprehensive but limited, for example, it cannot resolve hub and wingtip vortex losses. However, in the wind industry, BEM has been modified to take account of all variables using empirical models (Chamorro et al. 2012). Unfortunately, this modification is not always applicable to tidal current turbines for two main reasons. Firstly, due to the geometric blockage, tidal current turbines placed in confined arrays will experience an accelerated bypass fluid flow in the channel. This will greatly affect the axial induction factor which is an important factor in tip-loss correction calculations (Schubel & Crossley 2012). Some studies have shown BEM's ability to predict cavitation (Batten et al. 2008), however factors such as turbulence, waves and free-surface effects can lead to pressure differences along the blades resulting in inaccuracies in the model (Wimshurst et al. 2018, Buckland et al. 2013).

### **2.8.2 Computational fluid dynamics (CFD)**

Computational fluid dynamics (CFD) is a numerical tool widely used in analysing and understanding the field of fluid dynamics. There are four stages in solving a CFD problem which are: geometry and mesh generation, setting-up physical and boundary conditions, processing and post-processing, as shown in Figure 2.9.

CFD is heavily dependent on the development of computational technologies and

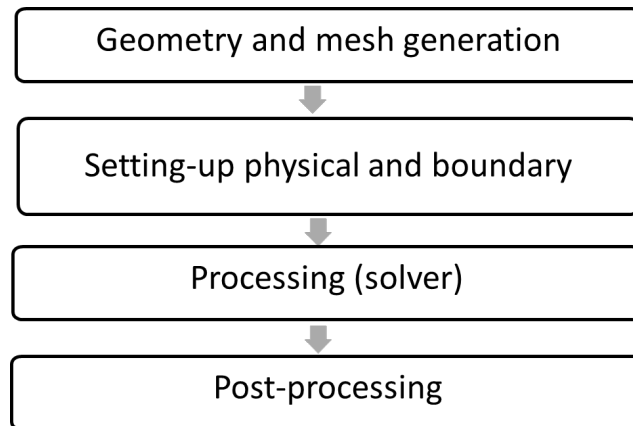


**Figure 2.9:** The procedure of solving a typical CFD problem.

the ability of the solver to solve ordinary and partial differential equations. However, solving complex fluid flow conditions demands high-quality computational resources and its success in solving such problems is dependent on the physical model applied, one such physical model is the turbulence model. Turbulence is an important aspect in the domain of fluid dynamics study. Furthermore, if turbulence is present in the fluid flow, it always appears to be dominant over all other flow conditions (Chung 2010, Flow 1981). Thus, turbulence modelling plays a huge role in increasing the quality and accuracy of wake modelling. The development of mathematical explanations to describe fluid flow has led to the creation of the Navier-Stokes (NS) equations. NS equations are inherently nonlinear, time-dependent and three-dimensional partial differential equations. CFD software solves these differential equations numerically to describe the fluid flow behaviour in complex fluid flow, for example including the effects of turbulence. Turbulence is often treated as an instability of laminar flow which occurs at high Reynolds numbers. The instabilities originate from the interaction between non-linear terms and viscous terms in the NS equations, which are fully time-dependent, fully three-dimensional and rotational. The three dimensional and rotational nature of the fluid flow leading to vortex shedding, i.e. vortex shedding is not possible in two-dimensional fluid flows. Consequently, two-dimensional wake prediction models fall short in fully approximating turbulent conditions when compared to three-dimensional models of fluid flow. Furthermore, the vortex structure has a long lifespan and moves along the flow, therefore certain turbulent quantities cannot be specified as local conditions. This indicates that the upstream profile and characteristics of the fluid flow are also of great importance (Flow 1981, John 2013).

Since the formation of the NS equations, there have been numerous attempts to solve the full equations but all efforts have fallen short. An alternative approach was used by simplifying the governing conditions, for example using turbulent flow approximations to reduce the number of coupled equations to less than five. These approaches are sometimes referred to as CFD turbulence closure models and they have proven sufficient to solve most fluid flow problems. There are several ways to close turbulent flows in the NS equations. There are two popular approaches, i.e. the Reynolds-averaged Navier-Stokes (RANS) equations and large-eddy simulation (LES) (Xue & Lin 2011).

### 2.8.3 Reynolds-averaged Navier-Stokes (RANS)

The wake behind a tidal current turbine is characterised by a high Reynolds number, as the flow is primarily driven by turbulence as opposed to viscosity. Hence, a conceptual RANS model will statistically average the fluid properties by including in the original NS equation. As a result, modelling of the turbulence is required to fully solve the fluid flow behaviour (Zhang et al. 2017). There is a wide range of turbulence closure models that have been developed, which add equations/relations for the Reynolds-stress and often introduce new flow variables that represent turbulence quantities. The turbulent models are shown in Figure 2.10, and are presented in order of increasing complexity (Laan 2014, Sodja 2007).

First-order models are based on the similarity between laminar and turbulent flow and are also known as eddy viscosity models. These models are based on the concept that the average turbulent flow field is similar to the corresponding laminar flow and the most widely used are the two-equation models. In a two-equation model, two partial differential equations are developed to solve the turbulent kinetic energy and the turbulent dissipation rate. The two-equation eddy viscosity models are capable of detailing more turbulence conditions and also provide better flow visualisation. Two-equation models perform well for fluid flow around complex geometries and are also suitable for open channels or enclosed environments with uniform geometry conditions (Flow 1981, Laan 2014). The  $k$ - $\varepsilon$  and  $k$ - $\omega$  models are well-known turbulence models generally known as the Reynolds-averaged turbulence models which are used to solve Reynolds stress (Jones & Launder 1972,

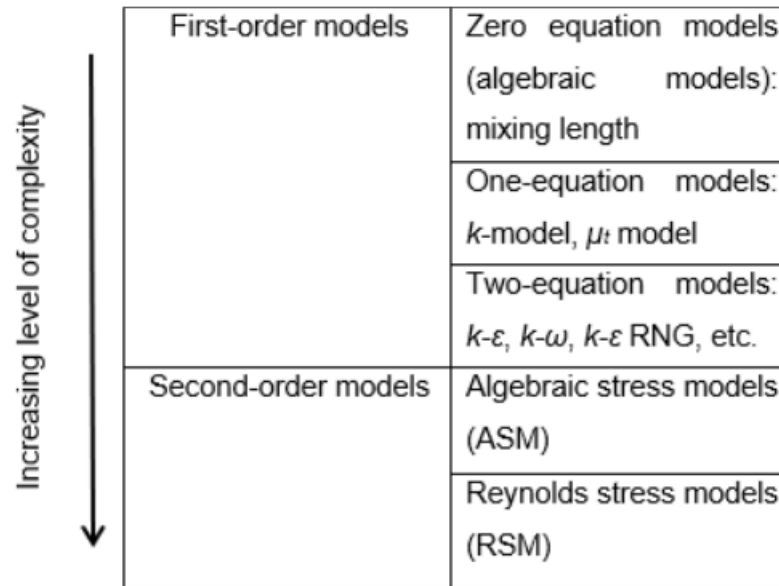


**Figure 2.10:** RANS turbulence closure models in increasing level of complexity.

Wilcox 1988).

The  $k$ - $\epsilon$  model is the most popular two-equation turbulence model. The standard  $k$ - $\epsilon$  model was developed by Launder and Spalding in 1974 (Launder & Spalding 1974) and is one of the most established models and is capable of handling various fluid flow conditions (Pope 2005). The  $k$ - $\epsilon$  model is a two-equation turbulence closure model, which consists of turbulent kinetic energy,  $k$  and rate of dissipation,  $\epsilon$ . It has a simple format, good performance and is widely valid for numerous applications. The  $k$ - $\epsilon$  model was considered to be single-length scale, a balance between the Reynolds stress and mean rate of strain in RANS. This model is most applicable when working far from solid boundaries, typically where there are no great pressure gradients (Sodja 2007). It is a useful and suitable model when assessing tidal current turbine performance and the fluid flow in the downstream wake. In some studies, it was found that the downstream turbulence intensity of an actuator disk using the  $k$ - $\epsilon$  model is more accurate than using the  $k$ - $\omega$  shear stress transport (SST) model, which tends to under-predict eddy viscosity and inaccurately predicts the wake recovery (Batten et al. 2013). Other studies have found that a turbine situated close to the water free surface faces problems where the wake cannot expand upwards, this creates an acceleration in the flow direction thus increasing the rate of wake recovery (Malki et al. 2013, Masters et al. 2013). Another well-known  $k$ - $\epsilon$

variant is  $k$ - $\varepsilon$  renormalisation group (RNG) model which accounts for a range of turbulent length scales. In this model, low scale motion elements are removed systematically through the application of statistical tools, here the governing equation is modified with respect to large motion elements (Laan 2014). This model is useful when performance is most important or when the flow structure of the far wake region is more important than the near wake (Edmunds et al. 2017).

The  $k$ - $\omega$  model is a two-equation model where  $\omega$ , is the ratio of the rate of dissipation,  $\varepsilon$ , over turbulence kinetic energy,  $k$ . In comparison to the  $k$ - $\varepsilon$  model, the  $k$ - $\omega$  model is better at predicting fluid flow conditions where there is a dominant adverse pressure-flow condition and boundary proximities (Pope 2005). The  $k$ - $\omega$  SST model is one of the most widely used variants of the  $k$ - $\omega$  model. It is a refined hybrid model developed by combining the best of both  $k$ - $\omega$  and  $k$ - $\varepsilon$  turbulence models (Menter 2009). The  $k$ - $\omega$  formula was applied to the boundary layer of the fluid flow to predict flow near wall boundaries while switching to  $k$ - $\varepsilon$  formula for resolving the free stream fluid flow (Menter 2009). This application helps to ease the sensitivity issue in the  $k$ - $\omega$  model, thus allowing for far wake modelling without any tune correction terms (Vogel & Willden 2020, Abolghasemi et al. 2016). The  $k$ - $\omega$  SST model is especially relevant in fluid models with adverse pressure gradients, for example the development of boundary layers around walls (Vogel & Willden 2020, Sanderse et al. 2011, Daly et al. 2013).

Some studies compare the AD and ALM methods using the unsteady RANS  $k$ - $\omega$  SST model (Deskos et al. 2017) and the results have been validated with experimental measurements (Mycek et al. 2014*a,b*). In both methods, the wake velocity and far wake turbulence agreed strongly with the experimental results. It is observed that the ALM method represents near wake better than the AD approach. However, the glsalm method slightly underpredicts the velocity deficit at the 2D to 4D region of the wake, while presenting a more accurate turbulence prediction. Using the  $k$ - $\omega$  SST model in the AD and ALM methods are unable to fully represent the blockage and bypass velocity. Additionally, solving ALM in  $k$ - $\omega$  SST model is around 50 times more computationally intensive than AD.

The second-order models utilise the second derivatives of the governing equation which are the Reynolds stresses and the turbulent fluxes. This model aims to over-



come the limitations of first-order models in dealing with turbulence isotropy and additional strains. However, the downside of this model is the large number of partial differential equations which involve many unknown terms and sometimes present difficulties in finding correlation. Popular second-order models include the Reynolds stress model (RSM) and the algebraic stress model. The RSM closes the RANS equations by solving additional transport equations for six independent Reynolds stresses. RSM is better able to handle anisotropic conditions than the group of first-order models. However, many higher-order turbulence correlations remain unsolved during the derivation of Reynolds stresses transportation equations for RSM (Laan 2014, Mishra & Aharwal 2018). The model is best suited in a situation when more than one source of fluid flow is available in a closed channel or unsymmetrical channel geometry. RSM provides better results than the  $k-\varepsilon$  model but requires higher computational capacity and is time-consuming (Mishra & Aharwal 2018). Some studies have been undertaken to investigate the effect of swirl in predicting wake recovery using RSM, the results have also been compared with experimental work (Li et al. 2019, Morris et al. 2016).

An extensive study has been completed in comparing the wake prediction of different types of RANS turbulence models such as RSM,  $k-\omega$  SST, standard  $k-\varepsilon$  and RNG  $k-\varepsilon$  using AD, the results are validated with experimental results (Nguyen et al. 2016), as shown in Figure 2.11. All four RANS turbulence models give comparable results in the far wake but differ considerably in the near wake region, standard  $k-\varepsilon$  shows the best agreement with experimental results in wake velocity and turbulence intensity distribution.

#### 2.8.4 Large-eddy simulation (LES)

Direct numerical simulation (DNS) is excellent at detailing turbulence; however it requires the resolution of turbulence scales of different lengths. Therefore, making DNS extremely demanding in terms of computational requirements. There is an alternative to DNS which is the Large-eddy simulation (LES). LES focuses on treating the eddies containing large-scale energy, this reduces computational time but is less accurate in comparison with DNS (Martínez-Tossas et al. 2015). The LES approach solves the Navier-Stokes equations for large eddies with sub-grid

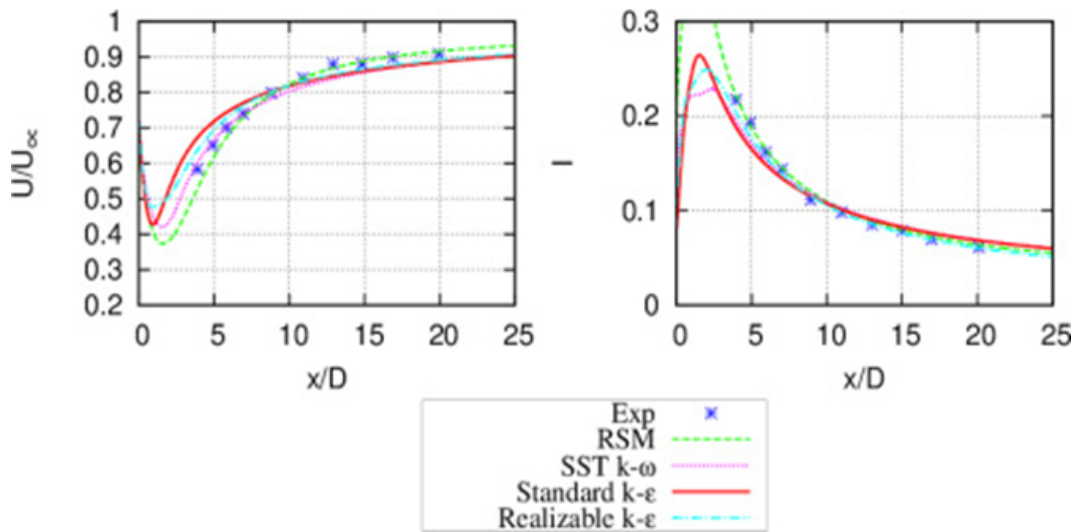


**Figure 2.11:** Comparison of velocity and turbulence intensity along the downstream centreline of experimental and numerical results of different RANS turbulence model (Nguyen et al. 2016).

eddies filtering, while small eddies are modelled. This is based on the assumption that the small eddies in the flow have a somewhat universal character that does not depend on flow geometry (Pope 2005). The small eddies are modelled using a sub-grid scale mode. LES is a popular turbulence model and is used extensively in the tidal-energy wake research domain, due to its ability to handle unsteady, anisotropic turbulent flows dominated by large-scale structures and turbulent mixing. Furthermore, this is a huge advantage over the RANS model, but LES requires higher computational needs when compared to RANS models. A study comparing LES and RANS has shown that the LES model is more capable of simulating turbulence generated by the turbine blade when compared to RANS models, however the flow was under-resolved when compared with the flow field data (Ahmed et al. 2017). The downside of LES, as detailed in the study, is computational inefficiency, for example, while it took a day for a RANS model to simulate a particular flow field condition, it took a week for the LES model to simulate the same conditions. However, there is a work-around to reduce the computational time for LES models, this is achieved by first running a RANS simulation to develop initial conditions and then these initial conditions can be used when simulating using the LES model (Blackmore et al. 2014). When comparing AD and ALM in LES, it is shown that ALM is more accurate than AD, despite being unable to fully resolve the fluid flow field (Kang et al. 2014). In one study, it is shown that ALM was able to simulate

a more stable fluid flow condition with less interaction with the shear layer using LES. However, the turbulence effect in the downstream wake was underestimated due to rotation effects as it continues further downstream (Ahmadi 2019). The ALM LES model has also shown a good correlation with experimental measurements especially at 3D to 4D downstream from the tidal current turbine rotor (Baba-Ahmadi & Dong 2017).

### 2.8.5 Numerical modelling of Tidal Current turbine

When simulating unsteady fluid flow around a tidal current turbine, the unsteady nature of the tidal current results in a variation in thrust and torque. These variations lead to issues such as a reduction of turbine power output, fatigue and a decrease in system reliability due to extreme fluctuating forces (Milne et al. 2016, Mycek et al. 2014a, Fernandez-Rodriguez et al. 2014). Table 2.7 details the findings of various single and multiple turbine arrays in terms of the model method used, computational requirements and numerical accuracy. From Table 2.7, it is clear that in terms of rotor representation methods, all are capable of accurately predicting thrust. However, there are inconsistencies in the near and far wake development for some methods. RRF, SMM and ALM are more computationally demanding than the AD and the AD+BEM approaches. Comparing turbulence models, LES is far more computationally expensive than the other methods, this is even more so in multiple turbine configurations. However, LES does show better accuracy in assessing and describing the wake development when compared to RANS.

AD has the least computational demand when it comes to predicting averaged wake velocity and turbulence intensity and it shows similar trends when compared with experimental results but seems to underpredict wake recovery. This could be due to the limitation of the actuator disk approach where detailed blade characteristics are absent for the model, resulting in the AD model's inability to account for swirling effects, leading to over-estimation of turbulent mixing in the wake which greatly impacts on the wake recovery of the far-wake region. This can be overcome by combining AD and BEM which provides blade properties to the disk. So, it is very suitable in determining thrust and averaged properties of a turbine's wake but this method has been shown to over-estimate when it is applied in arrays with differences up to 12% (Olczak et al. 2016). One downside of AD+BEM is the inability

**Table 2.7:** Summary of findings of different models in terms of blade and wake performance among single turbine and multiple turbine arrays.

No. of turbines	Rotor Method	Computational requirement	Performance		Ref
			Blade	Wake	
Single	ADM	Low (RANS)	-	Recovery was slow but showing similar trends	(Harrison <i>et al.</i> , 2010)
	ADM + BEM	Low (RANS)	High accuracy in thrust prediction but over-estimated power	High accuracy in predicting averaged velocity	(Guo, Zhou and Wang, 2015)
	ALM	Medium (RANS)	High accuracy in prediction of mean loads	High accuracy in far wake prediction but inconsistent in near wake	(Baba-Ahmadi and Dong, 2017) (Lin <i>et al.</i> , 2019)
		High (LES)	High accuracy in prediction of unsteady and mean loads	High accuracy in mean flow and turbulence characteristics prediction	
	SMM / RRF (Blade Resolve)	High (RANS)	The difference up to 10% with experiment	Very high accuracy in far wake	(Mcnaughton <i>et al.</i> , 2014) (Mozfari, 2014)
		Very High (LES)	The difference less than 3% with experimental findings	Very high accuracy in far wake with detailed blade tip vortices	(Zhang <i>et al.</i> , 2017) (Afgan <i>et al.</i> , 2013)
Multiple	ADM	Medium (RANS)	over-estimated thrust by 3% to 12%	The accuracy of the fluid flow in the wake has been assessed for up to twelve turbines	(Olczak <i>et al.</i> , 2016)
	ALM	High (RANS)	The difference in power prediction is less than 3% when compared with experimental findings	Flow characteristics has shown to validate well with experiment.	(Apsley, Stallard and Stansby, 2018) (Baratchi, Jeans and Gerber, 2017) (Ouro, Ramírez and Harrold, 2019)
		Very High (LES)			

to capture shed vortices (Guo et al. 2015). AD+BEM shows a higher accuracy in terms of velocity and turbulence intensity when compared with experiments carried out by Bahaj (Bahaj, Molland, Chaplin & Batten 2007) and various studies have also shown that this method is very sensitive to blade properties such as lift and drag (Guo et al. 2015). Some studies on AD+BEM have shown better wake recovery prediction due to increasing convection acceleration and also seabed influence (Masters et al. 2013, Zhang et al. 2017). For a turbine placed further from the seabed, the wake will typically recover over a short distance downstream from the turbine because there is more flow between the turbine and seabed which promotes better mixing of the wake with surrounding ambient free-stream fluid flow.

LES has shown better results in predicting the flow near the blade tip and past the turbine when compared with RANS as shown in Table 2.7. Moreover, LES is capable of predicting the unsteady conditions over a range of tip speed ratios (TSRs) while also producing a somewhat better set of averaged results (Baba-Ahmadi & Dong 2017, Afgan et al. 2013). It was noticed that most of the RANS models employed in the literature used the  $k-\omega$  SST turbulence model for wake prediction studies and it is well validated. However, RANS models show discrepancies in near wake development in most studies. This may be caused by the limitation of RANS in predicting flow separation such as tip-shed and structure vortices. Therefore, it would be wise to look into new effective turbulence closure models to resolve this issue. Furthermore, it was found from the body of literature that the capability to predict wake conditions, especially predicting wake recovery, is linked to turbulence intensity and the type of closure model used (Harrison et al. 2010, Zhang et al. 2017). Some studies have shown that the  $k-\omega$  model performs better in terms of prediction accuracy when compared to the  $k-\varepsilon$  model especially in the far wake region (Batten et al. 2013, Shives & Crawford 2014, Pang et al. 2020). One study has also suggested that the  $k-\omega$  SST model is limited because of its dependency on uniform flow treatment leading to a smoothening of the fluid flow near the turbine (Zhang et al. 2017).

A number of other studies have mentioned the effect of the turbine support structure imposing shadow effects on the downstream fluid flow. The support structure causes an unsteady axial-force which affects the rotor wake (Masters et al. 2013, Creech et al. 2017, Frost et al. 2015). However, the support structure only minorly

affects the wake in the previously mentioned studies but recent studies have shown the opposite effects which show the support structure imposing an obvious velocity deficit in the near wake region, yet it quickly recovers after 3D downstream of the rotor (Chen et al. 2017). This argument further explains the rather good correlation between RANS prediction and far wake experimental results. Further work has also been undertaken to study the effect of the support structure by isolating the support structure frequency from the measured load, and the results verified that there is little to no association between the performance and the support structure (Fernandez-Rodriguez et al. 2014). It is worth mentioning that the deployment of the turbine and its support structure cause the free surface height to drop around 1D downstream but soon recovers downstream of the tidal current turbine (Fernandez-Rodriguez et al. 2014, Lee et al. 2012).

## 2.9 Numerical modelling of TCT array

As detailed in Table 2.7, the two most used methods in tidal current turbine array studies are the AD+BEM method and the ALM method. In most array studies the focus is mainly on the prediction of wake conditions, array configuration and blockage effects. Studies undertaken using the AD+BEM method have shown to be lacking definitive turbine configuration and inconsistencies were observed in the prediction of power between the AD+BEM and AD methods (Batten et al. 2013). While ALM has shown better results in predicting power and fluid flow performance in most array studies, however the computational cost was significant (Apsley et al. 2018, Baratchi et al. 2017, Ouro et al. 2019). Many studies have been carried out to understand the relationship between tidal current turbine array operation and configuration to increase array power efficiency. A study has been carried out aiming to simplify the wake prediction which has drawn inspiration from wake models in the wind industry. In this study, a comparison of existing wake models to tidal arrays has demonstrated a discrepancy of 7-10% between the Jensen model and CFD models (Palm et al. 2010). Although, there are similar features between the Jensen model and the CFD model, some modification is needed in the Jensen model for application in the tidal industry such as taking blockage into account. In RANS turbulence models, the  $k-\omega$  SST has shown to be the most reliable method in predicting wake development because of its tendency to closely predict the wake recovery in comparison with other RANS turbulence models (Olczak et al. 2016).

However,  $k-\omega$  SST has the tendency to underpredict the velocities in the near wake, especially using the AD method (Apsley et al. 2018). The  $k-\omega$  SST model is suitable for predicting wake effects in tidal current turbine arrays with linear distance less 10D (Shives & Crawford 2016). Moreover, it was shown that the  $k-\varepsilon$  model is more suitable for predicting wake effects in tidal current turbine arrays with linear distance more than 10D (Apsley et al. 2018).

Various studies have shown that downstream turbines in an array have experienced a reduction in fluid flow speed and a decrease in power (Liu et al. 2016, Apsley et al. 2018). One early study has demonstrated that there is little difference in the velocity deficit of two downstream turbines with a linear distance of 5D and 8D (MacLeod et al. 2002). However, later studies found that using staggered array configurations yields an increase in the efficiency of the array's overall power (Bai et al. 2013, Nishino & Willden 2012). There are conflicting studies, a higher power output can be obtained by using non-staggered array configuration instead of staggered array configuration in AD RANS models (Hunter et al. 2015). On that account, it is much more important to understand the relationship between the upstream and downstream turbine's wake development to better optimise the tidal current turbine array. According to one study (Malki et al. 2014), the downstream turbine performance can be increased by as much as 10%, if the turbine is located behind and in between the uninterrupted accelerated flow of two upstream turbines (Malki et al. 2014). Figure 2.12 shows two different tidal current turbine array configurations of 14 turbines and the corresponding power output.

In Figure 2.12a, the turbines are arranged in four rows with turbine adjacent spacing of 3D and linear spacing of 10D. Figure 2.12b, shows a modified staggered arrangement with turbine adjacent spacing increased to 4D and the second and fourth row placing was moved to 1D away from the first and third rows with 38D row distance between the second and third rows. There were two benefits from this modification; firstly, the second and fourth rows were able to benefit from flow acceleration from the upstream turbines and secondly, the large linear distance between the second and third rows allows for greater fluid flow recovery (Malki et al. 2014). This effect has given a contradictory idea that the downstream row of turbines is producing more power than the upstream turbines, especially when using the AD method. Rather, it should be treated as synergistic effects whereby an array of devices can generate

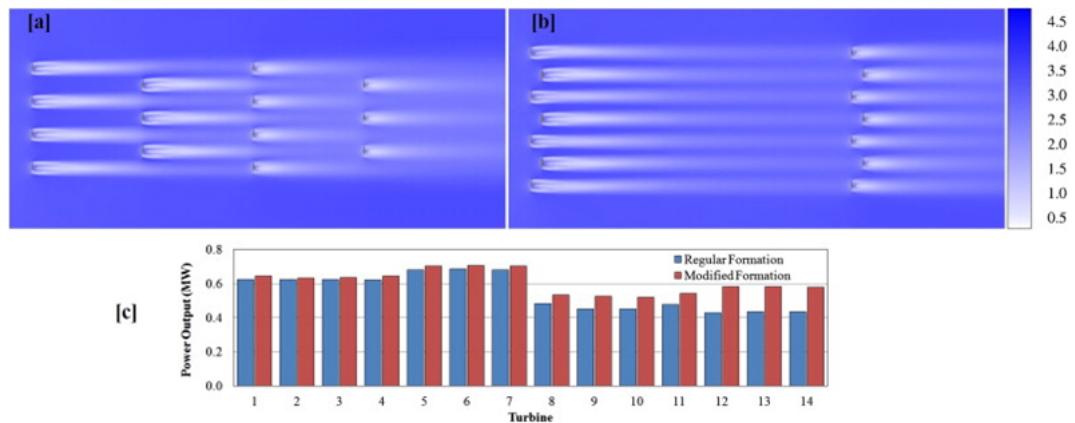


**Figure 2.12:** Velocity contour of (a) regular staggered and (b) modified staggered array arrangement and (c) power outputs for the two arrangements (Malki et al. 2014).

more power than an equivalent number of isolated machines which increases the overall efficiency of the tidal current turbine array (Myers & Bahaj 2012). Further studies have shown a reduction in power and thrust of two in-line tidal current turbines using RANS model, when the downstream turbine is within 1D of the upstream turbine wake (Apsley et al. 2018). However, the opposite occurs when the centre-line distance is above 1D (Malki et al. 2014, Bai et al. 2009). Moreover, studies completed using RANS models have shown that small row spacing in both linear and adjacent turbine distances produces an optimal energy capture in tidal arrays (Bahaj, Molland, Chaplin & Batten (2007), Bai et al. (2009)).

## 2.10 Conclusions

Most of the literature reviewed focuses on the studies and modelling of tidal current turbine wake behaviour and array wake interaction of horizontal-axis turbines. This chapter gives an insight into the basic understanding of physical and numerical fluid modelling, rotor representation methods and various turbulence closure methods. From the literature reviewed, the wake of a single turbine was well understood and studied with the maximum near wake region experiencing deficits in velocity of as much as 90% and the far wake region experiencing deficits in velocity ranging from 10% to 20%. The former will vary differently depending on the turbine properties and operating conditions, while the latter is independent of the tidal current



turbine properties and operating conditions.

The selection of a suitable modelling approach must take into account the overall objective of the studies. The CFD approach was found to be the most popular and suitable approach in most cases, it is able to predict turbine output, wake effects and array interaction. However, the CFD approach requires a higher computational requirement in order to obtain a more accurate turbine performance model. The strengths and weaknesses of each model have been discussed; for example, swirling was not included in AD and AD+BEM has no inclusion of tip vortices. Furthermore, it was also found that some models are more sensitive to certain input data; for example, AD is very sensitive to turbulence intensity input. The presence of a support structure was observed to affect the wake prediction, especially in the near wake region but not so much in the far wake region.

Overall, this chapter has confirmed that some AD+BEM, ALM and blade-resolved models (SMM/RRF) have high accuracy in predicting the wake and blade performance of tidal current turbines in CFD, given that the flow is steady and has low turbulence intensity. Although there is a significant advancement in flow modelling techniques using CFD, there are still aspects that have not yet been fully investigated and studied, such as the factors causing wake formation and disruption in turbine-to-turbine interaction. An in-depth investigation into the mentioned factors will be beneficial in predicting the placement of downstream TCTs in an array.

In terms of turbulence closure models in CFD, two important criteria must be taken into consideration, which are accuracy and computational cost. Thus, it was shown that the  $k-\omega$  SST model was the most suitable model for predicting fluid flow in the far wake region. But there is still much uncertainty with the  $k-\omega$  SST model on how it captures the properties of the wake, this is especially apparent in array modelling. That being so, further studies and experimental work are needed to validate the power output of a tidal current turbine array. Some early studies suggested that the array power output can differ by as much as 10% due to local blockage effects caused by the close vertical spacing of two turbines. Furthermore, most arrays studies have shown that CFD performed badly when it comes to predicting the wake of closely aligned turbines. Speculation suggests that it might be caused by the treatment of turbulent flow and rotor thrust.

One noticeable challenge in this domain is the lack of array field data for the validation of array modelling. Although, there are small-scale rotor model tests carried out in tanks and flumes which provide a good reference in the development of numerical models; however, small-scale rotor characteristics differ from commercial-size rotors due to the scaling of the rotor. Another interesting area which needs further work is the effect of floating foundations on the performance and operation of a tidal current turbine and floating tidal current turbine arrays.

# Chapter 3

## Theory

### 3.1 Introduction

In this chapter, the theory behind the development of the numerical model, used in this work, is described. The model is a modified actuator disk (AD) coupled with blade momentum element (BEM) theory and is solved using a computational fluid dynamics (CFD) solver. The CFD solver used in this research is ANSYS-CFX and the BEM theory was developed using MATLAB. ANSYS-CFX is an industry leading CFD software which is extensively used across industry and academia. Furthermore, this software is suitable for calculations on turbomachinery applications, among other applications, as it produces accurate results and undergoes extensive industry validation. MATLAB is a programming and numeric computing platform used to analyse data, develop algorithms, and create models. For that reason, it is suitable for use to develop the BEM model in this work.

This Chapter is divided into a number of sections, each of which describes the theory that has been employed in this research work. The first sub-section introduces some of the basic rotor definitions. Then the second sub-section provides details on the actuator disk theory and momentum theory, including the Betz limit. The third sub-section describes BEM theory along with Prandtl's loss correction and turbulent wake state correction model. The last sub-section focuses on the theory behind CFD which includes details of the Reynolds-averaged Navier-Stokes (RANS) equation,  $k-\omega$  shear stress transport (SST) model, near-wall region, discretisation (mesh) and ANSYS software application.

### 3.2 Basic rotor definitions

This section provides definitions of some of the basic rotor hydrodynamics quantities related to the tidal current turbine rotor. The Reynolds number,  $Re$ , is a dimensionless number that is used in fluid mechanics to describe flow and represent the ratio between inertia forces and viscous forces in a flow as given in Equation (3.1),

$$Re = \frac{UL}{\nu} \quad (3.1)$$

where  $U$  is the fluid velocity,  $L$  is the characteristic length such as rotor diameter or chord length, and  $\nu$  is the kinematic viscosity of the fluid. Laminar flows feature low Reynolds numbers. The higher the Reynolds number the more likely a flow is to be turbulent, and the finer the small length scales within the flow.

The tip speed ratio (TSR),  $\lambda$ , is a quantity commonly used in the design process of tidal current turbine blades and hence plays an important role in tidal current turbine hydrodynamics. The TSR is a dimensionless number indicating the ratio between the rotational speed at the tip of the rotor to the freestream velocity, given in Equation (3.2).

$$\lambda = \frac{\Omega R}{U} \quad (3.2)$$

where  $\Omega$  is the rotational angular velocity,  $R$  is the rotor radius and  $U$  is the freestream velocity. The local TSR,  $\lambda_r$ , can be defined as seen in Equation (3.3),

$$\lambda_r(r) = \frac{\Omega r}{U} \quad (3.3)$$

where  $r$  is the local radius,  $\Omega$  is the rotational angular velocity, and  $U$  is the freestream velocity.

In the design of a tidal current turbine rotor, turbine solidity is paramount and it is described as the ratio between the blade area and the swept area. The local solidity,  $\sigma(r)$  is defined in Equation (3.4),

$$\sigma(r) = \frac{Bc(r)}{2\pi r} \quad (3.4)$$

where  $B$  is the number of blades and  $c(r)$  is the chord length at position  $r$ . The overall solidity of the rotor can be obtained by integrating the local solidity along the radius.

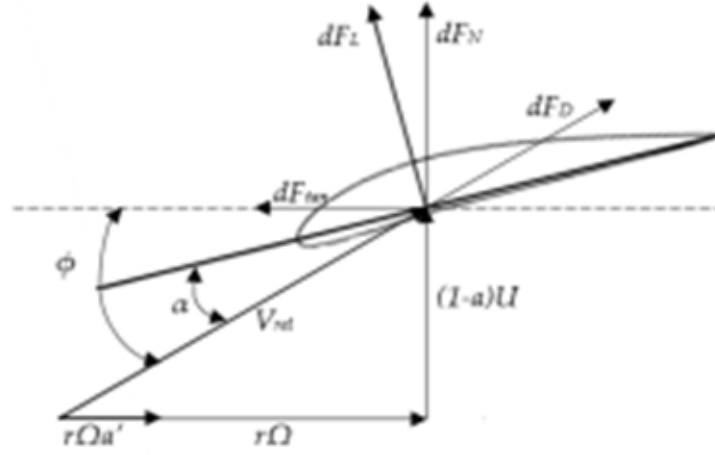


**Figure 3.1:** Section blade element diagram with angles, forces and velocities.

Figure 3.1 shows the hydrodynamic parameters on a tidal current turbine blade at a spanwise blade section.

Based on Figure 3.1, the local angle of attack,  $\alpha$ , can be defined as

$$\alpha = \phi - \gamma - \theta_p \quad (3.5)$$

where  $\alpha$  is the angle of attack,  $\phi$  is the relative angle of the tidal current flow,  $\gamma$  is the twist angle,  $\theta_p$  is the pitch angle. According to Figure 3.1,  $dF_{tan}$  is the tangential force,  $dF_L$  is the lift force,  $dF_N$  is the normal force, and  $dF_D$  is the drag force. The horizontal dotted line in Figure 3.1 represents the rotor plane. The axial velocity,  $U_z$  of the blade segment and the tangential velocity,  $U_\theta$  of the blade segment are given as

$$U_z = U(1 - a) \quad (3.6)$$

$$U_\theta = r\Omega + r\Omega a' = r\Omega(1 + a') \quad (3.7)$$

where  $a$  is the axial induction factor and  $a'$  is the angular (azimuthal) induction factor,  $U$  is freestream velocity  $r$  is the local radius and  $\Omega$  is the rotational velocity. The relative velocity of the flow to the blade is defined in Equation (3.8), and the relative angle is shown in Equation (3.9).

$$U_{rel} = \sqrt{U_z^2 + U_\theta^2} \quad (3.8)$$

$$\phi = \tan^{-1} \left( \frac{U_z}{U_\theta} \right) = \tan^{-1} \left( \frac{U(1-a)}{r\Omega(1+a')} \right) \quad (3.9)$$

Another important factor in blade design is the induction factor which consists of the axial induction factor,  $a$  and angular (azimuthal) induction factor,  $a'$ . The axial induction factor defines the fractional decrease in the tidal current velocity as it approaches the rotor plane, given in Equation (3.10), while the angular induction factor is defined in Equation (3.11),

$$a = \frac{U - U_z}{U} \quad (3.10)$$

$$a' = \frac{\Omega_i}{2\Omega} \quad (3.11)$$

where  $\Omega_i$  is the tangential velocity in the wake.

The thrust coefficient,  $C_T$  of a blade is the ratio between thrust force,  $T$  and dynamic pressure in the wind as defined in Equation (3.12):

$$C_T = \frac{T}{\frac{1}{2}\rho AU^2} \quad (3.12)$$

where  $\rho$  is the fluid density and  $A$  is the rotor swept area. While the power coefficient,  $C_P$  is the ratio between the mechanical power of the rotor,  $P$  and the kinetic energy in the fluid shown in Equation (3.13):

$$C_P = \frac{P}{\frac{1}{2}\rho AU^3} \quad (3.13)$$

### 3.3 Actuator Disk (AD) Theory

The function of a tidal current turbine rotor is to extract momentum and hydrokinetic energy from the incoming tidal current flow profile passing through the turbine. Thrust is obtained from an axial momentum analysis, and torque is obtained from an angular momentum analysis. To apply the principle of one-dimensional momentum, the tidal current turbine rotor in the flow-field can be analysed using the actuator disk theory which causes a difference in pressure in the fluid flowing across the rotor.

From the point of view of rotor hydrodynamic calculation, the fundamental idea of the actuator disk theory is to replace the actual rotor with a permeable porous disk of equivalent area where the forces from the blades are distributed averagely on the circular disk. The introduction of the actuator disk with distributed forces of the blades has an altering effect on the local velocities when flowing through the disk. Thus, affecting the entire flow-field around the rotor disk. The balance between the changed flow-field and applied forces from the disk is governed by the mass and momentum conservation law, this is equivalent to the axial and tangential momentum equations applied to a real tidal current turbine rotor.

The hydrodynamics of tidal current turbines is often described using the actuator disk concept, shown in Figure 3.2. This concept involves treating the turbine as an actuator disk and making assumptions about the flow using momentum theory. These assumptions include the homogeneity and steadiness of the flow, the incompressibility of the fluid, the absence of frictional drag, and an infinite number of blades. Additionally, the wake is assumed to be non-rotating. In this model, the static pressure far upstream and far downstream of the actuator disk is considered equal to the ambient static pressure.

The mass of the fluid passing through a given cross-sectional area of the stream-tube per unit time is  $\rho U_1 A_1$  where  $\rho$  is the density of the fluid,  $U_1$  is the free stream fluid velocity and  $A_1$  is the stream tube inlet area as shown in Figure 3.2. If  $A_d$  is the actuator disk area, and with respect to the conservation of mass, the following relation can be drawn:

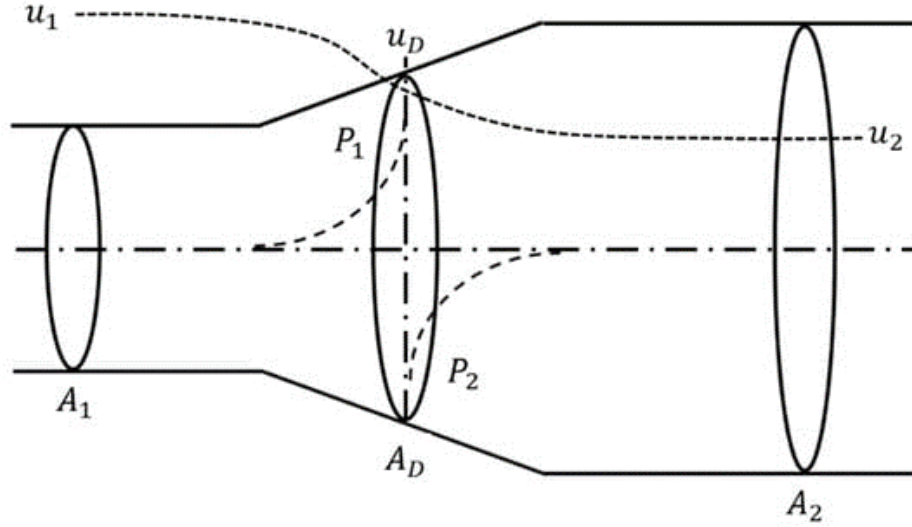


**Figure 3.2:** Actuator disk model of a rotor turbine.

$$\rho U_1 A_1 = \rho U_2 A_d = \rho U_4 A_4 \quad (3.14)$$

The actuator disk induces velocity in the stream tube where the difference between  $U_1$  and  $U_2$  is known as the axial induced velocity. The induced velocity, which is caused by the actuator disk, is expressed as a fraction of the freestream velocity, and in dimensionless form by dividing it by the freestream velocity:

$$\frac{U_1 - U_2}{U_1} = a \quad (3.15)$$

where  $a$  is the axial induction factor. The equation can be rearranged to express in terms of streamwise velocity component,  $U_2$ :

$$U_2 = U_1(1 - a) \quad (3.16)$$

According to the conservation of momentum, the net force acting on the control volume can be found. This force is equal and opposite to the thrust force of the fluid acting on the turbine. Hence, the thrust,  $T$  can also be expressed as the net sum of the forces on each side of the actuator disk:

$$T = (p_2 - p_3)A_d = (U_1 - U_4)\rho A_d U_1(1 - a) \quad (3.17)$$

Based on Bernoulli's equations, the pressure value can be expressed in terms of



upstream and downstream velocities:

$$U_4 = U_1(1 - 2a) \quad (3.18)$$

which is equivalent to:

$$U_2 = \frac{U_1 + U_4}{2} \quad (3.19)$$

By combining Equation (3.18) into Equation (3.17), the thrust on the turbine is given by:

$$T = 2\rho A_d U_1^2 a(1 - a) \quad (3.20)$$

The power,  $P$ , is equal to the thrust,  $T$ , times the fluid velocity at the turbine,  $U_2$ . Hence, the power extracted by the disk from the fluid can be determined based on Equation (3.18), (3.19) and (3.20):

$$P = T U_2 = 2\rho A_d U_1^3 a(1 - a)^2 \quad (3.21)$$

### 3.3.1 Betz Limit

The ratio between power extracted to the available power is known as power coefficient,  $C_P$ :

$$C_P = \frac{\text{Power extracted}}{\text{Power in the wind}} = \frac{\text{Power extracted}}{\frac{1}{2}\rho A_d U_1^3} \quad (3.22)$$

Equation (3.22) can be further simplified and expressed in terms of axial induction factor,  $a$ , by combining with Equation (3.21) :

$$C_P = 4a(1 - a)^2 \quad (3.23)$$

Similarly, the ratio between thrust exerted by turbine in the axial direction to incoming momentum of the flow (dynamic force) is known as thrust coefficient,  $C_T$ :

$$C_T = \frac{\text{Thrust by turbine}}{\text{Dynamic force}} = \frac{\text{Thrust by turbine}}{\frac{1}{2}\rho A_d U_1^2} \quad (3.24)$$

Equation (3.43) can be further simplified and expressed in terms of axial induction factor,  $a$ , by combining with Equation (3.20) :

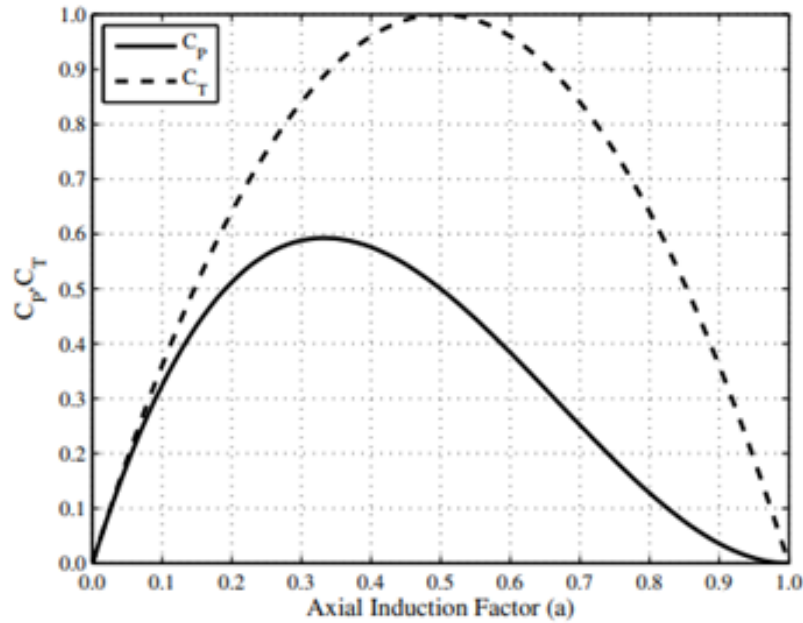


**Figure 3.3:** Power coefficient and thrust coefficient as a function of axial induction factor,  $a$ , for an ideal horizontal TCT.

$$C_T = 4a(1 - a) \quad (3.25)$$

The maximum power coefficient,  $C_P$ , occurs at  $\frac{dC_P}{da} = 0$  and by differentiating Equation (3.23), the following expression is obtained:

$$\frac{dC_P}{da} = 4a(1 - a)(1 - 3a) \quad (3.26)$$

Letting  $\frac{dC_P}{da} = 0$  will result in  $a = \frac{1}{3}$  and  $a = 1$ . When  $a = 1$ , will result in  $C_P = 0$ , while letting  $a = \frac{1}{3}$ , will result in  $C_P = 0.593$ . This is the maximum theoretical power coefficient for an ideal TCT and is known as the Betz limit. Figure 3.3 shows the power coefficient,  $C_P$ , and thrust coefficient,  $C_T$ , as a function of axial induction factor,  $a$ , for an ideal horizontal TCT.

### 3.4 Blade Element Momentum (BEM) Theory

Blade element momentum (BEM) theory is a hybrid of blade element (BE) theory and momentum theory. It can be used to assess the performance of a tidal current turbine blade. BEM theory is utilised by dividing the blade into a number of elements that are analysed independently, this method is commonly known as blade element theory (Hansen 2015). The hydrodynamic parameters of each element can be determined using BE theory. In this sub-chapter, the momentum theory, blade element theory and tip-loss correction will be discussed.

#### 3.4.1 Momentum Theory

The thrust and torque of a TCT can be determined through momentum analysis. Thrust is obtained from a momentum analysis, and torque is obtained from an angular momentum analysis. By utilising the actuator disk method, a one-dimensional momentum analysis can be performed. The local thrust force can be obtained by the principle of linear momentum which is applied to a local annulus control volume enclosed by a stream tube with one inlet (upstream) and one outlet (downstream). The local thrust,  $dT$  is given as:

$$dT = U_1 dm_1 - U_4 dm_4 \quad (3.27)$$

where  $U_1$  is the upstream velocity,  $U_4$  is the downstream velocity,  $m_1$  is the differential upstream mass flow rate and  $m_4$  is the differential downstream mass flow rate. Since the flow is incompressible, hence the mass flow rate is constant as given:

$$dm_1 = dm_4 = dm \quad (3.28)$$

The volume flow rate can be expressed as:

$$\frac{dm_1}{\rho} = U_2 \cdot dA_d = U_2 (2\pi r \cdot dr) \quad (3.29)$$

where  $dA_d$  is the differential actuator disk area,  $r$  is the local radius. Substituting Equation (3.18), (3.19) and (3.29) into Equation (3.27) gives:

$$dT = 4\pi r \rho U_1^2 a(1-a) dr \quad (3.30)$$

Similarly, the torque can be found by applying the conservation of angular momen-

tum to the control volume, an expression for the incremental torque,  $dM$ , on an annular ring of the rotating actuator disk can be obtained. The local torque,  $dM$  is given as:

$$dM = d\dot{m}(\Omega_i r)r \quad (3.31)$$

The mass flowrate in Equation (3.31) can be replaced by Equation (3.29) and by substituting Equation (3.11), (3.18), (3.19) into Equation (3.31), the expression can be given as:

$$dM = 4\pi r^3 \rho \Omega a' (1 - a) dr \quad (3.32)$$

The incremental local power,  $dP$ , generated by an annular ring can be expressed as:

$$dP = \Omega dM \quad (3.33)$$

By combining Equation (3.32) and (3.33), the following expression can be obtained:

$$dP = 4\pi r^3 \rho U_1 \Omega^2 a' (1 - a) dr \quad (3.34)$$

Equation (3.34) can be expressed in local tip speed ratio by substituting Equation (3.3) into Equation (3.34) to give:

$$dP = \frac{1}{2} \rho A_d U_1^3 \left[ \frac{8}{\lambda^2} a' (1 - a) \lambda_r^3 d\lambda_r \right] \quad (3.35)$$

The incremental local power,  $dP$ , generated from any annular ring is a function of the axial and angular induction factors and the tip speed ratio. The incremental local power coefficient for each annular ring is given by:

$$dP = \frac{dP}{\frac{1}{2} \rho A_d U_1^3} \quad (3.36)$$

Therefore, the overall power coefficient,  $C_P$  for a rotating actuator disk is a sum of all incremental local power coefficient,  $dC_P$  as given:

$$C_P = \frac{8}{\lambda^2} \int_0^\lambda a' (1 - a) \lambda_r^3 d\lambda_r \quad (3.37)$$

### 3.4.2 Blade Element Theory

Using blade element theory the rotor blade is divided into a number of elements or strips along the blade span. While the blade is rotating, each element sweeps and forms an annulus shape. The force and moment on each local element can be expressed as a function of lift and drag coefficient and angle of attack. There are some assumptions made while using blade element theory. Firstly, there is no hydrodynamics interaction between blade elements. Secondly, the blade's spanwise velocity components are to be ignored. Lastly, the forces and moments on the blade elements are only determined using the lift and drag coefficient characteristics of a three-dimensional hydrofoil blade. The further integration of the force over the length of the blade can determine the torque and thrust (Hansen 2015).

The lift coefficient,  $C_L$  and drag coefficient,  $C_D$  can be as described in Equation (3.38) and (3.39), where  $dF_L$  and  $dF_D$  are the differential lift and drag force acting on a blade element,  $U_{rel}$  is the relative velocity observed by the blade and  $c$  is the chord of the blade.

$$C_L = \frac{dF_L}{\frac{1}{2}\rho c U_{rel}^2 dr} \quad (3.38)$$

$$C_D = \frac{dF_D}{\frac{1}{2}\rho c U_{rel}^2 dr} \quad (3.39)$$

For the particular hydrofoil, the angle of attack,  $\alpha$ , can be used to determine the lift coefficient,  $C_L$ , and the drag coefficient,  $C_D$ , by interpolating with experimental or numerical data. The normal force,  $dF_N$ , and tangential force,  $dF_T$ , to the rotor plane are also important variables. The normal force,  $dF_N$ , is used to calculate thrust, while the tangential force,  $dF_T$ , is used to calculate torque. The expression for the force normal to the rotor plane,  $dF_N$ , and for the force tangential to the rotor plane,  $dF_T$ , are given as:

$$dF_N = dF_L \cos\phi + dF_D \sin\phi \quad (3.40)$$

$$dF_T = dF_L \sin\phi - dF_D \cos\phi \quad (3.41)$$

Both Equation (3.40) and (3.41) can be expressed in dimensionless form as a normal

coefficient,  $C_N$ , and tangential coefficient,  $C_{TAN}$ , in terms of  $C_L$  and  $C_D$ :

$$C_N = C_L \cos \phi + C_D \sin \phi \quad (3.42)$$

$$C_{TAN} = C_L \sin \phi - C_D \cos \phi \quad (3.43)$$

The blade element theory can be utilised in describing the thrust,  $dT$ , acting on an annular section at radius,  $r$ , is given as:

$$dT = BdF_N \quad (3.44)$$

where  $B$  is the number of blades on the rotor. By substituting Equation (3.38), (3.39) and (3.40), the thrust on a spanwise blade element can be defined as:

$$dT = \frac{1}{2} B \rho c \frac{U_1^2 (1-a)^2}{\sin^2 \phi} (C_L \cos \phi + C_D \sin \phi) dr \quad (3.45)$$

$$dT = \frac{1}{2} B \rho c U_{rel}^2 C_N dr \quad (3.46)$$

While similarly the torque acting on a spanwise blade element,  $dM$ , on an annular section at radius,  $r$ , is given as:

$$dM = BrdF_T \quad (3.47)$$

By substituting Equation (3.38), (3.39) and (3.41), the torque on a spanwise blade element can be defined as:

$$dM = \frac{1}{2} B \rho c r \frac{U_1 (1-a)(1+a') \Omega r}{\sin \phi \cos \phi} (C_L \sin \phi - C_D \cos \phi) dr \quad (3.48)$$

$$dM = \frac{1}{2} B \rho c U_{rel}^2 C_{TAN} dr \quad (3.49)$$

### 3.4.3 Blade element momentum (BEM) theory

The torque and thrust forces depend on the axial and tangential induction factors. To calculate these induction factors it is essential to employ the conservation of momentum and angular momentum. From the conservation of momentum in the

axial direction, two new expressions can be obtained for the thrust force,  $dT$ , and the torque,  $dM$ , for each spanwise blade element. Based on BEM theory, the thrust obtained from Equation (3.30) in momentum theory and Equation (3.45) in blade element theory gives:

$$4\pi r \rho U_1^2 a(1-a) dr = \frac{1}{2} B \rho c \frac{U_1^2 (1-a)^2}{\sin^2 \phi} (C_L \cos \phi + C_D \sin \phi) dr \quad (3.50)$$

By substituting Equation (3.4) and simplifying an expression for axial induction factor can be derived:

$$a = \frac{1}{1 + \frac{4 \sin^2 \phi}{\sigma C_N}} \quad (3.51)$$

Similarly, the torque is obtained from Equation (3.32) in momentum theory and Equation (3.48):

$$4\pi r^3 \rho \Omega a' (1-a) dr = \frac{1}{2} B \rho c r \frac{U_1 (1-a)(1+a') \Omega r}{\sin \phi \cos \phi} (C_L \sin \phi - C_D \cos \phi) dr \quad (3.52)$$

By substituting Equation (3.4) and simplifying an expression for angular induction factor can be derived:

$$a' = \frac{1}{\frac{4 \sin \phi \cos \phi}{\sigma C_{TAN}} - 1} \quad (3.53)$$

BEM method is often used to calculate the hydrodynamic loads acting on a tidal current turbine. The BEM theory makes a number of assumptions, some of which need to be corrected to deal with the TCT operating in a realm environment. Furthermore, there are losses experienced at the blade tips of a TCT. Studies have shown that thrust coefficients predicted using BEM theory method do not agree with experimental measurements (Zhang 2018) especially for induction factors greater than approximately 0.4 as shown in Figure 3.4. Therefore, some corrections are needed to address these issues.

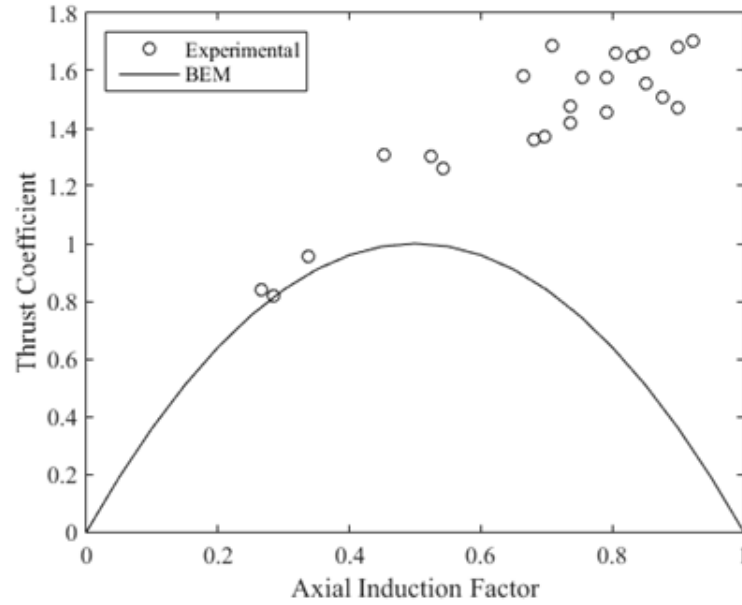


**Figure 3.4:** Comparison between experimental and numerical thrust coefficient at different axial induction factor (Zhang 2018).

#### 3.4.4 Prandtl's loss correction

Blade tip loss effects occur as blade tip is approached, i.e. blade tip losses. Tip losses occur because the pressure on the suction side of the blade is lower than the pressure side, thus air tends to leak around the tip from the lower to the upper surface. This reduces the lift forces and results in power loss near the tip of the TCT blade. BEM theory cannot directly determine tip loss in 3-dimensional flow conditions, the theory can be modified to include the effects of tip loss in the calculation. One of the most common and acceptable tip loss models is Prandtl's tip loss correction model. According to Prandtl, a correction factor,  $F$ , is introduced into BEM theory to determine force and torque (Tollmien et al. 1961). Hence, Prandtl's loss correction factor,  $F$ , is given (Tollmien et al. 1961).

$$F = \frac{2}{\pi} \cos^{-1} \left[ \exp - \left( \frac{\frac{B}{2}[R - r]}{r \sin \phi} \right) \right] \quad (3.54)$$

Prandtl's tip loss correction factor is a function of the number of blades, the angle of relative fluid, and the radial position along the blade (Tollmien et al. 1961). The tip loss correction factor,  $F$ , is included in the differential equations for thrust and torque as follows:



$$dF = 4F\pi r\rho U_1^2 a(1-a)dr \quad (3.55)$$

$$dM = 4F\pi r^3\rho\Omega a'(1-a)dr \quad (3.56)$$

Subsequently, tip loss correction can be applied to the axial induction factor and angular induction factors :

$$a = \frac{1}{1 + \frac{4F \sin^2 \phi}{\sigma C_N}} \quad (3.57)$$

$$a' = \frac{1}{\frac{4F \sin \phi \cos \phi}{\sigma C_{TAN}} - 1} \quad (3.58)$$

### 3.4.5 Turbulent wake state correction model

In Figure 3.4, when the axial induction factor,  $a$ , becomes larger than approximately 0.4 the BEM theory fails to produce accurate results. The axial induction factor,  $a$ , can become large at high tip speed ratios, which occurs when the fluid velocity is low, resulting in a high thrust loading on the turbine. Thus, it is necessary to include the turbulent wake state correction model when applying Prandtl's tip loss correction to account for the relationship between thrust coefficient and axial induction factor. Various turbulent wake state corrections have been developed to improve the BEM theory method. One of the most commonly used and studied turbulent wake state correction models is Glauert's correction model. When Glauert's empirical formula was first reported in a quadratic formula, the loss factor was ignored (Glauert 1926) as shown below:

$$C_T = 4a(1-a) \quad a \leq 0.4 \quad (3.59)$$

$$C_T = 0.889 - 0.444a + 1.556a^2 \quad a > 0.4 \quad (3.60)$$

The exclusion of the total loss factor in the Glauert empirical formula results in a gap appearing, a numerical instability, at a critical value of axial induction factor when trying to include Prandtl's loss correction. Consequently, many improvements have been made by various researchers to address this gap. Glauert, in his later work, further improved his correction formula to attempt to close this gap, the thrust

coefficient in this correction by Glauert is expressed as (Glauert 1926):

$$C_{T_{Glauert}} = 4aF(1 - a) \quad a \leq 0.4 \quad (3.61)$$

$$C_{T_{Glauert}} = 0.889F - 0.444aF + 1.556a^2F \quad a > 0.4 \quad (3.62)$$

Therefore, the axial induction factor is as follows:

$$a_{Glauert} = \frac{1}{1 + \frac{4F \sin^2 \phi}{\sigma(C_L \cos \phi + C_D \sin \phi)}} \quad C_T \leq 0.96F \quad (3.63)$$

$$a_{Glauert} = \sqrt{\frac{0.6423C_T}{F} - 0.5507 + 0.1427} \quad C_T > 0.96F \quad (3.64)$$

Another widely used turbulent wake state correction model is Buhl's correction (Buhl 2005). The thrust coefficient can be expressed as:

$$C_{T_{Buhl}} = 4aF(1 - a) \quad a \leq 0.4 \quad (3.65)$$

$$C_{T_{Buhl}} = \frac{8}{9} + \left(4F - \frac{40}{9}\right)a + \left(\frac{50}{9} - aF\right)a^2 \quad a > 0.4 \quad (3.66)$$

Therefore, the axial induction factor is as follows:

$$a_{Buhl} = \frac{1}{1 + \frac{4F \sin^2 \phi}{\sigma(C_L \cos \phi + C_D \sin \phi)}} \quad C_T \leq 0.96F \quad (3.67)$$

$$a_{Buhl} = \frac{18F - 20 - 3\sqrt{C_T(50 - 36F + 12F(3F - s))}}{36F - 50} \quad C_T > 0.96F \quad (3.68)$$

De Vries (de Vries 1979) has proposed a new modified approach to the axial induction factor, this method has a good improvement at smaller tip loss correction factors,  $F$ . The expression below shows De Vries' correction:

$$C_{T_{DeVries}} = 4aF(1 - aF) \quad (3.69)$$

Shen (Shen et al. 2005) proposed a new tip loss correction model to predict the physical behaviour in the proximity of the TCT blade tip. The local thrust coefficient is replaced by a linear relationship based on De Vries change when the value of the axial induction factor becomes greater than a critical value. The thrust coefficient can be expressed as:

$$C_{T_{Shen}} = 4aF(1 - aF) \quad a \leq \frac{1}{3} \quad (3.70)$$

$$C_{T_{Shen}} = 4 \left[ \frac{1}{9}F^2 + \left(1 + \frac{2}{3}F\right)aF \right] \quad a > \frac{1}{3} \quad (3.71)$$

Therefore, the axial induction factor is as follows:

$$a_{Shen} = \frac{1}{1 + \frac{4F \sin^2 \phi}{\sigma(C_L \cos \phi + C_D \sin \phi)}} \quad C_T \leq \frac{8}{9}F \quad (3.72)$$

$$a_{Shen} = \frac{2 + K_1 - \sqrt{4K_1(1 - F) + K_1^2}}{2(1 + FK_1)} \quad C_T > \frac{8}{9}F \quad (3.73)$$

$$K_1 = \frac{4F \sin^2 \phi}{\sigma(C_L \cos \phi + C_D \sin \phi)F_{Shen}} \quad (3.74)$$

$$F_{Shen} = \frac{2}{\pi} \cos^{-1} \left[ \exp \left( -g_1 \frac{\frac{B}{2}[R - r]}{r \sin \phi} \right) \right] \quad (3.75)$$

$$g_1 = \exp \left[ -\frac{1}{8}(B\lambda - 21) \right] + 0.1 \quad (3.76)$$

In most studies, the Prandtl tip loss correction factor and Glauert's empirical equation are used for analysing the performance of the TCT (Sun et al. 2017, Esfahanian et al. 2013, khchine & Sriti 2017, Sun et al. 2016). This approach is somewhat of a classical correction to the BEM theory method and one of the most considered because it is a linear correction and easy to implement and obtain the results. However, the linear correction method can be less accurate at lower loss correction factors and higher axial induction factors. As a consequence, non-linear correction

has been widely considered in recent studies. It is widely used in the BEM theory method to obtain the hydrodynamic loadings along the TCT (Arramach et al. 2017, Koh & Ng 2016, Lanzafame & Messina 2013). The two popular non-linear correction models used are Buhl's correction (Buhl 2005) and Shen's correction (Shen et al. 2005). Buhl (Buhl 2005) gave an improved nonlinear function for turbulent wake state effects and yields a better result than the linear function. However, Shen (Shen et al. 2005) corrected both the induced velocities and the mass flux for tip loss effects. Shen's correction has received more consideration in recent studies such as in (Koh & Ng 2016) since it has been proved to be the most dependable method for loss corrections (Pratumnopharat & Leung 2011).

A recent new development by Zhong (Zhong et al. 2020) based on Shen's correction model further improved the BEM theory method by introducing two new factors, the Zhong's modification has been validated (Zhong et al. 2020) and has shown improvement. The following are the two new factors by Zhong which are the downwash factor due to the three-dimensional effect,  $F_S$ , and the rotational effect factor,  $F_R$ , given:

$$F_S = \frac{2}{\pi} \cos^{-1} \left[ \exp \left( -\frac{R-r}{\bar{c}} \right)^{3/4} \right] \quad (3.77)$$

$$F_R = 2 - \frac{2}{\pi} \cos^{-1} \left[ \exp \left( -2B \left( 1 - \frac{1}{R} \right) \sqrt{1 - \lambda_r^2} \right) \right] \quad (3.78)$$

where  $\lambda_r$  is the local tip speed ratio and  $\bar{c}$  is the geometric mean chord length,

$$\bar{c} = \frac{S}{R-r} \quad (3.79)$$

where  $A_S$  is the blade area between the local radial position and the blade tip. Zhong in his work also corrected the lift and drag coefficients,  $C_L$  and  $C_D$ , of the local spanwise blade element:

$$C_L = \frac{1}{\cos^2 \alpha_i} (C_{L_e} \cos \alpha_i - C_{D_e} \sin \alpha_i) \quad (3.80)$$

$$C_D = \frac{1}{\cos^2 \alpha_i} (C_{L_e} \sin \alpha_i + C_{D_e} \cos \alpha_i) \quad (3.81)$$

where  $\alpha_i$  is the downwash angle which is calculated using Equation (3.82),  $C_{L_e}$ , and  $C_{D_e}$ , are the 2-dimensional hydrofoil's lift and drag coefficient at an effective angle

of attack,  $\alpha_e$ .

$$\alpha_e = \frac{C_{L2D}(\alpha)}{m}(1 + F_S) \quad (3.82)$$

where  $C_{L2D}(\alpha)$  is the 2-dimensional hydrofoil's lift coefficient at the local angle of attack,  $\alpha$ , and  $m$  is the curve slope of the linear zone of the hydrofoil lift coefficient profile before the stall angle.

### 3.5 Computational Fluid Dynamics (CFD)

This section provided details on the theory governing the CFD process. It should be noted that the work in this thesis only considers incompressible fluid flow conditions and as a result, the theory is described this way. Fluid mechanics is the study of fluids and can be divided into fluid statics and fluid dynamics. CFD utilises computational approaches to describe fluid motion through the use of a numerical technique. The velocity pressure field solutions from CFD, in most cases, are of most significance, for a given fluid's properties such as density, viscosity, and surface tension. The two main barriers in fluid mechanics to a workable model are viscosity and geometry (White 2009).

In some idealised cases, viscosity can be neglected which renders the fluid flow field inviscid. However, for real-life applications viscosity is present and can sometimes be varying also. These further increase the difficulty in constructing and using the basic equations to solve the fluid flow field (White 2009). Moreover, it can have a destabilising effect on the fluid flow field creating a disordered, random phenomenon known as turbulence. Furthermore, the difficulties increase when dealing with complex geometry features. Fortunately, with the help of CFD some of these difficulties imposed by the complex geometry and viscosity can be greatly reduced. CFD implements conservation principles, including the three fundamental conservation equations:

- Mass (continuity)
- Momentum (Newton's second law (Newton et al. 1729))
- Energy (first law of thermodynamics (Clausius 1879))

By utilising the conservation principles to fluid motion, it is viable to define the Navier Stokes (NS) Equations, which can be given in different forms. Equation (83) and (84) gives the Navier-Stokes Equations in incompressible vector form. These equations describe the motion of any Newtonian fluid.

$$\nabla \cdot \mathbf{V} = 0 \quad (3.83)$$

$$\rho \left( \frac{\partial \mathbf{V}}{\partial t} + \mathbf{V} \cdot \nabla \mathbf{V} \right) = -\nabla p + \mu \nabla^2 \mathbf{V} + \mathbf{S} \quad (3.84)$$

where  $\mathbf{V}$  is the velocity vector,  $t$  is time,  $\rho$  is density,  $p$  is the pressure,  $\mu$  is the viscosity,  $\mathbf{S}$  is a source term and  $\nabla^2$  is the Laplacian operator. Although the incompressible Navier-Stokes Equations indirectly describe turbulent flow fields, they are inherently difficult to solve due to the non-linear nature, specifically the convective acceleration term  $\mathbf{V} \cdot \nabla \mathbf{V}$ . In this thesis, the Reynolds-Averaged Navier-Stokes (RANS) method was utilised to numerically resolve the Navier-Stokes Equations, more details are provided on this topic in sub-chapter 3.5.1.

### 3.5.1 Reynolds-Averaged Navier-Stokes (RANS)

CFD is a computational-numerical technique used to solve fluid flow problems, and to be more specific is to solve the Navier-Stokes (NS) equations (Wilcox 1994). By obeying the conservation principles set out in the equations of conservation of mass, momentum and energy (Newton et al. 1729, Clausius 1879), the NS equations can be defined as given in Equation 3.85 to 3.88. These equations describe the motion of any Newtonian fluid in cartesian form.

$$\frac{\partial u}{\partial x} + \frac{\partial v}{\partial y} + \frac{\partial w}{\partial z} = 0 \quad (3.85)$$

$$\rho \left( \frac{\partial u}{\partial t} + u \frac{\partial u}{\partial x} + v \frac{\partial u}{\partial y} + w \frac{\partial u}{\partial z} \right) = -\frac{\partial p}{\partial x} + \mu \frac{\partial^2 u}{\partial x^2} + \frac{\partial^2 u}{\partial y^2} + \frac{\partial^2 u}{\partial z^2} + S_x \quad (3.86)$$

$$\rho \left( \frac{\partial v}{\partial t} + u \frac{\partial v}{\partial x} + v \frac{\partial v}{\partial y} + w \frac{\partial v}{\partial z} \right) = -\frac{\partial p}{\partial y} + \mu \frac{\partial^2 v}{\partial x^2} + \frac{\partial^2 v}{\partial y^2} + \frac{\partial^2 v}{\partial z^2} + S_y \quad (3.87)$$

$$\rho \left( \frac{\partial w}{\partial t} + u \frac{\partial w}{\partial x} + v \frac{\partial w}{\partial y} + w \frac{\partial w}{\partial z} \right) = -\frac{\partial p}{\partial z} + \mu \frac{\partial^2 w}{\partial x^2} + \frac{\partial^2 w}{\partial y^2} + \frac{\partial^2 w}{\partial z^2} + S_z \quad (3.88)$$

where  $x, y, z$  is the Cartesian coordinate system,  $u, v, w$  is the Cartesian velocity system,  $t$  is time,  $\rho$  is density,  $p$  is pressure,  $\mu$  is viscosity and  $S_{(x,y,z)}$  is a source term. However, NS equations are challenging to solve directly due to their non-linear nature, for example, the convective acceleration terms. Reynolds averaging is a common method used to approximate these equations and was first described by Osborne Reynolds in 1895 (Reynolds 1895). The instantaneous velocities are separated into two components such that  $u = \bar{u} + u'$ , where  $\bar{u}$  is the mean velocity, and  $u'$  is a fluctuation velocity. In this case, the mean component must have several properties such as the mean of the fluctuation is zero ( $\bar{u}' = 0$ ) and is known as a Reynolds operator. When combining Reynolds averaging with NS equations and then time averaging the results produces a time-averaged model of these equations which are known as Reynold-Averaged Navier-Stokes (RANS) equations, given in Equations (3.89) to (3.92) in Cartesian form and equation (3.93) as tensor form.

$$\frac{\partial \bar{u}}{\partial x} + \frac{\partial \bar{v}}{\partial y} + \frac{\partial \bar{w}}{\partial z} = 0 \quad (3.89)$$

$$\begin{aligned} \rho \left( \frac{\partial \bar{u}}{\partial t} + u \frac{\partial \bar{u}}{\partial x} + v \frac{\partial \bar{u}}{\partial y} + w \frac{\partial \bar{u}}{\partial z} \right) &= -\frac{\partial \bar{p}}{\partial x} + \mu \frac{\partial^2 \bar{u}}{\partial x^2} + \frac{\partial^2 \bar{u}}{\partial y^2} + \frac{\partial^2 \bar{u}}{\partial z^2} + S_x \\ &\quad -\rho \left( \frac{\partial \bar{u}'u'}{\partial x} + \frac{\partial \bar{u}'v'}{\partial y} + \frac{\partial \bar{u}'w'}{\partial z} \right) \end{aligned} \quad (3.90)$$

$$\begin{aligned} \rho \left( \frac{\partial \bar{v}}{\partial t} + u \frac{\partial \bar{v}}{\partial x} + v \frac{\partial \bar{v}}{\partial y} + w \frac{\partial \bar{v}}{\partial z} \right) &= -\frac{\partial \bar{p}}{\partial y} + \mu \frac{\partial^2 \bar{v}}{\partial x^2} + \frac{\partial^2 \bar{v}}{\partial y^2} + \frac{\partial^2 \bar{v}}{\partial z^2} + S_y \\ &\quad -\rho \left( \frac{\partial \bar{u}'v'}{\partial x} + \frac{\partial \bar{v}'v'}{\partial y} + \frac{\partial \bar{v}'w'}{\partial z} \right) \end{aligned} \quad (3.91)$$

$$\begin{aligned} \rho \left( \frac{\partial \bar{w}}{\partial t} + u \frac{\partial \bar{w}}{\partial x} + v \frac{\partial \bar{w}}{\partial y} + w \frac{\partial \bar{w}}{\partial z} \right) &= -\frac{\partial \bar{p}}{\partial z} + \mu \frac{\partial^2 \bar{w}}{\partial x^2} + \frac{\partial^2 \bar{w}}{\partial y^2} + \frac{\partial^2 \bar{w}}{\partial z^2} + S_z \\ &\quad -\rho \left( \frac{\partial \bar{u}'w'}{\partial x} + \frac{\partial \bar{v}'w'}{\partial y} + \frac{\partial \bar{w}'w'}{\partial z} \right) \end{aligned} \quad (3.92)$$

$$\rho \frac{D\bar{u}_i}{Dt} = -\frac{\partial \bar{p}}{\partial x_i} + \mu \Delta \bar{u}_i - \rho \left( \frac{\partial \bar{u}'_i \bar{u}'_j}{\partial x_j} \right) + S_i \quad (3.93)$$

where  $x, y, z$  is the Cartesian coordinate system,  $\bar{u}, \bar{v}, \bar{w}$  is the mean velocity component,  $u', v', w'$  is the velocity fluctuation,  $t$  is time,  $\rho$  is density,  $p$  is the pressure,  $\mu$  is the viscosity,  $S_{(x,y,z)}$  is a source term and  $i, j$  represent components in the  $i, j$ th direction.

This process creates six new terms, which are commonly known as Reynolds stresses and denoted by  $\tau_{i,j} = -\rho \bar{u}'_i \bar{u}'_j$ . These newly created terms have no additional equations which results in an incomplete equation and is often referred to as the RANS closure problem. Furthermore, to complete the equation, turbulence models are utilised to approximate the unknown terms.

### 3.5.2 $k - \omega$ shear stress transport (SST)

The turbulence model used, for the research detailed in this thesis, is the  $k - \omega$  shear stress transport (SST) model. The  $k - \omega$  SST model is a combination of the standard  $k - \omega$  and  $k - \varepsilon$  models defined by Menter (Menter 1993, 1994, Menter et al. 2014). The  $k - \omega$  SST model is a variation and improvement of the baseline (BSL) model. The BSL model varies between the  $k - \omega$  and  $k - \varepsilon$  models in an almost linear manner whereas the  $k - \omega$  SST model also accounts for the turbulent shear stress. The model uses the  $k - \omega$  definition in the inner part of the boundary layer and the  $k - \varepsilon$  definition outside the boundary layer.

Menter (Menter 1993) created one set of equations by blending the  $k - \omega$  and  $k - \varepsilon$  model equations, by first transforming the  $k - \varepsilon$  model into a  $k - \omega$  formulation, shown in Equation (3.94) .

$$\begin{aligned} \rho \frac{\partial \omega}{\partial t} + \rho \bar{u}_j \frac{\omega}{\partial x_j} &= \alpha^{\omega\varepsilon} \frac{\omega}{k} \tau_{ij} \frac{\partial \bar{u}_i}{\partial x_j} - \beta_2^{\omega\varepsilon} \rho \omega^2 \\ &+ \frac{\partial}{\partial x_j} \left[ (\mu + \sigma_2^{\omega\varepsilon} \mu_T) \frac{\partial \omega}{\partial x_j} \right] \\ &+ 2\rho \sigma_2^{\omega\varepsilon} \frac{1}{\omega} \frac{\partial k}{\partial x_j} \frac{\partial \omega}{\partial x_j} \end{aligned} \quad (3.94)$$



where  $\alpha^{\omega\varepsilon}$ ,  $\beta_2^{\omega\varepsilon}$ ,  $\sigma_2^{\omega\varepsilon}$  are the new closure coefficients,  $k$  is the specific turbulence kinetic energy,  $\varepsilon$  is the dissipation per unit mass,  $\omega$  is the specific dissipation rate,  $x_{(i,j)}$  is the Cartesian coordinate system,  $\bar{u}_i$  is the mean velocity component,  $t$  is time,  $\rho$  is density,  $\mu$  is the viscosity,  $\mu_T$  is the eddy-viscosity. The two models are combined to create a new set of equations for  $k$  and  $\omega$  as shown in Equations 3.95 and 3.96.

$$\rho \frac{\partial k}{\partial t} + \rho \bar{u}_j = \tau_{ij} \frac{\partial \bar{u}_i}{\partial x_j} - \beta_1^{SST} \rho k \omega + \frac{\partial}{\partial x_j} \left[ (\mu + \sigma_1^{SST} \mu_T) \frac{\partial k}{\partial x_j} \right] \quad (3.95)$$

$$\begin{aligned} \rho \frac{\partial \omega}{\partial t} + \rho \bar{u}_j \frac{\partial \omega}{\partial x_j} &= \alpha^{SST} \frac{\omega}{k} \tau_{ij} \frac{\partial \bar{u}_i}{\partial x_j} - \beta_2^{SST} \rho \omega^2 \\ &+ \frac{\partial}{\partial x_j} \left[ (\mu + \sigma_2^{SST} \mu_T) \frac{\partial \omega}{\partial x_j} \right] \\ &+ 2\rho(1-F) \sigma_2^{SST} \frac{1}{\omega} \frac{\partial k}{\partial x_j} \frac{\partial \omega}{\partial x_j} \end{aligned} \quad (3.96)$$

where  $\alpha^{SST}$ ,  $\beta_1^{SST}$ ,  $\beta_2^{SST}$ ,  $\sigma_1^{SST}$ ,  $\sigma_2^{SST}$  are the new combined closure coefficients,  $F_1$  is the blending function. A blending function,  $F_1$  is used to gradually change between the two methods in the desired regions. It is designed so that the  $k - \omega$  formulation is used in the near wake region and the  $k - \varepsilon$  formulation is used in the free shear layers. The coefficients also blended using Equation (3.97).

$$F_1 = \tanh \left[ \left( \min \left( \max \left( \frac{\sqrt{k}}{0.09 \omega y_s}; \frac{500 \nu}{y_s^2 \omega} \right); \frac{4 \rho \sigma_2^{\omega\varepsilon} k}{CD_{kw} y_s^2} \right) \right)^4 \right] \quad (3.97)$$

$$CD_{kw} = \max \left( 2 \rho \sigma_2^{\omega\varepsilon} \frac{1}{\omega} \frac{\partial k}{\partial x_j} \frac{\partial \omega}{\partial x_j}, 10^{-10} \right) \quad (3.98)$$

where  $k$  is the specific turbulence kinetic energy,  $\omega$  is the specific dissipation rate,  $y_s$  is the distance to the nearest surface,  $\rho$  is the density,  $\nu$  is the kinematic viscosity,  $\sigma_2^{\omega\varepsilon}$  is a closure coefficient and  $CD_{kw}$  is the cross-diffusion term.

The advantage of the  $k - \omega$  SST model is that it accounts for the turbulence shear stress by limiting the eddy-viscosity as shown in Equation (3.99). However, it is limited based on the assumption that the turbulent shear stress is proportional to

the specific turbulence kinetic energy in the logarithmic and wake regions of the turbulence boundary layer (Johnson & King 1984).

$$\mu_T = \frac{\rho a_1 k}{\max(a_1 \omega, S F_2)} \quad (3.99)$$

$$F_2 = \tanh \left[ \left( \max \left( 2 \frac{\sqrt{k}}{0.09 \omega y_s}; \frac{500 \nu}{y_s^2 \omega} \right) \right)^2 \right] \quad (3.100)$$

where  $\mu_T$  is the eddy-viscosity,  $a_1$  is a constant equal to 0.31,  $k$  is the turbulence kinetic energy,  $\omega$  is the specific dissipation rate,  $S$  is the invariant measure of the strain rate,  $F_2$  is the second blending function,  $y_s$  is the distance to the nearest surface,  $\rho$  is the density and  $\nu$  is the kinematic viscosity.

### 3.5.3 Near wall region

A boundary layer is a thin layer of fluid created when fluid moves past an object's surface. The fluid in the boundary layer is subjected to shearing effects which the velocity changes from zero at the surface to the free stream value away from the surface (White 2009). A boundary layer exists for all types of flows such as laminar, transitional and turbulent flow. The law of the wall, also known as the logarithmic law of the wall published by Theodore von Kármán in 1930 states that the turbulence near that boundary is a function only of the flow conditions pertaining to that wall and is independent of the flow conditions further away (Cengel & Cimbala 2013). Technically, the law of wall only applied to flow close to the wall ( below 20% of the height of the flow). However, it can also be used to provide a good approximation of the entire velocity profile of the fluid stream (White 2009).

Depending on Reynolds number, boundary layers may be either laminar (layered), or turbulent (disordered). For laminar flow conditions, the streamwise velocity changes uniformly as one moves away from the wall (Cengel & Cimbala 2013). For turbulent flow conditions, the streamwise velocity is characterised by unsteady (changing with time) swirling flows inside the boundary layer. The boundary layer of any wall in a turbulent flow can be divided into four regions based on the distance from the wall: viscous sublayer, buffer zone, fully turbulent log-law zone and outer region. Figure 3.5 Shows the sub-division of the boundary layer in near-wall region (Ansys 2009). In a CFD simulation, the prediction accuracy of the velocity gradient

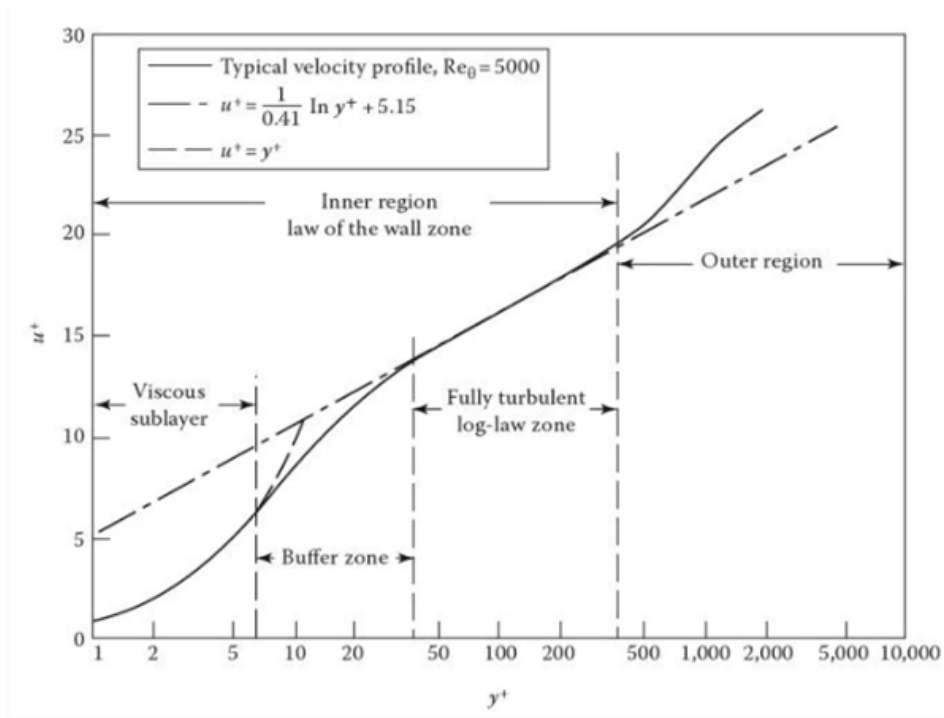


**Figure 3.5:** Sub-divisions of near-wall region in turbulent flow condition (Ansys 2009).

across the boundary layer is dependent on mesh constructed (Ansys 2009).

For turbulent flow conditions, the first cell ideally lies within the very thin viscous sub-layer (Cengel & Cimbala 2013). However, in some flow scenarios, the first cell would be outside the viscous sub-layer, especially for complex flows in complicated geometries and usually a very fine mesh resolution is required at the near wall to solve this problem, which would extensively increase computational time (Cengel & Cimbala 2013, Ansys 2009). A wall function is introduced to accurately predict the flow in the boundary layer. Ergo, to fully resolve the boundary layers in the near wall region requires appropriate mesh resolution and appropriate wall function (White 2009, Ansys 2009). One important parameter to determine the wall function is a dimensionless length value,  $y^+$ , which is a non-dimensional distance from the wall to the first node from the wall and can be determined using Equation (3.101).

$$y^+ = \frac{U^* y_s}{\nu} \quad (3.101)$$

where  $U^*$  is the friction velocity at the wall,  $y_s$  is the distance to the nearest wall

and  $\nu$  is the local kinematic viscosity of the fluid.

Based on Figure 3.5, in the inner region there are three sub-layers where the velocity profile can be determined as follows:

- **viscous sublayer** ( $0 < y^+ < 5$ ), near the wall, where viscous effects dominate the flow and the velocity profile is linear as seen in Equation (3.102).

$$U^* = y^+ \quad (3.102)$$

- **buffer zone** ( $5 < y^+ < 30$ ), in between sub-layers, where the velocity profile transitions from linear to logarithmic and no clear law can be observed.
- **fully turbulent log-law zone** ( $30 < y^+ < 300$ ), where the velocity profile follows a log-law up to the end of the boundary layer as seen in Equation (3.103), where  $\kappa \approx 0.41$  is the von Kármán constant and  $C^+$  is an empirical parameter (e.g.  $C^+ \approx 5$  in smooth walls):

$$U^* = \frac{1}{\kappa} \ln(y^+) + C^+ \quad (3.103)$$

Wall functions are used to significantly reduce computational expense by reducing the grid resolution and modelling the flow using semi-empirical functions as shown in Figure 3.6. A corresponding wall function grid can have the first cell with a  $y^+ = 100$  (Kalitzin et al. 2005). There are many different wall functions available and are typically used for different turbulence models. Wall functions will not be discussed here in detail as the topic is too vast, only a brief summary of their implications is provided. For a more detailed description, see (Kalitzin et al. 2005).

For the  $k - \omega$  model, an analytical expression is known for the viscous sublayer and there is an approximation for the logarithmic layer (Kalitzin et al. 2005). Whereas for the  $k - \varepsilon$  model there is no analytical expression for the viscous sublayer; so, an approximate is needed for all boundary layers. Many functions assume the first grid point is within the fully turbulent log-law region which has a significant impact on the result, this is not always the case. Therefore, the  $k - \omega$  model is more accurate for wall-bounded simulations. Hence, the use of  $k - \omega$  SST model is suitable for most wall conditions.

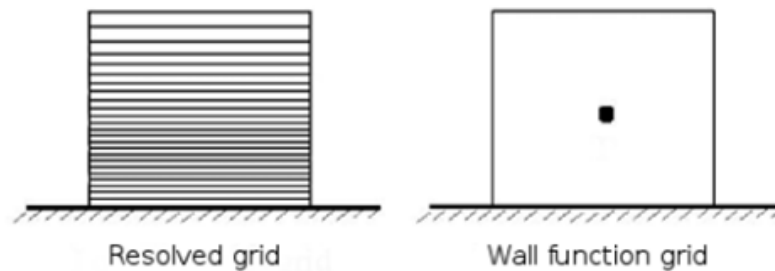


**Figure 3.6:** Difference in grid resolution using a wall function. (Kalitzin et al. 2005)

### 3.5.4 Discretisation

Computational machines do not treat motion equations in differential form, instead, it is solved in discretised form. The discretisation process is most commonly referred to as grid generation or meshing, which involves dividing the fluid domain into discrete points (also known as nodes) and volumes (also known as cells or elements). There are two types of meshing grids:

- **structured grids** are made up of hexahedral cells with each grid point being uniquely defined by indices  $i, j, k$ .
- **unstructured grids** have no particular ordering with point creation. The grid cells are commonly tetrahedral cells, although they can be made up of various cells including tetrahedral, hexahedral, prisms, pyramids and wedges such grids are known as hybrid or mixed grids.

When using a structured grid, it is easy to relate cells and their neighbours, this allows data to easily be calculated by adding or subtracting indices. However, it encounters difficulty when faced with a complex geometry that cannot be divided regularly. One way to overcome such a problem in a structured grid mesh is to divide the geometry into smaller blocks or parts where it can be discretised easier, this method is known as a multiblock approach. The multiblock approach tends to create ‘hanging nodes’ where the nodes only occur on one side of the block boundaries. Another popular approach that circumvents the complex geometry issues is the overset method, where the grids are created around boundaries independently and then overlapped. This method allows the transfer of data between grids within the overlapping region.

While the unstructured grids are more flexible and can be generated more easily using tetrahedral cells. It is also common to use hexahedral and prism cells to resolve the boundary layer. The unstructured grids method can handle refining and coarsening of a grid with ease. However, it requires more complex data structures to keep track of cells and their connections which can lead to higher computational memory requirements compared to structured grids. After the domain has been constructed to form a grid, the equations need to be discretised. Three main discretisation approaches that can be used which are the Finite Difference method (Finite Difference Method (FDM)), Finite Element Method (Finite Element Method (FEM)) and Finite Volume Method (Finite Volume Method (FVM)). Below is a brief description of each:

- The **Finite Difference method (FDM)** was first utilised by Euler (Blazek 2005) and was among the first discretisation methods. FDM was directly applied to the differential equations by utilising the Taylor series expansion to discretise the flow variables. Studies have shown that this method is simple to use and can achieve high order approximations with ease, producing high accuracy results. However, there were limitations to FDM, it can only work under a structured grid and could not be applied to body-fitted grids (Blazek 2005).
- The **Finite Element Method (FEM)**, as proposed by Turner in 1956, is a numerical technique originally developed for structural analysis (Turner et al. 1956). It has since been applied to various fields, including fluid dynamics. FEM can handle both structured and unstructured meshes, where grid nodes are used to represent the solution with high accuracy on smooth grids (Blazek 2005). It works by formulating the governing equations in an equivalent integral form. FEM is well-suited for problems with complex geometries and non-Newtonian fluids. It provides a rigorous mathematical foundation and can be mathematically equivalent to the finite volume method in certain cases. However, it comes with a higher numerical expense compared to some other numerical methods.
- The **Finite Volume Method (FVM)** was first employed in 1971 by McDonald (McDonald 1971) for two-dimensional flows and it directly utilises the

integral formulation of the Navier-Stokes equations, which allows for a conservative representation of the flow variables. This method discretises the computational domain into discrete control volumes or cells on which the surface integral is calculated. The accuracy of the FVM discretisation depends on the schemes used to define the control volumes. Control volumes can be defined using two different schemes: the cell-centred scheme and the cell-vertex scheme.

In the cell-centred scheme, the control volumes are defined around the cell centres (Blazek 2005). The cell centres represent the primary locations where the flow variables, such as velocity and pressure, are stored and computed. This scheme is more simple to implement and is commonly used in many FVM applications.

In the cell-vertex scheme, the flow variables are stored and calculated at each vertex location and can either have the control volume as the sum of the cells sharing a grid point (overlapping control) or the volume centred around a grid point (dual control) (Blazek 2005). The overlapping control calculates the vertex based on the surrounding cells. The dual control stores all variables at the node, with the control volume constructed based on the midpoints of the cells surrounding the node.

The choice between the cell-centred and cell-vertex schemes depends on the specific problem and the desired accuracy. Each scheme has its advantages and limitations, and the appropriate choice is determined based on factors such as the geometry of the problem, the behaviour of the flow, and the numerical accuracy requirements. The cell-centred scheme greatly depends on the grid's smoothness, but the cell-vertex scheme is not affected by this. However, both schemes can reach second or higher order accuracy if the grid is sufficiently smooth. The dual control in the cell-vertex scheme can experience difficulties at the boundary of solid walls as the node is on the wall which leads to discretisation errors when compared to the cell-centred scheme. When applying cell-centred scheme to an unstructured grid, the number of control volumes increases compared to the cell-vertex scheme. The increase in control volumes does suggest the cell-centred scheme is more accurate but it comes with additional computational power requirements. Typically, the cell-centred scheme requires approximately twice as much memory as the cell-vertex scheme. The FVM is very flexible and can be implemented on structured and unstructured grids. Hence, due to its flexibility, the FVM is the most widely used

discretisation process.

### 3.5.5 ANSYS software

The RANS equations and the numerical methods developed to solve the equations are commonly run on a high-performance computer using tried and tested CFD software codes. The CFD software used in this work is ANSYS, which has two available code options, namely ANSYS-CFX and ANSYS Fluent. Both ANSYS-CFX and ANSYS-Fluent are commercially available general-purpose CFD codes. The ANSYS-CFX has been applied to a broad range of industries and applications. It has been used extensively in the wind energy and tidal energy industries to study turbine rotor and porous disk approaches (Choi et al. 2013, Song & Perot 2015, Harrison et al. 2010). ANSYS-Fluent is more commonly used to model turbulence, heat transfer, and reactions, due to it having several solvers and discretisation types available. It has also been used in the wind industry to study single blades, full rotors and actuator disks (Lu et al. 2011, WuBow et al. 2007, Makridis & Chick 2013).

The rotor in this research is represented as an actuator disk, the porous disk is an excellent representation of an actuator disk in ANSYS which commonly features predefined momentum losses. Some similar porous disk approaches use analogous equations such as momentum and drag sinks to describe the porous disk. The porous disk features the same diameter as the rotor with a thin depth/thickness. The disk needs a thickness to avoid singularities caused by discontinuities in the pressure and velocity fields.

In ANSYS-CFX (Ansys 2009), the disk domain is defined as a porous media. There are several ways to define the momentum loss in the porous media such as by using permeability or/and loss coefficient. In this thesis, the loss coefficient and directional loss model were used to model an isotropic momentum loss. In ANSYS CFX the directional loss model adds a momentum source term to the flow, given by:

$$S = -K \frac{\rho}{2} u |u| \quad (3.104)$$

where  $K$  is the resistance coefficient which needs to be defined by the user in ANSYS CFX,  $\rho$  is the density of the fluid and  $u$  is fluid velocity. The term  $u|u|$  is to define the source term as a vector in the direction of the flow. The resistance is



applied as a loss across the disk thickness in ANSYS CFX, so it is required that the user specifies the loss as  $\frac{K}{d}$ , where  $d$  is the thickness of the disk.

While in ANSYS-Fluent (ANSYS 2012), a cell-zones analogy is used to define the porous media. It is modelled using an additional momentum source term, given in Equation (3.105), where two components are presented, namely a viscous loss term (linear) and an inertial loss term (quadratic).

$$S_i = \left( \sum_{i=1}^3 C_1 \mu u_i + \sum_{i=1}^3 C_2 \frac{1}{2} \rho u_i |u| \right) \quad (3.105)$$

$$S = -C_2 \frac{1}{2} \rho u |u| \quad (3.106)$$

where  $S_i$  is the source term for the  $i^{\text{th}}$  momentum equation,  $\mu$  is the fluid viscosity,  $u$  is the velocity and  $C_1$  and  $C_2$  are prescribed matrices. The momentum sink contributes to the pressure gradient in the porous zone, creating a pressure drop that is proportional to the fluid velocity squared in the cell (ANSYS 2012). For a simple homogeneous porous media in one direction, the permeability term can be eliminated ( $C_1 = 0$ ) (ANSYS 2012), and the resistance is applied as a loss across the disk thickness similar to ANSYS CFX. Furthermore, it required that the user specifies the loss as  $\frac{C_2}{d_t}$ , where  $d_t$  is the thickness of the disk.

### 3.6 Summary

This chapter has presented important key theories behind the development of the numerical model used in this work. The two main theories involved in this work were the actuator disk (AD) and blade momentum element (BEM) theory. Both theories were essential in the development of the BEM-AD model which will be discussed in the Methodology Chapter. Furthermore, since the work relied heavily on computational fluid dynamics simulations. Hence, the theory behind CFD was presented too. The chapter can be summarised as below:

- In the first section, some important basic rotor definitions were introduced like the concepts of Reynolds number,  $Re$ , the tip speed ratio of a blade, the solidity of a turbine, angle of attack, relative velocity, axial induction factor, angular induction factor, thrust coefficient and power coefficient. The use of thrust coefficient and power coefficient formulas was useful as it is utilised in

the CFD result analysis to estimate the thrust coefficient and power coefficient by the rotor disk.

- In section 3.3, the fundamental of actuator disk (AD) was presented which introduced the concept of streamtube wake, porous disk and also some critical assumptions made in AD theory. These assumptions include the homogeneity and steadiness of the flow, the incompressibility of the fluid, the absence of frictional drag, and an infinite number of blades. The sub-chapter also presented the thrust and power formulas defined with respect to the conservation of momentum. Furthermore, this sub-chapter also mentioned the Betz limit which dictates the maximum theoretical power coefficient,  $C_P$  able to achieve from an ideal rotor at the axial induction factor  $a = 1/3$ , which corresponds to a  $C_P$  of 0.593.
- In section 3.4, the two important theories in BEM theory were detailed in this sub-chapter which were the momentum theory and blade elements theory. In the momentum theory, the local trust and torque of a hydrofoil can be determined through one-dimensional momentum analysis. While, in the blade element theory, the turbine blade was divided into a number of elements and through the use of lift and drag coefficient, the local trust and torque of the blade element can be determined. BEM combines both theories to accurately calculate hydrodynamics loads acting on a turbine. However, there are shortcomings in BEM theory such as losses at the blade tip and inaccuracy in prediction at axial induction factor,  $a$ , greater than 0.4. As a result, a Prandtl's loss correction was introduced to address the losses at the blade tip and a correction model to tackle the accuracy issue of BEM at  $a > 0.4$ . This work utilised the correction model developed by Zhong (Zhong et al. 2020).
- In the section 3.5, the RANS equations are important governing equations behind CFD was presented in this sub-chapter. RANS is a time-averaged model that describes fluid motion with respect to the three fundamental conservation equations which were the conservation of mass, conservation of momentum and conservation of energy. However, RANS equations on their own are incomplete referred to as RANS closure problem. The  $k - \omega$  SST model was utilised in this work to complete the RANS equations and the formulas were detailed in the sub-chapter. The sub-chapter also described some important factors in CFD simulation such as near-wall region, and discretisation (mesh).

The sub-chapter 3.5.3 discussed the creation of a boundary layer when fluid flow passes an object's surface and the introduction of the wall function to accurately predict the boundary layer. The sub-chapter 3.5.4 discussed the type of grids and the type of discretisation methods to process the grids. Lastly, the subchapter also mentioned some key parameters involved in utilising the actuator disk model in ANSYS.

The upcoming chapter is the methodology chapter. In the methodology chapter, the AD theory and BEM theory mentioned in the theory chapter were utilised to develop a BEM-AD model which is crucial in the development of a single turbine model and turbines array model. A mesh study was also conducted on the developed model using the background knowledge mentioned in section 3.5.

# Chapter 4

## Methodology

### 4.1 Introduction

In this chapter, the detailed theories regarding AD theory and BEM theory were utilised to construct a BEM-AD model along with its variations and modifications. The developed modified BEM-AD model was later utilised to develop a turbine array model as detailed in this chapter as well.

The chapter has two main sub-chapters, the first sub-chapter focuses on the development of a hybrid BEM-AD disk model along with its various variations and modifications. In this sub-chapter, the numerical BEM model of the experimental blade was included along with the actuator disk configurations. The second sub-chapter focuses on the development of an aligned layout and staggered layout array models.

### 4.2 Single Turbine model

This sub-chapter focuses on the development of a hybrid BEM-AD model. In the first section, a detailed setup of an actuator disk (AD) model was presented, and the inflow condition was validated with experimental results (Harrison et al. 2010). The second section presented the BEM calculations of the experimental rotor blade, and the results were validated with experimental results (Harrison et al. 2010). The third section gives a detailed account of two variations of the BEM-AD model along with two different sets of empirical formulas to describe the disk properties

in CFD. The fourth section presents the hybrid of the two variations resulting in a hybrid modification to the BEM-AD model and a set of empirical formulas was created to describe the disk properties in CFD. The final section is a mesh study, which presents a method to reduce an overall number of elements while retaining accuracy. Additionally, a mesh sensitivity and independence study were carried out and the results are presented.

### 4.2.1 Actuator disk (AD) model

The computational fluid dynamics (CFD) approach was employed to simulate the actuator disk model. CFD is a method of analysing the fluid flow field, among other things, under certain conditions using computational methods (Ansys 2009). The software chosen for this work was the CFX package within ANSYS, and the processes involved in setting up the simulation are shown in Figure 4.1. In Figure 4.1, with respect to the specifics of this analysis, the computational domain is representative of the space in which the tidal current turbine, under the analysis, is situated and encompasses both the turbine represented by the actuator disk and the fluid. The first step in specifying the computational domain is to define the spatial dimensions and geometries of the various components.

The CFX software uses a method known as finite volume rendering, which divides the computational domain into sub-regions called control volumes, this process is known as meshing (Ansys 2009). In Figure 4.1, once the analytic domain geometries have been generated, they then proceed to the mesh generator. The number of nodes and elements in the mesh are critical to the computation analysis of the fluid flow simulation (Ansys 2009). The meshed geometries are then inputted into the setup of CFX along with required parameters such as boundary conditions, inflow conditions, and actuator disk domain properties, to name a few, before running the CFX solver to obtain a set of results. The physical properties can be grouped into two types which are the fluid domain parameters and the actuator disk domain parameters.

The CFD simulations follow four phases in their operations. Phase 1 is geometry set-up, phase 2 is meshing, phase 3 is parameter set-up, and phase 4 is solving and post-processing. For a functional solver and post-processor of results, each stage

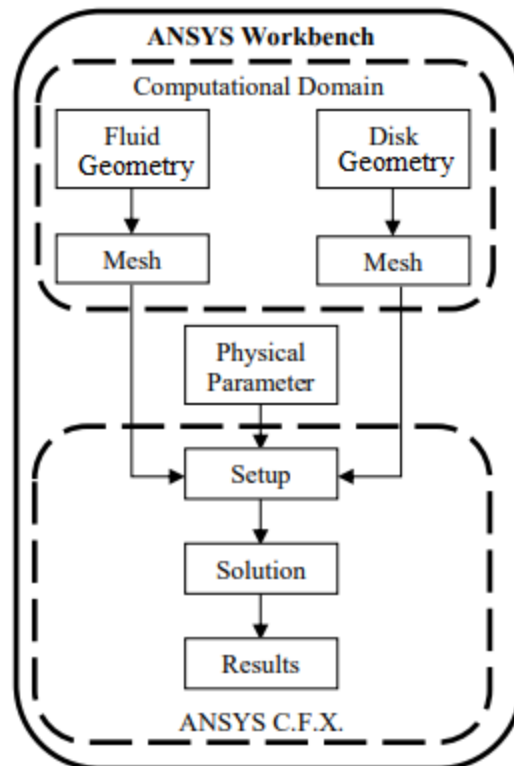


**Figure 4.1:** ANSYS CFX. Setup for actuator disk model.

must be furnished with the correct corresponding inputs and parameters. The ANSYS software setup for the simulations conducted consists of two branch domains that feed into the CFX solver software, as shown in Figure 4.2. The two domains are: the fluid domain and the actuator disk domain, the branches are made up of geometry and the meshed geometry of the domain which are inputted into the CFX solver for analysis.

The developed model has two domains: the fluid domain which allows for the computation of the distribution of current, turbulence and flow of fluid, and the actuator disk domain which describes the tidal current turbine blade properties in the actuator disk as porosity and resistance coefficient. Figure 4.3 shows the geometry of the fluid domain from the front view and the side view, this geometry is similar to the experimental measurements from (Harrison et al. 2010). Figure 4.3 shows the fluid domain has dimensions of  $6D$  (disk diameters) in width,  $6D$  in height and  $20D$  in length, with the actuator disk placed in mid-depth and  $5D$  from the inlet. The dimension of the geometry is represented by a number of diameters of the actuator

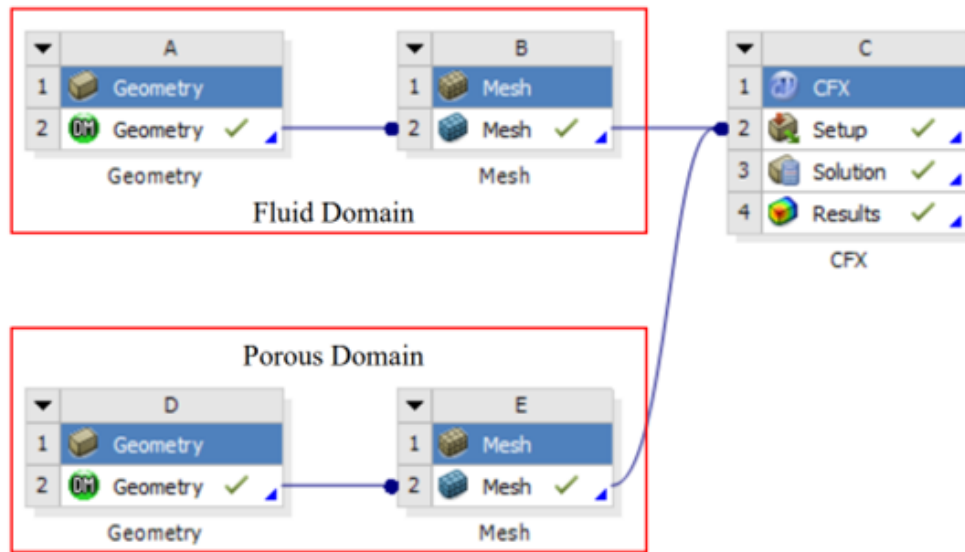


**Figure 4.2:** ANSYS CFX set-up branches outline.

disk domain, i.e. height of  $3D$ . A 2-dimensional fluid geometry was also developed by extruding the fluid domain from the side view to a thickness of  $0.001\text{m}$  (one-element thick), this 2-dimensional set up is used later in this work to compare against the 3-dimensional model.

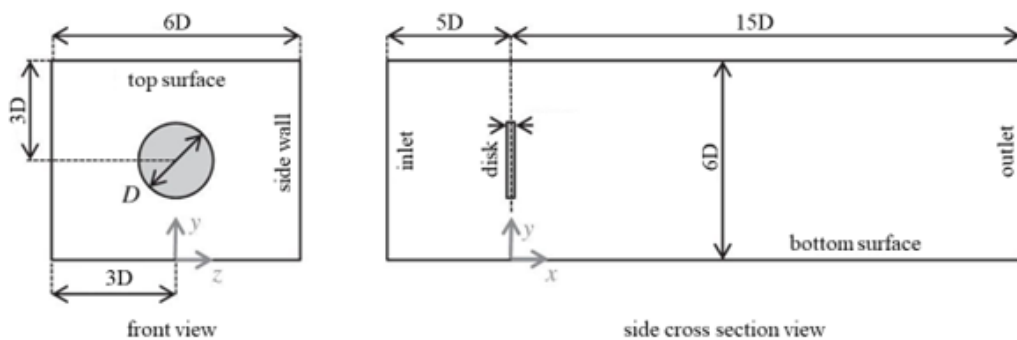


**Figure 4.3:** Geometry of the fluid domain.

The next step after a geometry construction is completed is to generate an appropriate mesh for the geometry, this will be explained in detail in a mesh independent study under the sub-section 4.2.5. After meshing, physical parameters need to be specified for the fluid domain such as describing the boundary face properties of

each face of the fluid domain and specification of a suitable turbulence model to be used to close the RANS equations.

In this work, the boundary layer conditions are not of specific interest and the free surface effect is insignificant as there is only a 0.2% depth change at the actuator disk region as suggested from the experiment measurements (Harrison et al. 2010). Therefore, symmetry conditions are used on the side and top surface boundaries. The outlet boundary was defined as an opening condition with zero relative pressure and zero turbulence gradients. The bottom surface boundary was described as a smooth wall with no slip. The inlet boundary was described by velocity, using  $U_{inlet}(z)$  profiles and turbulent kinetic energy  $k_{turb}(z)$  profiles. Both of these profiles can be determined using Equations (4.1), (4.2) and (4.3). (Nguyen et al. 2016),

$$U_{inlet}(z) = 2.5U^* \ln\left(\frac{zU^*}{\nu}\right) + A \quad (4.1)$$

$$k_{turb}(z) = \frac{3}{2}I_{mean}^2 U_{mean}^2 \quad (4.2)$$

$$\varepsilon = C_\mu^{\frac{3}{4}} \frac{k_{turb}^{\frac{3}{2}}}{l} \quad (4.3)$$

where  $U_{inlet}$  is the inlet velocity,  $U^*$  is the friction velocity,  $z$  is the distance from the bottom,  $A$  is a velocity constant with a value of  $0.197m/s$ ,  $\nu$  is the kinematic viscosity of water,  $k_{turb}$  is the turbulent kinetic energy,  $U_{mean}$  is the mean inlet velocity,  $I_{mean}$  is the mean turbulence intensity,  $\varepsilon$  is the turbulent dissipation rate,  $C_\mu$  is a constant of value 0.09 and  $l$  is the turbulence intensity,  $l = 0.07H$  (where  $H$  is the characteristic length).

Figure 4.4, shows a comparison of numerical inlet velocity and turbulence intensity with experimental inlet conditions. It was observed that the numerical inlet conditions match closely to the experimental conditions (Harrison et al. 2010).

Table 4.1 shows the summarised parameters of all the boundary faces. The CFD simulation in this study was calculated using ANSYS-Workbench, specifically ANSYS-CFX using the steady-state solution of the Reynolds-Averaged Navier-Stokes (RANS)



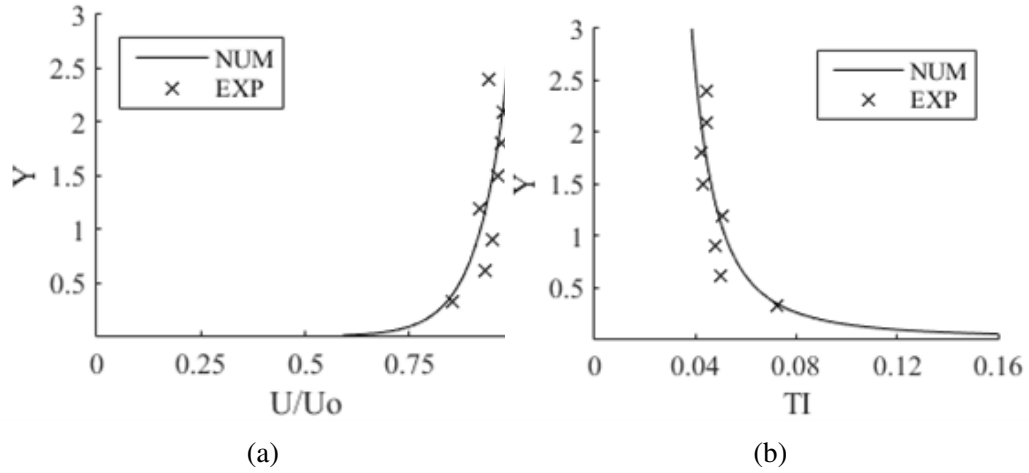


**Figure 4.4:** Velocity profile (a) and turbulence intensity profile (b) at the inlet comparing numerical and experimental inlet conditions.

equations (White 2009), together with the  $k - \omega$  SST turbulence model (Menter 1993). This model was chosen over the  $k - \varepsilon$  model based on the literature and some preliminary exploratory simulations which showed that the  $k - \omega$  SST model performs better inflows featuring adverse pressure gradients (Wilcox 1994) in terms of the accuracy to predict the flow properties. The  $k - \omega$  SST model was also used in the benchmark studies (Harrison et al. 2010). An extensive turbulence model study has been carried out by Nguyen (Nguyen et al. 2016), comparing the performance of different turbulence model effects on the basic actuator disk model with experimental measurements, refer to section 2.8.3 for details.

**Table 4.1:** summary of boundaries parameters

Boundaries	Parameters
Top	Symmetry
Lateral	Symmetry
Bottom	Smooth Wall
Outlet	Opening; entrainment; zero relative pressure and zero turbulence gradient
Inlet	Velocity profile and turbulent kinetic energy profile.

The disk domain in this study is described as a porous medium with dimensions of  $5m$  diameter and thickness of  $0.1m$ . The 2-dimensional model disk domain has a height of  $5m$  and length of  $0.1m$  with an extruded thickness of  $0.001m$  (identical to the fluid domain).

The experimental measurements used to assess the performance of the numerical models were based on the experiment carried out by Harrison, M.E., et al. from the University of Southampton (Harrison et al. 2010). In this experiment, the turbulence intensity was measured along with the velocity measurements behind a non-rotating porous disk representing a tidal current turbine. Measurements of the experiment were obtained using Acoustic Doppler Velocimetry with a sampling frequency of  $50\text{Hz}$  (Harrison et al. 2010). It has an accuracy of 1% and the duration of the burst is three minutes each. The mean inlet velocity is  $0.3\text{m/s}$  and the mean inlet turbulent intensity is 5%. The experimental disk has a resistance coefficient  $K = 2$  which corresponds to a thrust coefficient  $C_T = 0.86$ .

The disk domain in the basic actuator disk (AD) model describes its resistance coefficient and porosity similar to the experimental measurement. Hence, the basic AD model has a porosity of 0.58 and a resistance coefficient of  $K = 2$ . However, these parameters for this disk cater solely for thrust coefficient  $C_T = 0.86$ . That being so, a question can be raised on rotor characteristics? A solution to better describe the disk properties, based on the rotor geometry, BEM can be utilised to calculate the thrust coefficient or axial induction factor of the rotor which can then be translated into the disk's porosity and resistance coefficient. The subsection 4.2.3 and 4.2.4 describe some variations and a hybrid modification developed to improve the numerical prediction performance of the disk domain.

## 4.2.2 Numerical BEM turbine model

A numerical tidal current turbine model was developed using BEM theory in MATLAB. The numerical turbine model is used to determine the thrust coefficient of the turbine. The numerical results are then compared to the experimental measurement from Bahaj et. al. (Batten et al. 2007).

**Table 4.2:** Geometry parameter of the blade (Batten et al. 2007)

$r/R$	0.2	0.3	0.4	0.5	0.6	0.7	0.8	0.9	1
$c/R$	0.125	0.1156	0.1063	0.0969	0.0875	0.0781	0.0688	0.0594	0.05
$\phi$ (deg)	20	14.5	11.1	8.9	7.4	6.5	5.9	5.4	5

The three-bladed turbine has a diameter of 0.8m and blades are derived from the NACA 63(1)-8xx series hydrofoil. The chord ( $c/R$ ), twist ( $\phi$ ) and radius ( $r/R$ ) distributions are shown in Table 4.2. The lift and drag coefficient along the blade length are required in the BEM calculation. This can be obtained and solved using XFOIL software. The lift and drag coefficient between the angle of attack  $-10$  degrees to  $60$  degrees were obtained and are presented in Figure 4.5.

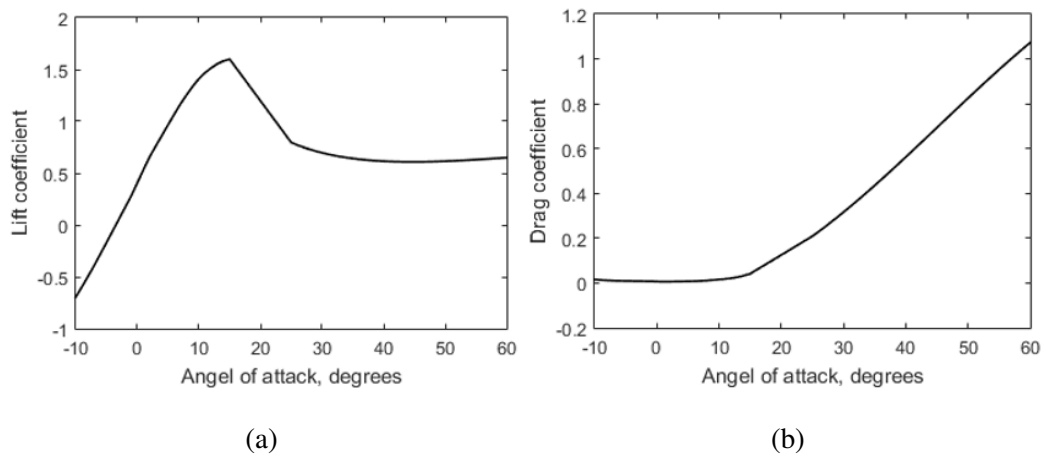


**Figure 4.5:** Lift coefficients (a) and drag coefficients (b) at angle of attack between  $-10$  degrees to  $60$  degrees.

To verify the prediction of the BEM simulation, the numerical results from the developed code were compared with experimental measurements using the same hydrofoil dataset as the experimental data, shown in Figure 4.6. For this comparison, the tidal current fluid speed is set to  $1.73\text{m/s}$ , background turbulence intensity of  $3\%$  is utilised and a hub pitch angle of  $20$  degrees is set. The numerical results show good agreement with the experimental measurements but there is slight under-prediction in thrust coefficient when tip speed ratio is greater than  $7$ . The tip speed ratio range utilised in this body of work ranges between  $4$  and  $7$ . Thus the current BEM numerical model is very appropriate for implementation in the BEM-AD model.

The BEM numerical model is an important feature in defining the disk properties in a BEM-AD model. It is crucial to translate the blade performance calculated in the BEM numerical model into inputs necessary for defining the AD in the CFD model. The two main crucial elements needed are the porosity and resistance co-

efficient of the disk domain. As mentioned in Chapter 3.5.5, these two factors can be determined using the thrust coefficient. The porosity and resistance coefficient of the disk domain can be determined using the thrust coefficient which is an output from the BEM numerical model.

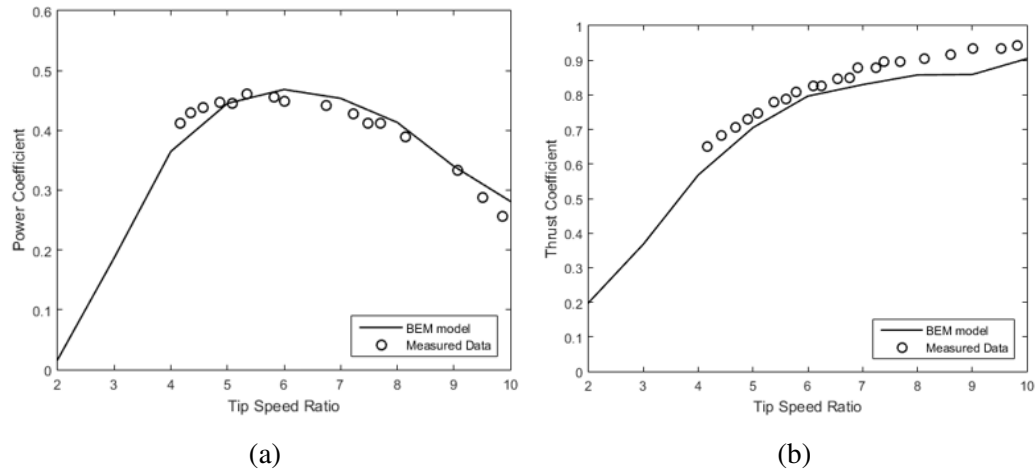


**Figure 4.6:** Comparison of numerical predicted power coefficients (a) and thrust coefficients (b) with experimental measurements (Batten et al. 2007) for a range of tip speed ratios

The BEM numerical model is an important feature in defining the disk properties in a BEM-AD model. It is crucial to translate the blade performance calculated in the BEM numerical model into inputs necessary for defining the AD in the CFD model. The two main crucial elements needed are the porosity and resistance coefficient of the disk domain. As mentioned in Chapter 3.5.5, these two factors can be determined using the thrust coefficient. The porosity and resistance coefficient of the disk domain can be determined using the thrust coefficient which is an output from the BEM numerical model.

Figure 4.7 shows the changing of the overall porosity and resistance coefficient of the disk at different blade tip speed ratios. In Figure 4.7, it is observed that when the tip speed ratio of the blade increases, the porosity of the disk decreases and the resistance coefficient of the disk increases. A relation between thrust coefficient and porosity is also presented in Figure 4.7, as thrust coefficient increases, porosity decreases.

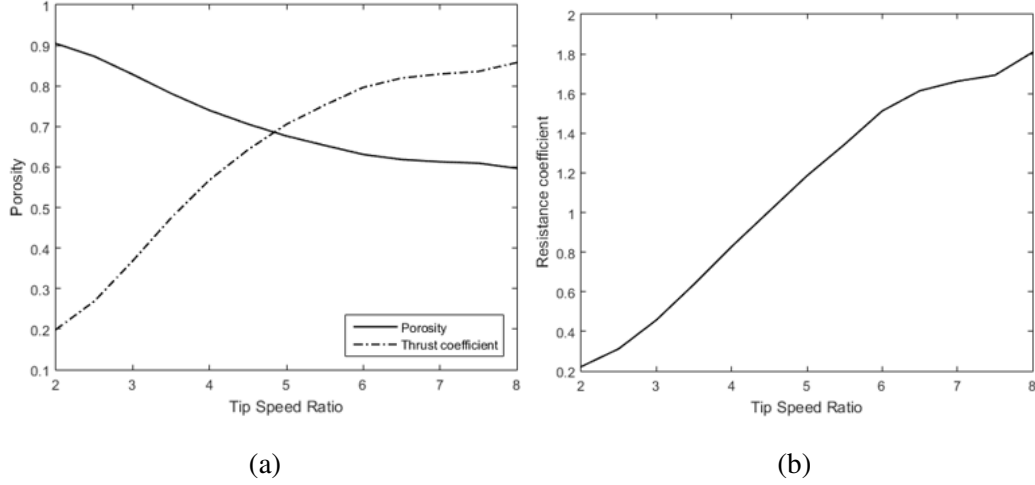


**Figure 4.7:** Porosity (a) and resistance coefficients (b) of the actuator disk domain at different tip speed ratios.

### 4.2.3 Velocity and radial variations

Two modification variations were introduced in this work to further improve the BEM-AD model and address some of the limitations of the actuator disk model approach especially in predicting wake properties in near wake region. The first variation of the developed BEM-AD model is a velocity variation which takes into account the velocity profile, where the disk experiences a non-uniform incoming velocity, and thus the disk has a varying porosity and resistance coefficient. Figure 4.8 shows the changing of porosity and resistance coefficient against normalised velocity. It is observed that when velocity increases, the porosity of the disk increases. While the resistance coefficient decreases, as velocity increases.

Based on the porosity and resistance coefficient determined through the BEM, shown in Figure 4.8, an empirical formula can be formed to explain the relationship between porosity,  $\theta$ , and resistance coefficient,  $k$ , with normalised velocity,  $u$ , as Shown in Equations (4.4) and 4.5).

$$\theta = -0.076u^3 + 0.369u^2 - 0.307u + 0.608 \quad (4.4)$$

$$k = 0.5227u^2 - 2.943u + 4.193 \quad (4.5)$$

Figure 4.9 shows the porosity and resistance coefficient of the numerical calculations and empirical calculations at different normalised velocities. The empirical calculation of porosity has a high correlation with the numerical calculations with an R-square value of 0.9982 and the empirical calculations of resistance coefficient also have a high correlation with the numerical calculations with an R-square value of 0.9917.

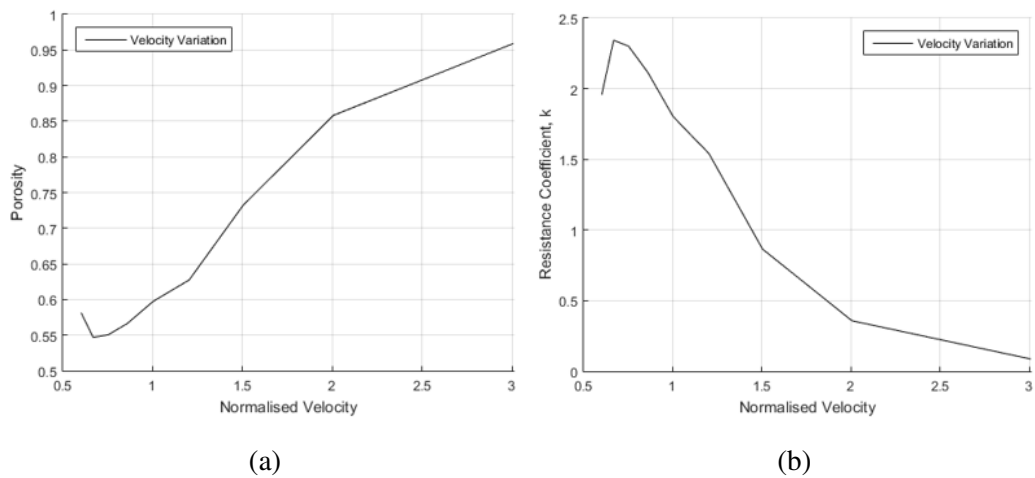


**Figure 4.8:** Porosity (a) and resistance coefficients (b) of the actuator disk domain at different normalised velocity.

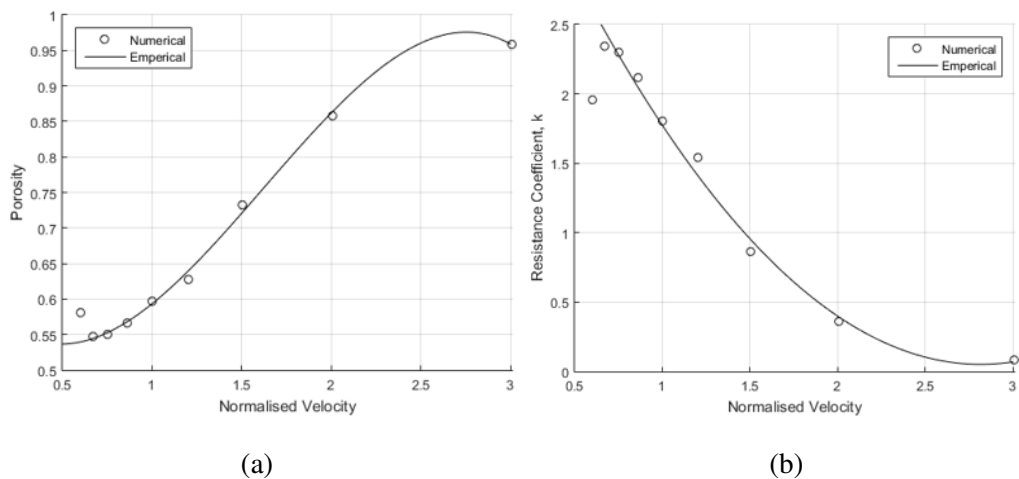


**Figure 4.9:** Numerical and empirical calculation of Porosity (a) and resistance coefficients (b) of the actuator disk domain at different normalised velocities.

The second variation of the developed BEM-AD model is a radial variation which

incorporates the blade element momentum theory into the design of the actuator disk, and thus the disk has a radial varying porosity and resistance coefficient along its annular radial location as shown in Figure 4.10. It is observed that as the radius increases, the porosity and resistance coefficient fluctuate around 0.58 and 2 respectively except for the tip region (at normalised radius = 1.0). The drastic change in porosity and resistance coefficient at the tip region is due to tip loss correction. Hence when forming an empirical formula to explain the relationship between porosity and resistance coefficient with annular radius, it would be best to exclude the tip.

Based on the porosity and resistance coefficient determined through BEM calculation, as shown in Figure 4.10, an empirical formula can be formed to explain the relationship between porosity,  $\theta$ , and resistance coefficient,  $k$ , with annular radius,  $R$ , as shown in Equations (4.6) and 4.7).

$$\theta = -0.1303R^2 + 0.1437R + 0.5472 \quad (4.6)$$

$$k = 1.348R^2 - 1.486R + 2.312 \quad (4.7)$$

Figure 4.11 shows the porosity and resistance coefficient of the numerical calculations and empirical calculations at different annular radius locations. The empirical calculation of porosity and resistance coefficient correlates well with the numerical calculations with an R-square value of 0.936 and 0.932 respectively excluding the tip region of the disk (blade tip region). The tip region has a porosity and resistance coefficient of 0.52 and 2.75 respectively.

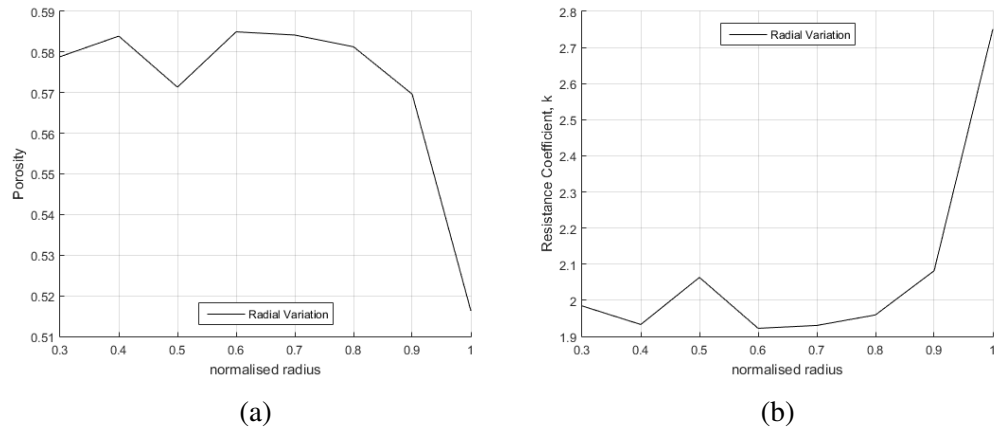


**Figure 4.10:** Porosity (a) and resistance coefficients (b) of the actuator disk domain at different normalised radii.

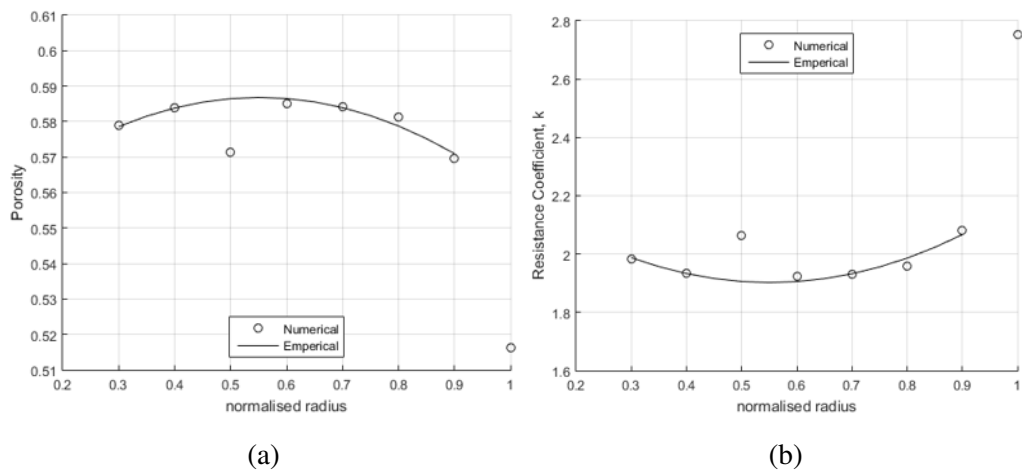


**Figure 4.11:** Numerical and empirical calculations of Porosity (a) and resistance coefficients (b) of the actuator disk domain at different normalised radius locations.



#### 4.2.4 Hybrid Modification

The hybrid modified BEM-AD model incorporates both variations in describing the porosity and resistance coefficient of the actuator disk. Therefore, there are now two factors affecting the porosity and resistance coefficient, i.e. the radius of the actuator disk and the velocity profile.

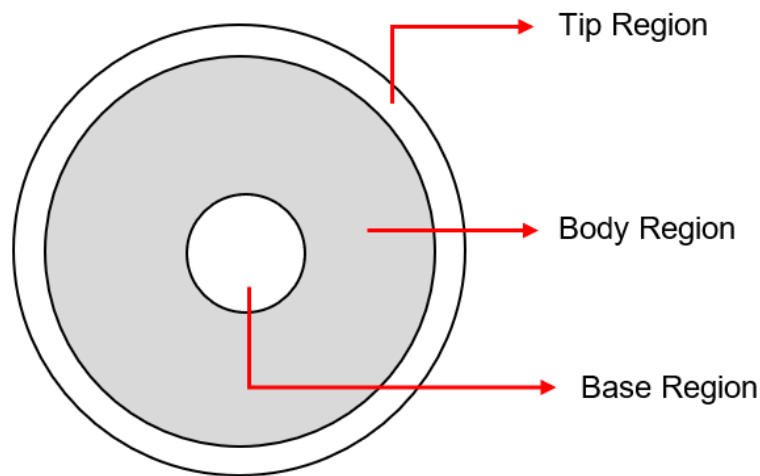


**Figure 4.12:** The disk domain separated into three regions.

When calculating the porosity and resistance coefficient of the disk domain, it is noticed that the base region (at normalised radius = 0.2) and tip region (at normalised radius = 0.9) tend to have outlier values compared to the trendline of the body region, due to geometry transition near the blade root and tip loss at the blade tip. Therefore, it is difficult to express this as a mathematical expression. Consequently, one way to overcome this difficulty is to exclude the base and tip region when forming the empirical formula. This also affects the disk domain configuration; the disk domain is separated into three annular zones to accurately reflect the blade properties in the disk domain as shown in Figure 4.12, where each zone will have its own empirical formula to describe porosity and resistance coefficient. Figure 4.13 shows the porosity and resistance coefficient of a blade body region determined through BEM calculations at different velocity and annular radius locations.

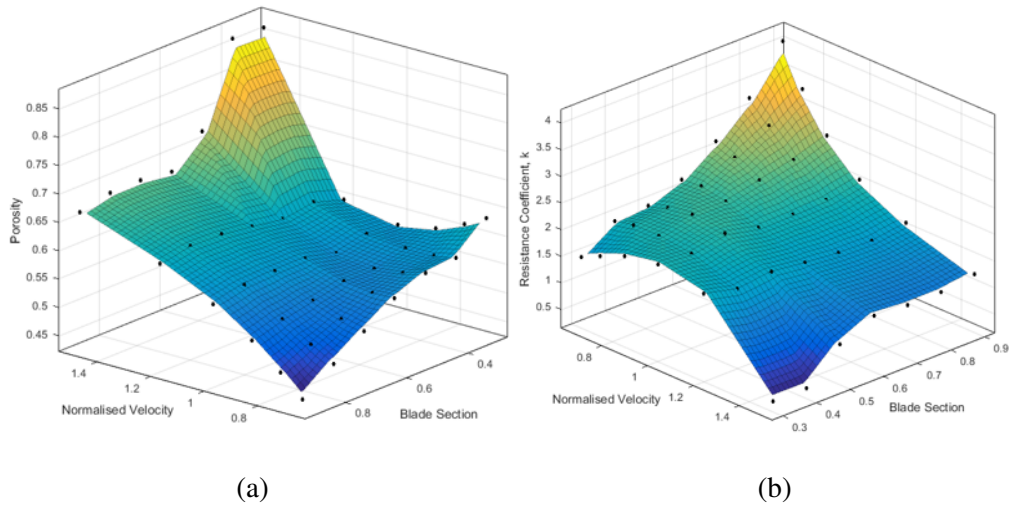


**Figure 4.13:** Porosity (a) and resistance coefficients (b) of the actuator disk domain at the different normalised radius and normalised velocity excluding base and tip regions.

Based on the porosity and resistance coefficient, determined through BEM calculations shown in Figure 4.13, an empirical formula can be formed to explain the relationship between porosity,  $\theta$ , and resistance coefficient,  $k$ , with normalised velocity,  $u$ , and annular radius,  $R$ , given in Equations (4.8) and 4.9).

$$\theta_{body} = 0.5729 + 0.02766u + 0.001946R + 0.01727u^2 + 0.01921uR + 0.002978R^2 + 0.006895u^3 - 0.03471u^2R + 0.01267uR^2 \quad (4.8)$$

$$k_{body} = 1.958 - 0.3879u - 0.08988R - 0.05596u^2 - 0.346uR + 0.04775R^2 + 0.2981u^2R - 0.1159uR^2 + 0.0615R^3 \quad (4.9)$$

Figure 4.14 shows the numerical calculations and empirical calculations of the porosity and resistance coefficient of an actuator disk domain's body region at different annular radius locations and normalised velocity. The empirical calculation of porosity has a good correlation with the numerical calculations with an R-square value of 0.9628 and a root mean square error (RMSE) value of 0.0147. The empirical calculation of the resistance coefficient has a good correlation with the numerical

calculations with an R-square value of 0.9883 and a RMSE value of 0.1185.

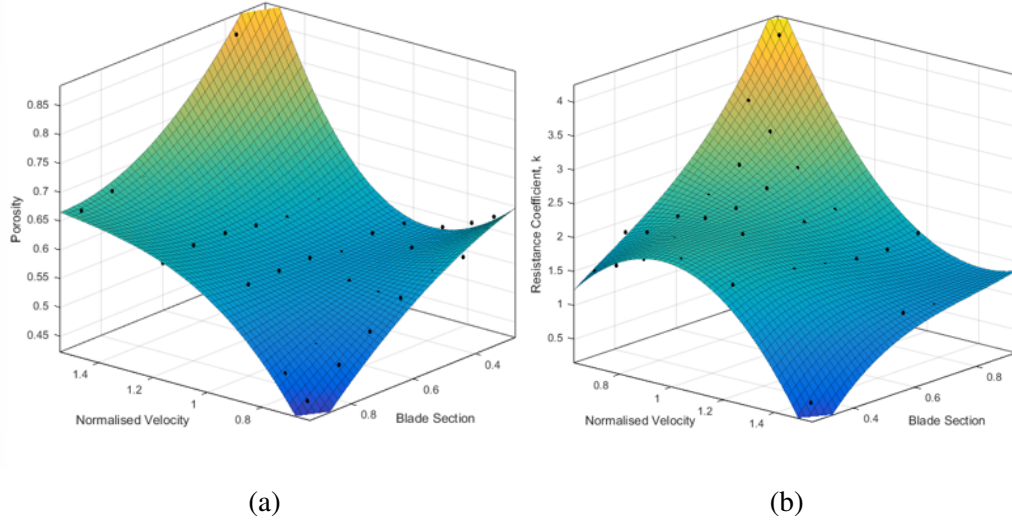


**Figure 4.14:** Numerical (dots) and empirical (contours) calculation of Porosity (a) and resistance coefficients (b) of the actuator disk domain's body region at different normalised radius locations and normalised velocity.

As mentioned earlier, the base and tip region of the blade are excluded when forming the empirical formula needed to describe the body region. An empirical formula can be formed to explain the relationship between porosity,  $\theta$ , and resistance coefficient,  $k$ , of the actuator disk domain's base region with normalised velocity,  $u$ , as shown in Equations (4.10) and 4.11).

$$\theta_{base} = 0.00134u^3 - 0.034u^2 + 0.276u - 0.225 \quad (4.10)$$

$$k_{base} = -0.00049u^3 + 0.012u^2 - 0.095u - 1.057 \quad (4.11)$$

Figure 4.15 shows the numerical calculations and empirical calculations of the porosity and resistance coefficient of an actuator disk domain's base region at different normalised velocities. The empirical calculation of porosity and resistance coefficient have a good correlation with the numerical calculations with an R-square value of 0.9992 and 0.9902 respectively.

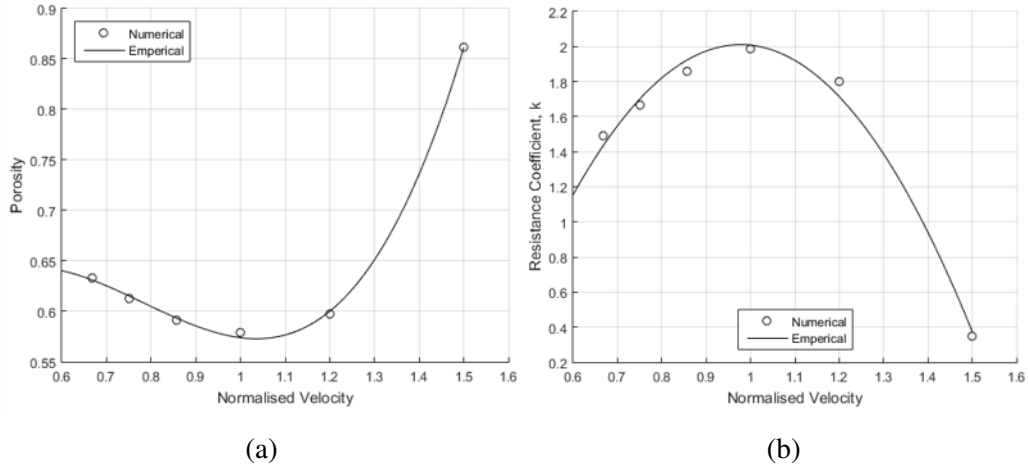


**Figure 4.15:** Numerical and empirical calculation of Porosity (a) and resistance coefficients (b) of the actuator disk domain's base region at different normalised velocities.

An empirical formula can be formed to explain the relationship between porosity,  $\theta$ , and resistance coefficient,  $k$ , of the actuator disk domain's base region with normalised velocity,  $u$ , as shown in Equations (4.12) and 4.13).

$$\theta_{tip} = 0.329 \log(u) + 0.502 \quad (4.12)$$

$$k_{tip} = 3.122u^{-2.05} \quad (4.13)$$

Figure 4.16 shows the numerical calculations and empirical calculations of the porosity and resistance coefficient of an actuator disk domain's tip region at different normalised velocities. The empirical calculation of porosity and resistance coefficient have a good correlation with the numerical calculations with an R-square value of 0.9830 and 0.9363 respectively.

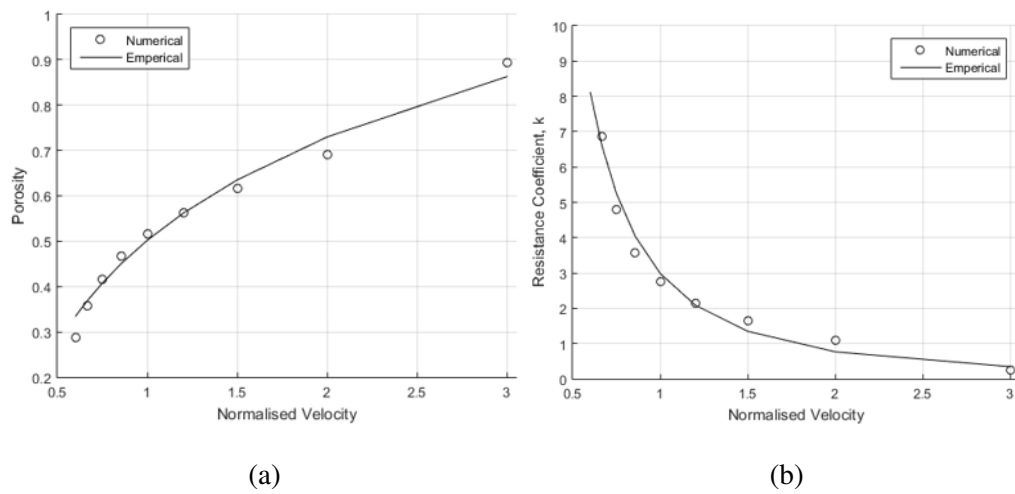


**Figure 4.16:** Numerical and empirical calculation of Porosity (a) and resistance coefficients (b) of the actuator disk domain's tip region at different normalised velocities.

### 4.2.5 CFD Meshing

A model with a well-constructed high-density mesh can significantly improve the accuracy of the simulation. However, to achieve this often demands a high computational cost. Thus, it is important to conduct a mesh sensitivity study to better investigate the most optimum mesh configuration and density. This sub-chapter provides a description of the mesh configuration and provides a mesh sensitivity study. Using the meshing software available in ANSYS, two domains have been constructed and discretised, which are the fluid domain and the disk domain. The meshing type used in all domains is tetrahedron unstructured mesh and has a smooth transition inflation with a growth rate value of 1.2.

An investigation was carried out to determine a method to reduce the need for a high density mesh (large numbers of fluid elements) to obtain the desired outcome. The method proposed in this work is a concentrated mesh zone approach. A normal mesh fluid domain in the main mesh domain with a constant element size; whereas in contrast, a concentrated mesh fluid domain has a region with a smaller element size value than the surrounding volume, this region is also known as the region of interest. Figure 4.17 shows the isometric cross-sectional view of a concentrated mesh fluid domain. As the element size decreases in a domain, the number of nodes and elements present in a domain increases. A higher number of elements tends to give a more accurate result but this is often dependant on mesh quality. In Figure 4.17, the sectional side view of a concentrated mesh fluid domain is shown, the region of interest is a semi-circular dome and a cylinder in the regions close to the actuator disk. The semi-circular dome has a radius of 3-disk diameters and is placed before the disk, whereas the cylinder disk has the same radius and is placed directly after the disk with a length extending to the end of the domain. The element size of the region of interest is smaller than the surrounding regions. The reason for this setup is to reduce the solver's computational time while not sacrificing the accuracy of results in the region of interest.

A comparison between the normal mesh fluid domain and concentrated mesh fluid domain of a basic actuator disk model is carried out. The configuration of the element size in the region of interest in the concentrated mesh fluid domain is the same as the element size in the normal mesh fluid domain; while the surrounding regions

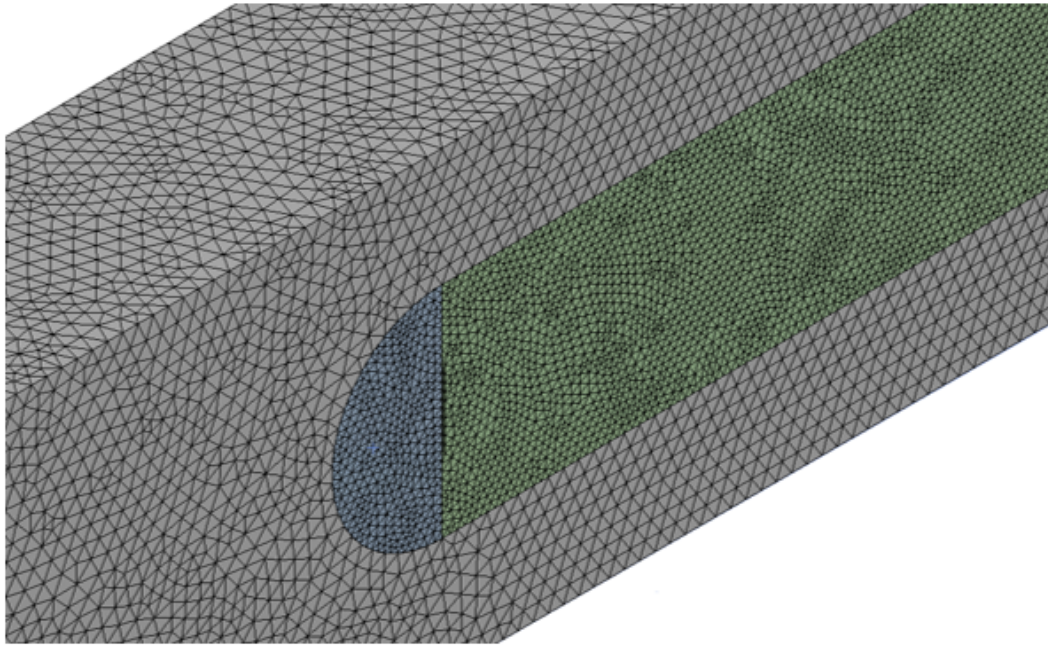


**Figure 4.17:** An isometric sectional view of the concentrated mesh fluid domain.

outside the concentrated mesh region have a larger element size, with a ratio between the surrounding region to concentrated mesh region of 1:4. In Figure 4.18, a comparison is given between the normal mesh and concentrated mesh fluid domain at 5D downstream from the disk in terms of velocity and turbulence intensity. The comparison results revealed that there is little difference in terms of downstream velocity and turbulence intensity, particularly in the region of interest. The time required for the normal mesh fluid domain to solve is 2 hours 57 minutes and the time required for the concentrated mesh fluid domain to solve is 1 hour 58 minutes. However, a slight overprediction was observed in the velocity prediction outside the region of interest in the concentrated mesh between the normalised vertical distance at 1.5 to 3.0 and -1.5 to -3.0; nonetheless, this doesn't affect the wake prediction of the disk. Ergo, to further improve the wake prediction of the disk; only needed to increase the mesh density in the region of interest.

An mesh independence study is important in creating an efficient computational simulation, while maintaining the finesse to capture areas of more complex fluid flow behaviour. Five meshes, each with a different number of elements, were investigated and compared for suitability for velocity at six different centreline locations downstream of the disk domain in a basic actuator disk model. These five meshes

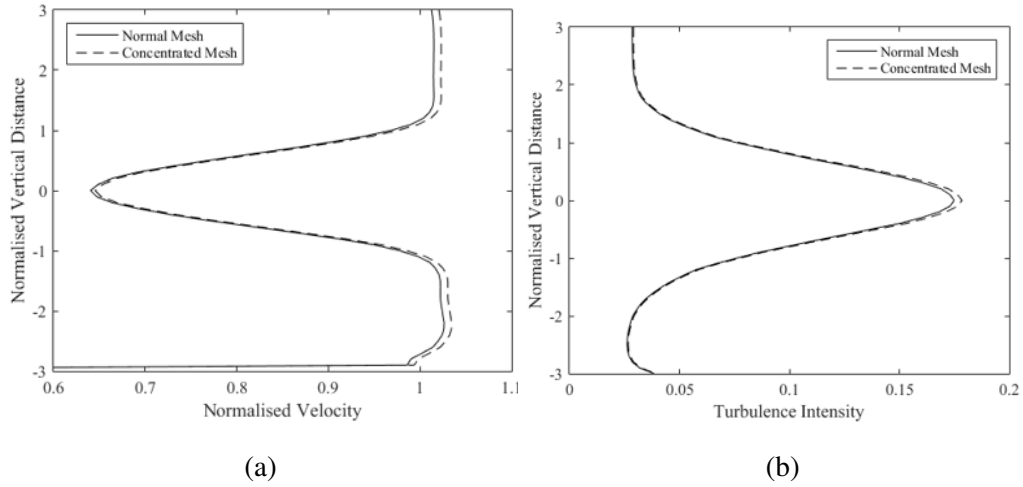


**Figure 4.18:** Vertical water column comparison between normal mesh (a) and concentrated mesh (b) fluid domains in terms of downstream velocity and turbulence intensity at 5D downstream from the actuator disk.

were produced by reducing the element size in the region of interest, as shown in Table 4.3, which shows the total number of elements for each mesh setup and also the ratio between the surrounding region to concentrated mesh. The disk domain was set to have an element size of  $0.01D$ . These studies were conducted on a Dell PC with 16GB RAM and Intel® Core™ i7-8700 3.20 GHz processor and the solvers were run in parallel across four processors to further reduce the computational time. The mesh independence study was conducted with maximum residuals of  $1 \times 10^{-5}$  and was allowed to run until the solution converged.

**Table 4.3:** Total number of elements of 5 different mesh setup.

Mesh	1	2	3	4	5
Ratio	1:4	1:6	1:7.5	1:12	1:30
Element size	0.075D	0.050D	0.040D	0.025D	0.010
No. of elements	$2.16 \times 10^5$	$5.18 \times 10^5$	$9.96 \times 10^5$	$1.76 \times 10^6$	$1.13 \times 10^7$

The six different point locations, P1 to P6 were taken from the centreline location with P1 being 2-disk diameters upstream and P2 to P6 located at downstream disk diameters distances of 3, 5, 8, 10 and 15 respectively. Table 4.4 presents summarised details on the mesh convergence study for each mesh setup and the computational time requirements. A percentage difference between each mesh setup at point locations P2 and P3 are included also.



**Table 4.4:** Summary of mesh study for different mesh setups, detailing number of elements, normalised velocity at point location P2 and P3 and convergence time.

Mesh	No. of elements	Normalised velocity at point location		Normalised velocity difference (%)		Solver Time (hrs: min: sec)
		P2	P3	$\Delta$ P2	$\Delta$ P2	
1	$2.16 \times 10^5$	0.835	0.886	–	–	00:58:35
2	$5.18 \times 10^5$	0.763	0.828	8.6	6.5	01:17:08
3	$9.96 \times 10^5$	0.732	0.808	4.0	2.4	01:57:08
4	$1.76 \times 10^6$	0.716	0.801	2.3	0.9	03:44:56
5	$1.13 \times 10^7$	0.714	0.802	0.3	0.1	08:14:21

Based on Table 4.4, the velocity at P3 converges for Mesh 3 where the percentage difference with Mesh 4 is 0.9% (less than 1%) and velocity at P2 converges for Mesh 4 where the percentage difference with Mesh 5 is 0.3% (less than 1%). This can be further observed in Figure 19 which shows the velocity at six different point locations for the range of mesh setups. It is observed that the velocities converge around Mesh 3 for all points with the exception of point 2 which converges for Mesh 4. Point 2 lies within the near wake region (less than 5 disk diameters from the disk). This being the case, if the study is only interested in results in the far wake region (more than 5 disk diameters from the disk), then Mesh 3 is suitable. However, the focus of this work is on the near and far wake regions. As a result, Mesh 4 was selected with a number of elements of  $1.76 \times 10^6$  and a convergence time of approximately 3 hours 44 minutes.

#### 4.2.6 Summary

The setup of the AD model in CFD was detailed using a porous disk to represent the turbine. The disk has a diameter of 5m and thickness of 0.1m, details of the fluid domain are presented in Figure 4.3. The inflow conditions of the fluid domain were described using Equations 4.1 to 4.3 and the inflow conditions results were against experimental conditions (Harrison et al. 2010). A BEM calculation of the experimental blade was presented, details of the blade's geometry parameters were shown in Table 4.2, and the calculated thrust and power coefficient though BEM was validated against experimental measurements (Batten et al. 2007).

Two sets of empirical formulas were generated for the velocity and radial variations to describe the porosity and resistance coefficient of the porous domain in CFD seen in Equations 4.4 to 4.7. The two variations were combined to produce a hybrid model and a set of empirical formulas was generated to describe the porous disk the porosity and resistance coefficient of the porous domain in CFD seen in Equations 4.8 to 4.13. A new meshing approach was used which was a concentrated mesh zone approach and a mesh sensitivity study was also conducted. The most optimum mesh size is  $1.76 \times 10^6$  elements which correspond to an element size of  $0.025D$ . The optimum ratio between the surrounding region to concentrated mesh is 1:12.

A multiple turbine study was conducted in this thesis, the multiple turbine model has the same fluid domain and disk domain characteristics and utilised the same mesh optimisation as well. For that reason, it is not detailed in the methodology.

### 4.3 Array Turbine model

The sub-chapter focuses on the development of an aligned layout and staggered layout array models. The first section presented the BEM calculations of the optimised rotor blade, and the results were validated with numerical results from the Yeo et al. 2022 model (Yeo et al. 2022). The second section presents a set of empirical formulas to describe the disk properties in CFD based on the optimised blade BEM calculations. The following section details the fluid domain setup for an ideal channel, headland and headland & island. The last section details the setup of Shannon Estuary's fluid domain and also a pseudo-transient approach to obtain time-varying results, the flow-field results of the simulated Shannon Estuary were validated against site measurements (O'Rourke et al. 2014).

#### 4.3.1 Optimised blade profile

Based on the methodology developed in the previous sub-chapter, an optimised blade profile was utilised to better predict the power and thrust coefficient of a tidal current turbine. The optimised blade is developed by Yeo et al. 2022 (Yeo et al. 2022) and is used to develop the numerical model in this work. The blade profile of the optimised blade is given in Table 4.6 showing the NACA profile of each

segment, the chord ( $c/R$ ) and the twist ( $\phi$ ). The optimised blade is modified from the NACA-6415 profile blade. Figure 4.19 shows the lift and drag coefficients of the NACA-6415 profile between -15 degrees to 20 degrees, this is obtained using XFOIL software.

**Table 4.5:** Geometry parameters of the Yeo et al. optimised blade (Yeo et al. 2022).

$r/R$	0.2	0.3	0.4	0.5	0.6	0.7	0.8	0.9	1
$c/R$	0.1560	0.1134	0.1025	0.0870	0.0741	0.0646	0.0576	0.0554	0.0532
NACA	4421	651,820	632,818	6415	6415	6415	6415	654,613	654,612
$\phi$ (deg)	21.42	15.23	11.3	8.69	8.46	5.68	5.96	4.99	4.02

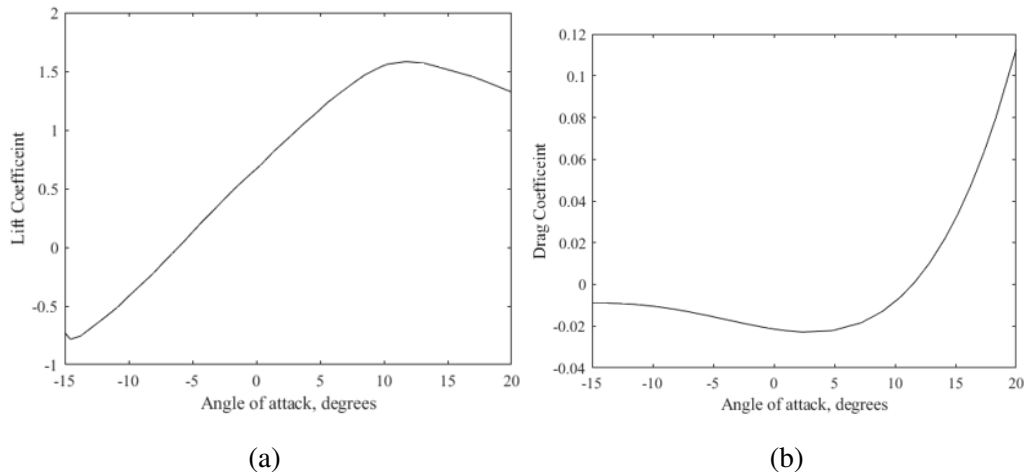


**Figure 4.19:** Lift coefficients(a) and drag coefficients (b) of NACA-6415 at angle of attack between -15 degrees to 20 degrees.

The BEM calculation for the optimised blade was validated against the numerical results from the Yeo et al. 2022 model (Yeo et al. 2022) as shown in Figure 4.20. For this comparison, the tidal current fluid speed is set to  $1.73\text{m/s}$ , background turbulence intensity of 3% is utilised and a hub pitch angle of 20 degrees is set. The numerical results show good agreement with the Yeo et al. model. Table 6 shows the comparative analysis of the power coefficient and thrust coefficient of the current model against the Yeo et al. model. The statistical analysis presented shows both the power coefficient and thrust coefficient correlate well with the Yeo et al. model with a mean absolute percentage error (MAPE) value of 5.49% and 3.26% respectively. The developed model also has a high R-square value and root mean

square error, RMSE value when compared with the Yeo et al. model.

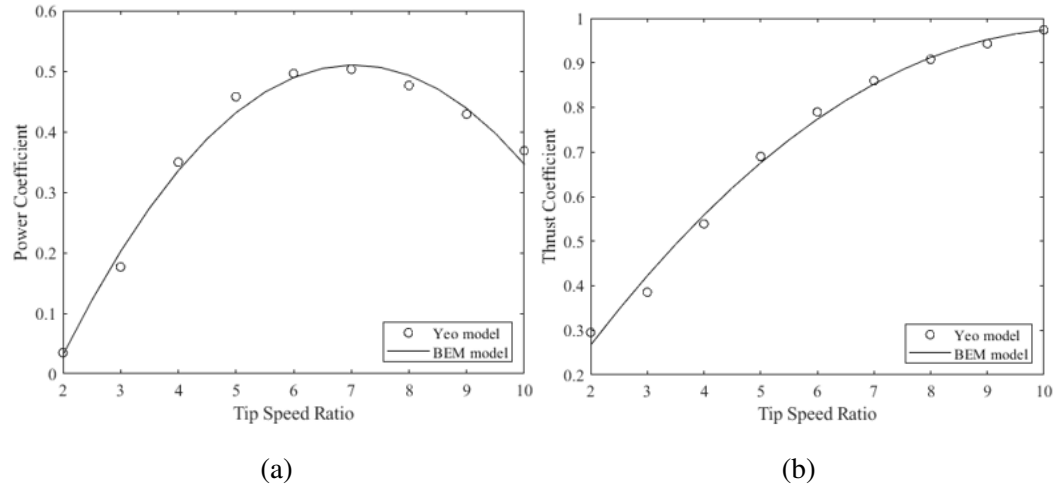


**Figure 4.20:** Comparison of numerical predicted power coefficients (a) and thrust coefficients (b) with the Yeo et al. model (Yeo et al. 2022) for a range of tip speed ratios.

**Table 4.6:** Comparative analysis of power and thrust coefficients for the current model against the Yeo et al. model (Yeo et al. 2022).

Coefficient	R-square	RMSE	MAPE
Power	0.9879	0.0168	5.49%
Thrust	0.9936	0.0188	3.26%

### 4.3.2 Optimised Modified BEM-AD model

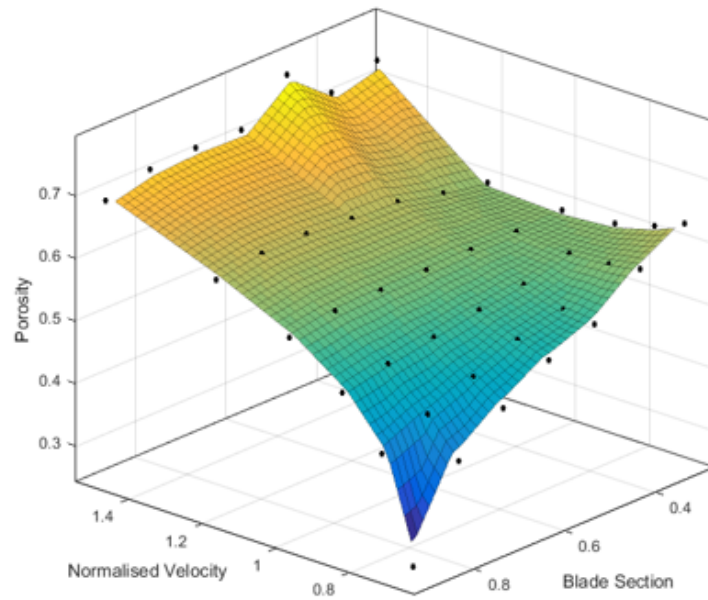
The optimised tidal current turbine blade was then incorporated into the detailing of the porosity and resistance coefficient of the hybrid modified BEM-AD model. As mentioned in the previous sub-section 4.2.4, the disk is divided into three regions: base region (at normalised radius = 0.2), body region (at normalised radius from 0.3 to 0.8) and tip region (at normalised radius = 0.9). Figure 4.21 shows the porosity and resistance coefficient of a blade body region determined through BEM calculations at different normalised velocities and annular radial locations for the optimised blade.

Based on the porosity and resistance coefficient determined through BEM calculations, shown in Figure 4.21, an empirical formula can be formed to explain the relationship between porosity,  $\theta$ , and resistance coefficient,  $k$ , with normalised velocity,  $u$ , and annular radius,  $R$ , given in Equations (4.14) and 4.15).

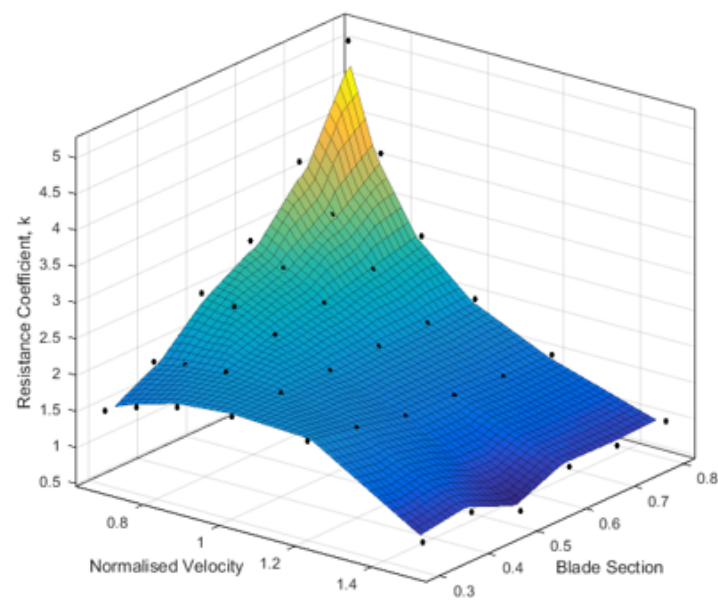
$$\theta_{body} = 0.59 + 0.0545u + 5.8710^3R - 9.7910^3u^2 + 0.0498uR - 7.12 \times 10^3R^2 + 0.0133u^3 - 0.0323u^2R + 4.75 \times 10^4uR^2 - 5.09 \times 10^3R^3 \quad (4.14)$$

$$k_{body} = -6.852 + 9.552u + 30.54R + 3.832u^2 - 50.95uR - 2.135R^2 - 4.847u^3 + 23.08u^2R - 5.556uR^2 + 6.129R^3 \quad (4.15)$$

Figure 4.22 shows the numerical calculations and empirical calculations for the porosity and resistance coefficient of an actuator disk domain's body region at different annular radial locations and normalised velocities for the optimised tidal current turbine blade. The empirical calculation of porosity has a good correlation with the numerical calculations with an R-square value of 0.9766 and a root mean square error (RMSE) value of 0.01638. The empirical calculation of the resistance coefficient has a good correlation with the numerical calculations with an R-square value of 0.9805 and a RMSE value of 0.1432.

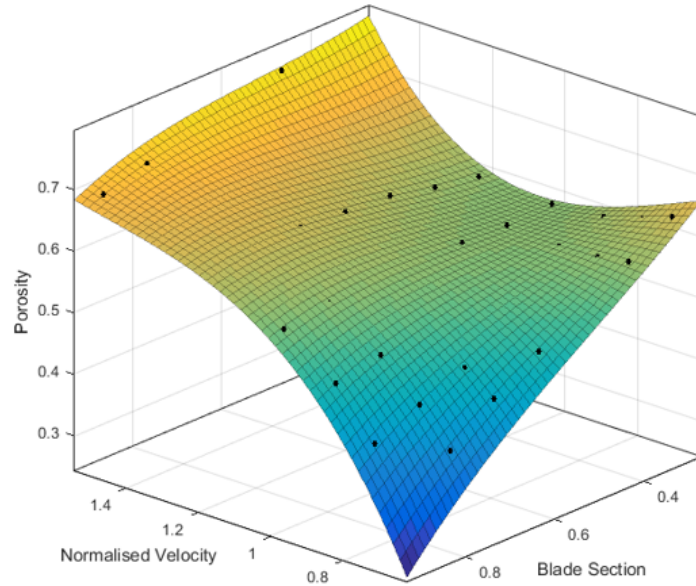


(a)

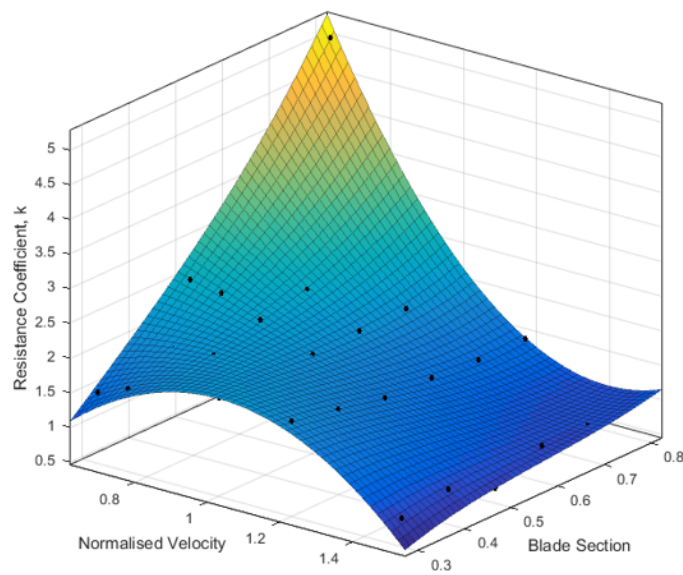


(b)

**Figure 4.21:** Porosity (a) and resistance coefficient (b) of the actuator disk domain at different normalised radial locations and normalised velocities excluding base and tip regions for the optimised tidal current turbine blade.



(a)



(b)

**Figure 4.22:** Numerical (dots) and empirical (contours) calculation of porosity (a) and resistance coefficient (b) of the actuator disk domain's body region at different normalised radial locations and normalised velocities for the optimised tidal current turbine blade.

As mentioned earlier, the base and tip region of the blade are excluded when forming the empirical formula needed to describe the body region. An empirical formula can be formed to explain the relationship between porosity,  $\theta$ , and resistance coefficient,  $k$ , of the actuator disk domain's base region with normalised velocity,  $u$ , given in Equations (4.16) and 4.17).

$$\theta_{base} = 0.5575u^2 - 1.1012u + 1.1253 \quad (4.16)$$

$$k_{base} = -4.1625u^2 + 8.3352u - 2.248 \quad (4.17)$$

Figure 4.23 shows the numerical calculations and empirical calculations of the porosity and resistance coefficient for an actuator disk domain's base region at different normalised velocities for the optimised tidal current turbine blade. The empirical calculations for porosity and resistance coefficient have a good correlation with the numerical calculations with an R-square value of 0.9820 and 0.9886 respectively.

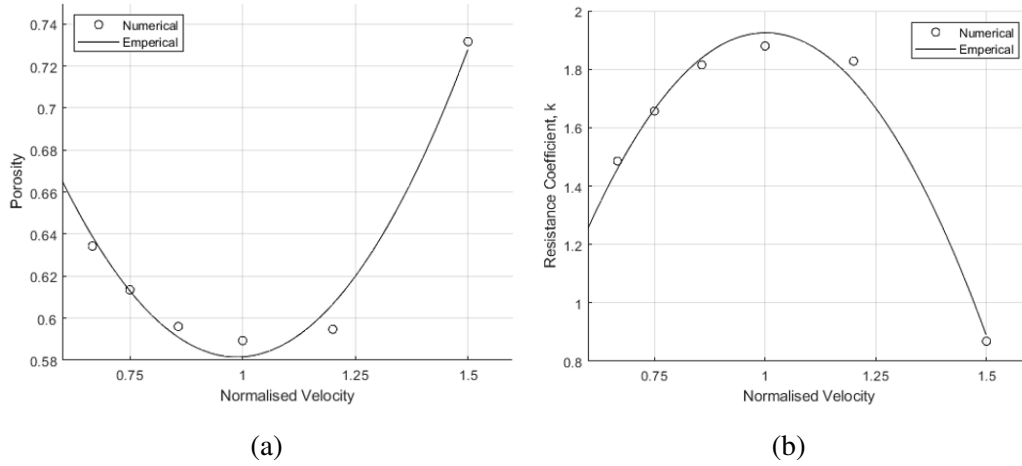
An empirical formula can be formed to explain the relationship between porosity,  $\theta$ , and resistance coefficient,  $k$ , of the actuator disk domain's tip region with normalised velocity,  $u$ , given in Equations (4.18) and 4.19).

$$\theta_{tip} = -0.0896u^2 + 0.5698u \quad (4.18)$$

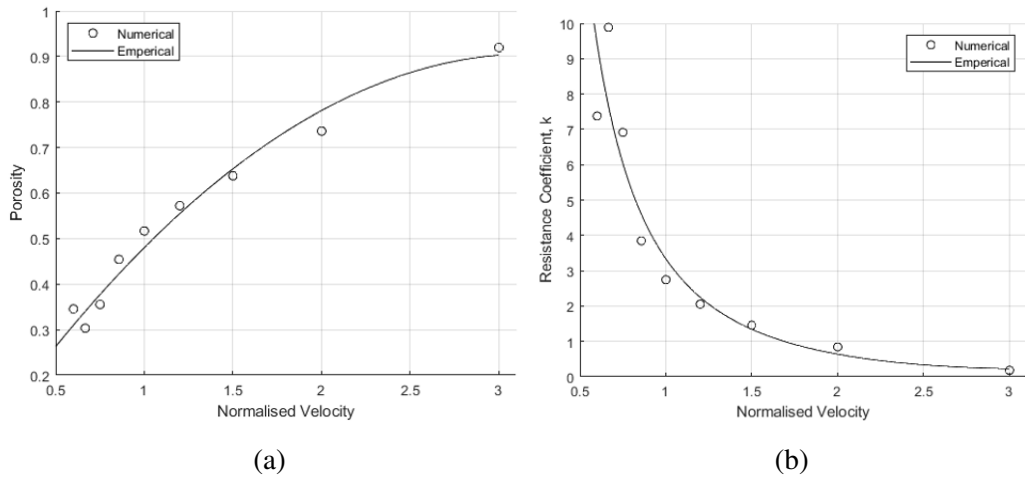
$$k_{tip} = 3.052u^{-2.31} \quad (4.19)$$

Figure 4.24 shows the numerical calculations and empirical calculations of the porosity and resistance coefficient for an actuator disk domain's tip region at different normalised velocities for the optimised tidal current turbine blade. The empirical calculation for porosity and resistance coefficient have a good correlation with the numerical calculations with an R-square value of 0.9757 and 0.9959 respectively.





**Figure 4.23:** Numerical and empirical calculation of porosity (a) and resistance coefficient (b) for the actuator disk domain’s base region at different normalised velocity for the optimised tidal current turbine blade.



**Figure 4.24:** Numerical and empirical calculation of porosity (a) and resistance coefficient (b) for the actuator disk domain’s tip region at different normalised velocities for the optimised tidal current turbine blade.

### 4.3.3 Aligned and Staggered Array Layout: Ideal Channel

A study was carried out to study the effects of different array layouts in an ideal channel. The turbine used in the array utilised the optimised tidal current turbine blade modified hybrid model detailed in sub-section 4.3.2, the turbine has a diameter of 20m. The channel has dimensions of 30D in width, 100D in length and a depth of 2D. The array placement in a rectangular zone, known as turbine deployed area (TDA), where the TDA is placed in the centre of the channel is illustrated in Figure 4.25. The TDA has dimensions of 10D in width, 10D in length and a depth of 2D. The TDA contains 12 turbines placed at mid-depth and arranged in 4 rows with each row containing 3 turbines; the first row's turbine is placed 2D away from the front of the TDA and the thickness of the disk in the array is 0.1D.

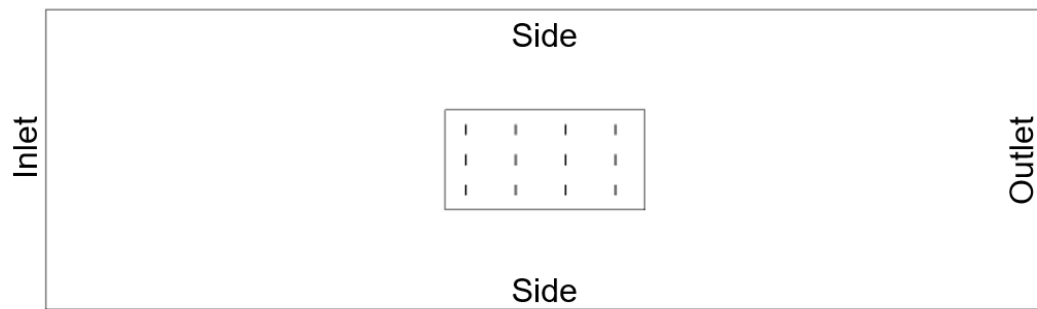


**Figure 4.25:** An ideal channel with tidal current turbine deployed area (TDA) located in the centre of the channel at mid-depth, shown from the top view.

Two different arrays were developed in this thesis, the first was the aligned layout array and the second was the staggered layout array, both containing 12 turbines, as shown in Figure 4.26. In the aligned layout array the lateral distance between each turbine from the centreline has a distance of 3D; the downstream distance between each row of columns has a distance of 5D. The staggered layout array has the same setup as the aligned layout array, with the exception of having the first and third row offset in the lateral distance of  $-0.75D$ , and the second and fourth row offset in the lateral distance by  $0.75D$ .

The solver was run using the  $k - \omega$  SST turbulence model. Table 4.7 shows the summarised parameters of all the boundary faces in the channel fluid. In this idealised channel, the inlet velocity is given as  $2m/s$  uniform flow with 5% turbulence

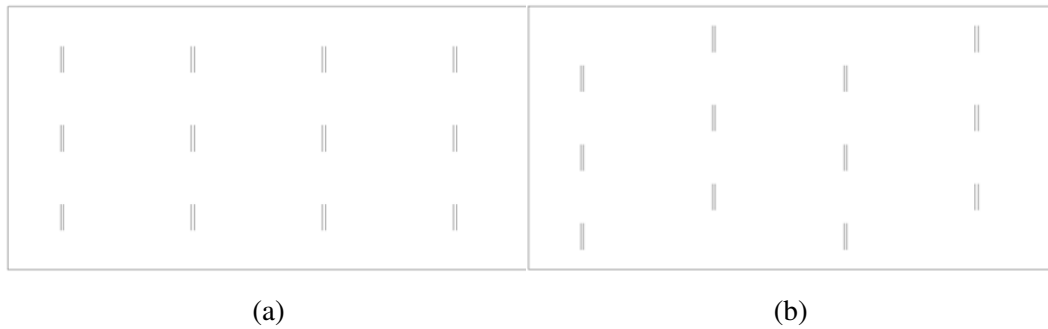


**Figure 4.26:** Aligned layout array (a) and staggered layout array (b) in the TDA at mid-depth, shown from the top view.

intensity, while the outlet boundary was defined as an opening condition with zero relative pressure and zero turbulence gradients. The seabed and surface boundaries were described as a free slip wall, and the side boundary was treated with the symmetry boundary condition.

**Table 4.7:** Summarised parameters of all boundaries in an ideal channel fluid domain.

<b>Boundaries</b>	<b>Parameters</b>
Surface	Free slip wall
Side	Symmetry
Seabed	Free slip wall
Outlet	Opening; entrainment; zero relative pressure and zero turbulence gradient
Inlet	Inlet velocity of $2m/s$ with $5\%$ turbulence intensity

Based on the mesh study conducted and presented in Sub-section 4.2.5, the mesh in the TDA domain which is the region of interest would have a mesh of element size of  $0.03D$  which corresponds to a mesh size of  $2.53 \times 10^7$  elements in the TDA as shown in Figure 27. While the channel fluid domain follows a ratio of 1:12 in terms of element size between the channel fluid domain to TDA domain which corresponds to a mesh size of  $2.72 \times 10^5$  elements. The tidal current turbine domain was set to have an element size of  $0.01D$  which corresponds to a mesh size of  $1.46 \times 10^6$  elements.

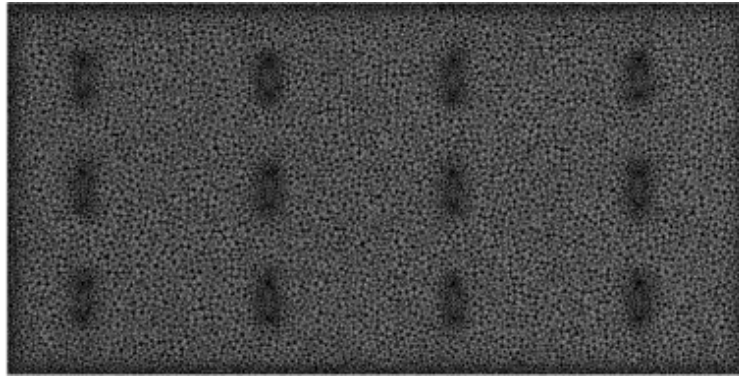


**Figure 4.27:** Mesh of turbine deployed area (TDA) for aligned layout array at mid-depth, shown from the top view.

#### 4.3.4 Aligned and Staggered Array Layout: Ideal Channel

A study was carried out to study the effects of a headland and a headland-island on aligned and staggered array layouts of tidal current turbines in an ideal channel.

##### Headland island

The channel has a dimension of  $60D$  in width,  $120D$  in length and a depth of  $2.5D$  with the headland located at the middle left-side (as seen from the inflow) of the channel and has a dimension of  $10D$  in width,  $15D$  in length and a depth of  $2D$ , as shown in Figure 4.28.

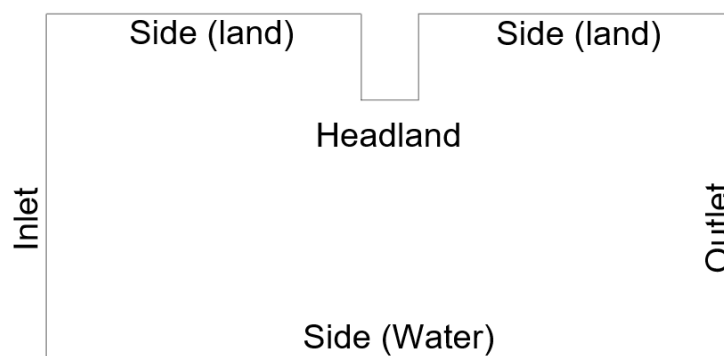


**Figure 4.28:** An ideal channel with headland located in the centre left-side (as seen from the inlet) of the channel at mid-depth, shown from top view.

The solver was run using the  $k - \omega$  SST turbulence model. Table 5.16 shows the summarised parameters of all the boundary faces in the channel with an ideal head-

land. In this idealised channel with headland the inlet velocity is given as  $2\text{ m/s}$  uniform flow with 5% turbulence intensity, while the outlet boundary was defined as an opening condition with zero relative pressure and zero turbulence gradients. The seabed, headland and side (land) boundaries were described as no-slip walls with a specified roughness of 200mm. The surface boundary was described as a free-slip wall, and the side (water) boundary was treated with the symmetry boundary condition.

**Table 4.8:** Summarised parameters of all boundaries in an ideal channel fluid domain containing headland.

Boundaries	Parameters
Surface	Free slip wall
Side	Symmetry
Seabed	Free slip wall
Outlet	Opening; entrainment; zero relative pressure and zero turbulence gradient
Inlet	Inlet velocity of $2\text{ m/s}$ with 5% turbulence intensity

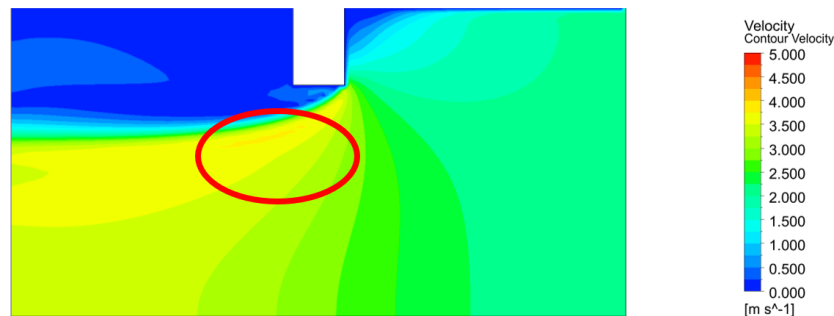


**Figure 4.29:** An ideal channel with headland located in the centre left-side (as seen from the inlet) of the channel at mid-depth, shown from the top view.

A preliminary run was conducted on the idealised channel with headland to observe the velocity flow as shown in Figure 4.29. It is observed that due to the presence of the headland in the channel, the velocity and flow direction were greatly affected. The flow was accelerated after flowing past the headland. Furthermore, this caused the incoming flow direction to change in a clockwise direction, while the flow also experienced an increase in velocity at a distance greater than  $5D$  away from the headland, but for flow within the  $5D$  distance from the headland; a region with sudden decline of velocity was observed. Hence, it is ideal to place the TDA in the

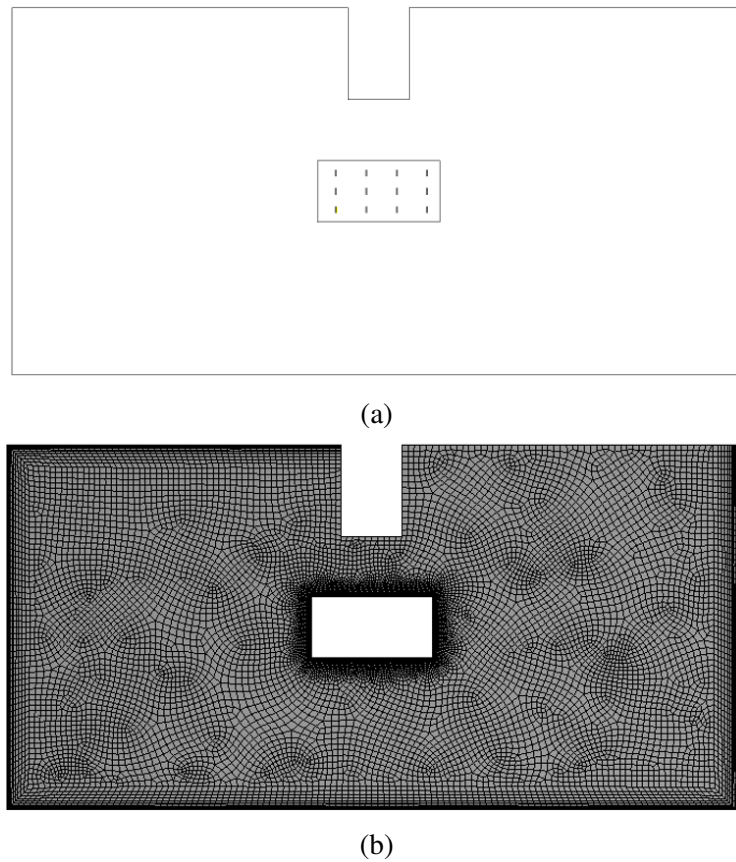


**Figure 4.30:** Geometry (a) and mesh (b) of an ideal headland channel with turbine deployed area (TDA) located in the centre of the channel at mid-depth, shown from the top view.

accelerated flow region represented by the red circle in Figure 4.29. Figure 4.30 shows the TDA placed in the centre of the channel, the setup and dimension of the TDA and the disk domain are the same as the settings detailed in sub-section 4.3.3.

Based on Sub-section 4.2.5 and 4.3.3, the mesh in the TDA domain and the domain containing the 12 turbines has the same number of elements as the mesh, as in Sub-section 4.3.3. While the channel fluid domain follows a ratio of 1:12 in terms of element size between the channel fluid domain to the TDA domain which corresponds to a mesh size of  $5.46 \times 10^5$  elements.

### Headland island

The channel has dimensions of  $120D$  in width,  $150D$  in length and a depth of  $2D$  with the headland located at the left-side outlet (as seen from the inlet) of the channel and an island located at the middle and  $55D$  from the outlet, as shown in Figure 4.31.

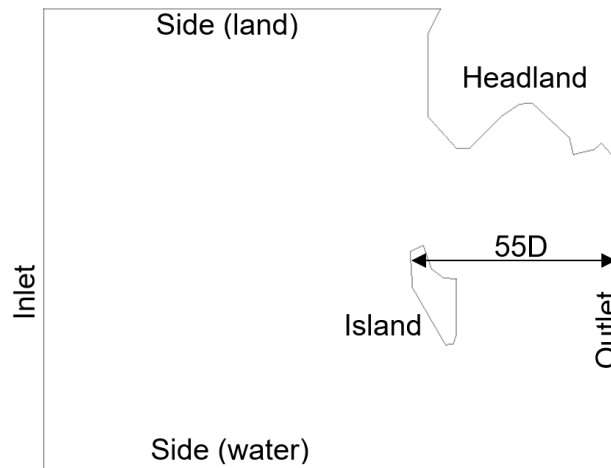


**Figure 4.31:** An ideal channel with headland and island at mid-depth, shown from the top view.

The solver was run using the  $k - \omega$  SST turbulence model. Table 4.9 shows the summarised parameters of all the boundary faces in the channel with headland and island. In this idealised channel with headland and island, the inlet velocity is given a  $2m/s$  uniform flow with 5% turbulence intensity, while the outlet boundary was defined as an opening condition with zero relative pressure and zero turbulence gradients. The seabed, headland, island and side (land) boundaries were described as no-slip walls with a specified roughness of 200mm. The surface boundary was described as a free-slip wall, and the side (water) boundaries were treated as symmetry.

A preliminary run was conducted on the idealised channel with headland and island to observe the velocity flow, as shown in Figure 4.32. It is observed that due to the presence of the headland and island in the channel, the velocity and flow direction were greatly affected. The flow was observed to accelerate greatly between the island and the headland. Hence, it is ideal to place the TDA in the accelerated flow region represented by the red circle in Figure 4.32.

**Table 4.9:** Summarised parameters of all boundaries in an ideal channel fluid domain containing headland and island.

Boundaries	Parameters
Surface	Free slip wall
Seabed	No slip wall, roughness of 200m
Headland	No slip wall, roughness of 200m
Isalnd	No slip wall, roughness of 200m
Side (land)	No slip wall, roughness of 200m
Side (water)	Symmetry
Outlet	Opening; entrainment; zero relative pressure and zero turbulence gradient
Inlet	Inlet velocity of $2m/s$ with 5% turbulence intensity

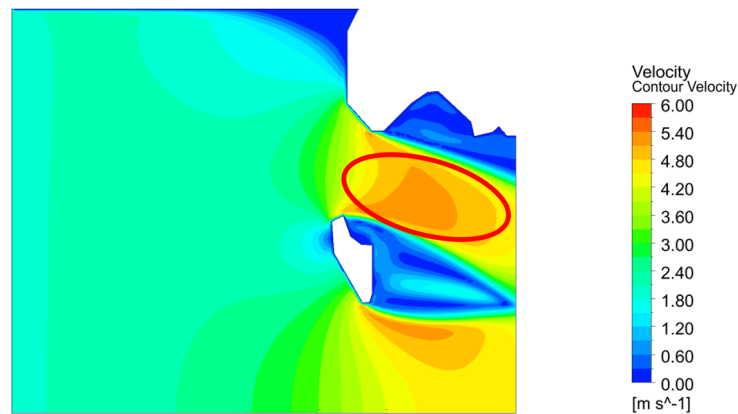
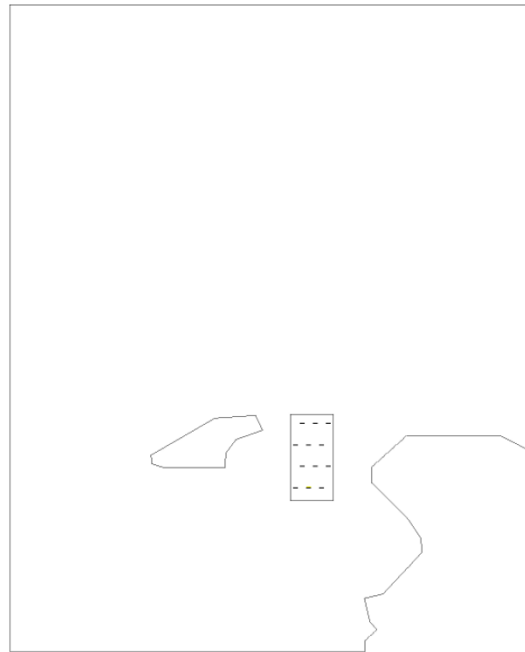


**Figure 4.32:** Velocity contour of an ideal channel with headland and island at mid-depth, shown from the top view.

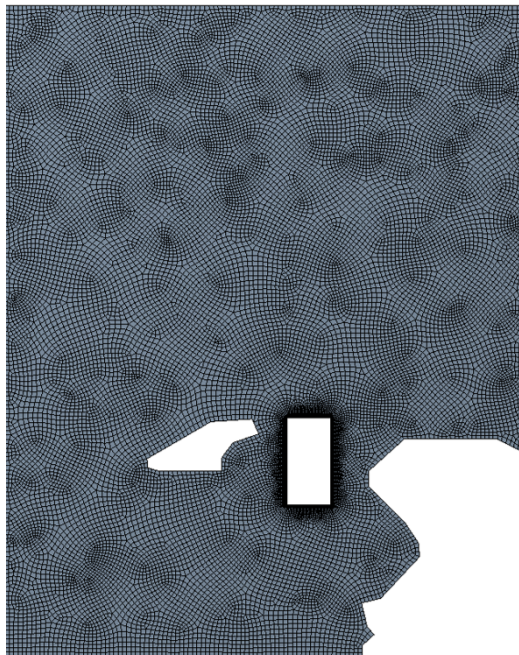
Figure 33 shows the TDA placed in between the headland and the island in the channel, the setup and dimensions of the TDA and the disk domain are the same as the settings provided in sub-section 4.3.3.

Based on Sub-section 4.2.5 and 4.3.3, the mesh in the TDA domain and the 12 turbines domain have the same number of elements and mesh setting as in Sub-section 4.3.3. While the channel fluid domain follows a ratio of 1:12 in terms of element size between the channel fluid domain to the TDA domain which corresponds to a mesh size of  $8.89 \times 10^5$  elements.





(a)



(b)

**Figure 4.33:** Geometry (a) and mesh (b) of the TDA located in between the headland and the island in the channel at mid-depth, shown from top view.

### 4.3.5 Shannon Estuary

A study was carried out to investigate the aligned and staggered array setups in the Shannon Estuary. Figure 4.34 shows the geometry of the Shannon estuary at mid-depth, shown from the top view, the estuary has a length of approximately 60km and the depth was based on the bathymetry of the Shannon estuary as shown in Figure 4.35.

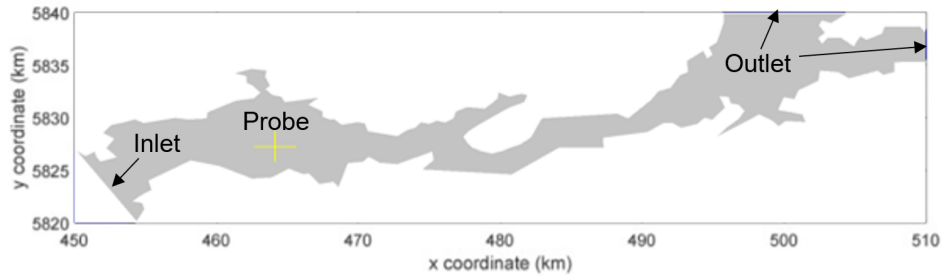


**Figure 4.34:** The Shannon Estuary at mid-depth, shown from the top view.

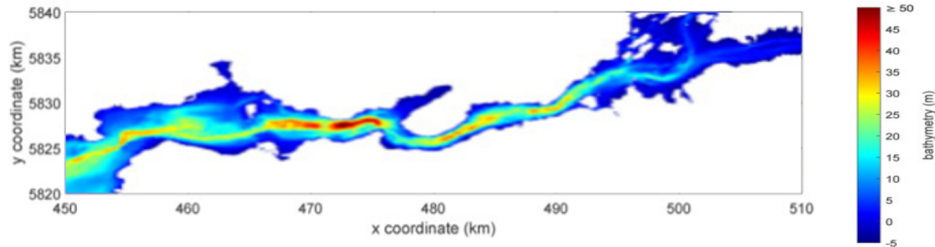


**Figure 4.35:** The bathymetry of Shannon Estuary at mid-depth, shown from the top view.

The solver was run using the  $k - \omega$  SST turbulence model. Table 4.10 shows the summarised parameters of all the boundary faces in the Shanon Estuary. The outlet boundary was defined as an opening condition with zero relative pressure and zero turbulence gradients. The seabed and side (land) boundaries were described as no-slip walls with a specified roughness of 50mm. While, the surface boundary was described as a free-slip wall. The inlet boundary was described by velocity  $U_{inlet}(z)$  profiles as expressed in Equation 4.20 and a turbulence intensity of 5%,

$$U_{inlet}(z) = U_{mid} \left( \frac{Z}{Z_{mid}} \right)^\alpha \quad (4.20)$$

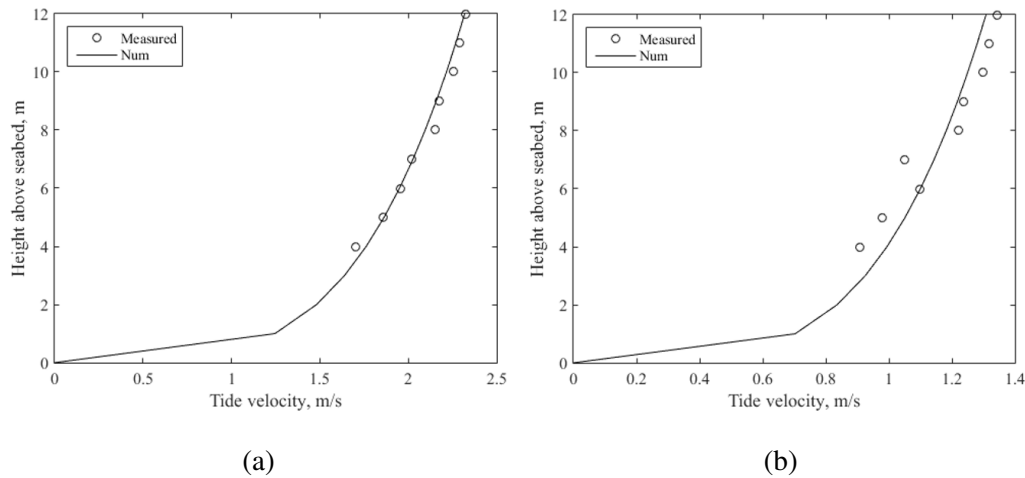


**Figure 4.36:** The velocity profile comparison of numerical and measured values (O'Rourke et al. 2014) at the probe in Shannon Estuary during spring tide (a) and neap tide (b).

$U_{mid}$  is the velocity at mid-depth,  $Z$  is depth,  $Z_{mid}$  is the mid-depth and  $\alpha = \frac{1}{4}$  based on studied by O'Rourke (O'Rourke et al. 2014).

**Table 4.10:** Summarised parameters of all boundaries in an ideal channel fluid domain containing headland and island.

Boundaries	Parameters
Surface	Free slip wall
Seabed	No slip wall, roughness of 50m
Side (land)	No slip wall, roughness of 50m
Outlet	Opening; entrainment; zero relative pressure and zero turbulence gradient
Inlet	Inlet velocity profile of $\alpha = 1/4$ with 5% turbulence intensity

Figure 4.36, shows a comparison of numerical velocity profile with measurement velocity profile in the Shannon Estuary at the probe location shown in Figure 4.34 during peak spring tide and neap tide. It was observed that the numerical velocity conditions match closely to the measured conditions.

Based on Sub-section 4.2.5 and 4.3.3, the Shannon Estuary's fluid domain follows a ratio of 1:12 in terms of elements size between the fluid domain to TDA domain which corresponds to a mesh size of  $8.79 \times 10^6$  elements as shown in Figure 37. The mesh in the TDA domain and the 12 turbines domain has the same number of

elements and mesh setting as detailed in Sub-section 4.3.3.

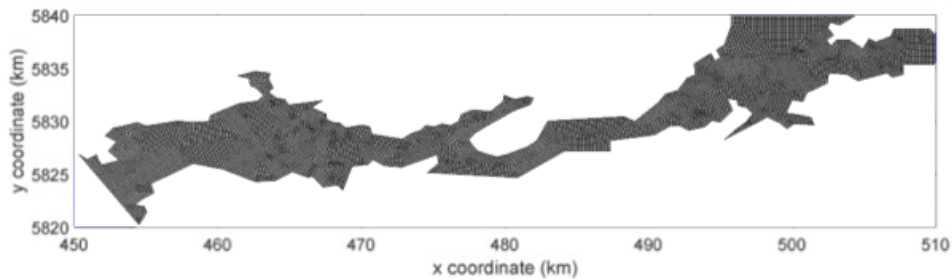


**Figure 4.37:** Mesh of the Shannon Estuary at mid-depth, shown from top view.

A preliminary run was conducted on the Shannon Estuary to observe the fluid flow field as shown in Figure 4.38. It is observed that due to the presence of the headland at around 480 km in the estuary and the narrowing of the estuary channel causes the fluid flow to accelerate during both flooding and ebbing. Hence, it is ideal to place the TDA in the accelerated flow region at around 480 km.

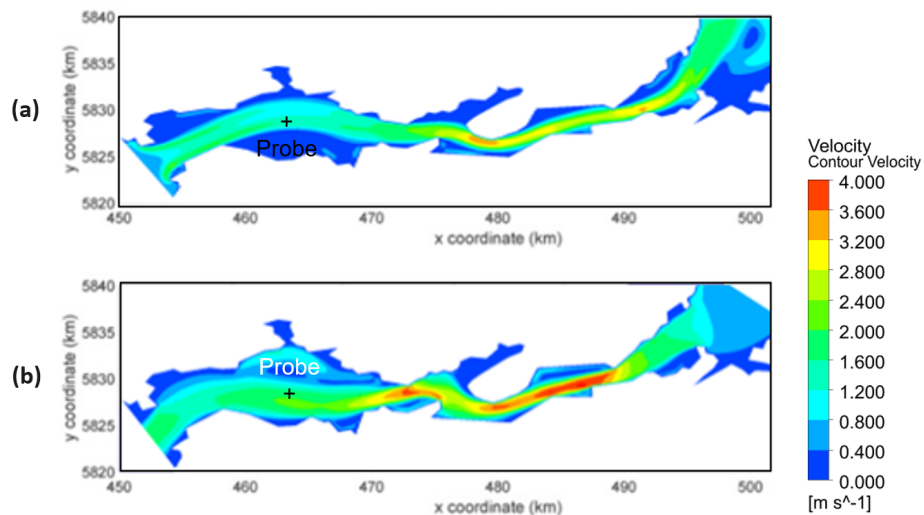


**Figure 4.38:** Velocity contour during flooding (a) and ebbing (b) in the Shannon Estuary at mid-depth, shown from top view during spring tide.

### 4.3.6 Shannon Estuary pseudo-transient simulation

Due to the nature of the RANS equation, the RANS model in CFD was unable to simulate a transient problem. One possible way to resolve this problem was through the use of a parameter function in ANSYS-CFX. This approach utilises the parametric configuration in ANSYS CFX to achieve a pseudo-transient state by treating the rate of change of tidal conditions as instantaneous individual parametric input and the resulting energy yield of the array as a series of instantaneous parametric outputs.

The annual tidal conditions of Shannon Estuary were separated into individual averaged 10-min interval inputs to be used in the RANS model for a single run. So, each individual averaged 10-min interval inputs will correspond to one RANS model run in CFD. The tidal conditions inputs were tidal velocity with respect to time and tidal height with respect to height. The inflow tidal velocity and tidal height parameters of Shannon Estuary were detailed in Nash's work from the University of Galway, refer to (Nash & Phoenix 2017) for more details. The parametric output is the energy yield of the turbines in the array and it is calculated by multiplying time (10min) with power extracted by the disk using Equations 3.21. As a result, in a single run of the RANS model in CFD, the individual 10-minutes interval inputs will correspond to an energy yield output. Thus, running a batch of averaged 10-min interval inputs in the RANS model in CFD will produce a pseudo-transient state output result. This method is named the RANS pseudo-transient method.

A study was conducted to validate the simulated fluid flow conditions of the Shannon Estuary against measurement data (O'Rourke et al. 2014) using the RANS pseudo-transient method at the probe location, shown in Figure 4.38. The parametric output for this study we set as mid-depth velocity at the probe location. Figure 4.39 shows a comparison of mid-depth velocity between the numerical results and measured data at the probe location during spring tide and neap tide over a day. It shows that the numerical results from the simulation match well with measured data at the probe location in Shannon Estuary. The numerical results during spring tide correlate more closely with measured data compared to the numerical results during neap tide, as shown in Figure 4.39.

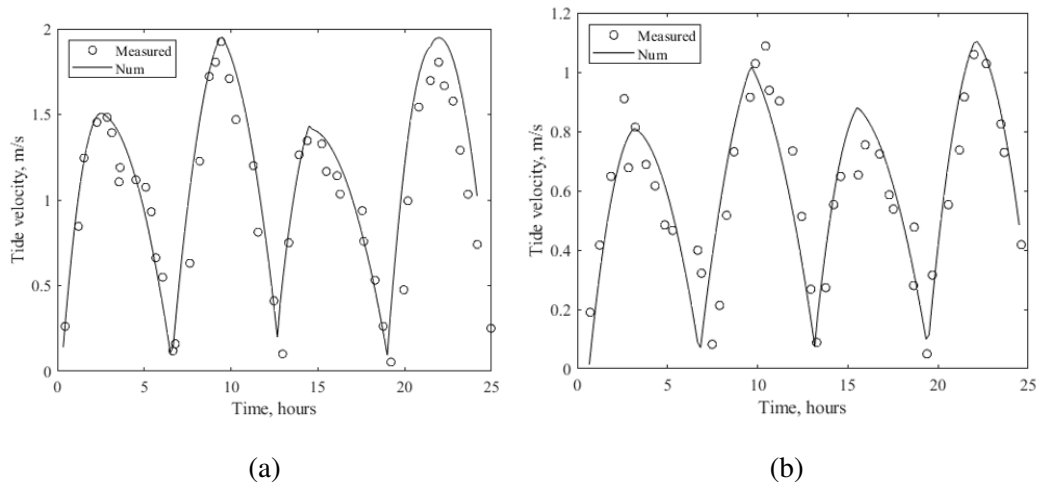


**Figure 4.39:** Tide velocity at mid-depth in the Shannon Estuary in a day during spring tide (a) and neap tide (b).

Table 4.11 shows the comparative analysis of numerical tide velocity during spring tide and neap tide with measured velocity in a day. During the spring tide, the numerical model has a high correlation with an R-square value of 0.948 but only a good root mean square error (RMSE) of 0.123. While, during the neap tide the numerical model has a low correlation with an R-square value of 0.888 and a low RMSE of 0.095. Overall, both the numerical results at spring tide and neap tide are taken to be highly correlated with measurements due to an R-square value greater than 0.85 and also have low error as the RMSE have a value less than 0.15. Figure 4.40, shows the numerical tidal flow velocity generated through the simulation in a lunar month (28 days) in the Shannon Estuary at the probe location. The lunar cycle is observed, there are two spring tides and two neap tides occurring over a lunar month in the Shannon Estuary.

**Table 4.11:** Statistical analysis of the numerical velocity against experimental measurements during spring tide and neap tide (O'Rourke et al. 2014)

Tide	Tide velocity			
	R-square	RMSE	MAE	MAPE
Spring	0.948	0.123	0.076	14%
Neap	0.888	0.095	0.076	17%

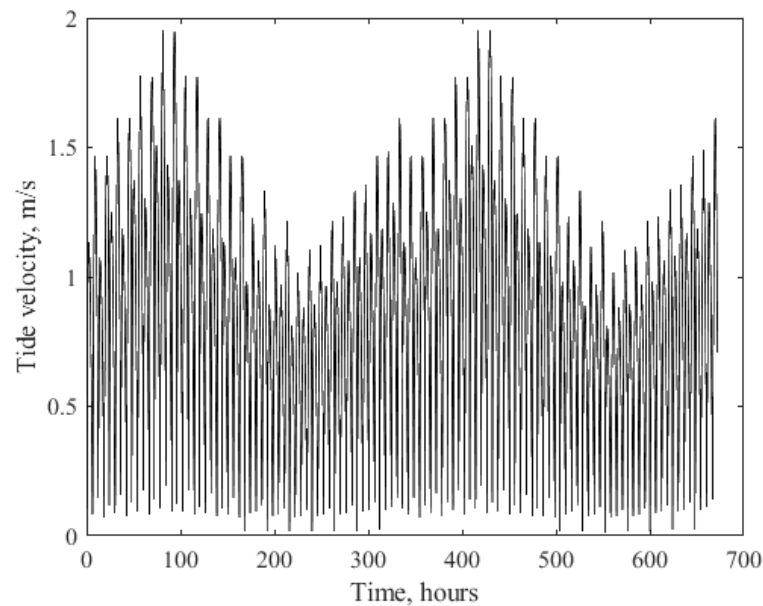


**Figure 4.40:** Tidal flow velocity at mid-depth in the Shannon estuary over a lunar month (28 days).

### 4.3.7 Summary

BEM calculations of the optimised blade developed by Yeo et al. 2022 (Yeo et al. 2022) were presented, details of the blade's geometry parameters were shown in Table 4.6, the calculated thrust and power coefficient though BEM was validated against Yeo et al. model. A set of empirical formulas was generated to describe the porous disk the porosity and resistance coefficient of the porous domain in CFD based on the optimised blade as seen in Equations 4.14 to 4.19. A 20m diameter turbine was used in developing the turbine array model of an aligned and staggered layout consisting of 12 turbines. The fluid domain's geometry and mesh for an ideal channel, headland and headland & island was detailed, the meshing of the fluid domain follows the same configuration identified in the mesh study done in the previous sub-chapter 4.2.5. This sub-chapter also presents the setup of the Shannon Estuary's fluid domain, the inlet velocity was described using Equation 4.20 with  $\alpha = \frac{1}{4}$ . A study was conducted to validate the simulated time-varying fluid flow conditions of the Shannon Estuary against measurement data (O'Rourke et al. 2014) using the RANS pseudo-transient method. The simulated fluid flow fluid was shown to correlate well with measurement data.

# Chapter 5

## Results and discussion

### 5.1 Introduction

This chapter presents the results and discussion of the work in the thesis. The chapter consists of three main sub-chapters which are the single turbine model, the multiple turbine model and the array model. The first sub-chapter presents a study on the AD study model, modified BEM-AD model's variations and hybrid, and mesh study. The second sub-chapter presents the multiple turbine studies which focus on investigating the effects of spacing, layout, turbine size and depth deployment on the turbine-to-turbine wake interactions. The last sub-chapter presents an evaluation of the performance of an aligned and staggered layout array for a range of different domain conditions such as: ideal channel, headland and headland & island. A case study on the energetic performance of deploying the developed aligned and staggered layout array is detailed.

### 5.2 Single Turbine model

This section focuses on the validation of the developed model against experimental measurements and also compares the wake predictions of various variations and modifications. The first and second sub-sections focus on investigating the AD model through comparison studies between the 2-dimensional and 3-dimensional AD model, and also comparison studies of the AD model between ANSYS-CFX and ANSYS-Fluent. The following sub-sections presented the results of the velocity variation, radial variation and modified hybrid BEM-AD model and were validated



against experimental measurements (Batten et al. 2013). The final sub-sections present an overall summary of the single turbine model sub-chapter.

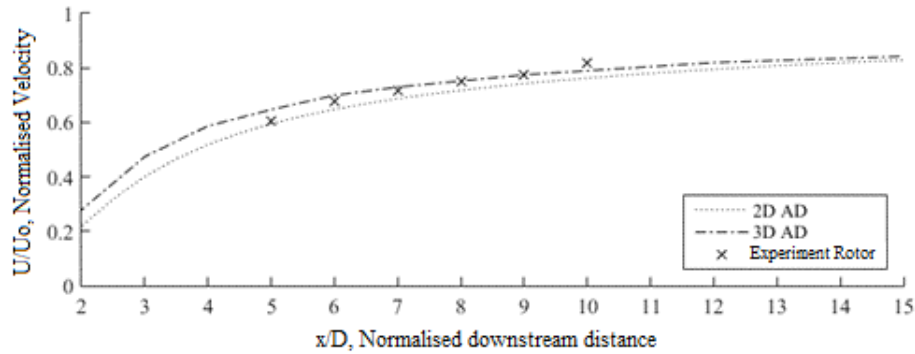
### 5.2.1 AD model study: 2-dimensional vs 3-dimensional model

An investigation was carried out to determine the difference between 2-dimensional and 3-dimensional domains when deploying actuator disk models in CFD. The results were compared against experimentally measured data (Batten et al. 2013). The two models compared are both standard actuator disk models with a thrust coefficient,  $C_T = 0.88$  and resistance coefficient,  $K = 2$ . The simulation was solved using the RANS  $k - \omega$  SST in ANSYS-CFX. Figure 5.1 shows a comparison of centreline downstream velocities and turbulence intensities for the 2-dimensional AD model, the 3-dimensional AD model and the experimental measurements (Batten et al. 2013).

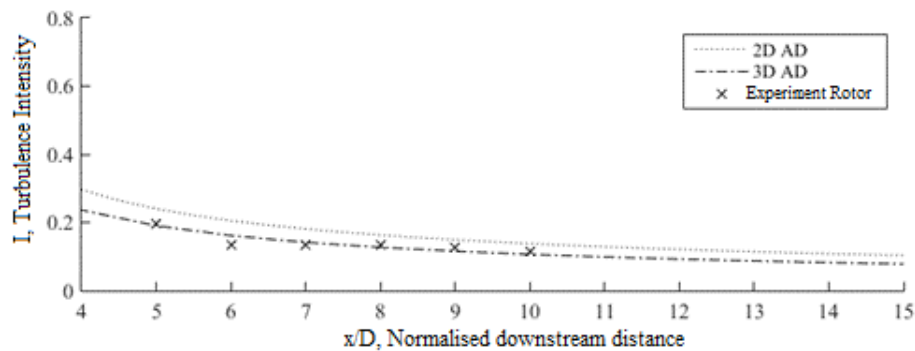
Both models predict similar downstream velocity and turbulence intensity trends. However, the 2-dimensional AD model slightly under predicts velocity and turbulence intensity downstream when compared to the experimental measurements. While the 3-dimensional AD model slightly over predicts velocity and turbulence intensity downstream when compared to the experimental measurements (Batten et al. 2013) in near wake region (before 5D). Figure 5.2 shows the vertical velocity and turbulence intensity at downstream distances of 5D, 8D and 10D.

It is noticeable at a 5D, both models do not fully capture the wake flow effects, with the 3-dimensional AD model over predicting the wake recovery and the 2-dimensional AD model under predicting the wake recovery. However, at a downstream distance of 8D and 10D, the 3-dimensional AD model predicts the wake more accurately than the 2-dimensional AD model. Table 5.1 shows a statistics analysis of the 2-dimensional and 3-dimensional AD models against experimental measurements in terms of coefficient of determination, R-square, root mean square error (RMSE), mean absolute error (MAE) and mean absolute percentage error (MAPE).

Table 5.1, shows that when comparing the two models with experimental measurements, the 2-dimensional AD model has a high degree of error and correlates less



(a)

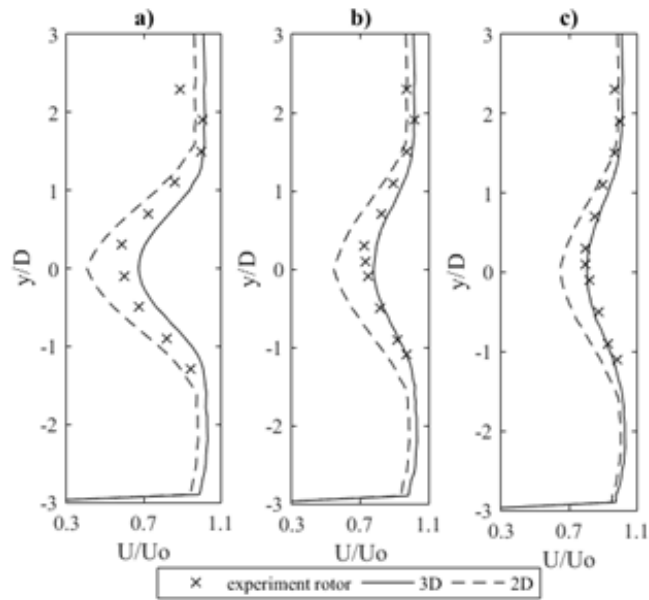


(b)

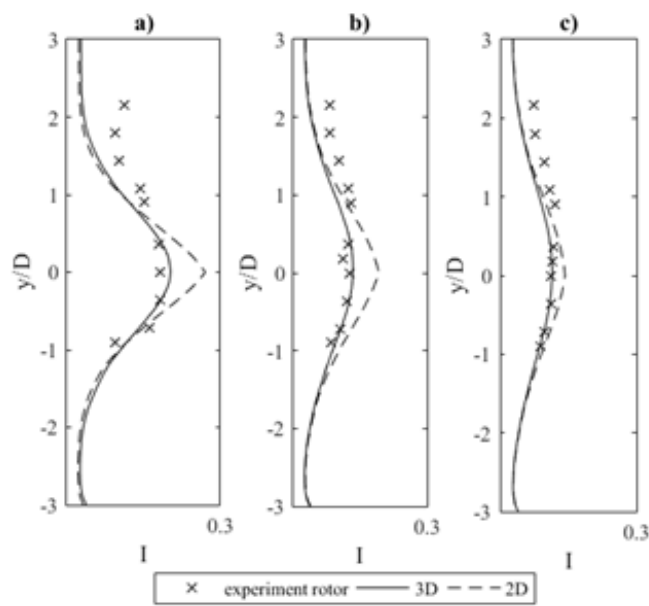
**Figure 5.1:** Comparison of downstream centreline normalised velocity (a) and turbulence intensity (b) of the 2-dimensional AD model and the 3-dimensional AD model with experimental measurements (Batten et al. 2013).

**Table 5.1:** Statistical analysis of 2-dimensional and 3-dimensional AD models against experimental measurements (Batten et al. 2013) for centreline downstream velocity and turbulence intensity.

AD model	Velocity				Turbulence Intensity			
	$R^2$	RMSE	MAE	MAPE	$R^2$	RMSE	MAE	MAPE
2-D	0.9865	0.0309	0.0293	4.01%	0.7962	0.0419	0.0376	26.5%
3-D	0.9891	0.0201	0.0164	2.42%	0.8026	0.0133	0.0111	8.2%



(a) vertical normalised velocity



(b) vertical turbulence intensity

**Figure 5.2:** Comparison of vertical normalised velocity and vertical turbulence intensity of 2-dimensional and 3-dimensional AD models with experimental measurements (Batten et al. 2013) at downstream distances of 5D(a), 8D(b) and 10D(c).

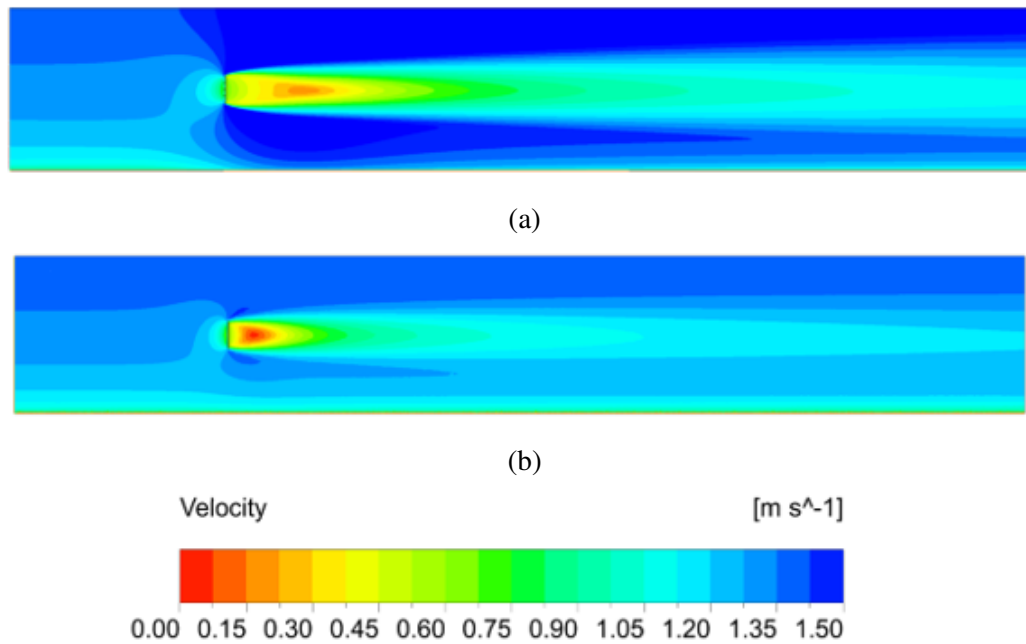


**Figure 5.3:** Velocity contour of the 2-dimensional AD model (a) and the 3-dimensional AD model (b).

with the experimental measurements when compared with the 3-dimensional AD model. Figure 5.3 and 5.4 show contour velocity and turbulence intensity plots for the 2-dimensional and 3-dimensional AD models respectively. The contour shape of both velocity and turbulence intensity for the 2-dimensional AD model is longer than that of the 3-dimensional AD model, the intensity of the contour is greater also. This shows that for the 2-dimensional AD model the wake takes longer to recover downstream of the turbine rotor. One significant reason behind a slow wake recovery rate for the 2-dimensional AD model is the turbulence being unable to dissipate downstream. This is due to the 2-dimensional domain having only a thin (one element thick) domain which results in less fluid surrounding the actuator disk. Ergo, this study has shown that the 3-dimensional AD model has better accuracy than the 2-dimensional AD model in capturing the downstream tidal current turbine wake effects. Also, it is paramount to have sufficient ambient fluid surrounding the downstream actuator disk streamtube to enable the wake to recover fully.

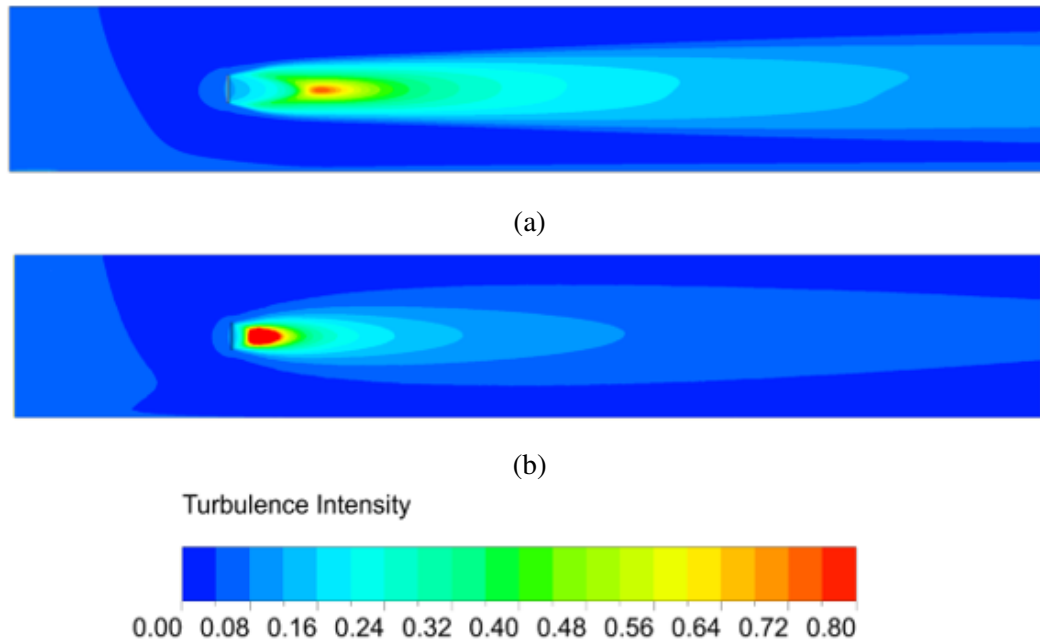


**Figure 5.4:** Turbulence intensity contour of the 2-dimensional AD model (a) and the 3-dimensional AD model (b).

### 5.2.2 AD model study: ANSYS-CFX vs ANSYS-Fluent

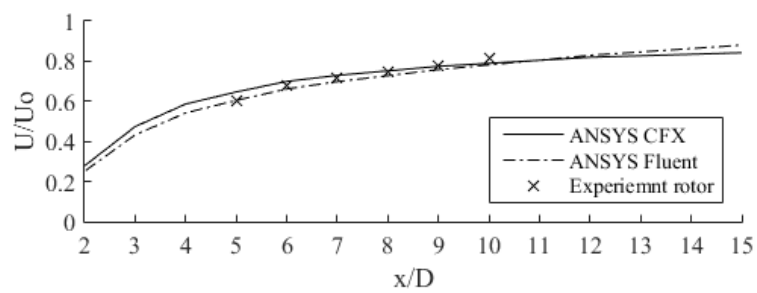
The section provides a detailed comparison between ANSYS-CFX and ANSYS-Fluent when deploying and simulating an actuator disk model in CFD. Both simulated models are standard actuator disk models with a thrust coefficient,  $C_T = 0.88$  and resistance coefficient,  $K = 2$ . The simulation was solved using the RANS  $k - \omega$  SST turbulence model. Figure 5.5 shows a comparison of centreline downstream velocities and turbulence intensities for ANSYS-CFX, ANSYS-Fluent and experimental measurements (Batten et al. 2013). According to Figure 5.5, the ANSYS-CFX and ANSYS-Fluent predictions have very similar velocity and turbulence intensity profiles compared to experimental measurements. The ANSYS-CFX AD model tends to slightly overpredict velocity up to a downstream distance of  $10D$  and turbulence intensity up to a downstream distance of  $8D$ . The ANSYS-Fluent AD model tends to slightly underpredict velocity and turbulence intensity when compared to experimental measurements. Figure 6 shows the predicted vertical velocity and turbulence intensity for the ANSYS-CFX AD model and the ANSYS-Fluent AD model at downstream distances of  $5D$ ,  $8D$  and  $10D$ .

**Table 5.2:** Statistical analysis of ANSYS-CFX and ANSYS-Fluent AD models against experimental measurements (Batten et al. 2013) for centreline downstream velocity and turbulence intensity.

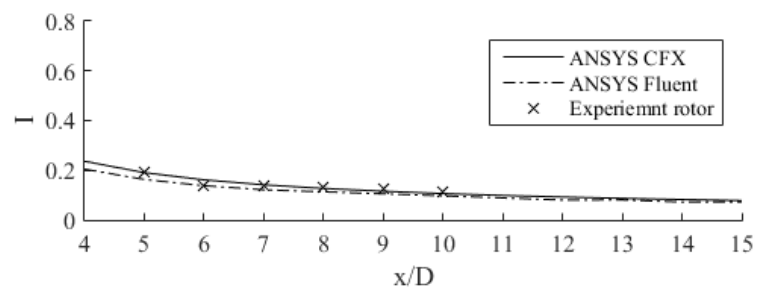
AD model	Velocity				Turbulence Intensity			
	$R^2$	RMSE	MAE	MAPE	$R^2$	RMSE	MAE	MAPE
CFX	0.9891	0.0201	0.0164	2.42%	0.8026	0.0133	0.0111	8.2%
Fluent	0.9932	0.0201	0.0191	2.63%	0.7954	0.0215	0.0190	13.6%

As observed in Figure 5.7, there is little difference in both ANSYS-CFX and ANSYS-Fluent in terms of downstream velocity and turbulence intensity beyond a downstream distance of 8D. Both ANSYS-CFX and ANSYS-Fluent overpredict in terms of downstream velocity with ANSYS-CFX overpredicting to a greater extent than ANSYS-Fluent. It is also observed that ANSYS-Fluent performed better at predicting velocity profile at downstream distance 5D when compared to ANSYS-CFX. Furthermore, it was noticed that ANSYS-Fluent is more sensitive to drag influence from the top and bottom surfaces. While in terms of downstream turbulence intensity, both ANSYS-CFX and ANSYS-Fluent underpredict above the depth  $y/D = 0.5$  at all downstream distances. Between the depth  $y/D = 0.5$  to  $-1.0$ , ANSYS-CFX overpredicts the downstream turbulence intensity profile, while ANSYS-Fluent underpredicts the downstream turbulence intensity profile. The ANSYS-CFX AD model seems to match the experimental measurement better than the ANSYS-Fluent AD model at a downstream distance of 5D. Table 5.2 provides details of a statistics analysis conducted to compare the ANSYS-CFX AD model and ANSYS-Fluent AD model against the experimental measurements.

Table 5.2 shows that both ANSYS-CFX and ANSYS-Fluent models have little difference when comparing in terms of velocity. When comparing turbulence intensity, ANSYS-CFX tends to perform better than ANSYS-Fluent.

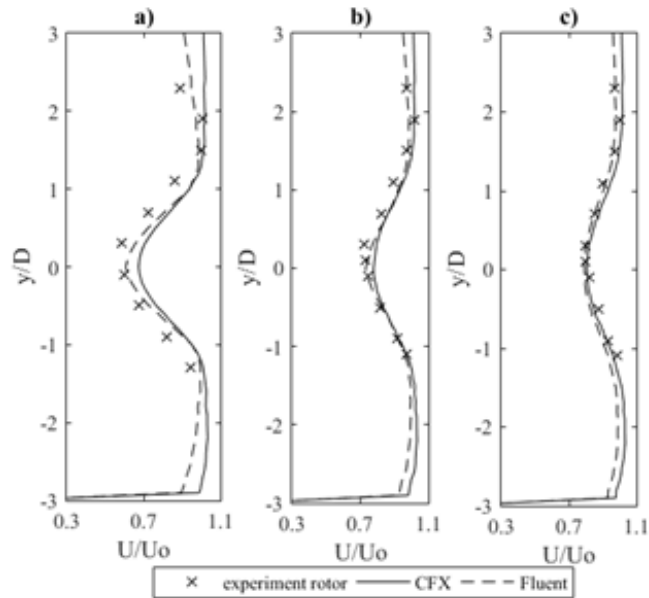


(a)

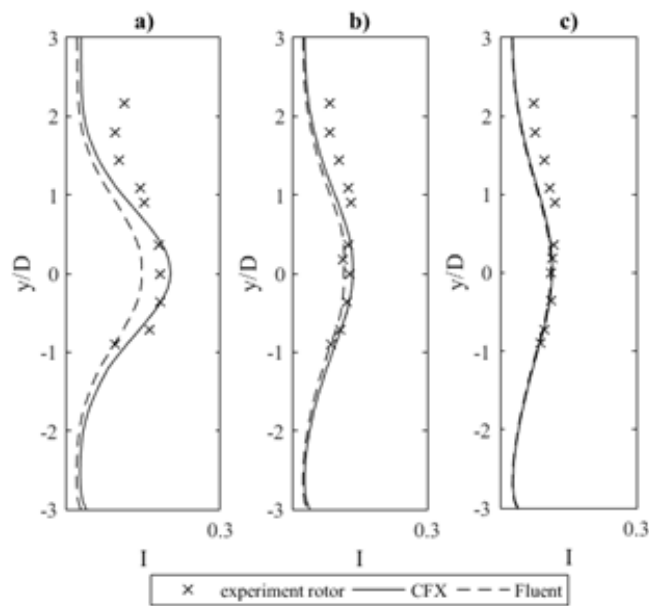


(b)

**Figure 5.5:** Comparison of predicted downstream centreline velocity (a) and turbulence intensity (b) for the ANSYS-CFX AD model and the ANSYS-Fluent AD model and compared with experimental measurements (Batten et al. 2013).



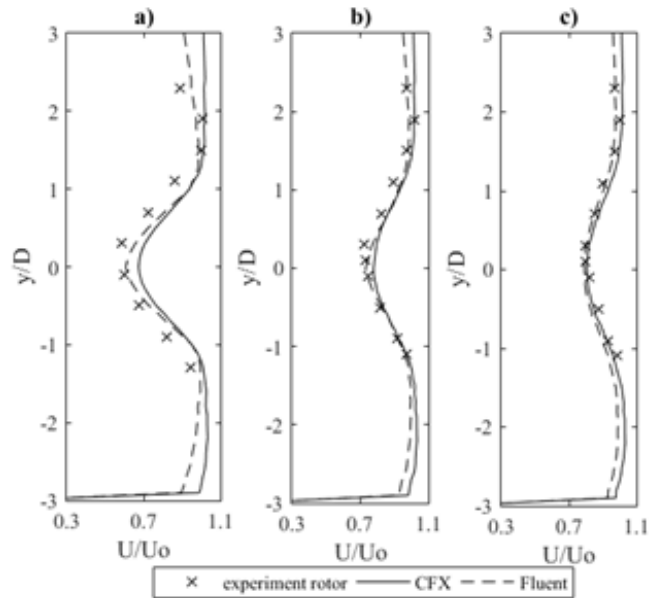
(a) vertical normalised velocity



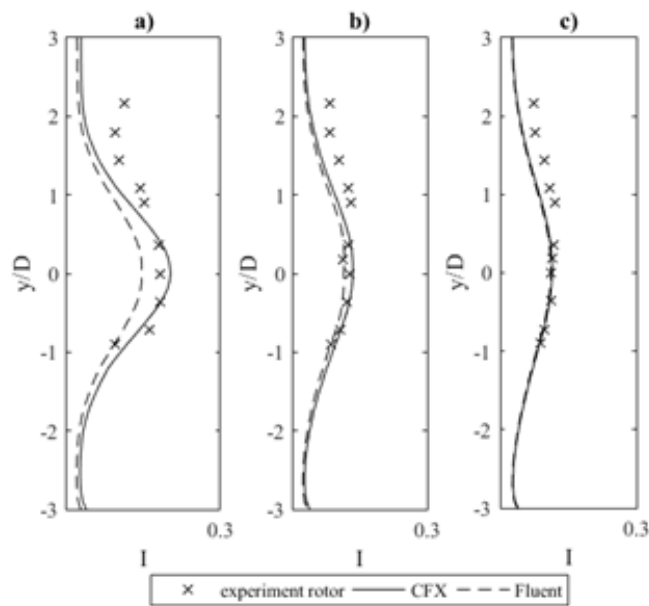
(b) vertical turbulence intensity

**Figure 5.6:** Comparison of vertical normalised velocity and vertical turbulence intensity of ANSYS-CFX and ANSYS-Fluent AD models with experimental measurements (Batten et al. 2013) at downstream distances of 5D(a), 8D(b) and 10D(c).





(a) vertical normalised velocity



(b) vertical turbulence intensity

**Figure 5.7:** Comparison of vertical normalised velocity and vertical turbulence intensity of ANSYS-CFX and ANSYS-Fluent AD models with experimental measurements (Batten et al. 2013) at downstream distances of 5D(a), 8D(b) and 10D(c).

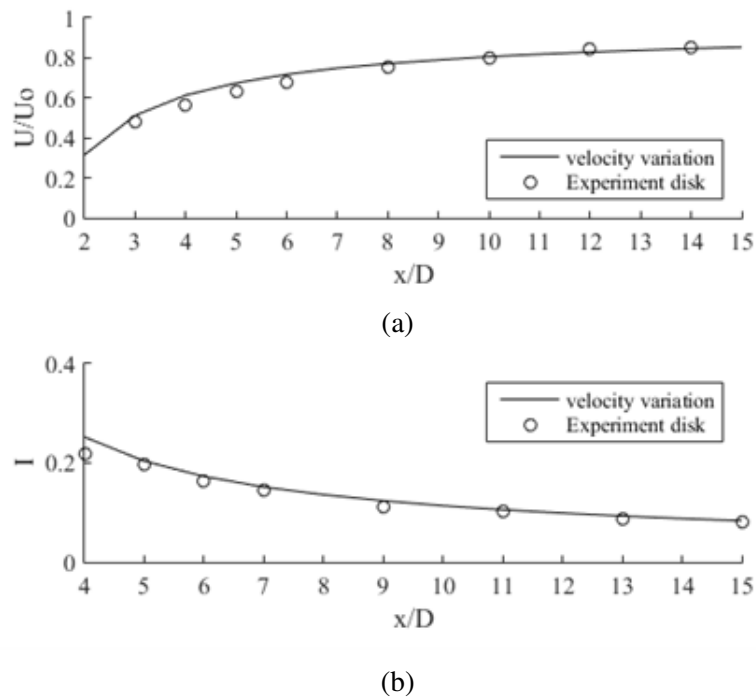


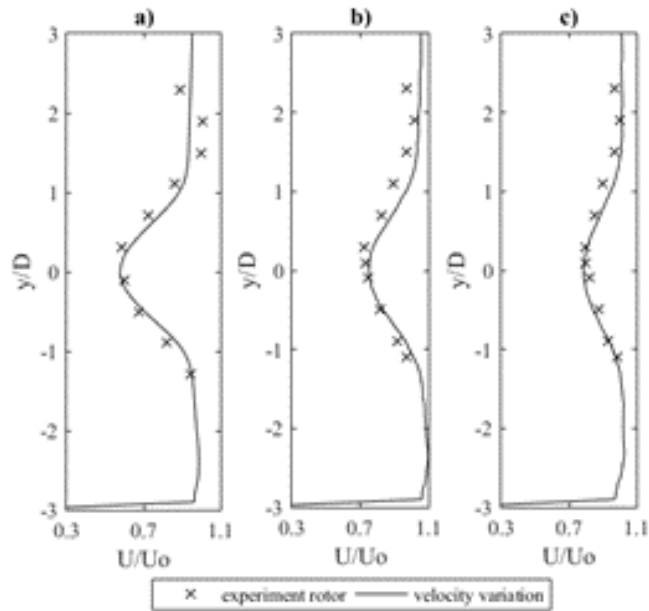
**Figure 5.8:** Comparison of downstream centreline velocity (a) and turbulence intensity (b) of the velocity variation bem-AD model against experimental measurements (Batten et al. 2013).

### 5.2.3 Modified BEM-AD model: Velocity Variation

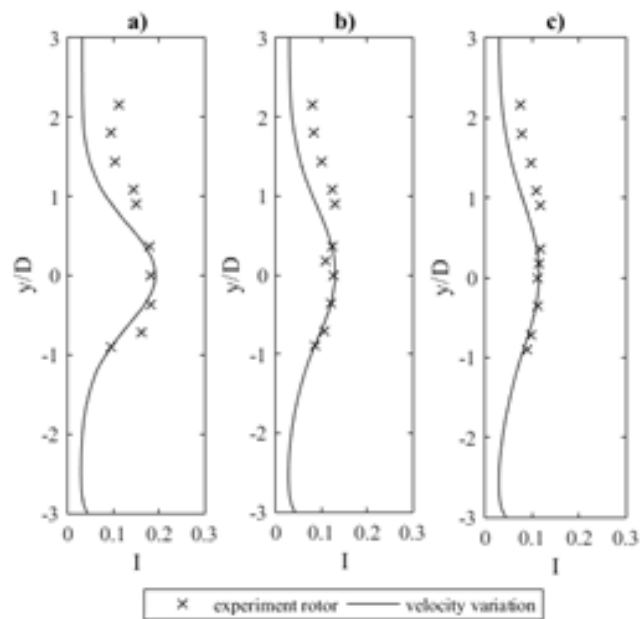
In this sub-section, the developed velocity variation BEM-AD model is validated against experimental measurements (Batten et al. 2013). The actuator disk's porosity and resistance coefficient take into account the velocity profile of the water column, details of this configuration are given in Chapter 4.2.3. Figure 5.8 shows the centreline downstream velocity and turbulence intensity of the velocity variation BEM-AD model against experimental measurements. The developed model matches well with the experimental measurements especially after a distance greater than  $8D$ . The model tends to over-predict in both velocity and turbulence intensity at downstream distances of less than  $7D$ .

Figure 5.9 shows the downstream velocity and turbulence intensity profile at downstream distances of  $5D$ ,  $8D$  and  $10D$ . The velocity profile at  $10D$  matches closely with the experimental measurements (Batten et al. 2013), but for the velocity profile over-predictions occur at  $5D$  and  $8D$ . Whereas, the turbulence intensity is under-

predicted at 5D, 8D and 10D. The results show that the velocity variation model can predict downstream velocity accurately at distances greater than 8D. However, it is observed that for vertical normalised depth above the centreline, the model is less accurate compared to below the centreline. The vertical normalised depth below the centreline has a more severe change in vertical velocity profile compared to the vertical normalised depth above the centreline due to the shear effect. This results in the actuator disk having a bigger variation in porosity and resistance coefficient below the actuator disk centreline compared to above the centreline which causes the model to describe the downstream wake below the centreline better than above the centreline.



(a) vertical normalised velocity



(b) vertical turbulence intensity

**Figure 5.9:** Comparison of vertical normalised velocity and vertical turbulence intensity of the velocity variation BEM-AD model with experimental measurements (Batten et al. 2013) at downstream distances of 5D, 8D and 10D.

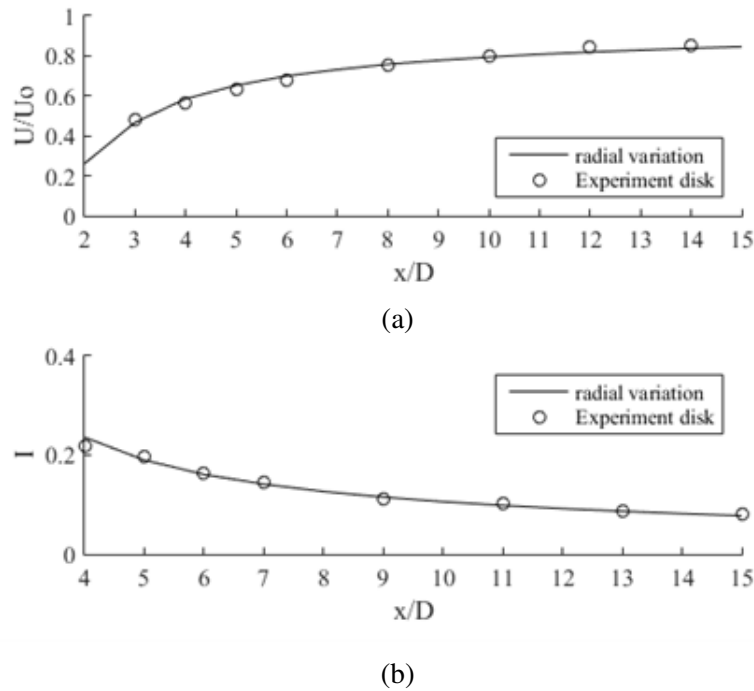


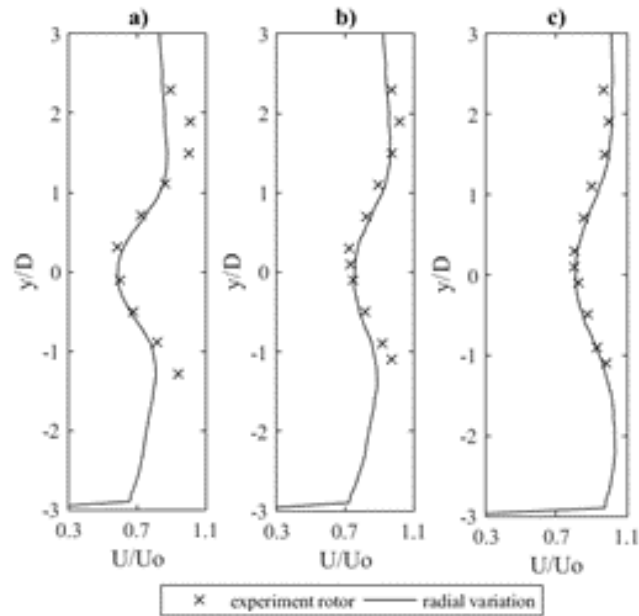
**Figure 5.10:** Comparison of downstream centreline velocity (a) and turbulence intensity (b) of the radial variation bem-AD model against experimental measurements (Batten et al. 2013).

#### 5.2.4 Modified BEM-AD model: Radial Variation

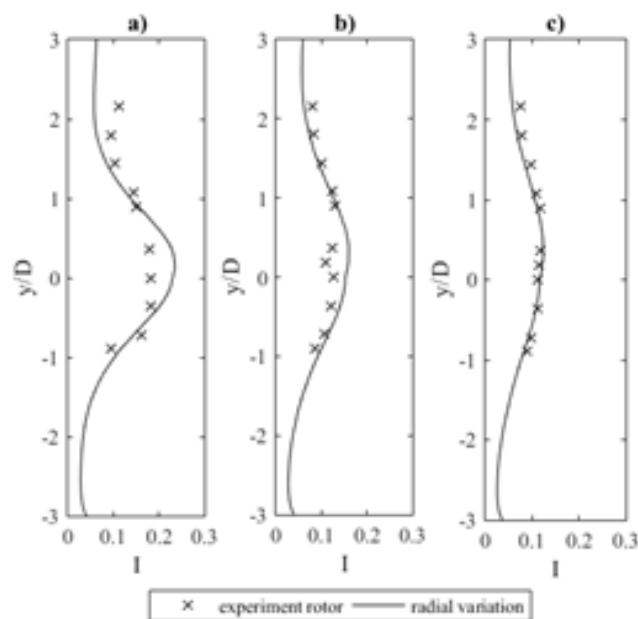
In this sub-section, the developed radial variation BEM-AD model is validated against experimental measurements (Batten et al. 2013). The blade element momentum theory method is incorporated into this model by defining the disk's porosity and resistance coefficient, details of this configuration are described in Chapter 4.2.3. Figure 5.10 shows the centreline downstream velocity and turbulence intensity of the radial variation BEM-AD model with experimental measurements. The developed model matches well with the experimental measurements, and it tends to perform better at predicting the centreline downstream wake than the velocity variation BEM-AD model especially at a downstream distance less than 8D.

Figure 5.11 shows the downstream velocity and turbulence intensity profile at downstream distances of 5D, 8D and 10D for the radial variation BEM-AD model. The velocity profile at 10D matches well with the experimental measurements (Batten et al. 2013) in both downstream velocity and turbulence intensity. It is noticed that

downstream velocity matches closely with the experimental measurements around the depth region of 1 to -1, while the model outside this region tended to underpredict the results. Furthermore, the downstream turbulence intensity was shown to be overpredicting around the depth region of 1 to -1. The high accuracy in predicting the downstream velocity at the depth region of 1 to -1 is contributed by the radial variation approach describing the porosity and resistance coefficient of the disk, while it is speculated that outside the depth region of 1 to -1, the wake prediction is less accurate. This might be due to the velocity profile not being taken into account while describing the disk properties.



(a) vertical normalised velocity



(b) vertical turbulence intensity

**Figure 5.11:** Comparison of vertical velocity and vertical turbulence intensity of the radial variation BEM-AD model with experimental measurements (Batten et al. 2013) at downstream distances of 5D, 8D and 10D.

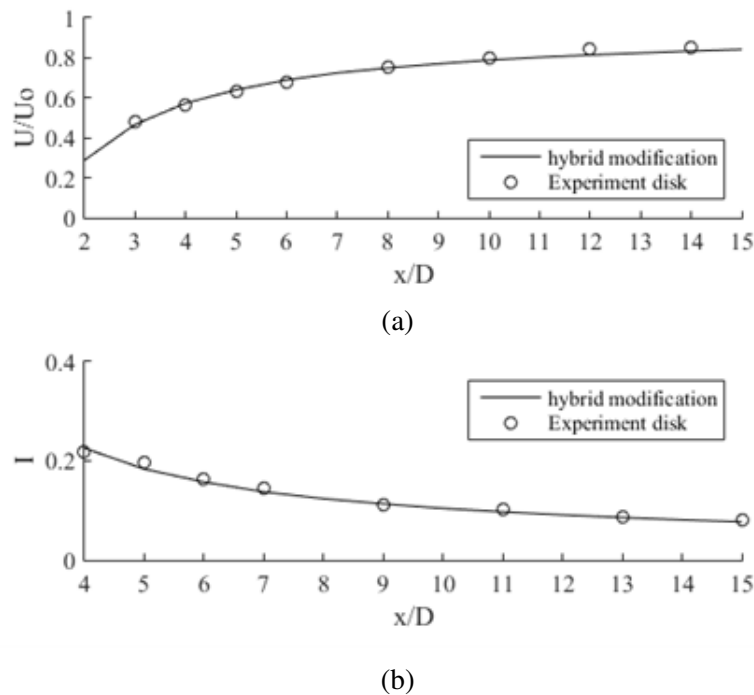


**Figure 5.12:** Comparison of downstream centreline velocity (a) and turbulence intensity (b) of the modified hybrid BEM-AD model against experimental measurements (Batten et al. 2013).

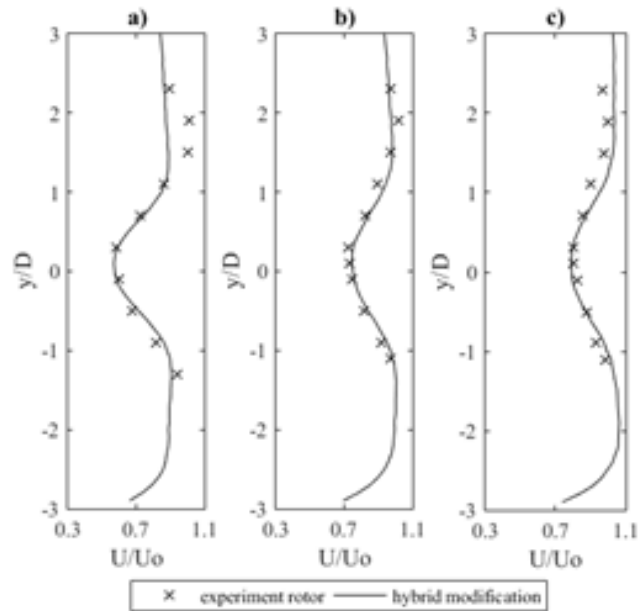
### 5.2.5 Modified BEM-AD model: Hybrid model

In this sub-section, the developed velocity variation and radial variation BEM-AD models were combined to form a hybrid modified BEM-AD model which includes the blade element momentum theory radial approach and the velocity profile in describing the disk properties, details of this configuration is described in Chapter 4.2.4. Figure 5.12 shows the centreline downstream velocity and turbulence intensity of the hybrid modified BEM-AD model against experimental measurements (Batten et al. 2013). The developed model matches closely with the experimental measurements, it is shown to perform better than both the velocity and radial variations. The combination of both variations greatly improves the ability of the hybrid model to predict downstream wake, this can be further observed in the vertical profile of downstream distance 5D, 8D and 10D in Figure 5.13 .

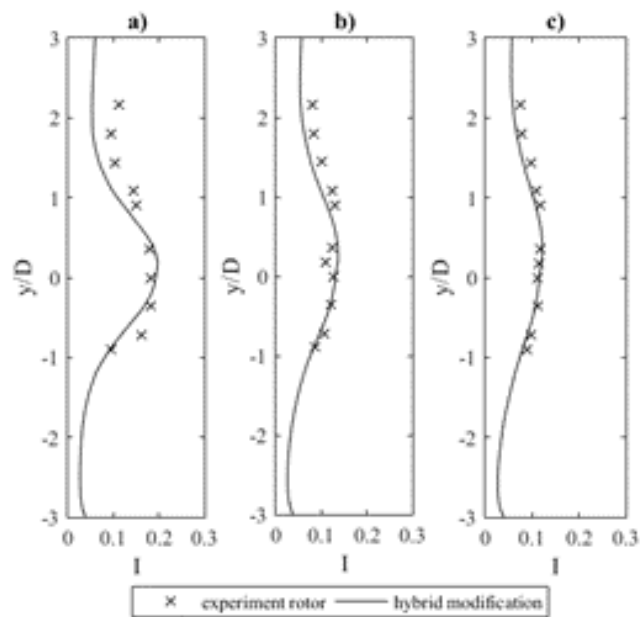
Figure 5.13 shows the downstream velocity and turbulence intensity profile at a downstream distance of 5D, 8D and 10D for the hybrid modified BEM-AD model.



The velocity profile at 10D matches well with the experimental measurements in both downstream velocity and turbulence intensity. It is observed that the accuracy of overall wake results greatly improved overall, especially for all results below a vertical normalised depth of 1. However, the results above the vertical normalised depth of 1 show underprediction in both downstream velocity and turbulence intensity. The reason for this might be due to the developed model not taking into account fluid surface conditions, i.e. the surface was treated as a symmetry boundary face. A relationship was observed between velocity and turbulence intensity, i.e. a higher downstream turbulence intensity will result in a higher downstream velocity. This shows that a high turbulence intensity promotes wake velocity recovery.



(a) vertical normalised velocity



(b) vertical turbulence intensity

**Figure 5.13:** Comparison of vertical velocity and vertical turbulence intensity of the modified hybrid BEM-AD model with experimental measurements (Batten et al. 2013) at downstream distances of 5D, 8D and 10D.

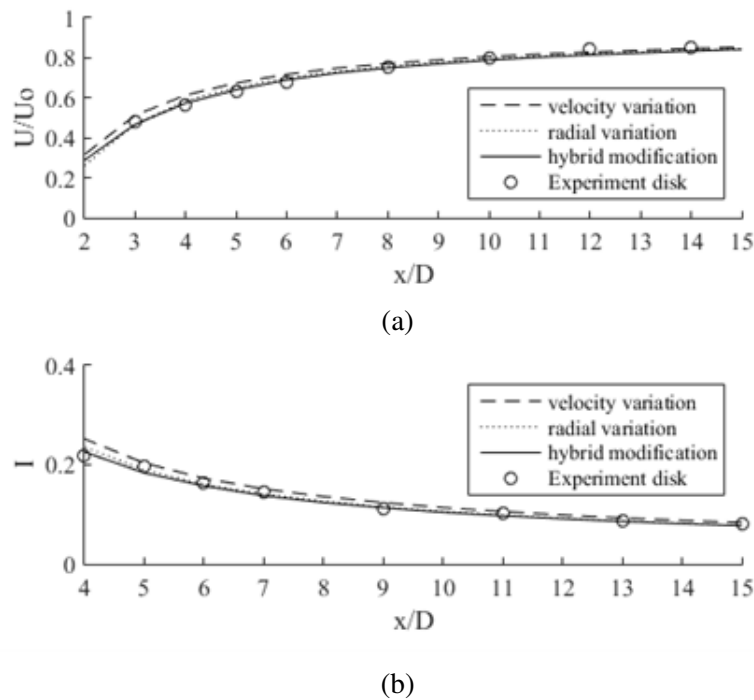


**Figure 5.14:** Comparison of downstream centreline velocity (a) and turbulence intensity (b) for the velocity variation model, radial variation model and hybrid modification model against experimental measurements (Batten et al. 2013).

### 5.2.6 Modified BEM-AD model: Overall Discussion

Overall, the modified hybrid BEM-AD model has proven to be the most accurate among all of the models proposed and investigated in this work, however all three models display a similar degree of accuracy after a downstream distance greater than  $8D$ . While at the downstream distance greater than  $5D$ , the ability of the radial variation model and modified hybrid model to capture the wake effects show little difference. However, for a downstream distance less than  $5D$ , the modified hybrid BEM-AD model provides the most accurate results. Figure 5.14 shows a comparison of centreline downstream velocity and turbulence intensity for the three models against experimental measurements. In Table 5.3, a statistical analysis is presented for each of the three studied models which are compared with experimental measurements of centreline downstream velocity and turbulence intensity.

The statistical analysis, presented in Table 5.3, shows that the velocity variation model has the worst correlation and the largest error among all three models, while

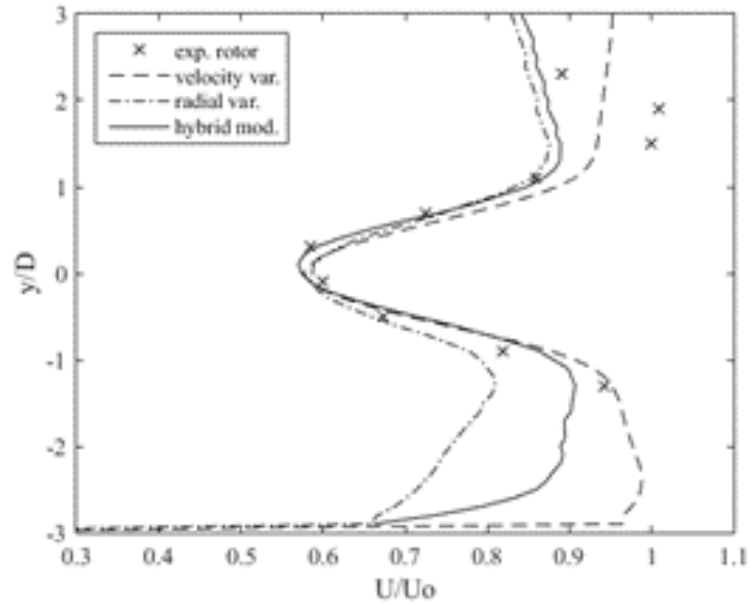
**Table 5.3:** Statistical analysis each of the three modified BEM-AD models against experimental measurements (Batten et al. 2013) for downstream centreline velocity and turbulence intensity.

Variation	Velocity				Turbulence Intensity			
	$R^2$	RMSE	MAE	MAPE	$R^2$	RMSE	MAE	MAPE
Velocity	0.9868	0.0283	0.0243	3.83%	0.9775	0.0145	0.0101	6.56%
Radial	0.9860	0.0154	0.0129	1.88%	0.9823	0.0077	0.0052	3.25%
Hybrid	0.9917	0.0131	0.0098	1.31%	0.9863	0.0058	0.0045	2.82%

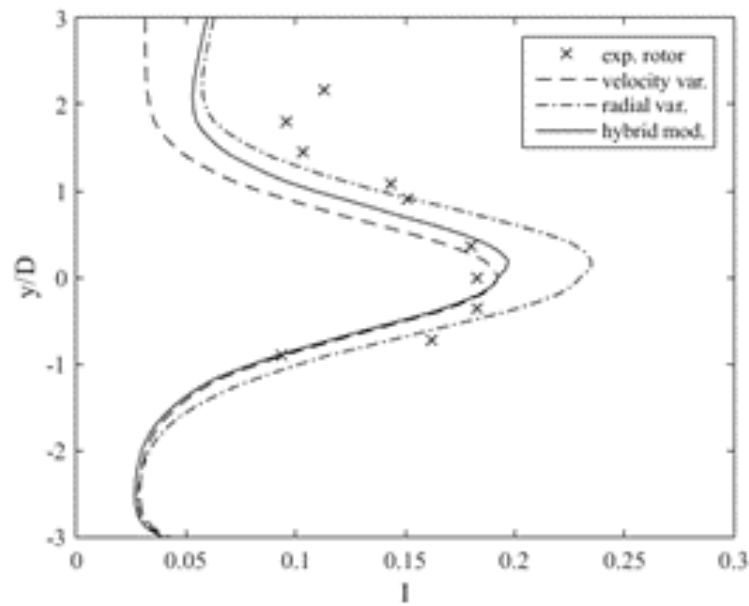
the radial variation model and the hybrid modified model show very similar correlation and error when compared with the experimental measurements. The hybrid modified model correlates best with the experimental measurements in terms of both downstream velocity and turbulence intensity with a coefficient of determination,  $R^2$  value of 0.9917 and 0.9863 respectively. The hybrid modified model has the smallest error among all three models, with a RMSE value of 0.0131 and 0.0058 and; MAPE value of 1.31% and 2.82% for velocity and turbulence intensity respectively.

To study the improvement of wake prediction in the near wake, the performance of all three models was observed at a downstream distance of  $5D$  in terms of velocity profile and turbulence intensity profile as shown in Figure 5.15. When observing in terms of velocity, there is little difference between all three models between a depth,  $y/D$ , of 1 to -1. The velocity variation seems to perform better below a depth of  $y/D = -1$ , while radial variation and hybrid modification perform better above a depth of  $y/D = 1$ . Overall, the hybrid modification has the optimum prediction both below a depth of  $y/D = -1$  and above a depth of  $y/D = 1$ . While when observing in terms of turbulence intensity, both the velocity variation model and the hybrid modification model perform well between a depth,  $y/D$ , of 1 to -1, however the radial variation model overpredicts the turbulence intensity between a depth,  $y/D$ , of 1 to -1. While all three models underpredict above a depth of  $y/D = 1$ . In Table 5.4, a statistical analysis is presented for each of the three studied models which are compared with experimental measurements in terms of downstream velocity profile and turbulence intensity profile at a downstream distance of  $5D$ .

The statistical analysis, presented in Table 5.4, shows that all three models correlate well with experimental measurements, with all three models having  $R^2$  value



(a) vertical normalised velocity



(b) vertical turbulence intensity

**Figure 5.15:** Comparison of downstream velocity profile and turbulence intensity profile for the velocity variation model, radial variation model and hybrid modification model against experimental measurements (Batten et al. 2013) at a downstream distance of  $5D$ .

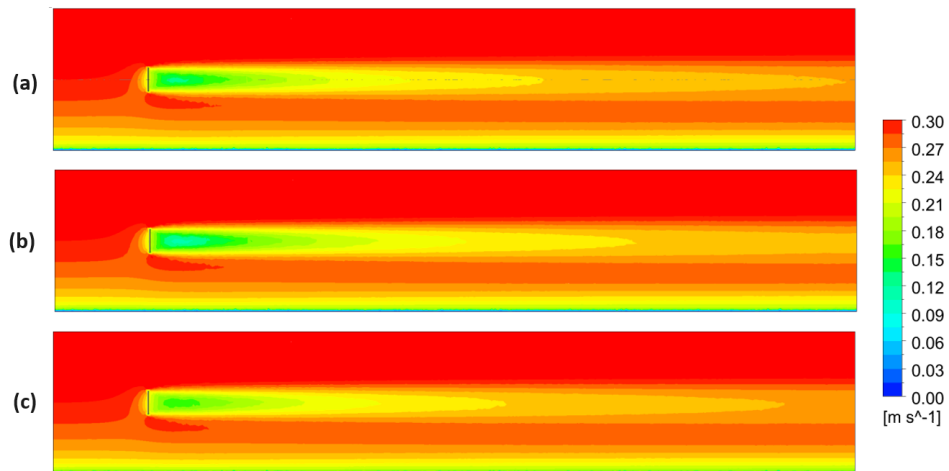
**Table 5.4:** Statistical analysis for each of the three modified BEM-AD models against experimental measurements (Batten et al. 2013) in terms of downstream velocity profile and turbulence intensity profile at a downstream distance of 5D.

Variation	Velocity				Turbulence Intensity			
	$R^2$	RMSE	MAE	MAPE	$R^2$	RMSE	MAE	MAPE
Velocity	0.9070	0.0480	0.0439	5.47%	0.7712	0.0470	0.0391	31.28%
Radial	0.8955	0.0767	0.0593	6.75%	0.8188	0.0328	0.0286	21.39%
Hybrid	0.8923	0.0576	0.0421	4.79%	0.8262	0.0329	0.0281	22.05%

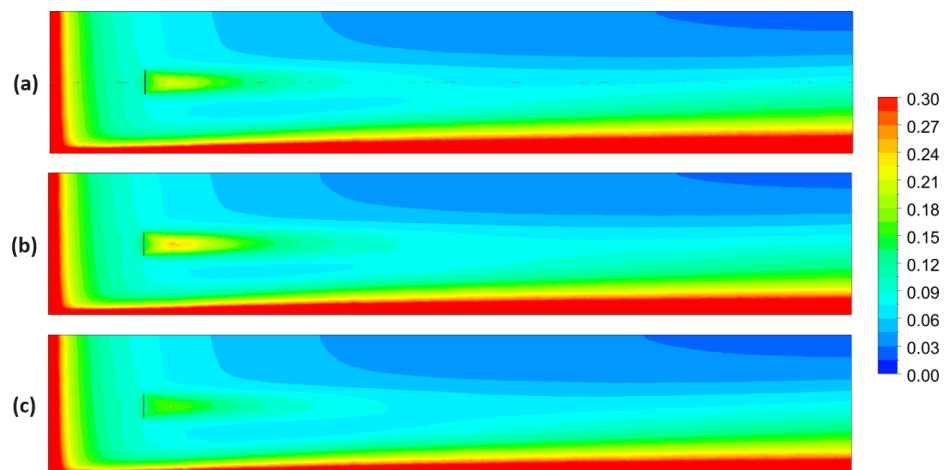
above 0.89. The velocity variation at a downstream distance of 5D has the highest correlation in terms of velocity profile with  $R^2$  value of 0.9070 but has the poorest correlation in terms of turbulence intensity profile with  $R^2$  value of 0.7712. The hybrid modification model has the lowest correlation among all three models in terms of velocity profile, while having the highest correlation in terms of turbulence intensity profile with  $R^2$  value of 0.8262. Furthermore, the hybrid modified model has the smallest error among all three models, with a RMSE value of 0.0576 and 0.00329 and; MAPE value of 4.79% and 22.05% for velocity and turbulence intensity respectively.

Figure 5.16 and 5.17 show contours of velocity and turbulence intensity comparison for the velocity variation model, radial variation model, and the hybrid modification model. It is shown in Figure 5.16 that the radial variation model has the longest downstream velocity wake, while the hybrid modification model has the shortest downstream velocity wake. Consequently, a shorter downstream velocity wake shape indicates a higher velocity wake recovery. This is also true for turbulence intensity contour, as shown in Figure 5.17, the radial variation model has a more intense downstream turbulence intensity wake than the velocity variation model and the hybrid modification model. While the hybrid modification model has the least intense downstream turbulence intensity wake. Thence, the more intense the downstream turbulence intensity wake, the lower the rate of wake velocity recovery.

Figure 5.18 shows the power density contour of the actuator disk for the velocity variation model, radial variation model and the hybrid modification model from the front view. It is observed that the velocity variation model has a higher power density near the edge of the actuator disk when compared with the other two models. This is due to the velocity variation model not taking radial blade element charac-



**Figure 5.16:** Velocity side-view contour of velocity variation model (a), radial variation model (b) and hybrid modification model (c).



**Figure 5.17:** Turbulence intensity side-view contour of velocity variation model (a), radial variation model (b) and hybrid modification model (c).

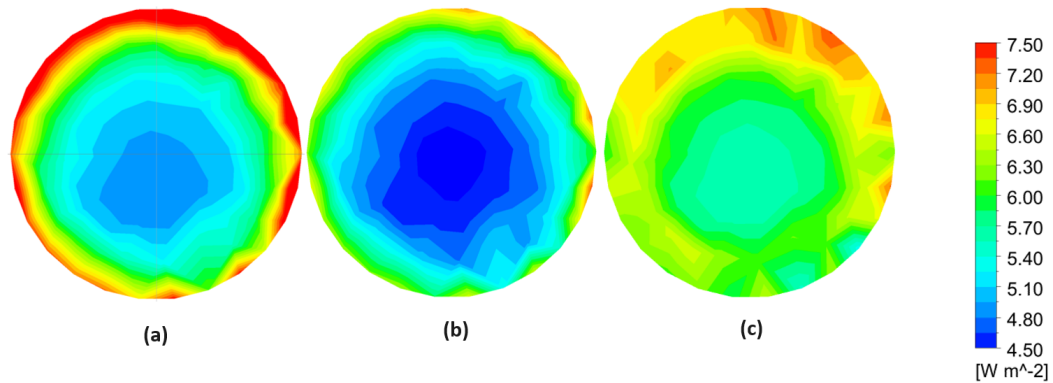


**Figure 5.18:** Power density contour of the actuator disk from front view for the velocity variation model (a), radial variation model (b) and the hybrid modification model (c).

teristics into account. Thus, some BEM calculated parameters were neglected, such as tip loss correction. Additionally, for the velocity variation model, the inclusion of the inflow velocity profile has an impact on the power density distribution on the actuator disk, where the lower part of the actuator disk experiences less intense conditions than the upper part of the disk

When observing the power density of the actuator disk for the radial variation model, a somewhat radially equal spacing annular ring from the centre of the disk can be seen, where the centre part of the disk has the lowest power density and outer annular part of the disk has the highest power density incoherent with the radial blade element characteristics. When observing the power density of the actuator disk for the velocity variation model, the edge of the disk was observed to have an overly high power density due to blade tip losses not taking into account and also the low density in the centre part of the disk is observed to be more towards the lower part of the disk. While observing the power density of the actuator disk for the hybrid modification model, both the inflow velocity profile and the radial blade element characteristics are taken into account when describing the actuator disk. It is observed that the lower part of the actuator disk is less intense than the upper part of the disk. Also, the power density increases moving outwards from the centre of the actuator disk. Table 5.5 provides a comparative analysis of the actuator disk for the velocity variation model, the radial variation model and the hybrid modification model in terms of thrust coefficient and power coefficient with a BEM numerical model.



**Table 5.5:** Comparative analysis of thrust coefficient and power coefficient of velocity variation, radial variation and hybrid modification against BEM numerical value.

	Thrust Coefficient, $C_P$				Power Coefficient, $C_P$			
	Numer.	Velocity	Radial	Hybrid	Numer.	Velocity	Radial	Hybrid
Coef.	0.7960	0.7571	0.6278	0.7919	0.4680	0.5229	0.4616	0.4714
Diff.	-	4.89%	21.13%	0.51%	-	11.73%	1.37%	0.72%

Table 5.5 shows the velocity variation model, radial variation model and hybrid modification model have a lower thrust coefficient prediction when compared to the numerical values which were 0.7571, 0.6278 and 0.7919 respectively. Furthermore, the velocity variation model and the hybrid modification model have a higher power coefficient prediction when compared to the numerical values which were 0.5229 and 0.4714 respectively; while the radial variation model has a lower power coefficient prediction when compared to the numerical value which is 0.4616.

The radial variation model has the highest difference when compared with the numerical value in terms of thrust coefficient which is 21.13% and the velocity variation model has the highest difference when compared with the numerical value in terms of power coefficient which is 11.73%. These indicate the velocity variation model, which incorporates the inflow velocity profile in describing the actuator disk, has predicted thrust better than the radial variation model. The radial variation model, which incorporates radial blade element characteristics in describing the actuator disk, has predicted the power coefficient more accurately than the velocity variation model.

Overall, the hybrid modification model, which incorporates both the inflow velocity profile and radial blade element characteristics in describing the actuator disk, predicted both thrust and power closest to BEM numerical value. Therefore, the hybrid modification model has the least difference when compared with the numerical thrust and power coefficients which were 0.51% and 0.72% respectively.

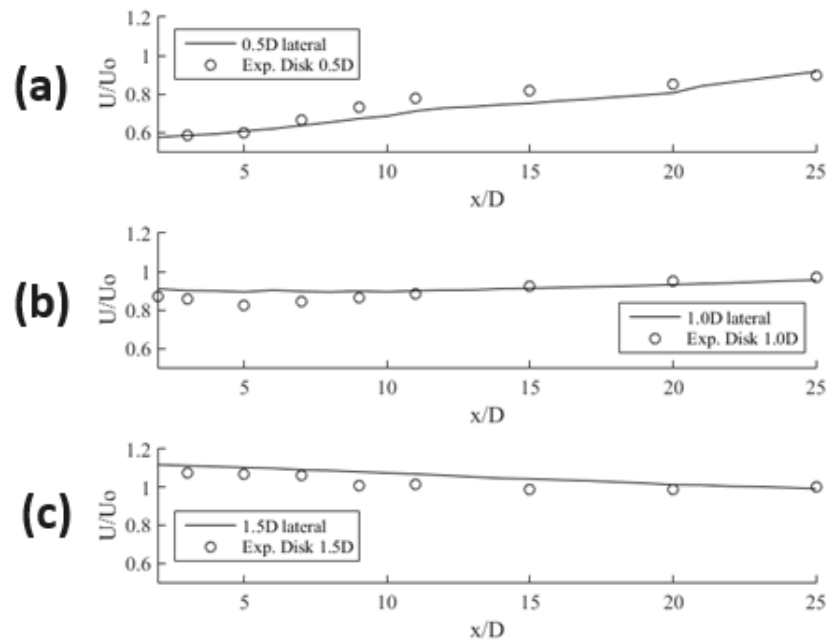


**Figure 5.19:** Comparison of centreline downstream velocity of the two turbine model with experimental measurements of the lateral distance of 0.5D (a), 1.0D (b) and 1.5D (c).

### 5.3 Multiple Turbine Model

The section in this research work primarily focussed on studies and investigations of downstream wake interactions of turbine-to-turbine conditions within the tidal current turbine array. The multiple turbines model utilised the same setup as the single turbine model, to capture the wake conditions and energetic output, with a focus on turbine spacing of two turbines, staggered arrangements of three turbines, different turbine sizes and placement of turbines at different depths.

#### 5.3.1 Turbine Lateral Spacing – Two turbines

A study was conducted to evaluate the ability of the hybrid modification model when considering multiple actuator disks. In this sub-section, the interaction of two rotor actuator disks using the hybrid modification model was shown and validated against experimental measurements (Stallard et al. 2013). Figure 5.19 shows the centreline downstream velocity of the two turbines model against experimental measurements of the lateral distance of 0.5D, 1.0D and 1.5D.

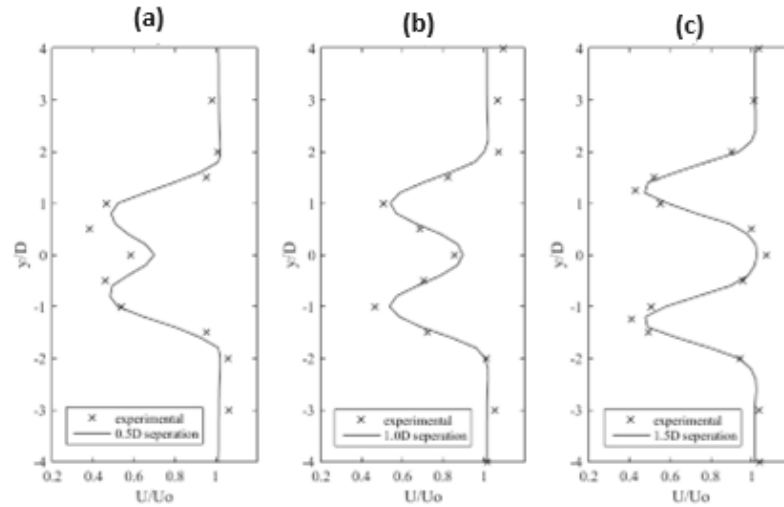


**Figure 5.20:** Comparison of velocity profile at downstream distance of 3D for the two turbines model at the lateral distance of 0.5D (a), 1.0D (b) and 1.5D (c) against experimental measurements.

Figure 5.19 shows that the centreline of the two turbine model matches closely with the experimental measurements. The study also shows the two turbines at a lateral distance of 0.5D experience a reduction in downstream centreline velocity to roughly around  $U/U_o = 0.6$  and slowly recover moving further downstream, this indicates the interaction of the two turbines significantly affects downstream wake velocity. While the two turbines at a lateral distance of 1.0D experience a reduction in downstream centreline velocity to roughly around  $U/U_o = 0.9$  and recover to around  $U/U_o = 1.0$  moving further downstream, this indicates the interaction of the two turbines affect downstream wake velocity very lightly. However, the two turbines at a lateral distance of 1.5D experience an increase in downstream centreline velocity to roughly around  $U/U_o = 1.1$  and recovers to approximately  $U/U_o = 1.0$  moving further downstream, this indicates the interaction of the two turbines has accelerated the downstream wake velocity. Figure 5.20 shows the velocity profile at a downstream distance of 3D (near wake region) for the two turbine models at the lateral distance of 0.5D, 1.0D and 1.5D validated against experimental measurements.

Figure 5.20 has shown that the downstream velocity profile of the two turbines model at a downstream distance of 3D (near wake region) matches closely with the experimental measurements. It is observed that at a downstream distance of 3D,

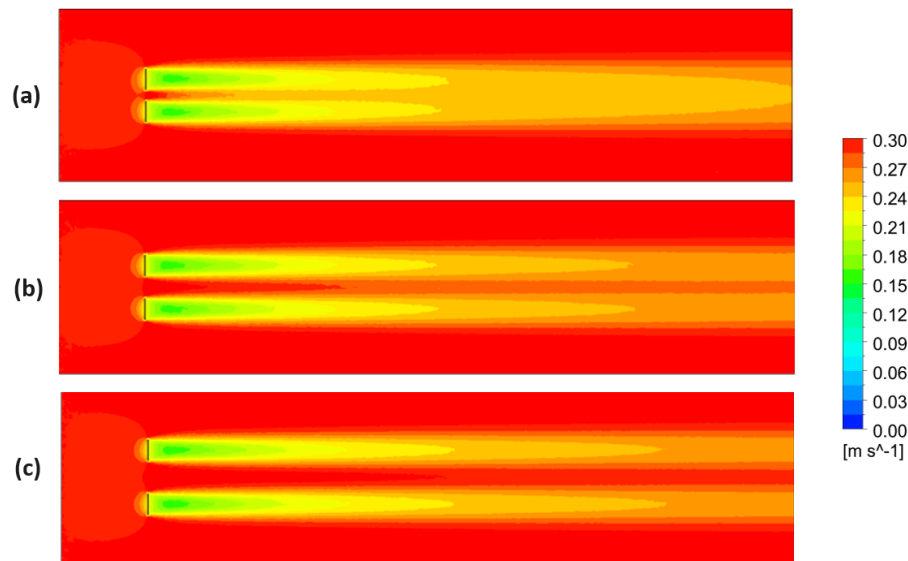


**Figure 5.21:** Velocity side-view contours of the two turbines model at the lateral distance of 0.5D (a), 1.0D (b) and 1.5D (c).

the two turbines model performs best at a lateral distance of 1.5D, it is observed that flow passing through between the two turbines experiences accelerated flow conditions. These can be further observed when looking at the velocity contour as shown in Figure 5.21. Figure 5.21 shows the velocity contour from the side view of the two turbines model at a lateral distance of 0.5D, 1.0D and 1.5D. For the lateral distance of 0.5D, the downstream wake flow merges in the near wake region and persists as a singular wake moving further downstream. At a lateral distance of 1.0D, the downstream wake flow remains separate at the near wake region by relatively faster moving fluid between the turbines. However, the far wake region tends to merge slightly. While, at a lateral distance of 1.5D, the downstream wake flow from the two turbines shows a clear separation caused by accelerated flow when passing between the turbines. Furthermore, the wake continues to separate even in the far wake region. Table 5.6, 5.7 and 5.8 shows a comparative analysis of the thrust coefficient and power coefficient of turbines in the two turbines model at a lateral distance of 0.5D, 1.0D and 1.5D against BEM numerical values.

Table 5.6, 5.7 and 5.8 shows that the turbines at a lateral distance 0.5D have the highest average thrust and power value of 175.99 N and 33.05 W respectively which correspond to an average thrust coefficient and average power coefficient of 0.8070 and 0.4806 respectively. While it is observed that at a lateral distance of 1.0D, the

**Table 5.6:** Comparative analysis of thrust coefficient and power coefficient for the two turbines model at the lateral distance of 0.5D against BEM numerical value.

	Numerical	Rotor 1		Rotor 2		average	
	Value	Value	Diff.	Value	Diff.	Value	Diff.
$C_T$	0.796	0.8081	1.51%	0.8059	1.24%	0.8070	1.38%
$C_P$	0.468	0.4802	2.60%	0.4811	2.80%	0.4806	2.70%
Thrust (N)	181.19	176.2	2.74%	175.75	3.00%	175.99	2.87%
Power (W)	31.83	33.20	4.42%	32.86	3.23%	33.05	3.83%

**Table 5.7:** Comparative analysis of thrust coefficient and power coefficient for the two turbines model at the lateral distance of 1.0D against BEM numerical value.

	Numerical	Rotor 1		Rotor 2		average	
	Value	Value	Diff.	Value	Diff.	Value	Diff.
$C_T$	0.796	0.8043	1.04%	0.8030	0.88%	0.8037	0.96%
$C_P$	0.468	0.4806	2.70%	0.4800	2.55%	0.4803	2.63%
Thrust (N)	181.19	175.4	3.19%	175.13	3.35%	175.27	3.27%
Power (W)	31.83	33.30	4.52%	32.78	2.98%	33.02	3.75%

average thrust and power value decrease slightly to 175.27 N and 33.02 W respectively which correspond to an average thrust coefficient and average power coefficient of 0.8037 and 0.4803 respectively. At a lateral distance of 1.5D, the average thrust increases back slightly to 175.45 N which corresponds to an average thrust coefficient of 0.8045; while the average power has little to no change. These indicate that a close lateral distance (less than 1.5D) encourages a greater thrust and power at the disk. Thence, the greater the lateral distance, the lower the thrust and power at the disk up until a lateral distance of 1.5D.

**Table 5.8:** Comparative analysis of thrust coefficient and power coefficient for the two turbines model at the lateral distance of 1.5D against BEM numerical value.

	Numerical	Rotor 1		Rotor 2		average	
	Value	Value	Diff.	Value	Diff.	Value	Diff.
$C_T$	0.796	0.8053	1.17%	0.8036	0.96%	0.8045	1.06%
$C_P$	0.468	0.4796	2.48%	0.4808	2.74%	0.4802	2.61%
Thrust (N)	181.19	175.6	3.07%	175.27	3.27%	175.45	3.17%
Power (W)	31.83	33.20	4.30%	32.84	3.17%	33.02	3.73%

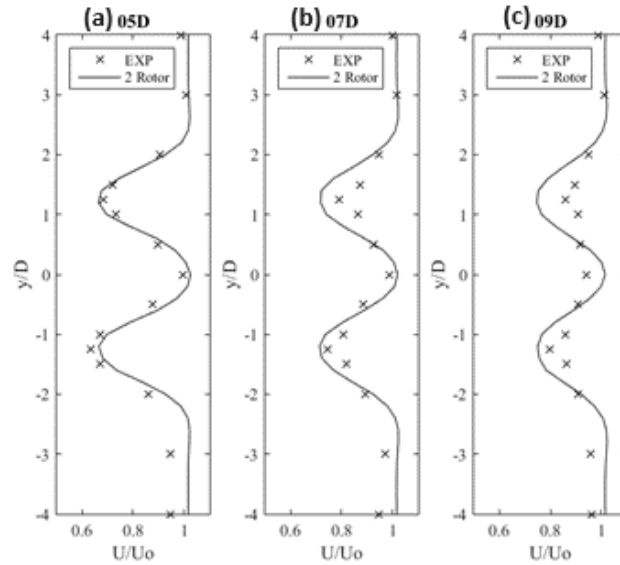
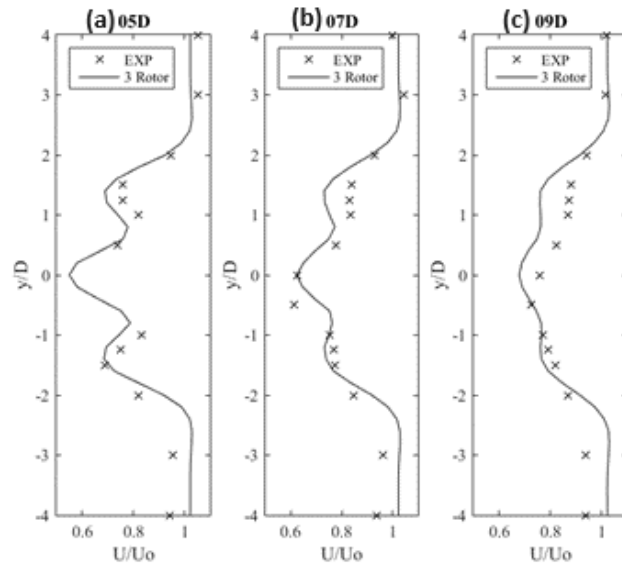


**Figure 5.22:** Comparison of velocity profile for the two turbines model at a downstream distance of 5D (a), 7D (b) and 9D (c) against experimental measurements.

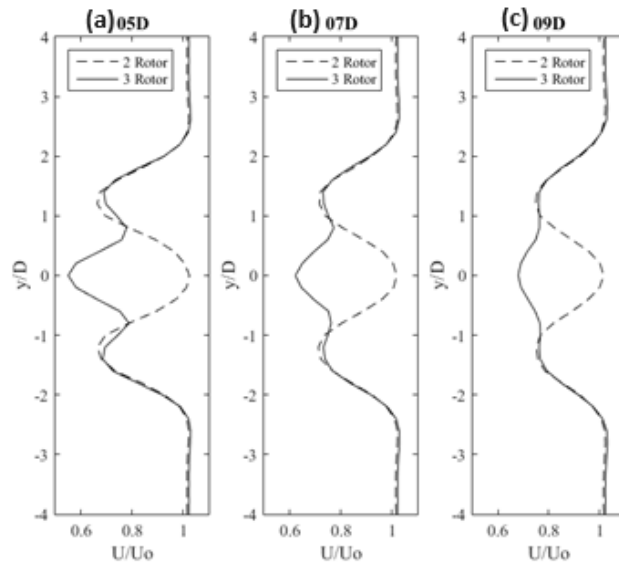
### 5.3.2 Turbine Lateral Spacing – Three turbines

In this sub-section the interaction of three rotor actuator disks using the hybrid modification model with two turbines at a lateral distance of  $1.5D$  in the first row and one turbine at the centreline in the second row (downstream  $5D$ ), the model was also validated against experimental measurements (Stallard et al. 2013). The three turbines model was also compared with the two turbines model at a lateral distance of  $1.5D$ . Figure 5.22 and 5.23 shows the velocity profile of two turbines model and three turbines model at a downstream distance of  $5D$ ,  $7D$  and  $9D$  and validated against experimental measurements.

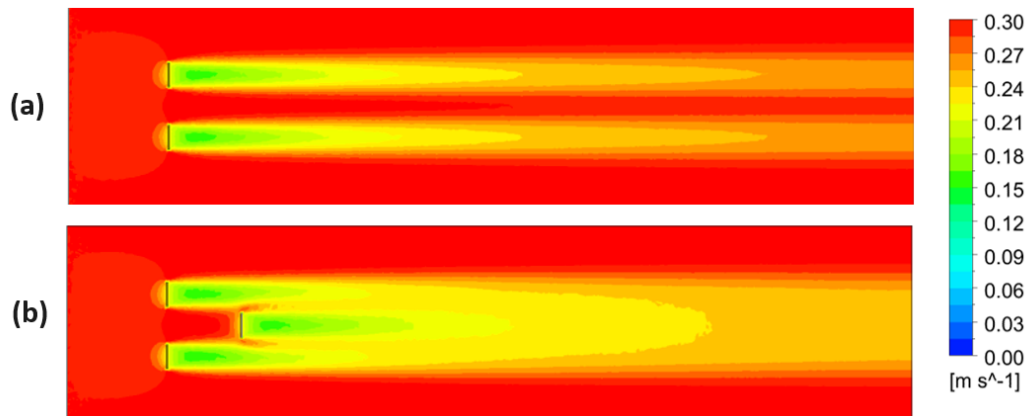
Figure 5.22 shows that the two turbines model matches quite well with experimental measurements especially at a downstream distance of  $5D$ , however at a downstream distance of  $9D$ , it was observed that the model underpredicts the velocity profile but overall, still follows the natural progression of the flow's wake recovery moving downstream. Figure 5.23 shows that the three turbines model matches well with experimental measurements. At a downstream distance of  $9D$ , it was observed that the model also underpredicts the velocity profile especially at the vertical distance  $y/D = 0$  to  $y/D = 2$ .



**Figure 5.23:** Comparison of velocity profile for the three turbines model at a downstream distance of 5D (left), 7D (centre) and 9D (right) against experimental measurements.



**Figure 5.24:** Comparison of velocity profile for the three turbines model at a downstream distance of 5D (left), 7D (centre) and 9D (right) against experimental measurements.



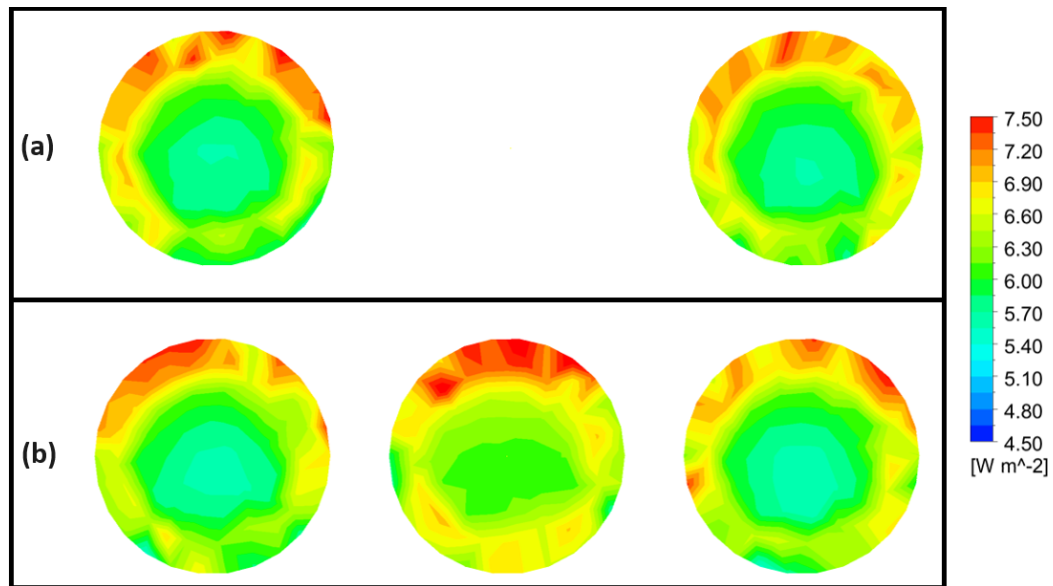
**Figure 5.25:** Velocity contour from side view of the two turbines model (a) and three turbines model (b).

Figure 5.24 shows the velocity profile of two turbines model compare against three models model at downstream distances of 5D, 7D and 9D. It is observed that the introduction of the downstream turbine (second row) has a clear effect on the downstream wake. At the downstream distance of 5D, the inclusion of the downstream turbine has accelerated the wake velocity recovery from the turbines at the first row, this effect continues further into the downstream distance of 7D. At a downstream distance of 7D, experiencing the blockage effect caused by the downstream turbine will accelerate flow around its edge and thus, improve the velocity wake recovery of the disk at the first row. At a downstream distance of 9D, the wakes from the three turbines have merged and ergo showed a somewhat similar downstream velocity between  $y/D = 1.5$  to  $y/D = -1.5$ . This can be further observed from the velocity contour from the side view of the three turbines model as seen in Figure 5.25.

Figure 5.25 shows that the introduction of a downstream turbine (second row) clearly accelerates the flow at the side of the turbine which slightly increases wake recovery. The accelerated flow around the edge of the downstream turbine continues further to a downstream distance of 7D. While, in the far wake region the wake from the three turbines can be observed to merge into one single wake. Figure 5.26 shows the power density contours of the disks for the two turbines model and the three turbines model from the front view.

Based on Figure 5.26, before the introduction of a downstream turbine (second





**Figure 5.26:** Power density front-view contour of the actuator disks of the two turbines model (a) and three turbines model (b).

row), the power density of both turbines was observed to be very similar and have little difference. After the introduction of the downstream turbine (the downstream turbine located in the centre), clearly shows to have a more intense power density than the upstream turbines (first row). Table 5.9 and 5.10 shows a comparative analysis of thrust coefficient and power coefficient for the two turbines model and three turbines model against BEM numerical value.

Based on Table 5.9 and 5.10, the Rotor 1 and Rotor 2 are upstream turbines (first row) and the Rotor 3 is the downstream turbine (second row). Before the introduction of the downstream turbine, the average thrust and power were 175.45 N and 33.02 W respectively which corresponded to a thrust coefficient and power coefficient of 0.8045 and 0.4802 respectively as given in Table 9. While, after the introduction of the downstream turbine, the average thrust and power increased to 178.63 N and 33.21 W respectively which corresponded to a thrust coefficient and power coefficient of 0.8191 and 0.4820 respectively as given in Table 10. Focusing on Rotor 3, it can be observed that the power value is clearly higher than the upstream turbines which were 33.59 W and corresponded to a power coefficient of 0.4918, this might be due to the accelerated flow caused by the upstream turbines. However, the thrust of Rotor 3 is lower compared to the upstream turbines which

**Table 5.9:** Comparative analysis of thrust coefficient and power coefficient for the two turbine model against BEM numerical value.

	Numerical	Rotor 1		Rotor 2		average	
	Value	Value	Diff.	Value	Diff.	Value	Diff.
$C_T$	0.796	0.8053	1.17%	0.8036	0.96%	0.8045	1.06%
$C_P$	0.468	0.4796	2.48%	0.4808	2.74%	0.4802	2.61%
Thrust (N)	181.19	175.6	3.07%	175.27	3.27%	175.45	3.17%
Power (W)	31.83	33.20	4.30%	32.84	3.17%	33.02	3.73%

**Table 5.10:** Comparative analysis of thrust coefficient and power coefficient for the three turbines model against BEM numerical value.

	Numer.l	Rotor 1		Rotor 2		Rotor 3		average	
	Value	Value	Diff.	Value	Diff.	Value	Diff.	Value	Diff.
$C_T$	0.796	0.8206	3.10%	0.8213	3.18%	0.8153	2.42%	0.8191	2.90%
$C_P$	0.468	0.4769	1.90%	0.4774	2.01%	0.4918	5.08%	0.4820	3.00%
Thrust (N)	181.19	178.98	1.22%	179.13	1.14%	177.80	1.87%	178.63	1.41%
Power (W)	31.83	33.01	3.71%	33.05	3.82%	33.59	5.52%	33.21	4.35%

was 177.80 N giving a thrust coefficient of 0.8153.

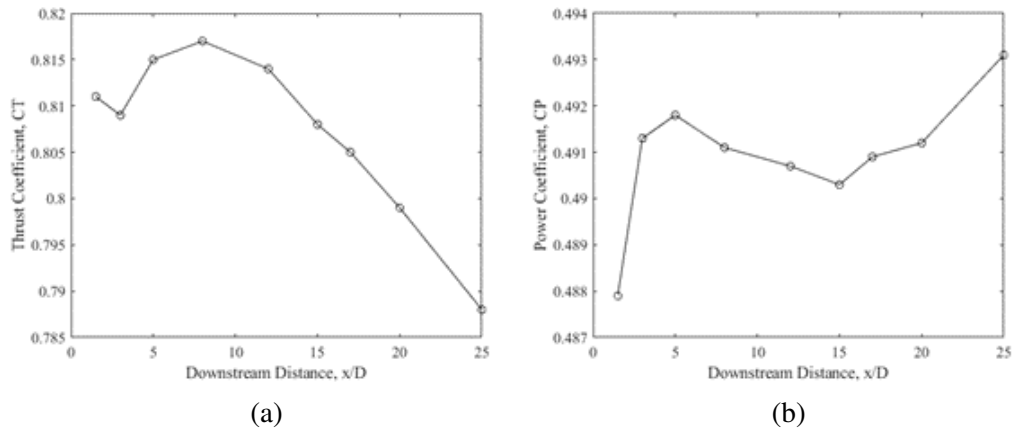


**Figure 5.27:** Thrust coefficient (a) and power coefficient (b) of the second row turbine at a range of downstream spacing settings.

### 5.3.3 Turbines Staggered Layout – downstream spacing

In this sub-section, the impact of the downstream spacing of the second row turbine on the performance of the third turbine in a three-rotor actuator disk staggered layout is presented. Figure 5.27 shows the thrust coefficient and power coefficient of the second row turbine at different downstream spacing. As shown in Figure 5.27, as the downstream spacing of the second row increases after a downstream spacing of 3D, the thrust coefficient increases and peaks at 8D and a downstream distance greater than 8D, the thrust coefficient was observed to decrease. It is observed that the desirable thrust coefficient occurs between downstream spacing from 5D to 12D.

As the downstream spacing of the second row increases from 3D to 5D, the power coefficient increases, and from downstream spacing from 5D to 15D, the power coefficient was observed to decrease and then the power coefficient increases again at downstream distance greater than 15D as seen in Figure 5.27. It is observed that the desirable power coefficient occurs between downstream spacing from 3D to 8D and also after 20D. Hence, the optimal downstream spacing for deploying a second row turbine would be at 5D which yields a good compromise between spacing, thrust and power coefficient.

The downstream spacing of the second row turbine has an impact on downstream velocity recovery of wake, this is evident in Figure 5.28. Figure 5.28 shows the centreline normalised downstream velocity after the second row turbine at down-

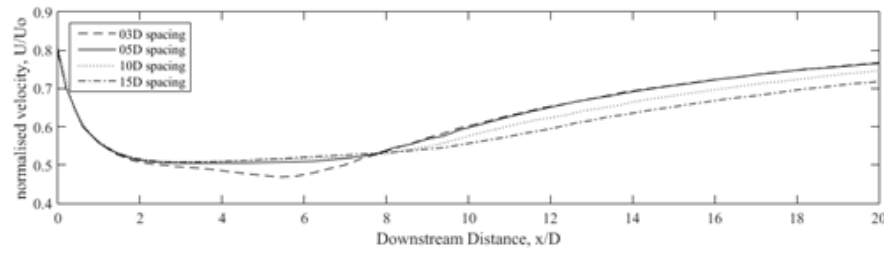


**Figure 5.28:** The centreline downstream velocity after the second row turbine at downstream spacing scenarios of 3D, 5D, 10D and 15D.

stream spacing scenarios of 3D, 5D, 10D and 15D. It is observed that regardless of downstream spacing, all spacing scenarios experience a similar reduction in velocity before a downstream distance of 3D. The 3D spacing scenario was seen to experience the greatest and longest reduction in velocity, as it is seen to reduce in velocity up to the downstream distance of 6D. On the other hand, all spacing scenarios except the 3D spacing scenario experience a slow recovery in the wake between the downstream distance of 3D to 8D. While, after the downstream distance of 8D, all spacing scenarios started to recover with a 3D spacing scenario and a 5D spacing scenario having a higher velocity recovery rate, followed by a 10D spacing scenario and then a 15D spacing scenario which has the lowest velocity recover rate.

The continued reduction of velocity seen in the 3D spacing scenario between 3D to 6D downstream distance was due to the wake of the first row turbines combining with the wake of the second row turbine. However, the combination of wake from the first row turbines also promotes velocity recovery after a downstream distance of 6D which results in the 3D spacing scenario having a high wake recovery rate. For that reason, it may be the case that the occurrence of merging wakes from the first and second row turbines can actually promote wake recovery after a downstream distance of 8D. Figure 5.29 shows the velocity contour from the top view for downstream spacing scenarios of 3D, 5D, 8D, 10D and 15D.

It can be observed at the spacing of the 3D scenario, the wakes from first and second row turbines completely merge together with the wake having a much wider shape with a greater reduction in velocity in the near wake region. However, the wake is also shorter in shape which indicates faster wake recovery. While, at the spacing of the 5D scenario, the wakes from the first row turbines are shown to have

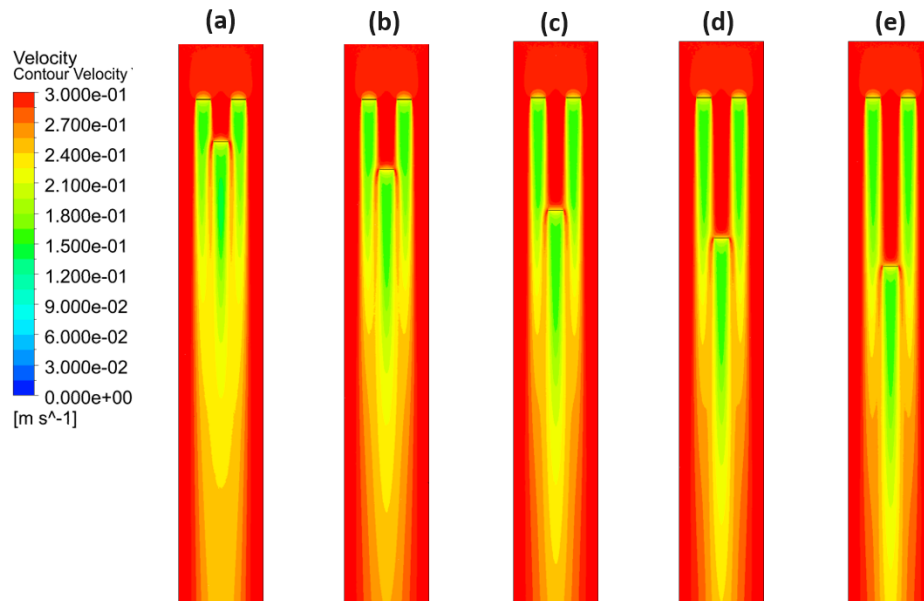


**Figure 5.29:** The centreline downstream velocity after the second row turbine at downstream spacing scenarios of 3D (a), 5D (b), 8D (c), 10D (d) and 15D (e).

“semi-merged” with the second row turbine’s wake, which resulted in the wake having a slimmer shape compared to the 3D spacing scenario and length similar to the 3D spacing scenario. This indicates faster wake recovery but this setting doesn’t experience a greater reduction in velocity in the near wake region. While for any spacing scenarios greater than 5D, the wake has shown to lightly merge or does not merge at all as shown in the velocity contour for spacing scenarios of 8D, 10D and 15D. Furthermore, the downstream wake shape and length are solely driven by the turbine of the second row turbine.

Figure 5.30 shows the velocity profile for the downstream spacing scenario of 3D, 5D, 10D and 15D at 5D downstream distance after the second row turbine. It can be seen that all downstream spacing scenarios have experienced similar reductions in velocity between a distance of 1 to -1, with the 3D spacing scenario having a greater reduction due to the merging of wakes from the first row of turbines. However, at a lateral distance greater than 1 and less than -1, the larger the downstream spacing scenarios, the smaller the reduction in velocity.

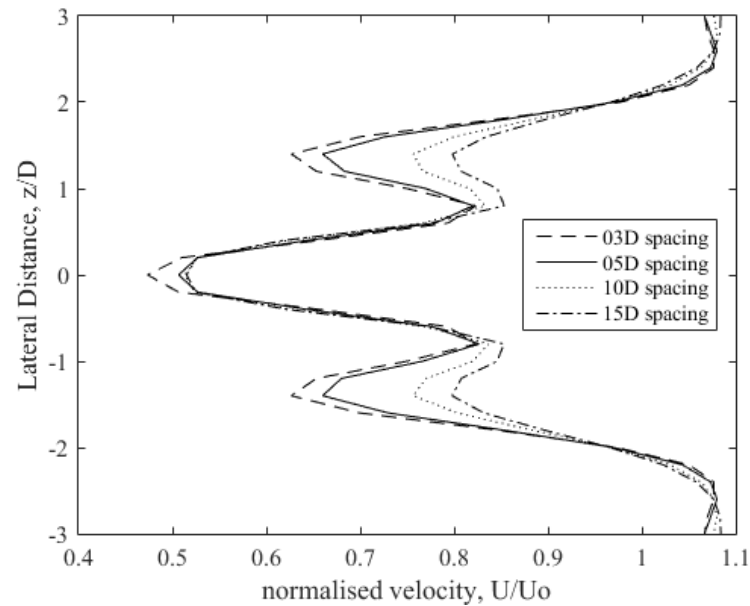
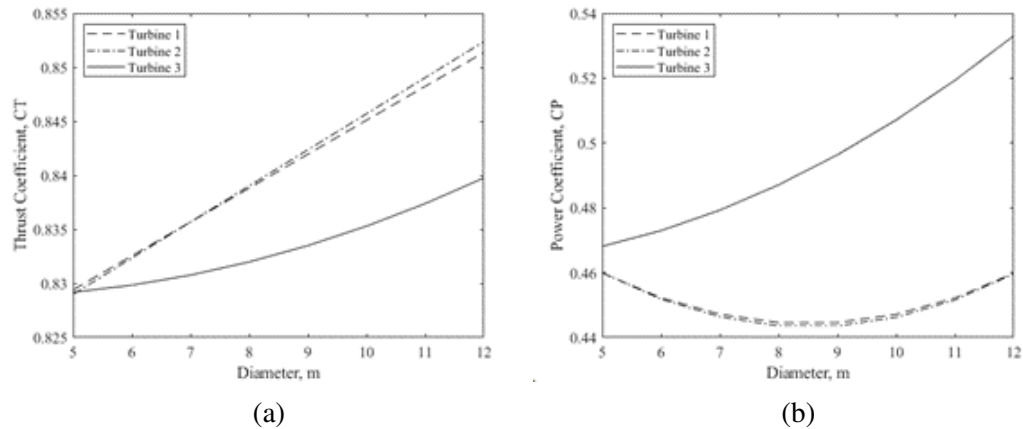


**Figure 5.30:** Velocity profile at 5D downstream distance after second row turbine for downstream spacing scenarios of 3D, 5D, 10D and 15D.

### 5.3.4 Turbine Size and Depth Investigation

#### Turbine Size Investigation

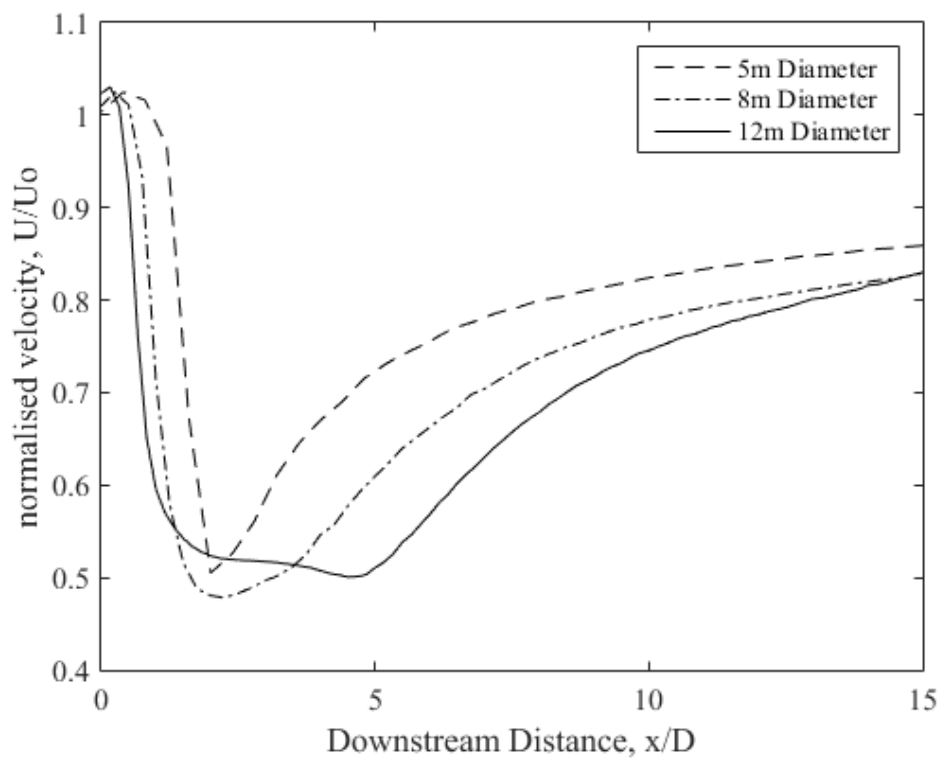
An investigation was conducted to study the effect of the turbine size on the performance of the turbine and the wake of the second row turbine, the distance between the first row and second row remains unchanged as turbine size is changed. Figure 5.31 shows the thrust coefficient and power coefficient as turbine size is increased from a diameter of 5m to 12m for the three turbines in a staggered layout at mid-depth with two turbines in the first row and one turbine in the second row. As observed in Figure 5.31, the thrust coefficient of turbines 1 and 2 (first row) increases linearly as the diameter of the turbine increases. While the thrust coefficient of turbine 3 (second row) increases exponentially as the diameter of the turbine increases overall turbine 3 has a smaller thrust coefficient than turbines 1 and 2. As shown in Figure 5.31, the power coefficient of turbine 3 (second row) increases exponentially as the diameter of the turbine increases. While the power coefficient of turbines 1 and 2 (first row) has a positive parabolic relationship as diameter increases with the minimum point occurring at a diameter of 8.5m, overall turbine 3 has a larger power coefficient than turbines 1 and 2.



**Figure 5.31:** Thrust coefficient (a) and power coefficient (b) of the three turbines in the staggered layout for diameter ranging from 5m to 12m.

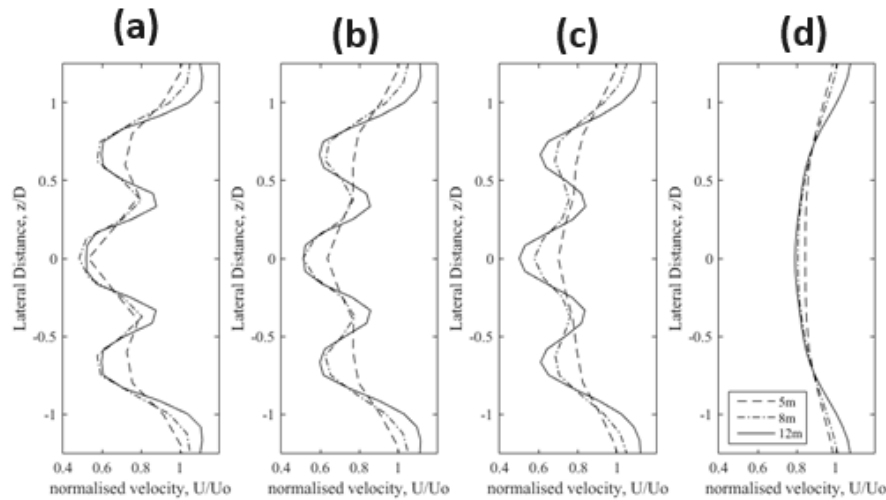
In an ideal situation, the thrust and power coefficient of turbines 1 and 2 (first row) should be constant regardless of diameter size. However, the study has shown that the power and thrust coefficient is not constant as the diameter increases because of the velocity profile of the water column. As the turbine size increases, the greater the effects of the velocity profile have on the thrust and power coefficient of the turbines. This also indicates that the depth at which the turbine is located has an impact on the thrust and power coefficient of the turbine.

Figure 5.32 shows the centreline downstream wake velocity of turbine 3 (second row) at mid-depth considering three different turbine diameters of 5m, 8m and 12m. It is observed that as turbine size increases, the velocity recovery decreases. As the 5m diameter turbine has the highest recovery and the 12m diameter turbine has the lowest recovery rate. As seen in Figure 5.32, the 5m diameter turbine experiences a sudden reduction in velocity from a downstream distance of  $0D$  to  $3D$  and the velocity starts to recover after a  $3D$  distance downstream. While the 12m diameter turbine experiences a sudden reduction in velocity from a downstream distance of  $0D$  to  $2D$ , the velocity continues to experience a much steadier reduction between  $2D$  to  $5D$  distance, and velocity started to recover after a  $5D$  distance downstream. Ergo, the smaller-size turbine has a shorter velocity reduction phase in the downstream wake than the larger-size turbine.



**Figure 5.32:** Centreline downstream velocity of Turbine 3 (second row) at mid-depth for turbine size of 5m, 8m and 12m.





**Figure 5.33:** Lateral velocity profile at mid-depth at downstream distances of 5D (a), 7D (b), 9D (c) and 25D (d) for turbine diameter of 5m, 8m, and 12m.

Figure 5.33 shows the lateral velocity profile at mid-depth for a turbine with a diameter of 5m, 8m, and 12m at downstream distances of 5D, 7D, 9D and 25D. It is shown that the 5m diameter turbine has a more rapid wake recovery in its lateral velocity profile compared to the 8m and 12m diameter turbine. Additionally, at a 9D downstream distance, the wake has been shown to recover to a normalised velocity of greater than 0.8. The lateral profile of the 8m and 12m diameter turbine has shown little difference in its 5D and 7D downstream lateral velocity profile; however, at the downstream distance of 9D, the 8m diameter turbine has shown to have a more rapid wake recovery than that of the 12m diameter turbine. At a downstream distance of 25D, all diameter size turbine shows little difference to each other and the lateral velocity profile is greater than the normalised velocity of 0.8. The difference in the recovery rate of the wake is greatly affected by the mixing rate of the wake from the first row with the second row of turbines. This can be further observed in the velocity contour as provided in Figure 5.34.

Figure 5.34 shows the top-view velocity contour for a turbine with a diameter of 5m, 8m and 12m. When keeping the distance between the first row and second row unchanged, the increase in turbine diameter size has been to have a great impact on the mixing of the downstream wake. It can be observed for a 5m diameter turbine, the wakes from first and second row turbines completely merge together, and the wake is shown to be shorter in shape which indicates the wake recovers

faster. While, for an 8m diameter turbine, the wakes from the first row turbines are shown to have “semi-merged” with the second row turbine’s wake in the near wake region and completely merge afterwards in the far wake region. Whereas, for a 12m diameter turbine the wakes from the first row turbines are shown to have only “semi-merged” with the second row turbine’s wake and did not completely merge afterwards in the far wake region. This also explains the similarities in the lateral velocity profile between the 8m and 12m diameter turbines at downstream distances of 5D and 7D as shown in Figure 5.33 because the wake only “semi-merges”. While at a downstream distance of 9D, the 8m diameter turbine has a more rapid velocity recovery than the 12m diameter turbine because the wakes from the 8m diameter turbine have merged but the 12m diameter turbine wakes do not merge at all.

### **Turbine Depth Investigation**

As mentioned in the turbine size study, the placement of the turbine at different depths would have an impact on the performance and downstream wake of the turbine. Accordingly, an investigation was conducted to study the effect of the depth position on the performance of the turbine and the wake of the second row turbine, the diameter of the turbine was kept at 10m. Figure 5.35 shows the thrust coefficient and power coefficient as depth position increases for the three turbines in a staggered layout with two turbines in the first row and one turbine in the second row. The normalised depth is measured from the surface to the seabed with 0 being at the surface and 1 being at the seabed.

As observed in Figure 5.35, the thrust coefficient of all turbines decreases exponentially as depth increases where the thrust coefficient of turbine 3 (second row) has a smaller thrust coefficient than turbine 1 and 2 (first row). The power coefficient of all turbines also decreases as depth increases with turbine 3 (second row) having a greater power coefficient than turbines 1 and 2 (first row). The change in power coefficient is fairly linear with respect to change in depth. While, the change in thrust coefficient follows an exponential progression with respect to change in depth. The change of thrust coefficient above a depth of 0.5 (mid-depth) has a slower rate of change when compared to the thrust coefficient below a depth of 0.5 which has a faster rate of change. Figure 5.36 shows the centreline downstream wake velocity of turbine 3 (second row) at three different depths of 0.25, 0.5 and 0.75.

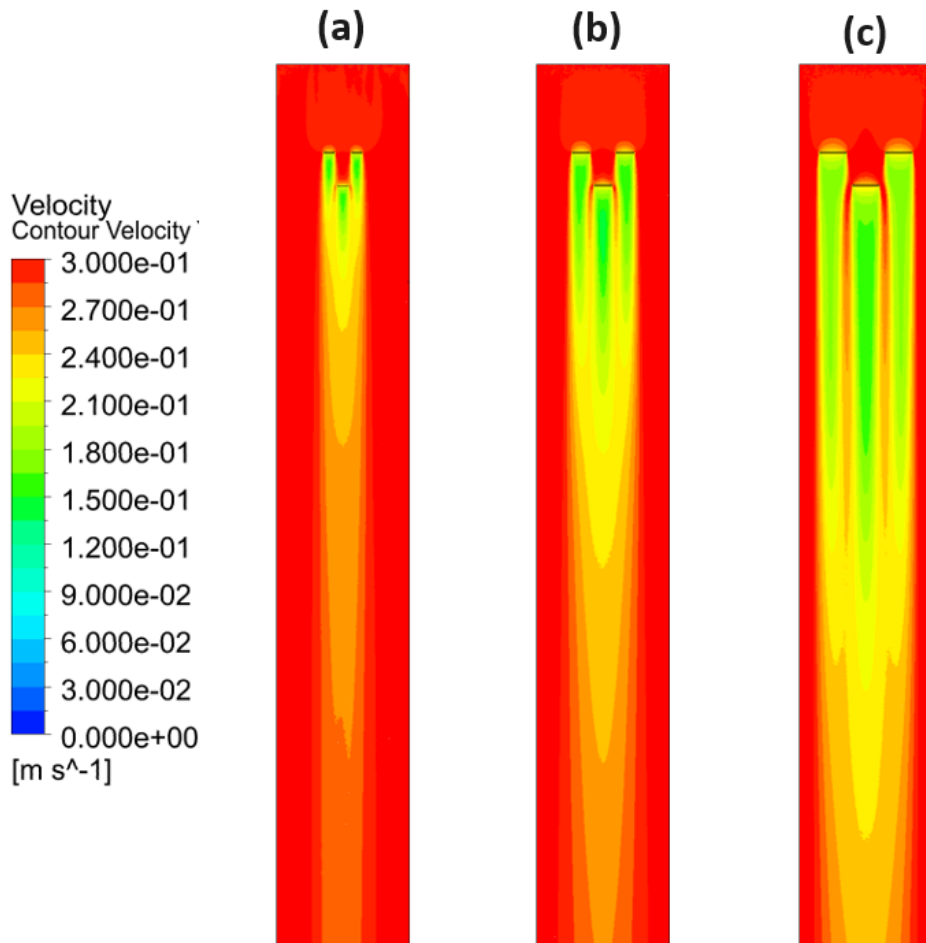


**Figure 5.34:** Velocity top-view contour of turbine diameter size: 5m (a), 8m (b) and 12m (c).

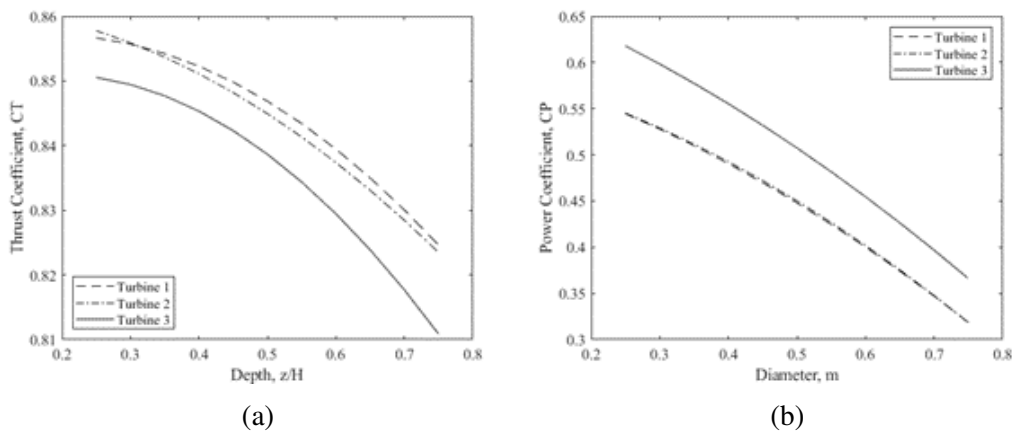


**Figure 5.35:** Thrust coefficient (a) and power coefficient (b) of all three turbines in a staggered layout at different depth placements.

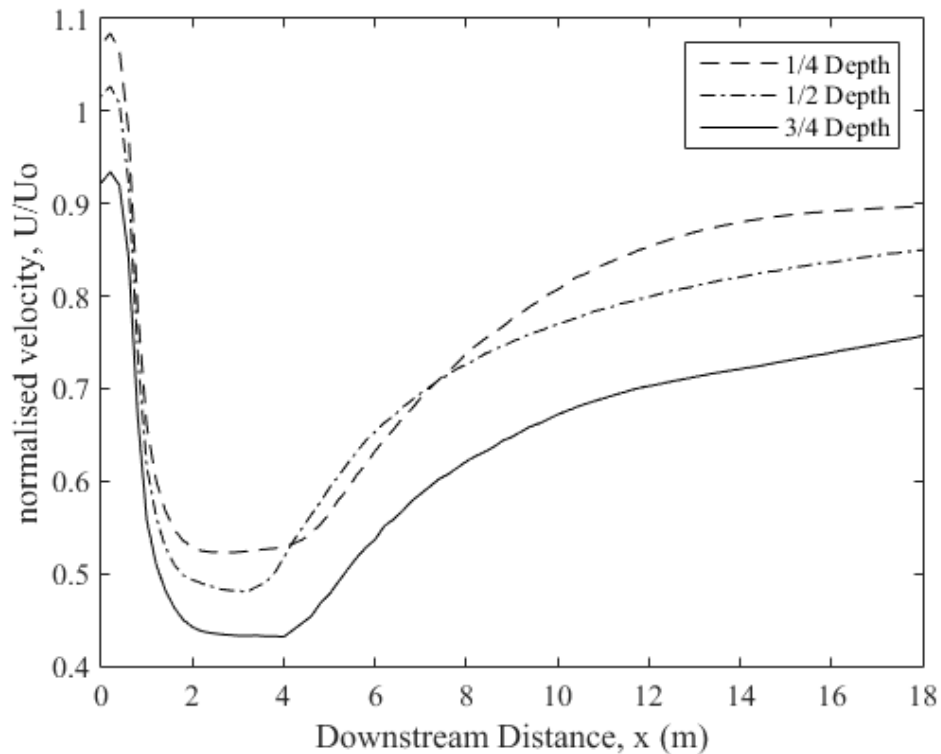


**Figure 5.36:** Centreline downstream velocity of Turbine 3 (second row) at mid-depth for turbine size of 5m, 8m and 12m.

It is observed that as the depth from the surface increases, the velocity recovery decreases. At a normalised depth of 0.25 the turbine has the highest recovery, and at the 0.75 depth the turbine has the lowest recovery rate. As shown in Figure 5.36, all turbine depths experience a sudden reduction in velocity from a downstream distance of 0D to 2D with a 0.25 normalised depth having the least velocity reduction and a 0.75 normalised depth having the most velocity reduction. The velocity continues to experience a much steadier reduction after 2D distance with a 0.25 normalised depth having the longest reduction phase lasting until 5D distance, while a 0.5 normalised depth develops the shortest reduction phase lasting until a 3D distance downstream. At the normalised depth of 0.25, the wake recovery starts at a 5D distance downstream; followed by the normalised depth of 0.75 where wake recovery starts at a 4D distance downstream; and then at a normalised depth of 0.5 the wake recovery starts at a 3D distance downstream. From the previous turbine size study, one of the key findings is the length of the reduction phase is related to

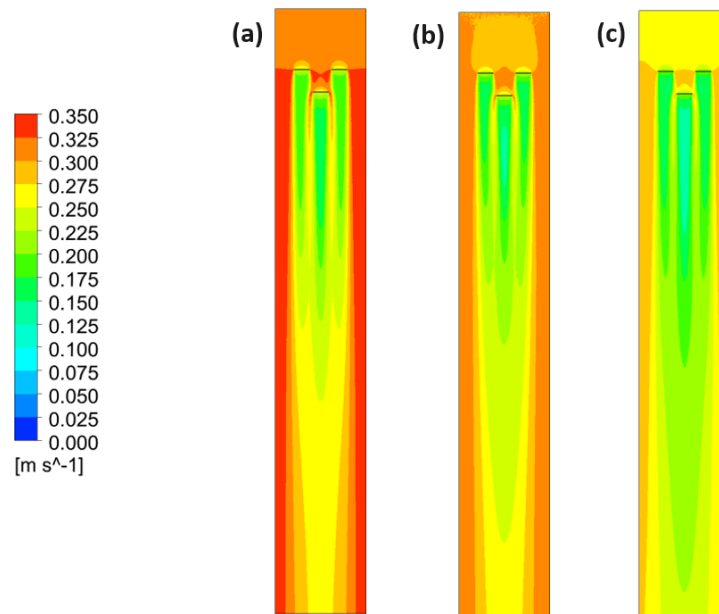


**Figure 5.37:** Velocity top-view contour of turbines at normalised depths: 0.25H (a), 0.50H (b) and 0.75H (c).

the mixing condition of wakes from the first row with wakes from the second row. Consequently, observing the velocity contour of the turbines at different normalised depths can aid in understanding this phenomenon as shown in Figure 5.37.

Figure 5.37 shows the velocity top-view contour for a turbine at a normalised depth of 0.25, 0.50 and 0.75. It was shown that the wakes at a normalised depth of 0.75 does not merge which indicates the wake would have a slower recovery rate. Also, the wakes at a normalised depth of 0.25 and 0.50 have “semi-merge”, where the contour shape at a normalised depth of 0.50 is shown to be shorter compared to a normalised depth of 0.25. Therefore, the wake at a normalised depth of 0.5 would have a greater wake recovery at distances before  $8D$  downstream compared to the wake at a normalised depth of 0.25.

On that account, the wake recovery would be affected by the availability of the ambient fluid outside the streamtube to mix with the wake. By observing the side-view velocity can help understand this phenomenon as shown in Figure 5.38. Figure 5.38 shows the velocity side-view contour for turbine 3 at a normalised depth of 0.25, 0.50 and 0.75. It is shown that at normalised depths of 0.25 and 0.75 due to the close proximity to the surface and seabed, there is less available ambient fluid to mix with

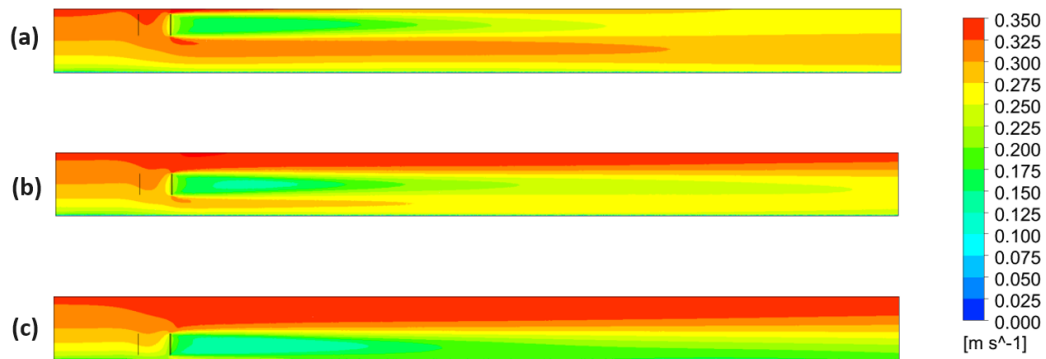


**Figure 5.38:** Centreline velocity side-view contour of turbine at normalised depths: 0.25H (a), 0.50H (b) and 0.75H (c).

the wake. While the wake at a normalised depth of 0.50 was ample ambient fluid to mix with the wake. As a result, the turbine's wake at a normalised depth of 0.50 has the shortest velocity reduction phase which only lasted from a distance of  $2D$  to  $3D$  as shown in Figure 35. The wake at a normalised depth of 0.75 has a shorter velocity reduction phase compared to the wake at a normalised depth of 0.25 due to the available ambient fluid velocity above the turbine at a normalised depth of 0.75 which is greater than the available ambient fluid velocity below the turbine at a normalised depth of 0.25. However, if a different diameter size turbine was used, the changes to the length of the velocity reduction phase would be different also. In the case of the smaller turbine evaluation, the effect of the velocity profile of the water column has a lesser impact on the wake recovery which results in the turbine at the depth near to the seabed experiencing a longer velocity reduction phase.

### 5.3.5 Summary

The lateral spacing of  $1.5D$  is the minimum allowable lateral spacing that allows for the deployment of third turbines in between the two turbines downstream. However, it is shown that at the lateral spacing of  $1.5D$ , the power and thrust of the two turbines were affected. Existing literature has suggested that for a consistence power and thrust on the turbine, a minimum of  $6D$  spacing is needed (Stallard et al. 2013). In a staggered layout with 3 turbines, the power and thrust of the 2 turbines upstream actually decrease with the introduction of a third turbine downstream. However, the power and thrust of the third turbine are greater than the 2 turbines upstream due

to the flow being accelerated by the upstream turbines. Furthermore, the 5D is the most optimum downstream distance for the second-row turbine in a staggered layout with 3 turbines giving a high thrust and power coefficient at the turbine while also providing good wake recovery due to the mixing of upstream turbine wake and downstream turbine wake. The greater the turbine size, the slower the recovery rate of the downstream turbine wake due to a greater influence from the vertical velocity profile. So a bigger size turbine would need a longer downstream distance for the wake to recover. Also, the depth placement position of the tidal current turbine should be less than the  $\frac{3}{4}$  depth distance from the surface to avoid the shear effect from the seabed, the closer the turbine is to the surface the greater the power and thrust on the turbine.

## 5.4 Array Turbine Model

This sub-chapter focussed on presenting the results of the developed turbine array model using an optimised tidal current turbine blade. The turbine (disk domain) in this sub-chapter has a diameter of 20m and a thickness of 0.1m. The sub-chapter presents an evaluation of the performance of an aligned and staggered layout array for a range of different domain conditions such as: ideal channel, headland and headland & island. A case study on the energetic performance of deploying the developed aligned and staggered layout array is detailed.

### 5.4.1 Array Configuration: Aligned vs Staggered

An investigation was carried out to evaluate the difference, in turbine power performance, between aligned and staggered tidal current turbine array layouts consisting of 12 turbines in an ideal tidal channel. Figure 5.39 shows the velocity top-view contour of the aligned and staggered array at mid-depth. In the aligned layout, it is shown that all turbines are in the wake of the previous row of turbines with the exception of the first row. This means that all turbines located after the first row interact with the wake of the previous row which results in the turbines after the first row having a decreased power output. Furthermore, since the turbines in each row are aligned, it greatly affects the wake recovery after interacting with each row. Before the wake from the first row of the turbine can further recover, it has to interact with the second row. Furthermore, the same happens with the wake after the second row of turbines resulting in the wake having a “staging” effect, this can be further observed when looking at a power output of each row of the turbine array as shown in Table 5.11. Whereas, in the staggered layout, it is observed that the turbines in the third and fourth rows are affected by the wake of the upstream turbines. The wake from the first and second rows has sufficient distance before interacting with the third and fourth turbine rows, therefore the wake has enough time to recover to an acceptable speed as shown in Figure 5.39. Furthermore, when the flow passes through the gap between turbines in the first row; it is observed that the flow actually accelerates slightly which slightly increases the power output of the second row turbine as provided in Table 5.11.

Figure tab:Ideal presents the total power and average power coefficient of each row of turbines for each tidal current turbine array layout. In the aligned layout array,



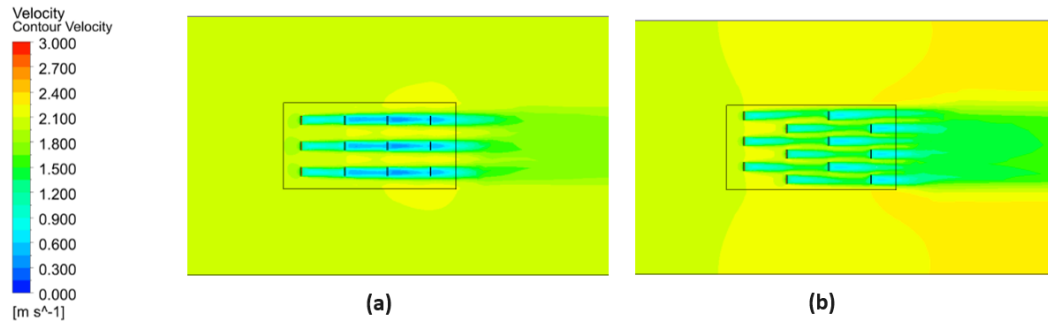


**Figure 5.39:** Mid-depth velocity top-view contour of aligned (a) and staggered (b) array layout.

**Table 5.11:** Power and average power coefficient of each row of turbines in the aligned and the staggered layout.

Layout		Row 1	Row 2	Row 3	Row4	Total
Aligned	Power (MW)	2.014	0.461	0.197	0.223	2.895
	Avg. CP	0.521	0.119	0.051	0.058	0.187
Staggered	Power (MW)	2.248	2.282	1.128	1.096	6.753
	Avg. CP	0.581	0.590	0.292	0.283	0.437

the first row of turbines has the highest total power and average power coefficient of 2.014MW and 0.521 respectively and the third row has the lowest total power and average power coefficient of 0.197MW and 0.051 respectively. The power output of the second row of turbines is roughly 5 times less than the first row and the power output of the third row of turbines is roughly 3 times less than the second row of turbines. This decrease is due to the wake not having enough downstream distance to recover and the wakes stack on each other. However, the power output of the fourth row of turbines is slightly greater compared to the third row of turbines, this is due to the accelerated flow of the fluid passing through the gap between turbines of each row, which aids in the wake recovery of the wake of third row turbines.

In the staggered layout array of tidal current turbines, the second row of turbines has the highest total power and average power coefficient of 2.282MW and 0.590 respectively and the fourth row has the lowest total power and average power coefficient of 1.096MW and 0.283 respectively. The total power of the third and fourth rows of turbines is roughly half of the total power of the first and second rows of turbines. The wake from the first and second rows of turbines have a longer distance to recover the flow velocity before interacting with turbines in the third and fourth

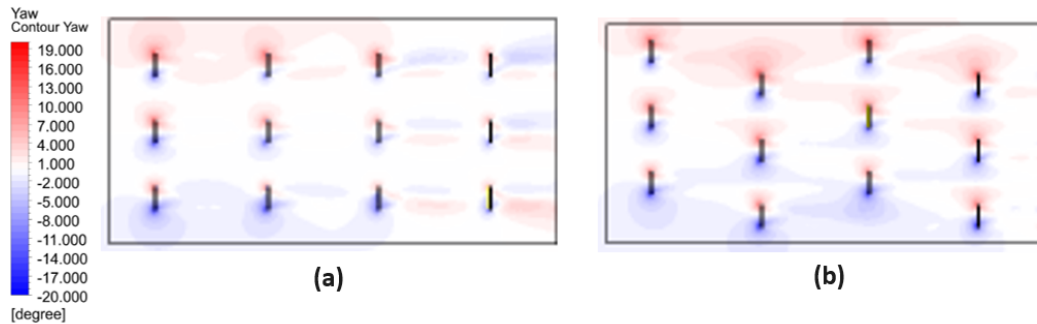


**Figure 5.40:** Direction of the incoming flow from horizontal when interacting with the array of tidal current turbines for aligned (a) and staggered (b) array layout.

rows compared to the aligned layout of tidal current turbines. Overall, the staggered layout has total power and an average power coefficient of almost 2.3 times greater than the aligned layout of tidal current turbines.

The performance of both arrays of tidal current turbines can be further increased by yawing the turbine into the flow. Figure 5.40 shows the angle of the incoming flow when interacting with the array of turbines. The direction of the incoming flow should be horizontal in an ideal channel, however the presence of the array of turbines affects the flow direction when interacting with the turbines. It is observed that when the flow approaches a turbine, it experiences a flow change in direction in both the clockwise and anti-clockwise direction especially at the tip of the turbine. As a result, a resultant angle should be obtained and the optimised yaw angle of the turbine. Table 5.12 and 5.13 show the yaw angle of each turbine in the aligned and staggered layout of tidal current turbines. In both the aligned and staggered array, the turbines located in the middle of each row (turbines 2, 5, 8 and 11) have little to no change in yaw angle. While turbines 1, 4, 7 and 10 are yawing in the clockwise direction and turbines 3, 6, 9 and 12 are yawing in the anti-clockwise direction in both aligned and staggered layout. Row 3 experiences the greatest yaw among all rows in both aligned and staggered layouts.

Figure 5.41 and 5.42 show the velocity top-view contour of the aligned and staggered array at mid-depth without yaw and with yaw. In Figure 5.41, it is observed that the aligned array layout with yaw greatly altered the wake of the second, third and fourth row of turbines. The yawing of turbines in the aligned array layout greatly improved its power performance, this can be further observed in Table 5.14.

**Table 5.12:** Yaw angle from the horizontal of each turbine in the aligned array layout.

Layout							
Row 1		Row 2		Row 3		Row 4	
Turbine	Yaw (deg)	Turbine	Yaw (deg)	Turbine	Yaw (deg)	Turbine	Yaw (deg)
1	-1.7	4	-5.1	7	-6.9	10	-3.6
2	0.1	5	0.1	8	0.0	11	-0.1
3	1.7	6	5.3	9	7.1	12	3.3

**Table 5.13:** Yaw angle from the horizontal of each turbine in the staggered array layout.

Layout							
Row 1		Row 2		Row 3		Row 4	
Turbine	Yaw (deg)	Turbine	Yaw (deg)	Turbine	Yaw (deg)	Turbine	Yaw (deg)
1	-1.4	4	-1.3	7	-3.3	10	-2.6
2	0.3	5	-0.3	8	1.3	11	-0.3
3	11.8	6	1.4	9	5.2	12	2.2

In Figure 5.42, it is observed that the staggered array layout with yaw slightly altered the wake of the third and fourth row of turbines. The yawing of turbines in the staggered array layout slightly improved its power performance, this can be further observed in Table 5.15.

Table 5.14 shows that the yawing greatly improves the overall power performance of the aligned layout array by 35.5% from 2.895MW to 3.925MW. Row 3 shows the highest increases in performance of 189.9% from 0.197MW to 0.571MW and

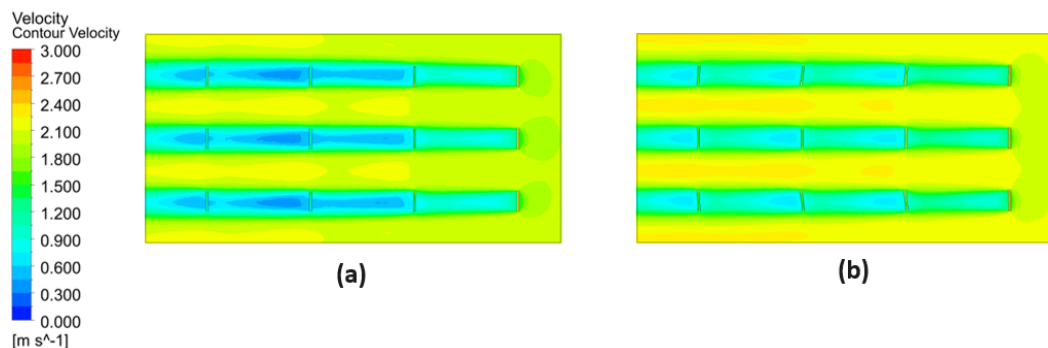


**Figure 5.41:** Mid-depth velocity top-view contour of aligned array layout without yaw (a) and yaw (b).

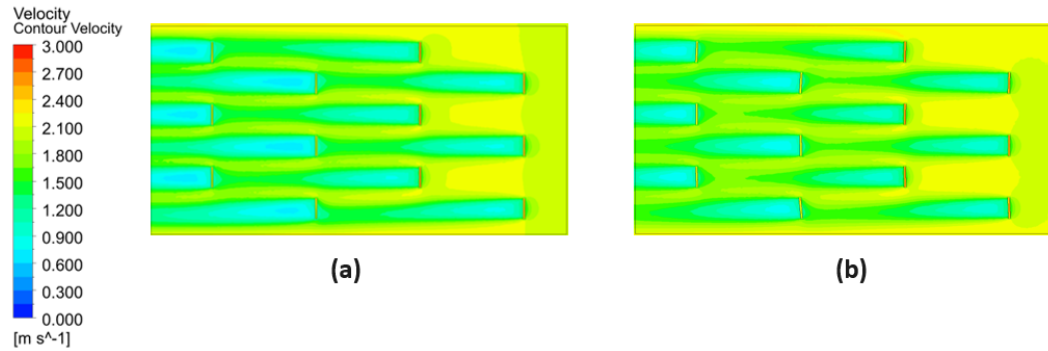


**Figure 5.42:** Mid-depth velocity top-view contour of aligned staggered layout without yaw (a) and with yaw (b).

**Table 5.14:** Power and average power coefficient of each row of turbines in aligned layout without yaw and with yaw.

Layout		Row 1	Row 2	Row 3	Row4	Total
Aligned	Power (MW)	2.014	0.461	0.197	0.223	2.895
	Avg. CP	0.521	0.119	0.051	0.058	0.187
Aligned (yaw)	Power (MW)	2.118	0.722	0.571	0.514	3.925
	Avg. CP	0.547	0.187	0.148	0.133	0.254
Difference		5.1%	56.7%	189.9%	129.9%	35.5%

Row 1 shows the lowest increases of 5.1% from 2.014MW to 2.118MW. Table 5.15 shows that the yawing improves the overall power performance of the staggered layout array by 12.0% from 6.753MW to 7.562MW. Row 3 and row 4 show the highest increases of 35.6% and 34.1% respectively and row 1 and row 2 show little to no changes in their power performance. The effect of yawing shows a greater impact on the aligned layout array when compared to the staggered layout array.

**Table 5.15:** Power and average power coefficient of each row of turbines in aligned layout without yaw and with yaw.

Layout		Row 1	Row 2	Row 3	Row4	Total
Staggered	Power (MW)	2.248	2.282	1.128	1.096	6.753
	Avg. CP	0.581	0.590	0.292	0.283	0.437
Staggered (yaw)	Power (MW)	2.282	2.282	1.529	1.469	7.562
	Avg. CP	0.590	0.590	0.395	0.380	0.489
Difference		1.5%	0.0%	35.6%	34.1%	12.0%

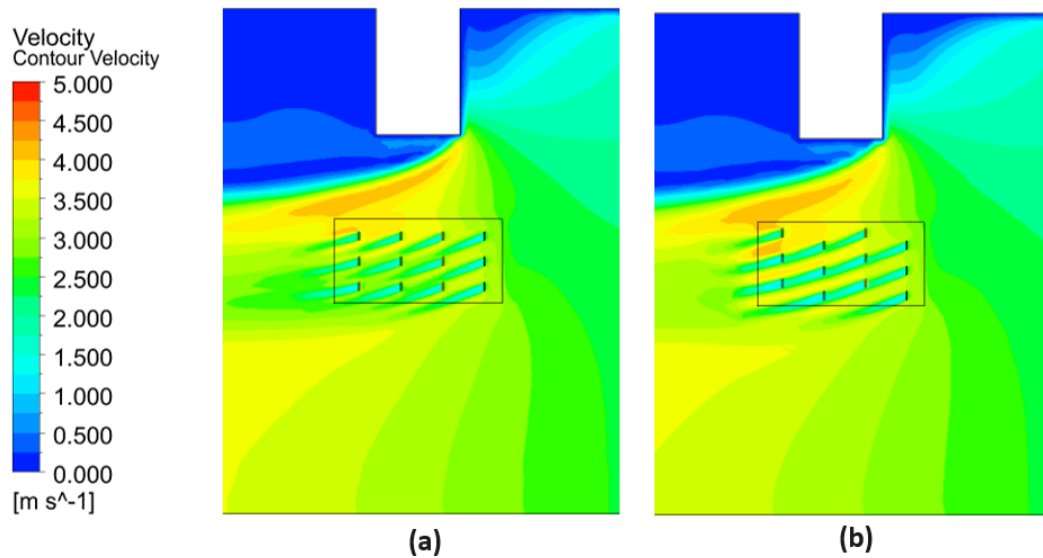


**Figure 5.43:** The velocity top-view contour of aligned layout array (a) and staggered layout array (b) in an idealised channel with headland at mid-depth.

#### 5.4.2 Idealised Tidal Channel: Headland (location and yaw)

An investigation was carried out to evaluate the effects of an idealised channel with a headland on the power performance of the turbines in an array. Figure 5.43 shows the velocity top-view contour of the aligned and staggered array placed near a headland at mid-depth. The rectangular box containing the 12 turbines is known as the turbine deployed area (TDA). The TDA is placed 200m away from the headland and the TDA also has a centre alignment with the headland.

In Figure 5.43, it is observed that the presence of the headland in the channel has greatly affected the flow direction and speed of the fluid. This change has also affected the wake of turbines in both the aligned and staggered layout array. In Figure 5.43, the wake developed in the aligned array was observed to be affected by the presence of the headland and the wake flow direction has changed causing the flow to move away from interacting with downstream turbines, which allows the wake to fully recover. As observed, the wakes from the first row of turbines have changed direction and avoided interacting with the second row turbines, which allows the wakes from the first row turbines to recover fully before interacting with the third row of turbines.

**Table 5.16:** Total power of each row of turbines in the aligned and staggered layout in an idealised channel with headland.

Layout					
Layout	Row 1	Row 2	Row 3	Row4	Total
Aligned	2.248	2.282	1.128	1.096	6.753
Staggered	2.282	2.282	1.529	1.469	7.562

In Figure 5.43, the wake developed in the staggered array was observed to be affected by the presence of the headland and the wake flow direction changed causing the flow to interact with the downstream turbines, which reduces both wake recovery and power performance. As observed, the wake from the first row of turbines has changed direction causing it to interact with the second row of turbines, which causes the wake to experience a “stacking” effect resulting in a further reduction in the wake velocity. Table 5.16 shows the total power of each row of turbines in the aligned and staggered layout array in an idealised channel with headland.

According to Table 5.16, the aligned layout array was shown to have a total power of 41.254MW, which is greater than the staggered layout array with a total power of 29.918MW. In the aligned layout array, row 1 has the lowest power of 8473.9kW because the incoming flow before the turbines in row 1 is not affected by the presence of the headland. However, the flow and wake after row 1 due to the presence of the headland has its flow velocity and direction affected which results in an increase in power performance of rows 2, 3 and 4; with row 4 having the highest power of 11488.9kW due to some of the turbines in row 4 experiencing the highest accelerated flow caused by the headland as shown Figure 5.43.

In the staggered layout array, row 1 has the highest power of 8473.9kW because the incoming flow before the turbines in row 1 is not affected by the presence of the headland. However, the flow and wake after row 1 due to the presence of the headland has its flow velocity and direction affected which results in a decrease in power performance of rows 2 and 3, with row 3 having the lowest power of 5864.5kW. Yet, row 4 does not follow the trend to continue decreasing in total power but increases to obtain a total power of 8103.5kW; this is due to some of the turbines in row 4 experiencing the highest accelerated flow caused by the headland as shown in Figure 5.43. Consequently, some investigations were needed to study how the

placement of the TDA would affect the power performance of both the aligned and staggered layout arrays. Two investigations were conducted, one on the effects of distance between TDA and headland on power performance and the other on the effects of TDA alignments on power performance.

### **Gap distance between headland and TDA**

An investigation on the array's power performance at 100m, 200m and 400m distance between TDA and headland was conducted. Figure 5.44 shows the velocity contour of the aligned and staggered array at various gap distances between the TDA and the headland. The Investigation did not place the TDA at a distance less than 100m from the headland to avoid interacting with the low velocity flow region caused by the headland.

In Figure 5.44, it is observed that the wake of the turbines is highly affected the nearer the TDA is to the headland. In the aligned layout array, at 100m distance the wake from the turbines from the first row and the second row has shown to interact with the downstream turbines, while the wake from the turbines from the third row has shown to not interact with the downstream turbines. Furthermore, the third and fourth rows were also observed to be in the accelerated flow zone caused by the headland. While at a 200m distance, the effects of the headland lessened greatly. Hence, the wake of the turbines experienced a significantly less change to its flow direction and speed; thus, the wake of the turbines will interact with the downstream turbines.

In the staggered layout array, at a 100m distance, the wake of turbines has been shown to interact with the downstream turbines, but at the same time the second, third and fourth rows were also observed to be in the accelerated flow zone caused by the headland. While at a 200m distance, the effects of the headland have lessened greatly. Hence, the wake of the turbines experienced a reduced change to its flow direction and speed; thus, the wake of the turbines was observed to partially interact with the downstream turbines. Table 5.17 and 5.18 show the total power of each row of turbines in the aligned and staggered layout arrays at various gap distances between the TDA and the headland.

From Table 5.17, when the gap distance between the TDA and the headland de-

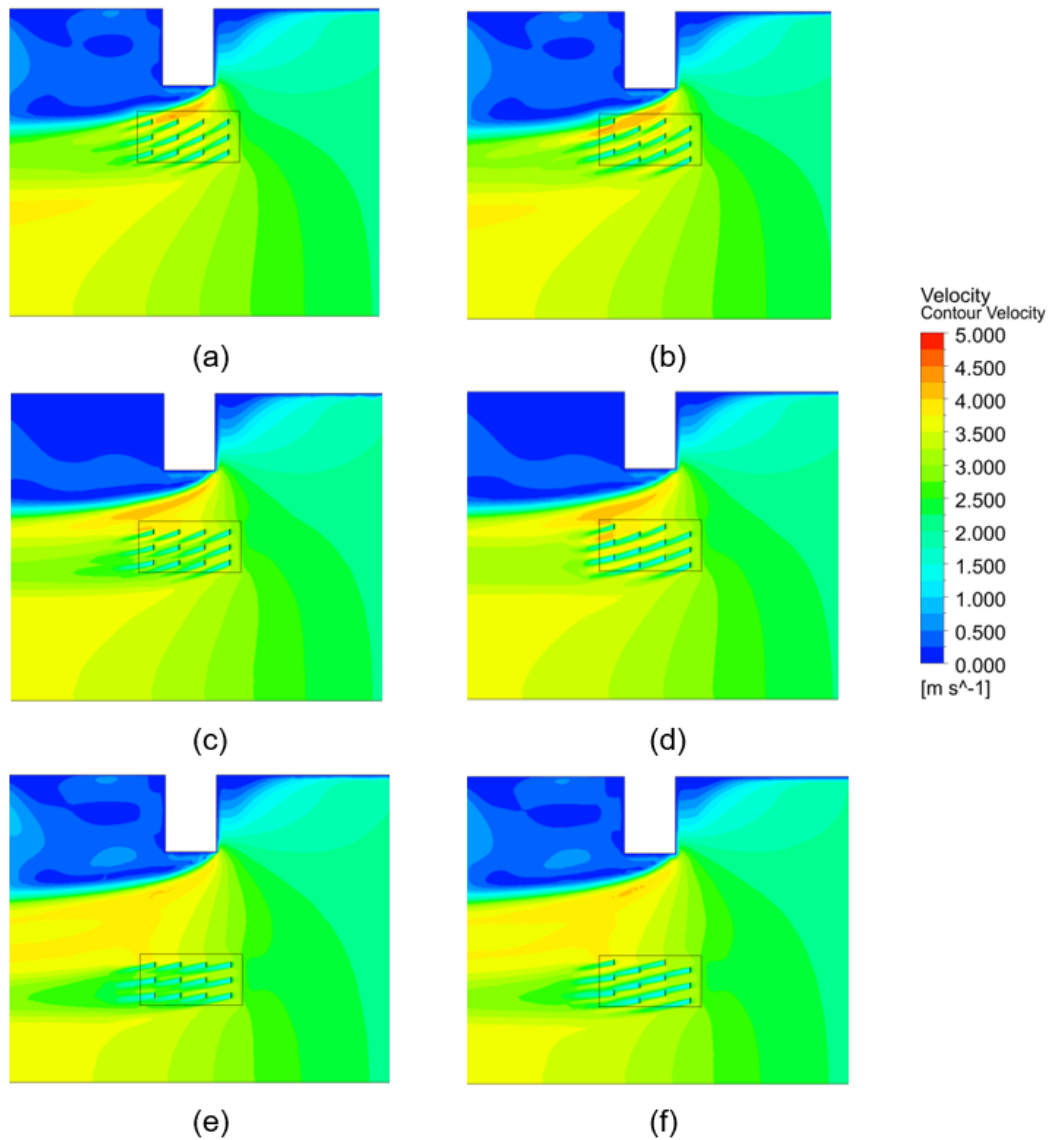


**Figure 5.44:** The velocity top-view contour of aligned (a, c and e) and staggered (b, d and f) layout array at mid-depth of various gap distance between TDA and headland: 100m (a and b), 200m (c and d) and 400m (e and f).

**Table 5.17:** Total power of each row of turbines in the aligned layout at various gap distances between the TDA and the headland.

Aligned Layout	Power (kW)					
	Row 1	Row 2	Row 3	Row 4	Total	Difference
Gap – 100 m	9146.2	10098.4	12685.8	14799.0	46.729	13.3%
Gap – 200 m	8473.9	10537.0	10754.2	11488.9	41.254	-
Gap – 400 m	7742.2	8092.6	8767.7	7753.9	32.356	21.6%



**Table 5.18:** Total power of each row of turbines in the staggered layout at various gap distances between the TDA and the headland.

Staggered Layout	Power (kW)					
	Row 1	Row 2	Row 3	Row 4	Total	Difference
Gap – 100 m	9288.4	12409.8	11776.1	10212.5	43.687	46.0%
Gap – 200 m	8610.9	7339.4	5864.5	8103.5	29.918	-
Gap – 400 m	7696.2	5877.8	5228.6	8831.3	27.634	7.6%

creases from 200m to 100m, the overall power of the aligned array increases 13.3%, from 41.254MW to 46.729MW. Row 3 and 4 show the highest increases in power due to being in the accelerated flow zone caused by the headland. When the gap distance between the TDA and the headland is increased from 200m to 400m, the overall power of the aligned array decreased 21.6%, from 41.254MW to 32.356MW. Since the effects of the headland have reduced at the 400m distance, it is observed that the total power of each row is roughly between the range of 7700kW to 8800kW.

From Table 5.18, when the gap distance between the TDA and the headland decreases from 200m to 100m, the overall power of the staggered array increased by 46.0%, from 29.918MW to 43.687MW. Rows 2, 3 and 4 show the highest increase in power due to being in the accelerated flow zone caused by the headland. When the gap distance between the TDA and the headland increased from 200m to 400m, the overall power of the aligned array decreased 7.6%, from 29.918MW to 27.634MW. Row 2 shows the highest decrease in power due to not being in the accelerated flow zone caused by the headland.

### **TDA and headland alignment**

An investigation of the array's power performance at the front, centre and back of the TDA alignments against headland was conducted. Figure 5.45 shows the velocity contour of the aligned and staggered array for a range of TDA alignment scenarios with the headland. The investigation was conducted at a gap distance of 200m between the headland and the TDA.

From Figure 5.45, it is observed that in the aligned layout array, the front alignment scenario takes the greatest advantage of the accelerated flow zone with at least three

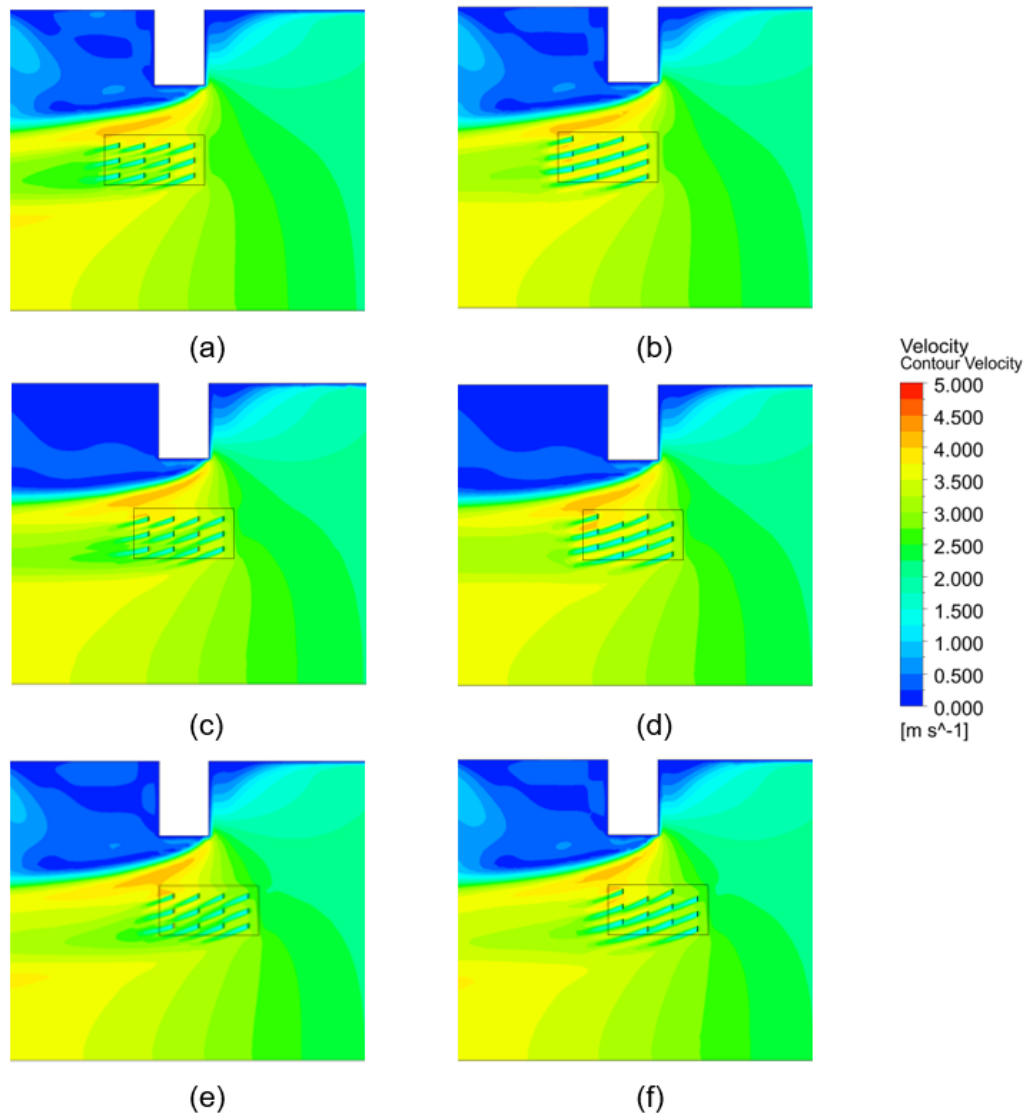


**Figure 5.45:** The velocity top-view contour of aligned (a, c and e) and staggered (b, d and f) layout array at mid-depth at different TDA and headland alignments scenarios: front (a and b), centre (c and d) and back (e and f).

**Table 5.19:** Total power of each row of turbines in the aligned layout at different alignments scenarios of the TDA with the headland.

Aligned	Power (kW)					
Layout	Row 1	Row 2	Row 3	Row 4	Total	Difference
Front	10615.4	12509.2	9658.3	10389.4	43.172	4.7%
Centre	8473.9	10537.0	10754.2	11488.9	41.254	-
Back	6610.8	8190.6	9242.9	11598.5	35.643	13.6%

**Table 5.20:** Total power of each row of turbines in the staggered layout at different alignments scenarios of the TDA with the headland.

Staggered	Power (kW)					
Layout	Row 1	Row 2	Row 3	Row 4	Total	Difference
Front	11002.6	6689.6	4021.0	7830.6	29.544	1.3%
Centre	8610.9	7339.4	5864.5	8103.5	29.918	-
Back	6735.7	5830.6	7187.7	10386.5	30.140	0.7%

rows gaining the advantage as compared to the centre alignment scenario, while the back alignment scenario takes the least advantage from of the accelerated flow zone with at least one row gaining the advantage when compared to the centre alignment scenario.

In the staggered layout array, the front alignment scenario seems to only benefit the first row, while the rest of the rows experience wake from the upstream turbines. Besides, the back alignment scenario seems to gain a better advantage over the staggered array due to the first and second rows experiencing fewer effects from the headland; this might mean that there will be a decrease in power but at the same time the wake from the turbines in first and second row affects the downstream turbine (third and fourth row) less. On top of that, the third and fourth rows were also located in the accelerated flow zone caused by the headland which greatly increases the power of the third and fourth rows. Table 5.19 and 5.20 show the total power of each row of turbines in the aligned and staggered layout array at different alignments scenarios of the TDA with the headland.

From Table 5.19, the overall power in an aligned layout array at the centre alignment scenario and front alignment scenario were 41.254MW and 43.172MW with 4.7% difference between them. In the front alignment scenario, rows 1 and 2 expe-

rience a significant increase in total power, but rows 3 and 4 experience a decrease in power when compared to the centre alignment scenario. Although rows 3 and 4 in the centre alignment scenario were placed in the accelerated flow zone caused by the headland, the power doesn't increase for the turbines in rows 3 and 4 due to the effects of the wake of the turbine from upstream (Rows 1 and 2).

From Table 5.19, the overall power in an aligned layout array at the centre alignment scenario and back alignment scenario were 41.254MW and 35.643MW with a 13.6% difference between them. In the front alignment scenario centre alignment against the headland to back alignment, all rows in the back alignment scenario experience a decrease in power when compared to the centre alignment scenario except for row 4, which experiences a slight increase in power. Rows 1 and 2 in the back alignment scenario experience a significant decrease in power because rows 1 and 2 are not placed in the accelerated flow zone caused by the headland. Furthermore, the wake produced by turbines in rows 1 and 2 has a significant impact on the downstream turbines (rows 3 and 4); thus the power performance of rows 3 and 4 will be affected. However, rows 3 and 4 in the back alignment scenario were placed in the accelerated flow zone caused by the headland meaning the wake recovers faster, which lessens the effects of the upstream wake on the turbines in rows 3 and 4.

From Table 5.20, the overall power in a staggered layout array at the centre alignment scenario and front alignment scenario were 29.918MW and 29.544MW with a 1.3% difference between them. Rows 2, 3 and 4 in the front alignment scenarios experienced a decrease in total power when compared to the centre alignment scenario except row 1 in the front alignment scenario which saw a significant increase in total power compared to the centre alignment scenario. Although all of the rows in the front alignment were placed in the accelerated flow zone caused by the headland only row 1 obtained the advantage. The presence of the headland has caused the flow direction and velocity to change, this change has caused the wake produced by the turbines in rows 1, 2 and 3 to be in line with the downstream turbines resulting in a decrease in the total power of row 2, 3 and 4.

From Table 5.20, overall power in a staggered layout array at the centre alignment scenario and front alignment scenario were 29.918MW and 30.140MW with 0.7%

difference between them. Rows 1 and 2 in the back alignment scenario experienced a decrease in power when compared to the centre alignment scenario, this is due to the turbines in rows 1 and 2 in the back alignment scenario not being placed in the accelerated flow zone caused by the headland. Although the wake caused by rows 1 and 2 in the back alignment scenario is in line with the downstream turbines (rows 3 and 4) which is expected to experience a decrease in power performance since rows 3 and 4 in the back alignment were situated in the accelerated flow zone caused by the headland, the effects from the upstream wake was greatly reduced. Furthermore, rows 3 and 4 in the back alignment scenario also benefit from the accelerated flow zone caused by the headland.

### **Turbine yawing**

An investigation on the effect of yawing of the power performance of the aligned and staggered array was conducted. Figure 5.46 shows the velocity contour of the aligned and staggered array layouts without yaw and with yaw. The investigation was conducted at a gap distance of 200m between the headland and the TDA with the aligned array using front alignment between the TDA and the headland, while the staggered array using back alignment between the TDA and the headland. From Figure 5.46, it is observed that there is little change experienced in the wake from turbines due to yawing. This can be due to the presence of headland having a greater effect on the wake and flow compared to the effect from yawing. Tables 5.21 and 5.22 show the total power of each row of turbines in the aligned and staggered layout arrays without yaw and with yaw.

From Table 5.21, the overall power of the aligned array increases by 0.8% with yawing from 43.172MW to 43.525MW. Rows 1, 2 and 3 show a slight increase in power, except for row 4 which shows a decrease in power. The reason row 4 experiences a decrease in power is due to the wake from upstream turbines creates a greater reduction in the wake velocity because of the effect of yawing. From Table 5.22, the overall power of the staggered array layout decreases by 0.8% with yawing from 30.140MW to 29.889MW. Rows 1 and 2 show an increase in power, while rows 3 and 4 show a decrease in power due to a reduction of wake velocity from yawing upstream turbines.

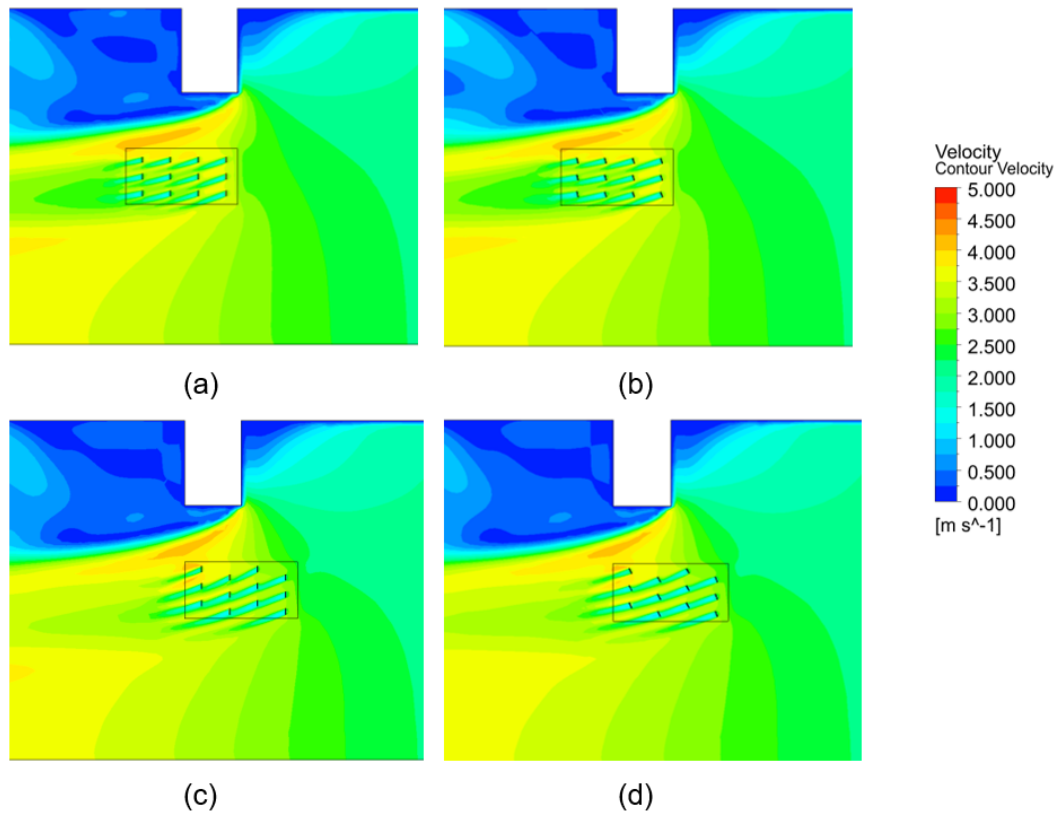


**Figure 5.46:** The velocity contour of aligned layout array without yaw (a) and with yaw (b); and the velocity contour of staggered layout array without yaw (c) and with yaw (d).

**Table 5.21:** Total power of each row of turbines in the aligned array without yaw and with yaw.

Aligned Layout	Power (kW)					
	Row 1	Row 2	Row 3	Row 4	Total	Difference
No Yaw	10615.4	12509.2	9658.3		10389.4 43.172	-
Yaw	10734.4	13355.7	9733.7	9701.4	43.525	0.8%

**Table 5.22:** Total power of each row of turbines in the staggered array without yaw and with yaw.

Staggered Layout	Power (kW)					
	Row 1	Row 2	Row 3	Row 4	Total	Difference
No Yaw	6735.7	5830.6	7187.7	10386.5	30.140	-
Yaw	6999.1	9467.3	6317.2	7105.1	29.889	0.8%

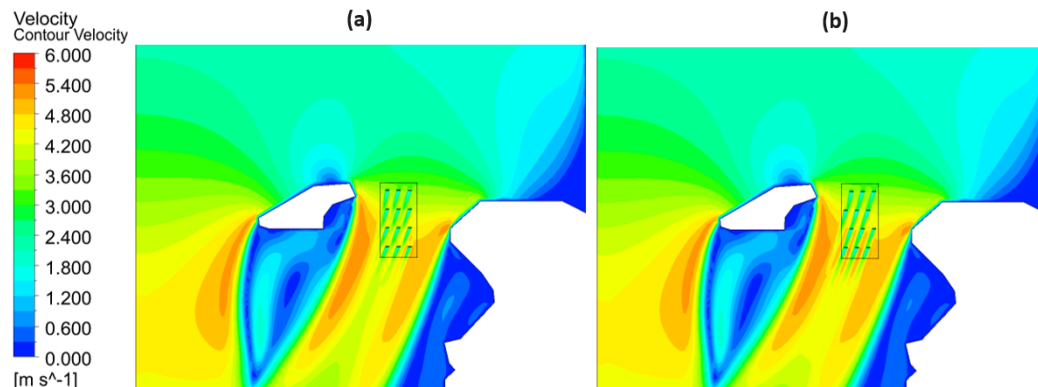


**Figure 5.47:** The velocity contour of the aligned (a) and the staggered (b) array layouts in an idealised channel with a headland and island at mid-depth.

### Summary

Overall, in an ideal channel with a headland, the aligned array performs better than the staggered array. The best distance between the TDA and the headland is 100m in both the aligned and the staggered array layouts. For the aligned array layout, the front alignment of the TDA with headland yields a better power performance. While for the staggered array layout, the back alignment of the TDA with the headland yields a better power performance. The presence of yawing from the turbine has little effect on the array layout's overall power performance.

### 5.4.3 Idealised Tidal Channel: Headland and Island

An investigation was carried out to evaluate the effects of an idealised channel with a headland and island on the power performance of a tidal current turbine array. Figure 5.47 shows the velocity top-view contour of the aligned and staggered array placed between a headland and island at mid-depth.

In Figure 5.47, it is observed that the presence of the headland and the island in the channel has greatly affected the flow direction and speed of the fluid flow field. This change has also affected the wake of turbines in both the aligned and staggered array layouts. For the aligned array layout, the wake produced by the turbines has a changed direction causing the turbine wakes to misalign with the downstream turbines which allows the turbine wakes to fully recover. In Figure 5.47, the turbine wake developed in the staggered array was observed to be affected by the presence

**Table 5.23:** Total power of each row of turbines in the aligned and the staggered array layouts between the headland and the island in an idealised channel.

Power (kW)					
Layout	Row 1	Row 2	Row 3	Row 4	Total
Aligned	11735.6	19082.0	22768.0	26888.0	80.474
Staggered	11729.5	11338.9	16763.7	15883.0	55.715

of the headland and the island and has changed the flow direction causing the flow to interact with the downstream turbines. This effectively reduces both wake recovery and power performance. Table 5.23 shows the total power of each row of turbines in the aligned and the staggered array layouts between headland and island in an idealised channel.

According to Table 5.23, the aligned array layout was shown to have a total power of 80.474MW, which is greater than the staggered array layout with a total power of 55.715MW. In the aligned array layout, the total power of each row increases moving from row 1 to row 4; this increase in power is due to the array being in the accelerated flow zone between the headland and the island. In the staggered array layout, all rows have a lower total power when compared to row 1 due to the wake being in line or partially in line with the downstream turbine.

An investigation of the effect of yawing on the power performance of the aligned and staggered array layouts was conducted. Figure 5.48 and 5.49 show the velocity contour of the aligned and staggered array layouts without yaw and yaw. From Figure 5.48, it is observed that there is little change to the wake from turbines due to yawing in the aligned array. This may be due to the flow between the headland and island having a greater effect on the wake and flow compared to the effect from yawing. Table 5.24 shows the total power of each row of turbines in the aligned array layout without yaw and with yaw. From Table 5.24, the overall power of the aligned array layout increases by 2.0% with yawing, from 80.474MW to 82.059MW. Rows 1, 2 and 3 show a slight increase in power, except for row 4 which shows a slight decrease in power. The reason row 4 experiences a decrease in power is due to the wake velocity reduction from the upstream turbines due to yawing.

In the staggered array layout, the TDA was rotated 20 degrees clockwise and yaw



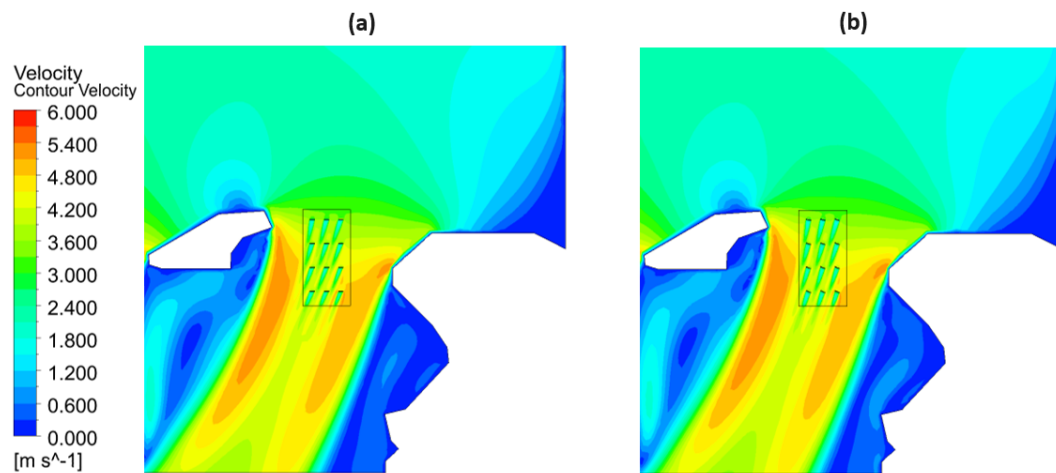


**Figure 5.48:** The velocity contour of the aligned array layout without yaw (a) and with yaw (b) between a headland and an island in an idealised channel.

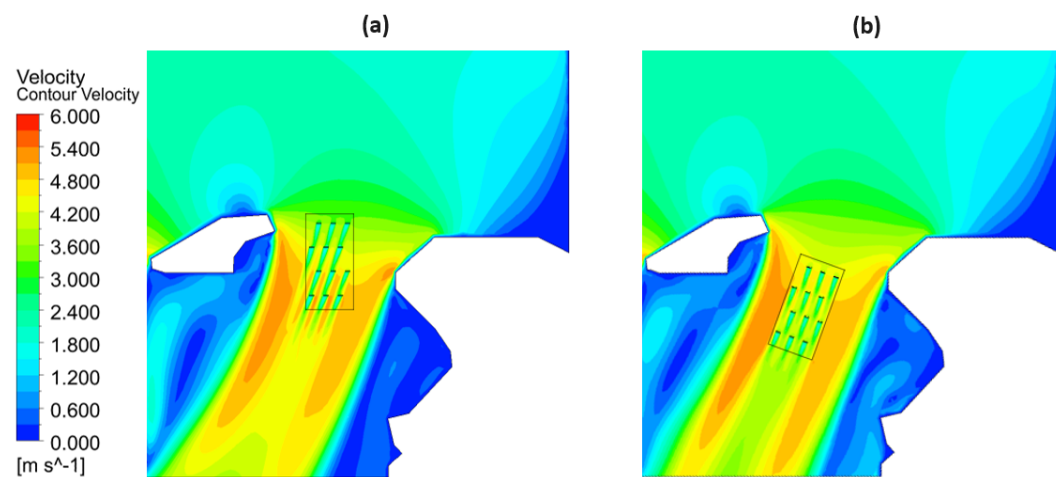


**Figure 5.49:** The velocity contour of the staggered array layout without yaw (a) and with yaw (b) between a headland and an island in an idealised channel.

**Table 5.24:** Total power of each row of turbines in the aligned array layout without yaw and with yaw between a headland and an island in an idealised channel.

Aligned	Power (kW)					
Layout	Row 1	Row 2	Row 3	Row 4	Total	Difference
No Yaw	11735.6	19082.0	22768.0	26888.0	80.474	-
Yaw	12305.5	20217.0	23500.5	26036.0	82.059	2.0%

**Table 5.25:** Total power of each row of turbines in the staggered array layout without yaw and with yaw between a headland and an island in an idealised channel.

Staggered	Power (kW)					
Layout	Row 1	Row 2	Row 3	Row 4	Total	Difference
No Yaw	11729.5	11338.9	16763.7	15883.0	55.715	-
Yaw	22293.0	29534.3	22138.9	19833.8	93.800	68.4%

was also applied. From Figure 5.49, it is observed that there is a significant change to the wake from turbines due to yawing and rotation of the TDA in the staggered array layout. The wakes from the turbines in the staggered array layout were shown to avoid being in line with downstream turbines which allows the wake to recover fully and thus increase the power performance. Table 5.25 shows the total power of each row of turbines in the staggered layout array without yaw and with yaw. From Table 5.25, the overall power of the staggered array layout increased 68.4% with yawing and rotation of TDA, from 55.715MW to 93.8MW. All rows in the staggered array layout experience a huge increase in the total power performance.

### Summary

Overall, in an ideal channel with a headland and island, yawing of the turbines has been shown to increase the total power performance of both the aligned and the staggered array layouts. The staggered array with yawing and rotated TDA can achieve a total power bigger than the aligned array layout with yawing.

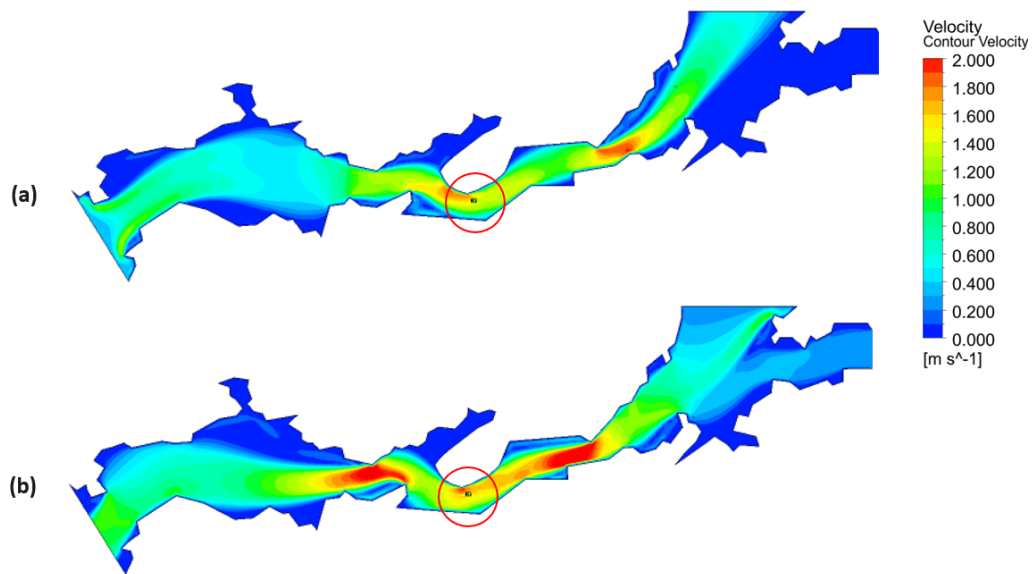


**Figure 5.50:** The velocity top-view contour of turbine array layout deployed in the Shannon Estuary at peak spring tide during flooding (a) and ebbing (b) at mid-depth.

#### 5.4.4 Case Study: Shannon Estuary

Both the aligned and the staggered layout arrays with yawing were deployed in the Shannon Estuary as shown in Figure 5.50. Figure 5.50 shows the velocity contour of the turbine array deployed in Shannon Estuary at peak spring tide during flooding and ebbing. The array is deployed at the estuary in a narrow channel near a headland, this location is ideal for capturing the accelerated flow during both flooding and ebbing tide. Figure 5.51 and 5.52 show the zoom-in view of the velocity contour of the aligned and the staggered array layouts at peak spring tide during flooding and ebbing.

In Figure 5.51, it is observed that during flooding, the wake produced by the turbines in the yaw-aligned array layout was in line with the downstream turbines particularly the wake of the first row of turbines which greatly affected the second row of turbines. The wake from the turbines in the third and fourth rows experience the greatest change in the direction, therefore the wake is less in line with the downstream turbines. During ebbing, the wake produced by the turbines in a yaw-aligned array layout was less in line with the downstream turbines. Resulting in a decrease in power performance in the downstream turbines within the array of turbines.

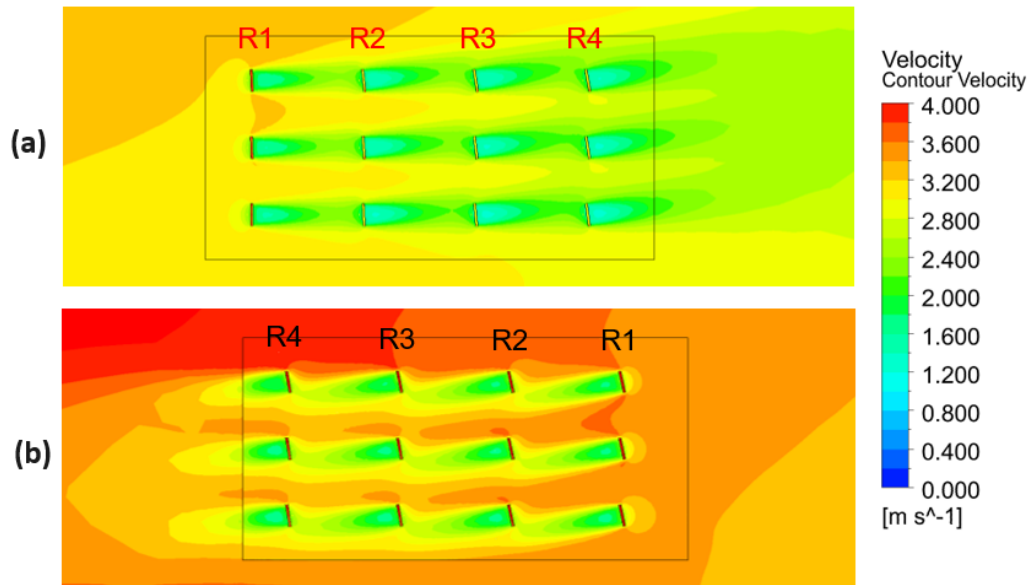


**Figure 5.51:** The velocity top-view contour of a yaw-aligned array at peak spring tide during flooding (a) and ebbing (b) at mid-depth.

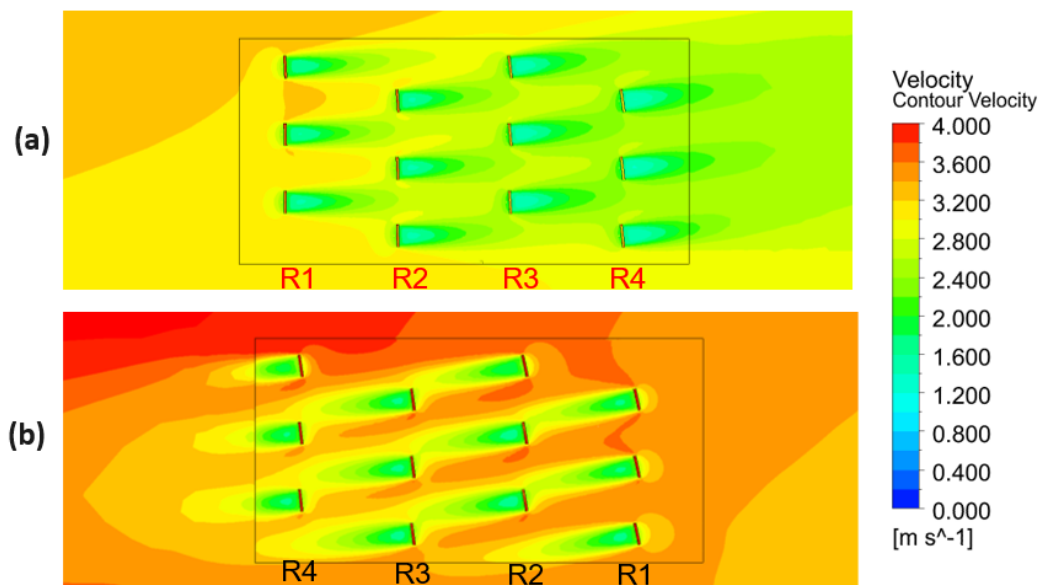


**Figure 5.52:** The velocity top-view contour of a turbine array layout deployed in Shannon Estuary at peak spring tide during flooding (a) and ebbing (b) from top view at mid-depth.

In Figure 5.52, it is observed that during the flood tide, the wake produced by the turbines in the yaw-aligned array layout was all out of line with the downstream turbines. Hence, the wake from the upstream turbines will have little effect on the power performance of the downstream turbines. During the ebb tide, some of the wake produced by the turbines in the yaw-aligned array was in line with the downstream turbines. Hence, some of the downstream turbines will experience a decrease in power performance, especially the turbines in the second and third row of the array layout. Table 5.26 shows the total power of each row of turbines in the aligned and staggered array layouts at peak spring tide during flood and ebb.

From Table 5.26, the staggered array layout provides a 16.5% higher power output than the staggered array layout during flooding and a 7.8% higher power output during ebbing. During the flood tide in the aligned array layout, it is observed that row 1 has a total power of two times greater than rows 2, 3 and 4; this is because the wake from the upstream turbines is in line with the downstream turbines resulting in a decrease in power performance in the downstream turbines. While in the staggered array during the flood tide, it is observed that rows 1 and 2 have a total power output greater than rows 3 and 4 because the wake from rows 1 and 2 has a direct effect on the power output of rows 3 and 4.

During the ebb tide, the aligned array has shown to have a high power performance in each row especially as the row number increases from 1 to 4, the total power output of each row increases also. This is a result of the downstream row being located in a region with a higher fluid flow speed. While in the staggered array layout during flooding, it is observed that rows 1 and 4 have a total power output greater than rows 2 and 3 because the wake from the upstream turbines is in line with some of the turbines in rows 2 and 3; thus, reducing the power output.

An investigation was conducted to evaluate the power performance of a normal actuator disk, the modified disk developed in this thesis and the modified disk with yaw utilised in the array deployed in the Shannon estuary at peak spring tide during flooding and ebbing. Table 5.27 and 5.28 presented the total power of each row of turbines in the aligned and staggered array layouts at peak spring tide during the flood and ebb for the actuator disk model, modified disk model, and yaw-modified disk model.

**Table 5.26:** Total power of each row of turbines in the aligned and staggered array layouts at peak spring tide during flood and ebb.

Power (kW)							
Tide	Layout	R1	R2	R3	R4	Total	Diff.
Flood	Aligned	8.69	4.9	4.51	4.43	22.53	-
	Staggered	8.1	7.41	5.69	5.05	26.25	16.5%
Ebb	Aligned	10.94	11.7	12.04	12.3	46.97	-
	Staggered	11.76	9.96	10.3	11.28	43.31	7.8%

**Table 5.27:** Total power of each row of turbines in the aligned array layout at peak spring tide during flood and ebb for the actuator disk model, modified disk model, and yaw-modified disk model.

Aligned Layout - Power (kW)							
Tide	Disk	R1	R2	R3	R4	Total	Diff.
Flood	Actuator	8.77	5.02	4.65	4.63	23.07	2.4%
	Modified	8.69	4.90	4.51	4.43	22.53	-
	Modified (yaw)	8.67	4.92	4.57	4.57	22.73	0.9%
Ebb	Actuator	10.91	11.66	12.01	12.27	46.84	0.3%
	Modified	10.94	11.70	12.04	12.30	46.97	-
	Modified (yaw)	10.97	11.74	12.05	12.33	47.10	0.5%

From Table 5.27, in the aligned array layout during the flood tide, the actuator disk model provides a 2.4% greater power output than the modified disk model with a tidal current turbine array total power of 23.07MW and 22.53MW respectively. During the ebb tide, the actuator disk model provides a 0.3% smaller power output than the modified disk model with a tidal current turbine array total power of 46.84MW and 46.97MW respectively. The actuator disk model was shown to over-predict the power of the turbines compared to the modified disk model in an aligned array layout during flooding and slightly underpredict the power of the turbines when compared to the modified disk model in an aligned array layout during ebbing.

Additionally, from Table 5.28 in the staggered array layout during the flood tide, the actuator disk provides a 2.8% greater power output than the modified disk model with a tidal current turbine array total power of 26.98MW and 26.25MW respectively. During the ebb tide, the actuator disk provides 0.7% greater power output than the modified disk model with a tidal current turbine array total power of 43.60MW and 43.31MW respectively. The actuator disk model in a staggered array

**Table 5.28:** Total power of each row of turbines in the staggered array layout at peak spring tide during flood and ebb for the actuator disk model, modified disk model, and yaw-modified disk model.

Staggered Layout - Power (kW)							
Tide	Disk	R1	R2	R3	R4	Total	Diff.
Flood	Actuator	8.09	7.41	6.42	5.05	26.98	2.8%
	Modified	8.10	7.41	5.69	5.05	26.25	-
	Modified (yaw)	8.20	7.50	5.78	5.13	26.63	1.4%
Ebb	Actuator	11.67	10.34	10.52	11.07	43.60	0.7%
	Modified	11.76	9.96	10.30	11.28	43.31	-
	Modified (yaw)	11.75	9.97	10.33	11.28	43.33	0.1%

layout was shown to overpredict the power of the turbines compared to the modified disk model during flooding and it slightly overpredicts the power output of the turbines when compared to the modified disk model during ebbing. The normal actuator disk model has a constant porosity and resistance coefficient regardless of the change in velocity (and radial change in disk from BEM), unlike the modified disk model which incorporates the change in velocity and radial change in the disk and includes the BEM theory method. Hence, the modified disk model is more likely to predict the turbine power and downstream wake of a tidal current turbine array in the Shannon Estuary when compared to the standard actuator disk model.

Applying yawing to the modified disk model can improve the power prediction of the tidal current turbines as shown in Table 5.27 and 5.28. In the aligned array layout during the flood tide, the effect of yawing provides an increase on the modified disk model's total tidal current turbine array power by 0.9%, from 22.53MW to 22.73MW. While during the ebb tide, the effect of yawing provides an increase on the modified disk model's total tidal stream turbine array power by 0.5%, from 46.97MW to 47.10MW. In the staggered array layout during the flood tide, the effect of yawing provides an increase on the modified disk model's total tidal current turbine array power by 1.4%, from 26.25MW to 26.63MW. While during the ebb tide, the effect of yawing provides an increase on the modified disk model's total tidal current turbine's array power by 0.1%, from 43.31MW to 43.33MW. It is observed that the yawing effect only slightly increases the overall tidal current turbine array total power with a greater increase in power experienced during the flooding phase of the tidal flow.

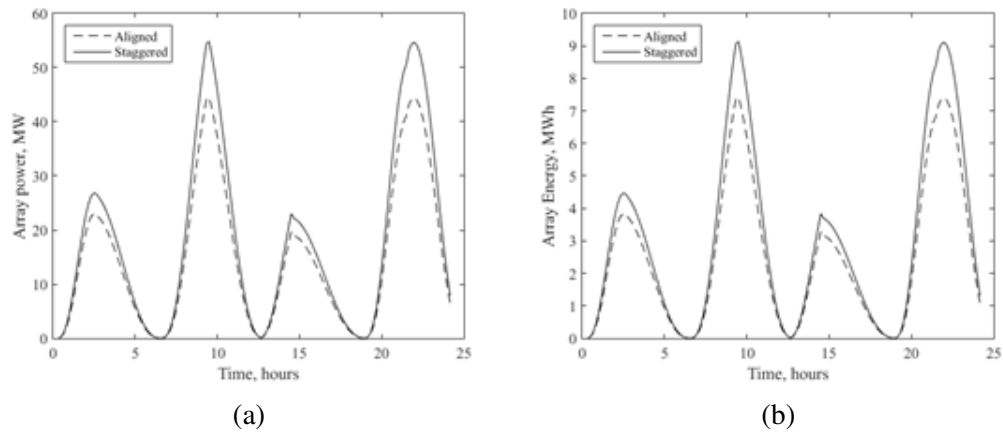


**Figure 5.53:** The tidal current turbine array power (a) and tidal current turbine array energy output, calculated in 10-minute intervals, (b) for aligned and staggered array layouts for a day during spring tide.

Both the yaw-aligned and yaw-staggered array layouts developed have been deployed in the Shannon Estuary to determine the total tidal current turbine array power output and the array energy in 10-minute intervals at different tidal speeds. Figure 5.53 and 5.54 shows the tidal current turbine array power and the tidal current turbine array energy in 10-minute intervals for the aligned and staggered array layouts in a day during spring and neap tide. It is observed that the spring tide overall has a higher power output and energy output when compared to the neap tide. Also, the ebb tide phase outputs higher power and energy than the flood tide phase.

In Figure 5.53 during spring tide, the maximum power produced by the aligned tidal current turbine array during the flood phase is 44.456MW and during the ebbing phase is 22.70MW. This corresponds to a maximum tidal current turbine array energy output calculated in 10-minute intervals of 7.424MWh and 3.797MWh respectively. While the maximum power produced by staggered array layout during the flood phase is 44.830MW and during the ebb phase, at spring tide, is 26.559MW which corresponds to a maximum energy output of the tidal current turbine array, calculated in 10-minute intervals, of 8.705MWh and 4.427MWh respectively.

In Figure 5.53 during neap tide, the maximum power produced by aligned array layout during the flood phase is 8.090MW and during the ebb phase is 4.480MW



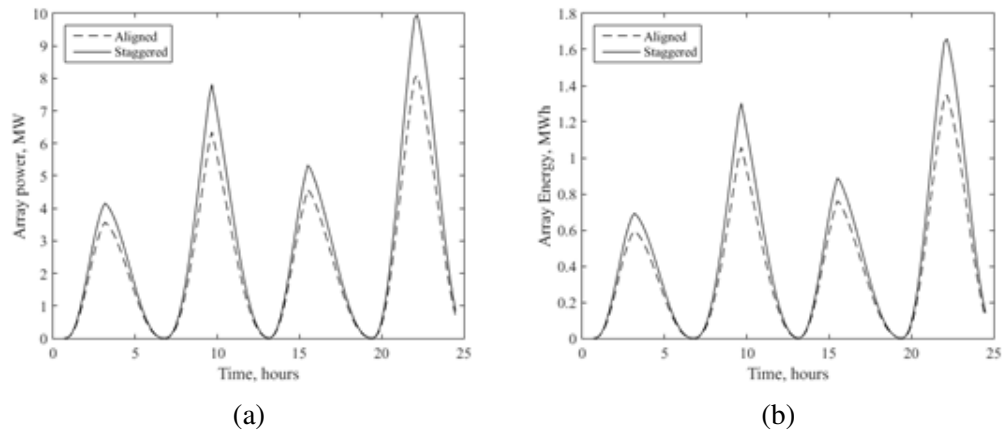


**Figure 5.54:** The tidal current turbine array power (a) and tidal current turbine array energy output, calculated in 10-minute intervals, (b) for aligned and staggered array layouts for a day during neap tide.

which corresponds to a maximum energy output of the tidal current turbine array, calculated in 10-minute intervals, of 1.348MWh and 0.747MWh respectively. While the maximum power produced by staggered array layout during the flood phase is 9.841MW and during the ebb phase, at spring tide, is 5.221MW which corresponds to a maximum energy output of the tidal current turbine array, calculated in 10-minute intervals, of 1.660MWh and 0.870MWh respectively.

Figure 5.55 shows the tidal current turbine array power for aligned and staggered array layouts for a lunar month (28 days). The staggered array layout was shown to have an overall total power output higher than that of the aligned array layout, the fluctuation of the power follows the same fluctuation pattern as the change of tidal speed in a lunar month.

Table 5.29 shows the total energy output of the tidal current turbine array for a day during spring and neap tide for aligned and staggered array layouts. During the spring tide, the aligned array layout has a total energy output of 361.20MWh and the staggered array layout has a total energy output of 436.78MWh. The staggered array layout provides 20.9% additional energy when compared to the aligned array layout during spring tide. While during the neap tide, the aligned array layout has a total energy output of 56.25MWh and the staggered array layout has a total energy output of 67.83MWh. In this case, the staggered array layout provides 20.6% additional

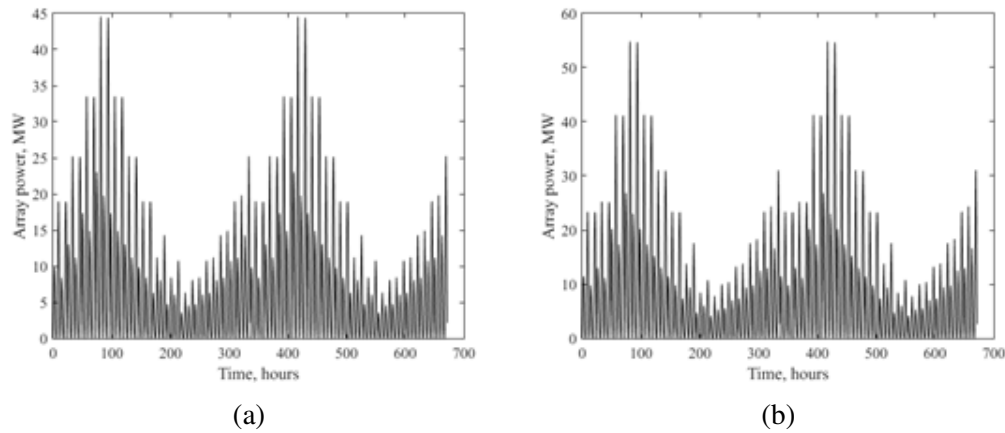


**Figure 5.55:** The tidal current turbine array power in a lunar month for the aligned array layout array (a) and the staggered array layout (b).

**Table 5.29:** Total array energy in a day during spring and neap tide for the aligned and the staggered array layouts.

Layout	Spring Tide		Neap Tide	
	Total Array Energy (MWh)	Diff. (%)	Total Array Energy (MWh)	Diff. (%)
Aligned	361.20	-	56.25	-
Staggered	436.78	20.9%	67.83	20.6%

energy when compared to the aligned array during spring tide.

Figure 5.56 shows the cumulative energy outputted, in a day during spring tide and neap tide, for the aligned and the staggered array layouts. The staggered array layout was observed to capture energy more efficiently when compared to the aligned array layout during both the spring and neap tide. From Figure 5.56, in a single day there are two high energy capture phases (between 8.5 to 11 hours and 20.5 to 23 hours) and two low energy capture phases (between 2 to 4.5 hours and 14.5 to 17 hours) during both the spring and neap tide. The high energy capture phase corresponds to the ebb tide and the low energy capture phase corresponds to the flood tide. It is observed that the low energy capture phase during neap tide has a higher capture rate compared to during spring tide. Figure 5.57 shows the cumulative energy outputted for the aligned and staggered array layouts. From Figure 5.57, in a lunar month there are two high energy capture phases (between 0 to 6 days and 14 to 20 days) and two low energy capture phases (between 7 to 13 days and 21 to 27 hours). The high energy capture phase corresponds to the spring tide and the low energy capture

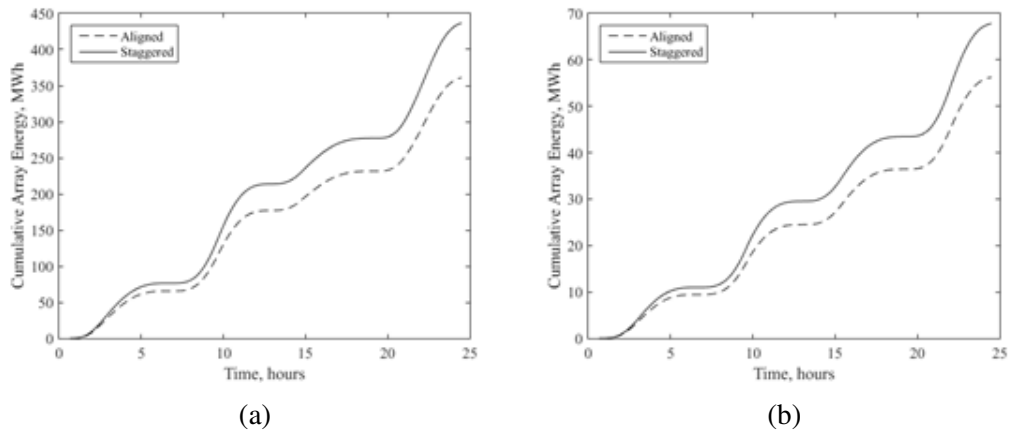


**Figure 5.56:** Cumulative energy outputted in a day during spring tide (a) and neap tide (b) for aligned and staggered array layouts.

**Table 5.30:** Total energy outputted by the tidal current turbine array, for a half lunar month, a lunar month, and a year, for the aligned and the staggered array layouts.

Spring Tide				
Layout	Half month (14days)	Monthly (28 days)	Annual (364 days)	Diff. (%)
Aligned	2.334	4.667	60.670	-
Staggered	2.761	5.523	71.793	18.33%

phase corresponds to the neap tide. The spring tide period has a higher energy capture rate than the neap tide period.

Table 5.30 shows the total energy outputted by the tidal current turbine array, for a half lunar month, a lunar month, and a year, for the aligned and the staggered array layouts. Overall, the staggered array layout array outputs 18.33% additional energy when compared to the aligned array layout, which corresponds to an annual energy output of 60.670GWh and 71.793GWh respectively.

### 5.4.5 Overall Summary

The staggered layout array model was shown to perform better than the aligned layout array by 35.5% without yaw and 12.0% with yaw in an ideal channel condition. In the headland channel condition, it was determined that the most ideal gap distance between TDA and headland is between 5D to 10D gap distance. At

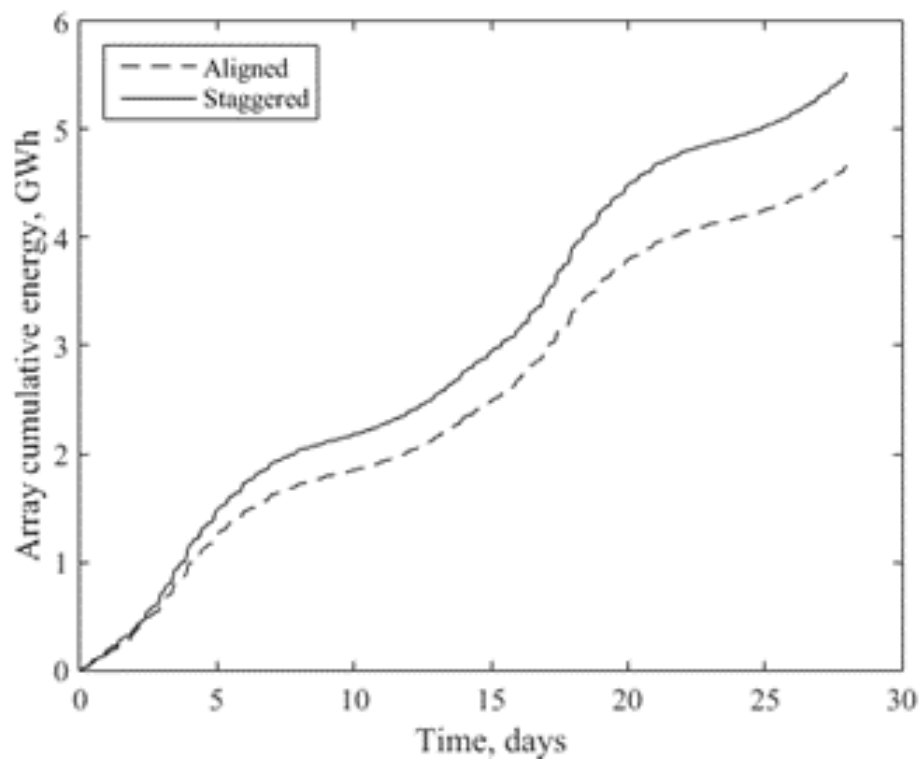


**Figure 5.57:** Cumulative energy outputted in a lunar month for an aligned array layout and a staggered array layout.

a gap distance of less than  $5D$ , the flow would be turbulent and; at a gap distance of more than  $10D$ , the flow starts to decelerate rapidly. The best alignment scenario for the aligned layout array would be the front-alignment scenario and for the staggered layout array would be the back-alignment scenario. For the headland and island channel condition, the yawed-staggered layout array performed better than the yawed-aligned layout array. In the Shannon estuary, it is determined that the staggered layout array performs about 20% better than the aligned layout array in terms of energy extraction. In a year the achievable energy extraction by the aligned layout array is 60.67 GWh and 71.79 GWh by the staggered layout array. A comparison was undertaken between a regular actuator disk model and the modified hybrid BEM-AD model in the array. It was determined that the regular actuator disk model overpredicts by 2.4% for the aligned layout array and 2.8% for the staggered layout array.

# Chapter 6

## Conclusions

### 6.1 Summaries and conclusions

This research was focused on the development of a three-dimensional hydrodynamic flow model to facilitate the simulation of a tidal current turbine array. Particular attention was placed on optimising the energy extraction with of the tidal current turbine array while also considering hydro-environmental impacts. The developed hydrodynamic models will be beneficial in the commercialisation of tidal energy extraction, as it will involve the deployment of hundreds of turbines in commercialised arrays. To date, there has been insufficient research undertaken on investigating the viability of large-scale deployments of tidal current turbines. Furthermore, this is greatly affected by the ability of the developed hydrodynamic model to accurately predict energy extraction and hydro-environmental impact, while also maintaining computational efficiency. One major focus of this research was to develop a numerical model capable of accurately predicting energy extraction of a tidal current turbine array, including site characteristics, such as hydrodynamics characteristics by the landscape, individual turbines and the interaction between tidal current turbines in an array. This enables a more accurate estimation of the energy capture of a turbine or from the array of turbines. This approach also takes into account the power available in the wake, considering adjacent turbines in an array which are greatly affected by the interactions between turbines. This research has three primary stages which were:

- The single turbine model stage
- Multiple turbines model stage

- Turbine array model stage

The first stage in this research work mainly focused on the methodology and model development of a single tidal current turbine capable of predicting turbine wake and energetic performance. The single turbine model was developed based on an actuator disk (AD) and blade element momentum (BEM) theory, this approach utilised BEM numerical calculations to describe the disk properties in the AD model (known as the BEM-AD model). The BEM-AD model was used to quantify some of the tidal current turbine blade properties through BEM calculations to parameterise the porosity and resistance coefficient needed for the AD model. In this work a novel approach was taken in describing the disk domain properties (which were the porosity and resistance coefficient); rather than treating the disk properties as one single-averaged value, the disk was treated as a gradient change based on velocity profile and blade element, both of these descriptions are known as velocity variation and radial variation. In both variations two empirical formulas were developed to describe the gradient change of the disk domain's porosity and resistance coefficient based on the incoming flow velocity profile for the velocity variation; and based on the annular element of the disk domain for radial variations. A further modification was devised by combining both variations to obtain a hybrid model known as the modified hybrid BEM-AD model. The modified hybrid BEM-AD model has the advantages of both variations but more complex empirical formulas are needed to explain the disk properties. A range of investigations and studies were undertaken using these models. An investigation was undertaken on model and software suitability by comparing between the performance of the 2-dimensional and 3-dimensional AD model and between ANSYS CFX and FLUENT. A mesh study was also conducted, in this study a new approach to meshing was used. The method proposed in this work is a concentrated mesh zone approach, which only allows for an increase in the mesh density in the region of interest. Additionally, a mesh sensitivity study was also carried out to determine the optimum mesh size.

The following were some of the key conclusions from the research conducted for stage one:

- The 3-dimensional model proved to have better accuracy than the 2-dimensional model in capturing the downstream tidal current turbine wake effects due to the 3-dimensional model having sufficient ambient fluid surrounding the

downstream actuator disk streamtube, this enables the wake to recover appropriately.

- There is little difference between ANSYS CFX and ANSYS FLUENT especially in predicting downstream velocity, however the ANSYS CFX tends to predict downstream turbulence intensity better than ANSYS FLUENT.
- The concentrated mesh zone approach shows little or no difference in terms of predicting downstream velocity and turbulence intensity, however the computational time needed was greatly reduced, i.e. by half using the concentrated mesh zone approach.
- The mesh sensitivity study has determined the mesh size of  $1.76 \times 10^6$  elements is the most optimum for the single turbine model. The element size is  $0.025D$  and the ratio between the surrounding region to concentrated mesh is 1:12.
- The velocity variation BEM-AD model performed better at estimating thrust coefficient and provides an excellent prediction of downstream wake velocity. Additionally, this approach is suitable for fluid domains with high velocity profile gradients.
- The radial variation BEM-AD model performs well at estimating power coefficient and provides an excellent prediction of downstream wake turbulence intensity; it is suitable for fluid domains with low velocity profile gradients.
- The modified hybrid BEM-AD model most accurately predicted both thrust and power when compared to BEM numerical values with a difference of 0.51% and 0.72% respectively. Importantly, this approach is capable of accurately capturing the fluid flow conditions for all velocity profile conditions.

The second stage in this research work primarily focussed on studies and investigations of downstream wake interactions of turbine-to-turbine conditions within the tidal current turbine array. The multiple turbines model utilised the same setup as the single turbine model, to capture the wake conditions and energetic output, with a focus on turbine spacing of two turbines, staggered arrangements of three turbines, different turbine sizes and placement of turbines at different depths.



The following were some of the key conclusions from the research conducted for stage two:

- The minimum tidal current turbine lateral spacing for 2 turbines in an ideal channel is  $1.5D$ , which is the minimum distance needed for the deployment of the third turbine in between the two turbines downstream. Although there is a benefit, the power and thrust at a lateral distance of  $1.5D$  is slightly lower than at a lateral distance of  $0.5D$ . Existing literature has suggested that for a consistence power and thrust on the turbine, a minimum of  $6D$  spacing is needed (Stallard et al. 2013).
- In a staggered layout with 3 turbines, the power and thrust of the 2 turbines upstream actually decrease with the introduction of a third turbine downstream. However, the power and thrust of the third turbine are greater than the 2 turbines upstream due to the flow being accelerated by the upstream turbines.
- The  $5D$  is the most optimum downstream distance for the second-row turbine in a staggered layout with 3 turbines giving a high thrust and power coefficient at the turbine while also providing good wake recovery due to the mixing of upstream turbine wake and downstream turbine wake.
- The greater the turbine size, the slower the recovery rate of the downstream turbine wake due to a greater influence from the vertical velocity profile. So, a bigger size turbine would need a longer downstream distance for the wake to recover.
- The depth placement position of the tidal current turbine should be less than the depth distance from the surface to avoid the shear effect from the seabed, the closer the turbine to the surface the greater the power and thrust on the turbine.

The third stage in this research work mainly focussed on the development of a turbine array model using an optimised tidal current turbine blade. This model is capable of simulating environmental wake conditions produced by the tidal current turbine array and estimating energy extraction of the tidal stream turbine array. The modified hybrid BEM-AD model developed in the first stage was utilised in the creation of the turbine array model, two new empirical formulas were developed to

describe the gradient change of the disk domain's porosity and resistance coefficient using the optimised blade by Yeo et al. (Yeo et al. 2022). Two types of array layout were developed in this thesis which were the aligned layout and staggered layout arrays. The concentrated mesh zone approach was also applied in the turbines in the array model (known as the turbine deployment array (TDA)), the model followed a fluid element size of  $0.025D$  and the ratio between the surrounding region to a concentrated mesh of 1:12 determined during the mesh study in the first stage. The turbine array model was further improved by allowing the individual turbines in the array to yaw to an ideal angle to optimise energy extraction and wake interactions. Studies were conducted to investigate the performance of the turbine array model in an ideal channel, headland channel and headland & island channel. Finally, the developed turbine array model was then used to evaluate the hydro-environmental impact and energy extraction at a selected location. Due to the nature of a RANS equation model, it is unable to simulate a transient problem; as a consequence, a novel approach was used to fully estimate the annual energy extraction by the array at the selected site. The novel approach utilises the parametric configuration in ANSYS CFX to achieve a pseudo-transient state by treating the rate of change of tidal conditions as instantaneous individual parametric input and the resulting energy yield of the array as a series of instantaneous parametric outputs.

The following were some of the key conclusions from the research conducted for stage three:

- The BEM calculations for the optimised blade were validated against the Yeo et al. numerical calculations. The optimised blade BEM model shows a high correlation with the Yeo et al. model and has a low percentage difference in both power and thrust coefficient, with values of 5.49% and 3.26% respectively.
- In an ideal channel condition, the staggered layout array model was shown to perform better than the aligned layout array by 35.5% without yaw and 12.0% with yaw. Yawing of the turbine in the array was shown to also improve downstream wake recovery.
- In the headland channel condition, it was determined that the most ideal gap distance between TDA and headland is between  $5D$  to  $10D$  gap distance.

The best alignment scenario for the aligned layout array would be the front-alignment scenario and for the staggered layout array would be the back-alignment scenario.

- For the headland and island channel condition, it is determined that without yawing, the aligned layout array performed better than the staggered layout array. While with yawing, the staggered layout array performed better than the aligned layout array. The yawing of the staggered layout array greatly improved the power output by 68.4%.
- The fluid flow model of the Shannon Estuary was validated with site measurements. The developed fluid flow model shows a close correlation and low error with the tidal velocity of the Shannon Estuary. The fluid flow model shows a 14% difference with site measurements during spring tide and a 17% difference with site measurements during neap tide.
- In the Shannon estuary, it is determined that the staggered layout array performs about 20% better than the aligned layout array in terms of energy extraction. In a year the achievable energy extraction by the aligned layout array is 60.67 GWh and 71.79 GWh by the staggered layout array.
- A comparison was undertaken between a regular actuator disk model and the modified hybrid BEM-AD model in the array. It was determined that the regular actuator disk model overpredicts by 2.4% for the aligned layout array and 2.8% for the staggered layout array.

## 6.2 Further work

The energy extraction tidal turbine array model developed in this research is a very effective modelling system. It provides low computational cost simulations with optimal accuracy and has the capability to simulate hydrodynamic flow fields, including quantifying tidal energy extraction. Ergo, it has many potential uses within this field of scientific research, tidal energy extraction and turbine development. The following are recommendations for future research which would further improve the work under taken in this thesis:

- A further investigation of the energy extraction by the turbine array at other potential locations in the Shannon Estuary to provide a more detailed study of

the potential extractable energy of the entire Shannon Estuary. Also, to carry out a study on other promising tidal resource sites in Ireland.

- Development of an algorithm methodology to determine an optimised number of turbines and turbine placement in the turbines array model based on maximising power output and minimising velocity deficit from the turbines.
- The model could be further improved by incorporating a full water quality model to enable a further investigation into effective ways to include environmental constraints (e.g. wave conditions at the surface, sediments in the fluid, etc.) into the flow field and array optimisations. This could allow a more detailed relationship to be developed between environmental and hydrodynamic impacts; thus, providing more accurate estimations of the flow field especially for wake predictions.
- Implementations of an actual existing turbine unit into the turbine array model for more accurate technical predictions of the extractable energy at potential sites, to reflect the current state-of-the-art tidal current turbine technologies.
- Incorporating the turbine array model into economic viability studies, hence designing the turbine array to minimise levelised cost of energy by optimising the array layout and turbine numbers to achieve a suitable balance between decreased costs due to economies of volume and diminishing returns due to global blockage effects.

# Bibliography

Abolghasemi, M. A., Piggott, M. D., Spinneken, J., Viré, A., Cotter, C. J. & Crammond, S. (2016), 'Simulating tidal turbines with multi-scale mesh optimisation techniques', *J. Fluids Struct.* **66**, 69–90.

**URL:** <http://dx.doi.org/10.1016/j.jfluidstructs.2016.07.007>

Afgan, I., McNaughton, J., Rolfo, S., Apsley, D. D., Stallard, T. & Stansby, P. (2013), 'Turbulent flow and loading on a tidal stream turbine by LES and RANS', *Int. J. Heat Fluid Flow* **43**, 96–108.

**URL:** <http://dx.doi.org/10.1016/j.ijheatfluidflow.2013.03.010>

Aghsaee, P. & Markfort, C. D. (2018), 'Effects of flow depth variations on the wake recovery behind a horizontal-axis hydrokinetic in-stream turbine', *Renew. Energy* **125**, 620–629.

**URL:** <https://doi.org/10.1016/j.renene.2018.02.137>

Ahmadi, M. H. (2019), 'Influence of upstream turbulence on the wake characteristics of a tidal stream turbine', *Renew. Energy* **132**, 989–997.

**URL:** <https://linkinghub.elsevier.com/retrieve/pii/S096014811831005X>

Ahmadian, R. & Falconer, R. A. (2012), 'Assessment of array shape of tidal stream turbines on hydro-environmental impacts and power output', *Renew. Energy* **44**(2012), 318–327.

**URL:** <http://dx.doi.org/10.1016/j.renene.2012.01.106>

Ahmed, M. R. (2012), 'Blade sections for wind turbine and tidal current turbine applications-current status and future challenges', *Int. J. Energy Res.* **36**(7), 829–844.

**URL:** <http://doi.wiley.com/10.1002/er.2912>

- Ahmed, U., Apsley, D. D., Afgan, I., Stallard, T. & Stansby, P. K. (2017), 'Fluctuating loads on a tidal turbine due to velocity shear and turbulence: Comparison of CFD with field data', *Renew. Energy* **112**, 235–246.  
**URL:** <http://dx.doi.org/10.1016/j.renene.2017.05.048>
- Andersson, J., Hellsmark, H. & Sandén, B. A. (2018), 'Shaping factors in the emergence of technological innovations: The case of tidal kite technology', *Technological Forecasting and Social Change* **132**, 191–208.
- ANSYS (2012), *ANSYS FLUENT Solver Theory Guide*.
- Ansys, C. (2009), 'ANSYS CFX-solver theory guide', *ANSYS CFX Release 15.1.7*(April), 724–746.  
**URL:** <http://scholar.google.com/scholar?hl=en&btnG=Search&q=intitle:ANSYS+CFX-Solver+Theory+Guide#0>
- Apsley, D. D., Stallard, T. & Stansby, P. K. (2018), 'Actuator-line CFD modelling of tidal-stream turbines in arrays', *J. Ocean Eng. Mar. Energy* **4**(4), 259–271.  
**URL:** <https://doi.org/10.1007/s40722-018-0120-3>
- Arramach, J., Boutammachte, N., Bouatem, A. & Mers, A. A. (2017), 'Prediction of the wind turbine performance by using a modified bem theory with an advanced brake state model', *Energy Procedia* **118**, 149–157.
- Atlantis Project (2010), 'Project development and operation: MeyGen.'
- Baba-Ahmadi, M. H. & Dong, P. (2017), 'Validation of the actuator line method for simulating flow through a horizontal axis tidal stream turbine by comparison with measurements', *Renew. Energy* **113**, 420–427.  
**URL:** <https://linkinghub.elsevier.com/retrieve/pii/S0960148117304469>
- Bahaj, A., Blunden, L. & Anwar, A. (2008), 'Tidal-current Energy Device Development and Evaluation Protocol', *Urn 08/1317* pp. 1–42.
- Bahaj, A., Molland, A., Chaplin, J. & Batten, W. (2007), 'Power and thrust measurements of marine current turbines under various hydrodynamic flow conditions in a cavitation tunnel and a towing tank', *Renew. Energy* **32**(3), 407–426.  
**URL:** <https://linkinghub.elsevier.com/retrieve/pii/S0960148106000516>

- Bahaj, A., Myers, L., Thomson, M. & Jorge, N. (2007), 'Characterising the wake of horizontal axis marine current turbines', *7th Eur. Wave Tidal Energy Conf.* (January).
- Bahaj, A. S., Myers, L. E., Rawlinson-Smith, R. I. & Thomson, M. (2011), 'The Effect of Boundary Proximity Upon the Wake Structure of Horizontal Axis Marine Current Turbines', *Offshore Mech. Arct. Eng.* **134**(No. 2), 021104.
- Bai, G., Li, J., Fan, P. & Li, G. (2013), 'Numerical investigations of the effects of different arrays on power extractions of horizontal axis tidal current turbines', *Renew. Energy* **53**, 180–186.
- Bai, L., Spence, R. R. G. & Dudziak, G. (2009), 'Investigation of the Influence of Array Arrangement and Spacing on Tidal Energy Converter (TEC) Performance using a 3-Dimensional CFD Model', *Proc. 8th Eur. Wave Tidal Energy Conf. Uppsala, Sweden* pp. 654–660.
- Baratchi, F., Jeans, T. L. & Gerber, A. G. (2017), 'Actuator line simulation of a tidal turbine in straight and yawed flows', *Int. J. Mar. Energy* **19**, 235–255.
- Batten, W., Bahaj, A., Molland, A. & Chaplin, J. (2007), 'Experimentally validated numerical method for the hydrodynamic design of horizontal axis tidal turbines', *Ocean Eng.* **34**(7), 1013–1020.  
**URL:** <https://linkinghub.elsevier.com/retrieve/pii/S0029801806001843>
- Batten, W., Bahaj, A., Molland, A. & Chaplin, J. (2008), 'The prediction of the hydrodynamic performance of marine current turbines', *Renew. Energy* **33**(5), 1085–1096.  
**URL:** <https://linkinghub.elsevier.com/retrieve/pii/S0960148107002133>
- Batten, W., Harrison, M. & Bahaj, A. (2013), 'The accuracy of the actuator disc-RANS approach for predicting the performance and far wake of a horizontal axis tidal stream turbine', *Philos. Trans. R. Soc. London A Math. Phys. Eng. Sci.* **371**(1985).  
**URL:** <http://rsta.royalsocietypublishing.org/content/371/1985/20120293.abstract>
- Blackmore, T., Batten, W. M. J. & Bahaj, A. S. (2014), 'Influence of turbulence on the wake of a marine current turbine simulator', *Proc. R. Soc. A Math. Phys. Eng.*

- Sci.* **470**(2170), 20140331.  
**URL:** <https://royalsocietypublishing.org/doi/10.1098/rspa.2014.0331>
- Blazek, J. (2005), *Computational Fluid Dynamics: Principles and Applications*, second edn, Elsevier.
- Boyle, G. (2004), *Renewable Energy: Power for a Sustainable Future*, 2 edn, OUP Oxford, 2012, Oxford.
- Branlard, E. (2017), *Wind Turbine Aerodynamics and Vorticity-Based Methods - Fundamentals and Recent Applications*, 1st ed edn, Springer International Publishing.
- Buckland, H. C., Masters, I., Orme, J. A. & Baker, T. (2013), 'Cavitation inception and simulation in blade element momentum theory for modelling tidal stream turbines', *Proc. Inst. Mech. Eng. Part A J. Power Energy* **227**(4), 479–485.  
**URL:** <http://journals.sagepub.com/doi/10.1177/0957650913477093>
- Buhl, M. L. (2005), 'A new empirical relationship between thrust coefficient and induction factor for the turbulent windmill state'.  
**URL:** <http://www.osti.gov/bridge>
- Cengel, Y. & Cimbala, J. (2013), *Fluid Mechanics Fundamentals and Applications*, third edn, McGraw Hill.
- Chamorro, L. P., Arndt, R. & Sotiropoulos, F. (2012), 'Reynolds number dependence of turbulence statistics in the wake of wind turbines', *Wind Energy* **15**(5), 733–742.  
**URL:** <http://doi.wiley.com/10.1002/we.501>
- Chamorro, L. P., Hill, C., Morton, S., Ellis, C., Arndt, R. E. & Sotiropoulos, F. (2013), 'On the interaction between a turbulent open channel flow and an axial-flow turbine', *J. Fluid Mech.* **716**(February), 658–670.
- Charlier, R. H. & Finkl, C. W. (2009), *Ocean Energy: Tide and Tidal Power*, Springer Science & Business Media.
- Chawdhary, S., Hill, C., Yang, X., Guala, M., Corren, D., Colby, J. & Sotiropoulos, F. (2017), 'Wake characteristics of a TriFrame of axial-flow hydrokinetic



- turbines', *Renew. Energy* **109**, 332–345.  
**URL:** <http://dx.doi.org/10.1016/j.renene.2017.03.029>
- Chen, H., Tang, T., Ait-Ahmed, N., Benbouzid, M. E. H., Machmoum, M. & Zaim, M. E.-H. (2018), 'Attraction, Challenge and Current Status of Marine Current Energy', *IEEE Access* **6**, 12665–12685.  
**URL:** <https://ieeexplore.ieee.org/document/8264692/>
- Chen, Y., Lin, B., Lin, J. & Wang, S. (2017), 'Experimental study of wake structure behind a horizontal axis tidal stream turbine', *Appl. Energy* **196**, 82–96.  
**URL:** <http://dx.doi.org/10.1016/j.apenergy.2017.03.126>
- Choi, N. J., Nam, S. H., Jeong, J. H. & Kim, K. C. (2013), 'Numerical study on the horizontal axis turbines arrangement in a wind farm: Effect of separation distance on the turbine aerodynamic power output', *Journal of Wind Engineering and Industrial Aerodynamics* **117**, 11–17.
- Chowdhury, M. S., Rahman, K. S., Selvanathan, V., Nuthammachot, N., Suklueng, M., Mostafaeipour, A., Habib, A., Akhtaruzzaman, M., Amin, N. & Techato, K. (2021), 'Current trends and prospects of tidal energy technology', *Environ. Dev. Sustain.* **23**(6), 8179–8194.  
**URL:** <https://doi.org/10.1007/s10668-020-01013-4>
- Chung, T. J. (2010), *Computational fluid dynamics, second edition*, Vol. 9780521769.
- Churchfield, M. J., Li, Y. & Moriarty, P. J. (2013a), 'A large-eddy simulation study of wake propagation and power production in an array of tidal-current turbines.', *Philos. Trans. A. Math. Phys. Eng. Sci.* **371**(1985), 20120421.  
**URL:** <http://www.ncbi.nlm.nih.gov/pubmed/23319713>
- Churchfield, M. J., Li, Y. & Moriarty, P. J. (2013b), 'A large-eddy simulation study of wake propagation and power production in an array of tidal-current turbines', *Philos. Trans. R. Soc. A Math. Phys. Eng. Sci.* **371**(1985).
- Clausius, R. (1879), *The Mechanical Theory of Heat*, second edn, Macmillan and Co.
- Consul, C. A., Willden, R. H. J. & McIntosh, S. C. (2013), 'Blockage effects on the hydrodynamic performance of a marine cross-flow turbine', *Philos. Trans. R.*

- Soc. A Math. Phys. Eng. Sci.* **371**(1985), 20120299.  
**URL:** <https://royalsocietypublishing.org/doi/10.1098/rsta.2012.0299>
- Council, W. E. (2016), 'World Energy Resources Marine Energy | 2016', *World Energy Resour.* .
- Cozzi, L., Gould, T., Bouckart, S., Crow, D., Kim, T.-Y., McGlade, C., Olejarnik, P., Wanner, B. & Wetzel, D. (2020), 'World Energy Outlook 2020', **2050**(October), 1–461.  
**URL:** [https://www.oecd-ilibrary.org/energy/world-energy-outlook-2020\\_557a761b-en](https://www.oecd-ilibrary.org/energy/world-energy-outlook-2020_557a761b-en)
- Creech, A. C., Borthwick, A. G. & Ingram, D. (2017), 'Effects of support structures in an LES actuator line model of a tidal turbine with contra-rotating rotors', *Energies* **10**(5).
- Creel, L. (2003), 'Ripple effects: Population and coastal regions', *Popul. Ref. Bur.* p. 8.  
**URL:** [http://www.prb.org/pdf/RippleEffects\\_Eng.pdf%5Cnhttp://pdf.usaid.gov/pdf\\_docs/Pnadd169.p](http://www.prb.org/pdf/RippleEffects_Eng.pdf%5Cnhttp://pdf.usaid.gov/pdf_docs/Pnadd169.p)
- Daly, T., Myers, L. E. & Bahaj, A. S. (2013), 'Modelling of the flow field surrounding tidal turbine arrays for varying positions in a channel', *Philos. Trans. R. Soc. A Math. Phys. Eng. Sci.* **371**(1985), 20120246.  
**URL:** <https://royalsocietypublishing.org/doi/10.1098/rsta.2012.0246>
- de Vries (1979), *Fluid Dynamic Aspects of Wind Energy Conversion*, AGARD.
- Deskos, G., Abolghasemi, M. A. & Piggott, M. D. (2017), 'Wake predictions from two turbine parameterisation models using mesh-optimisation techniques', *Proc. 12th Eur. Wave Tidal Energy Conf. 27th Aug -1st Sept 2017, Cork, Irel.* (August), 1–10.
- Divett, T., Vennell, R. & Stevens, C. (2013), 'Optimization of multiple turbine arrays in a channel with tidally reversing flow by numerical modelling with adaptive mesh', *Philos. Trans. R. Soc. A Math. Phys. Eng. Sci.* **371**(1985), 20120251.  
**URL:** <https://royalsocietypublishing.org/doi/10.1098/rsta.2012.0251>
- Draycott, S., Payne, G., Steynor, J., Nambiar, A., Sellar, B. & Venugopal, V. (2019), 'An experimental investigation into non-linear wave loading on horizontal axis

- tidal turbines', *J. Fluids Struct.* **84**, 199–217.  
**URL:** <https://doi.org/10.1016/j.jfluidstructs.2018.11.004>
- Edmunds, M., Williams, A. J., Masters, I. & Croft, T. N. (2017), 'An enhanced disk averaged CFD model for the simulation of horizontal axis tidal turbines', *Renew. Energy* **101**, 67–81.  
**URL:** <http://dx.doi.org/10.1016/j.renene.2016.08.007>
- Esfahanian, V., Pour, A. S., Harsini, I., Haghani, A., Pasandeh, R., Shahbazi, A. & Ahmadi, G. (2013), 'Numerical analysis of flow field around nrel phase ii wind turbine by a hybrid cfd/bem method', *Journal of Wind Engineering and Industrial Aerodynamics* **120**, 29–36.
- Fairley, I., Masters, I. & Karunarathna, H. (2015), 'The cumulative impact of tidal stream turbine arrays on sediment transport in the Pentland Firth', *Renew. Energy* **80**, 755–769.  
**URL:** <http://dx.doi.org/10.1016/j.renene.2015.03.004>
- Fallon, D., Hartnett, M., Olbert, A. & Nash, S. (2014), 'The effects of array configuration on the hydro-environmental impacts of tidal turbines', *Renew. Energy* **64**, 10–25.  
**URL:** <http://dx.doi.org/10.1016/j.renene.2013.10.035>
- Fernandez-Rodriguez, E. (2014), 'Analysis of Floating Support Structures for Marine and Wind Energy', (December).
- Fernandez-Rodriguez, E., Stallard, T. & Stansby, P. (2014), 'Experimental study of extreme thrust on a tidal stream rotor due to turbulent flow and with opposing waves', *J. Fluids Struct.* **51**, 354–361.  
**URL:** <https://linkinghub.elsevier.com/retrieve/pii/S0889974614002151>
- Filho, G. L. T., dos Santos, I. F. S. & Barros, R. M. (2017), 'Cost estimate of small hydroelectric power plants based on the aspect factor'.
- Flow, V. F. (1981), 'Viscous Fluid Flow Measurement', *Meas. Control* **14**(1), 17–17.  
**URL:** <http://journals.sagepub.com/doi/10.1177/002029408101400103>
- Fouz, D. M., Carballo, R., López, I. & Iglesias, G. (2022), 'Tidal stream energy potential in the shannon estuary', *Renewable Energy* **185**, 61–74.

- Frost, C., Morris, C. E., Mason-Jones, A., O'Doherty, D. M. & O'Doherty, T. (2015), 'The effect of tidal flow directionality on tidal turbine performance characteristics', *Renew. Energy* **78**, 609–620.  
**URL:** <http://dx.doi.org/10.1016/j.renene.2015.01.053>
- Funke, S. W., Farrell, P. E. & Piggott, M. D. (2014), 'Tidal turbine array optimisation using the adjoint approach', *Renew. Energy* **63**, 658–673.  
**URL:** <http://dx.doi.org/10.1016/j.renene.2013.09.031>
- Gant, S. & Stallard, T. (2008), 'Modelling a tidal turbine in unsteady flow', *Proc. Int. Offshore Polar Eng. Conf.* (January 2008), 473–479.
- Garanovic, A. (2023), 'Meygen sets record with world's first 50gwh of electricity generated by tidal energy'.  
**URL:** <https://www.offshore-energy.biz/meygen-sets-record-with-worlds-first-50gwh-of-electricity-generated-by-tidal-energy/>
- Garrett, C. & Cummins, P. (2007), 'The efficiency of a turbine in a tidal channel', *J. Fluid Mech.* **588**, 243–251.  
**URL:** [https://www.cambridge.org/core/product/identifier/S0022112007007781/type/journal\\_article](https://www.cambridge.org/core/product/identifier/S0022112007007781/type/journal_article)
- Glauert, H. (1926), *The Analysis of Experimental Results in the Windmill Brake and Vortex Ring States of an Airscrew*, H.M. Stationery Office.
- González-Gorbeña, E., Rosman, P. C. & Qassim, R. Y. (2015), 'Assessment of the tidal current energy resource in são marcos bay, brazil', *Journal of Ocean Engineering and Marine Energy* **1**, 421–433.
- Greaves, D. & Iglesias, G. (2018), *Wave and Tidal Energy*, John Wiley & Sons.
- Guillou, N. & Thiébot, J. (2016), 'The impact of seabed rock roughness on tidal stream power extraction', *Energy* **112**, 762–773.  
**URL:** <https://linkinghub.elsevier.com/retrieve/pii/S0360544216308271>
- Guo, Q., Zhou, L. & Wang, Z. (2015), 'Comparison of BEM-CFD and full rotor geometry simulations for the performance and flow field of a marine current turbine', *Renew. Energy* **75**, 640–648.  
**URL:** <https://linkinghub.elsevier.com/retrieve/pii/S0960148114006740>

- Hachmann, C., Stallard, T., Stansby, P. & Lin, B. (2020), 'Experimentally validated study of the impact of operating strategies on power efficiency of a turbine array in a bi-directional tidal channel', *Renew. Energy*.
- URL:** <https://doi.org/10.1016/j.renene.2020.06.090>
- Hansen, M. (2015), *Aerodynamics of Wind Turbines*, Routledge.
- URL:** <https://www.taylorfrancis.com/books/9781317671039>
- Harrison, M. E., Batten, W. M., Myers, L. E. & Bahaj, A. S. (2010), 'Comparison between CFD simulations and experiments for predicting the far wake of horizontal axis tidal turbines', *IET Renew. Power Gener.* **4**(6), 613–627.
- Holst, M. A., Dahlhaug, O. G. & Faudot, C. (2015), 'CFD Analysis of Wave-Induced Loads on Tidal Turbine Blades', *IEEE J. Ocean. Eng.* **40**(3), 506–521.
- URL:** <http://ieeexplore.ieee.org/document/6895177/>
- Hunter, W., Nishino, T. & Willden, R. H. (2015), 'Investigation of tidal turbine array tuning using 3D Reynolds-Averaged Navier–Stokes Simulations', *Int. J. Mar. Energy* **10**, 39–51.
- URL:** <https://linkinghub.elsevier.com/retrieve/pii/S221416691500003X>
- Iglesias, I., Bio, A., Bastos, L. & Avilez-Valente, P. (2021), 'Estuarine hydrodynamic patterns and hydrokinetic energy production: The douro estuary case study', *Energy* **222**.
- Ivanell, S., Mikkelsen, R., Sørensen, J. N. & Henningson, D. (2010), 'Stability analysis of the tip vortices of a wind turbine', *Wind Energy* **13**, 705–715.
- John, D. (2013), *Fundamentals of Aerodynamics*, Vol. 53.
- Johnson, D. & King, L. (1984), A new turbulence closure model for boundary layer flows with strong adverse pressure gradients and separation, American Institute of Aeronautics and Astronautics.
- Jones, W. & Launder, B. (1972), 'The prediction of laminarization with a two-equation model of turbulence', *Int. J. Heat Mass Transf.* **15**(2), 301–314.
- URL:** <https://linkinghub.elsevier.com/retrieve/pii/0017931072900762>
- Jump, E., Wills, T. & Macleod, A. (2019), *Review of tidal turbine wake modelling methods—state of the art*.

Jung, H., Kanemoto, T. & Liu, P. (2017), 'A Numerical Prediction of Tip Vortices from Tandem Propellers in the Counter-Rotating Type Tidal Stream Power Unit', *J. Power Energy Eng.* **05**(12), 66–74.

Kabir, A., Lemongo-Tchamba, I. & Fernandez, A. (2015), 'An assessment of available ocean current hydrokinetic energy near the north carolina shore', *Renewable Energy* **80**, 301–307.

Kalitzin, G., Medic, G., Iaccarino, G. & Durbin, P. (2005), 'Near-wall behavior of rans turbulence models and implications for wall functions', *Journal of Computational Physics* **204**, 265–291.

Kang, S., Yang, X. & Sotiropoulos, F. (2014), 'On the onset of wake meandering for an axial flow turbine in a turbulent open channel flow', *J. Fluid Mech.* **744**, 376–403.

**URL:** [https://www.cambridge.org/core/product/identifier/S0022112014000822/type/journal\\_article](https://www.cambridge.org/core/product/identifier/S0022112014000822/type/journal_article)

Khan, M., Bhuyan, G., Iqbal, M. & Quaiocoe, J. (2009), 'Hydrokinetic energy conversion systems and assessment of horizontal and vertical axis turbines for river and tidal applications: A technology status review', *Applied Energy* **86**, 1823–1835.

Khan, M. J., Iqbal, M. T. & Quaiocoe, J. E. (2008), 'River current energy conversion systems: Progress, prospects and challenges'.

khchine, Y. E. & Sriti, M. (2017), 'Tip loss factor effects on aerodynamic performances of horizontal axis wind turbine', *Energy Procedia* **118**, 136–140.

Koh, W. & Ng, E. (2016), 'Effects of reynolds number and different tip loss models on the accuracy of bem applied to tidal turbines as compared to experiments', *Ocean Engineering* **111**, 104–115.

Laan, M. P. V. D. (2014), *Efficient Turbulence Modeling for CFD Wake Simulations*.

Lande-Sudall, D., Stallard, T. & Stansby, P. (2018), 'Co-located offshore wind and tidal stream turbines: Assessment of energy yield and loading', *Renew. Energy* **118**, 627–643.

**URL:** <https://linkinghub.elsevier.com/retrieve/pii/S0960148117310248>

- Lanzafame, R. & Messina, M. (2013), 'Advanced brake state model and aerodynamic post-stall model for horizontal axis wind turbines', *Renewable Energy* **50**, 415–420.
- Launder, B. E. & Spalding, D. B. (1974), 'The numerical computation of turbulent flows', *Comput. Methods Appl. Mech. Eng.* **3**(2), 269–289.
- Lee, H. M. & Wu, Y. (2015), 'A Tomo-PIV study of the effects of freestream turbulence on stall delay of the blade of a horizontal-axis wind turbine', *Wind Energy* **18**(7), 1185–1205.  
**URL:** <http://doi.wiley.com/10.1002/we.1754>
- Lee, J. H., Park, S., Kim, D. H., Rhee, S. H. & Kim, M.-C. (2012), 'Computational methods for performance analysis of horizontal axis tidal stream turbines', *Appl. Energy* **98**, 512–523.  
**URL:** <https://linkinghub.elsevier.com/retrieve/pii/S0306261912003042>
- Li, X., Li, M., Jordan, L. B., McLelland, S., Parsons, D. R., Amoudry, L. O., Song, Q. & Comerford, L. (2019), 'Modelling impacts of tidal stream turbines on surface waves', *Renew. Energy* **130**, 725–734.  
**URL:** <https://doi.org/10.1016/j.renene.2018.05.098>
- Liu, J., Lin, H. & Purimitla, S. R. (2016), 'Wake field studies of tidal current turbines with different numerical methods', *Ocean Eng.* **117**, 383–397.  
**URL:** <http://dx.doi.org/10.1016/j.oceaneng.2016.03.061>
- Lu, Q., Chen, J., Cheng, J., Qin, N. & Danao, L. A. M. (2011), Study of cfd simulation of a 3-d wind turbine, IEEE, pp. 596–600.
- Ma, P., Yang, Z., Wang, Y., Liu, H. & Xie, Y. (2017), 'Energy extraction and hydrodynamic behavior analysis by an oscillating hydrofoil device', *Renewable Energy* **113**, 648–659.
- MacLeod, A. J., Barnes, S., Rados, K. G. & Bryden, I. G. (2002), 'Wake effects in tidal current turbine farms', *MAREC 2002, Int. Conf. Mar. Renew. Energy - Conf. Proc.* pp. 49–53.
- Maduka, M. & Li, C. W. (2022), 'Experimental evaluation of power performance and wake characteristics of twin flanged duct turbines in tandem under bi-directional tidal flows', *Renewable Energy* **199**, 1543–1567.

- Makridis, A. & Chick, J. (2013), 'Validation of a cfd model of wind turbine wakes with terrain effects', *Journal of Wind Engineering and Industrial Aerodynamics* **123**, 12–29.
- Malki, R., Masters, I., Williams, A. J. & Nick Croft, T. (2014), 'Planning tidal stream turbine array layouts using a coupled blade element momentum – computational fluid dynamics model', *Renew. Energy* **63**, 46–54.  
**URL:** <https://linkinghub.elsevier.com/retrieve/pii/S0960148113004412>
- Malki, R., Williams, A. J., Croft, T. N., Togneri, M. & Masters, I. (2013), 'A coupled blade element momentum - Computational fluid dynamics model for evaluating tidal stream turbine performance', *Appl. Math. Model.* **37**(5), 3006–3020.  
**URL:** <http://dx.doi.org/10.1016/j.apm.2012.07.025>
- Martínez-Tossas, L. A., Churchfield, M. J. & Leonardi, S. (2015), 'Large eddy simulations of the flow past wind turbines: actuator line and disk modeling', *Wind Energy* **18**(6), 1047–1060.  
**URL:** <http://doi.wiley.com/10.1002/we.1747>
- Masters, I., Malki, R., Williams, A. J. & Croft, T. N. (2013), 'The influence of flow acceleration on tidal stream turbine wake dynamics: A numerical study using a coupled BEM-CFD model', *Appl. Math. Model.* **37**(16-17), 7905–7918.  
**URL:** <http://dx.doi.org/10.1016/j.apm.2013.06.004>
- Masters, I., Williams, A., Croft, T. N., Togneri, M., Edmunds, M., Zangiabadi, E., Fairley, I. & Karunarathna, H. (2015), 'A comparison of numerical modelling techniques for tidal stream turbine analysis', *Energies* **8**(8), 7833–7853.
- McDonald, P. W. (1971), The computation of transonic flow through two-dimensional gas turbine cascades, American Society of Mechanical Engineers.
- Mcnaughton, J., Afgan, I., Apsley, D. D., Rolfo, S., Stallard, T. & Stansby, P. K. (2014), 'A simple sliding-mesh interface procedure and its application to the CFD simulation of a tidal-stream turbine', *Int. J. Numer. Methods Fluids* **74**(4), 250–269.
- Menter, F. (1993), Zonal two equation k-w turbulence models for aerodynamic flows, American Institute of Aeronautics and Astronautics.



- Menter, F. R. (1994), 'Two-equation eddy-viscosity turbulence models for engineering applications', *AIAA J.* **32**(8), 1598–1605.
- Menter, F. R. (2009), 'Review of the shear-stress transport turbulence model experience from an industrial perspective', *Int. J. Comput. Fluid Dyn.* **23**(4), 305–316.  
**URL:** <http://www.tandfonline.com/doi/abs/10.1080/10618560902773387>
- Menter, F. R., Kuntz, M. & Langtry, R. (2014), 'Ten years of industrial experience with the sst turbulence model'.  
**URL:** <https://www.researchgate.net/publication/228742295>
- Milne, I., Day, A., Sharma, R. & Flay, R. (2016), 'The characterisation of the hydrodynamic loads on tidal turbines due to turbulence', *Renew. Sustain. Energy Rev.* **56**, 851–864.  
**URL:** <https://linkinghub.elsevier.com/retrieve/pii/S1364032115013623>
- Mishra, P. & Aharwal, K. R. (2018), 'A review on selection of turbulence model for CFD analysis of air flow within a cold storage', *IOP Conf. Ser. Mater. Sci. Eng.* **402**(1).
- Morris, C. E., O'Doherty, D. M., Mason-Jones, A. & O'Doherty, T. (2016), 'Evaluation of the swirl characteristics of a tidal stream turbine wake', *Int. J. Mar. Energy* **14**(January 2013), 198–214.
- Mozfari, A. T. J. (2014), 'Numerical investigation of Marine Hydrokinetic Turbines : methodology development for single turbine and small array simulation , and application to flume and full-scale reference'.
- Mueller, M. & Wallace, R. (2008), 'Enabling science and technology for marine renewable energy', *Energy Policy* **36**, 4376–4382.
- Mycek, P., Gaurier, B., Germain, G., Pinon, G. & Rivoalen, E. (2014a), 'Experimental study of the turbulence intensity effects on marine current turbines behaviour. Part I: One single turbine', *Renew. Energy* **68**, 876–892.
- Mycek, P., Gaurier, B., Germain, G., Pinon, G. & Rivoalen, E. (2014b), 'Experimental study of the turbulence intensity effects on marine current turbines behaviour. Part II: Two interacting turbines', *Renew. Energy* **68**(June), 876–892.

- Myers, L. & Bahaj, A. S. (2009), 'Near wake properties of horizontal axis marine current turbines', *Proc. 8th Eur. Wave Tidal Energy Conf.* pp. 558–565.  
**URL:** <http://eprints.soton.ac.uk/333968/>
- Myers, L. E. & Bahaj, A. S. (2010), 'Experimental analysis of the flow field around horizontal axis tidal turbines by use of scale mesh disk rotor simulators', *Ocean Eng.* **37**(2-3), 218–227.  
**URL:** <http://dx.doi.org/10.1016/j.oceaneng.2009.11.004>
- Myers, L. E. & Bahaj, A. S. (2012), 'An experimental investigation simulating flow effects in first generation marine current energy converter arrays', *Renew. Energy* **37**(1), 28–36.  
**URL:** <http://dx.doi.org/10.1016/j.renene.2011.03.043>
- Nachtane, M., Tarfaoui, M., Goda, I. & Rouway, M. (2020), 'A review on the technologies, design considerations and numerical models of tidal current turbines', *Renewable Energy* **157**, 1274–1288.
- Nachtane, M., Tarfaoui, M., Moumen, A. E., Saifaoui, D. & Benyahia, H. (2019), 'Design and hydrodynamic performance of a horizontal axis hydrokinetic turbine', *International Journal of Automotive and Mechanical Engineering* **16**, 6453–6469.
- Nago, V. G., dos Santos, I. F. S., Gbedjinou, M. J., Mensah, J. H. R., Filho, G. L. T., Camacho, R. G. R. & Barros, R. M. (2022), 'A literature review on wake dissipation length of hydrokinetic turbines as a guide for turbine array configuration'.
- Nairn, R. (2005), *Ireland's Coastline Exploring its Nature and Heritage*, The Collins Press.
- Nash, S. & Phoenix, A. (2017), 'A review of the current understanding of the hydro-environmental impacts of energy removal by tidal turbines', *Renew. Sustain. Energy Rev.* **80**(January), 648–662.  
**URL:** <http://dx.doi.org/10.1016/j.rser.2017.05.289>
- Newton, I., Motte, A. & Machin, J. (1729), *The Mathematical Principles of Natural Philosophy*, number v. 1 in 'The Mathematical Principles of Natural Philosophy', B. Motte.  
**URL:** <https://books.google.ie/books?id=Tm0FAAAAQAAJ>

- Nguyen, V. T., Guillou, S. S., Thiébot, J. & Santa Cruz, A. (2016), 'Modelling turbulence with an Actuator Disk representing a tidal turbine', *Renew. Energy* **97**(November), 625–635.
- Nishino, T. (2013), 'Beyond the Betz Theory - Blockage, Wake Mixing and Turbulence', (May).
- Nishino, T. & Willden, R. H. J. (2012), 'The efficiency of an array of tidal turbines partially blocking a wide channel', *J. Fluid Mech.* **708**, 596–606.  
**URL:** [https://www.cambridge.org/core/product/identifier/S0022112012003497/type/journal\\_article](https://www.cambridge.org/core/product/identifier/S0022112012003497/type/journal_article)
- Nuernberg, M. & Tao, L. (2018), 'Experimental study of wake characteristics in tidal turbine arrays', *Renew. Energy* **127**(2018), 168–181.  
**URL:** <https://doi.org/10.1016/j.renene.2018.04.053>
- NWE Secretariat (2021), 'Magallanes reinstall ATIR tidal turbine at EMEC'.
- O'Doherty, T., O'Doherty, D. & Mason-Jones, A. (2018), Tidal Energy Technology, in 'Wave Tidal Energy', pp. 105–150.
- Olczak, A., Stallard, T., Feng, T. & Stansby, P. K. (2016), 'Comparison of a RANS blade element model for tidal turbine arrays with laboratory scale measurements of wake velocity and rotor thrust', *J. Fluids Struct.* **64**, 87–106.  
**URL:** <http://dx.doi.org/10.1016/j.jfluidstructs.2016.04.001>
- O'Rourke, F., Boyle, F. & Reynolds, A. (2010), 'Tidal current energy resource assessment in Ireland: Current status and future update', *Renew. Sustain. Energy Rev.* **14**(9), 3206–3212.  
**URL:** <http://dx.doi.org/10.1016/j.rser.2010.07.039>
- O'Rourke, F., Boyle, F. & Reynolds, A. (2014), 'Ireland's tidal energy resource; An assessment of a site in the Bulls Mouth and the Shannon Estuary using measured data', *Energy Convers. Manag.* **87**, 726–734.
- Ouro, P., Ramírez, L. & Harrold, M. (2019), 'Analysis of array spacing on tidal stream turbine farm performance using Large-Eddy Simulation', *J. Fluids Struct.* **91**, 102732.  
**URL:** <https://linkinghub.elsevier.com/retrieve/pii/S0889974619301161>

- Ouro, P. & Stoesser, T. (2019), 'Impact of Environmental Turbulence on the Performance and Loadings of a Tidal Stream Turbine', *Flow, Turbul. Combust.* **102**(3), 613–639.
- Palm, M., Huijsmans, R., Pourquie, M. & Sijstra, A. (2010), Simple Wake Models for Tidal Turbines in Farm Arrangement, in '29th Int. Conf. Ocean. Offshore Arct. Eng. Vol. 3', ASMEDC, pp. 577–587.  
**URL:** <https://asmedigitalcollection.asme.org/OMAE/proceedings/OMAE2010/49118/577/345920>
- Pang, C. M., Kennedy, D. M. & O'Rourke, F. (2020), 'Comparison of RANS turbulence models in predicting wake development in a 2-dimensional actuator disk model', *ECOS 2020 - Proc. 33rd Int. Conf. Effic. Cost, Optim. Simul. Environ. Impact Energy Syst.* pp. 156–167.
- Pang, C. M., Rourke, F. O. & Kennedy, D. (2019), 'The Effects of Inflow Turbulence Intensity on predicting wake velocity in a two dimensional RANS Actuator disc model', *EWTEC 2019* (September).
- Pope, S. B. (2005), *Turbulent Flows*, 1 edn, Cambridge University Press, Cambridge.
- Pratumnopharat, P. & Leung, P. (2011), 'Validation of various windmill brake state models used by blade element momentum calculation', *Renewable Energy* **36**, 3222–3227.
- Priegue, L. & Stoesser, T. (2017), 'The influence of blade roughness on the performance of a vertical axis tidal turbine', *International Journal of Marine Energy* **17**, 136–146.
- Ramos, V., Carballo, R., Álvarez, M., Sánchez, M. & Iglesias, G. (2013), 'Assessment of the impacts of tidal stream energy through high-resolution numerical modeling', *Energy* **61**, 541–554.  
**URL:** <http://dx.doi.org/10.1016/j.energy.2013.08.051>
- Ramírez, R. D. M., Cuervo, F. I. & Rico, C. A. M. (2016), 'Technical and financial valuation of hydrokinetic power in the discharge channels of large hydropower plants in colombia: A case study', *Renewable Energy* **99**, 136–147.

Reynolds, O. (1895), 'Iv. on the dynamical theory of incompressible viscous fluids and the determination of the criterion', *Philosophical Transactions of the Royal Society of London. (A.)* **186**, 123–164.

Roc, T., Conley, D. C. & Greaves, D. (2010), 'Accounting for Turbulence in a Regional Numerical Model for Tidal Current Turbine Farm Planning', *3rd Int. Conf. Ocean Energy, Bilbao* pp. 1–6.

Rusu, E. & Venugopal, V. (2019), *Offshore Renewable Energy: Ocean Waves, Tides and Offshore Wind*, MDPI.

**URL:** <http://www.mdpi.com/books/pdfview/book/1132>

Sanderse, B., Pijl, S. & Koren, B. (2011), 'Review of computational fluid dynamics for wind turbine wake aerodynamics', *Wind Energy* **14**(7), 799–819.

**URL:** <http://doi.wiley.com/10.1002/we.458>

Sangiuliano, S. J. (2017), 'Planning for tidal current turbine technology: A case study of the gulf of st. lawrence', *Renewable and Sustainable Energy Reviews* **70**, 805–813.

Schubel, P. J. & Crossley, R. J. (2012), 'Wind Turbine Blade Design', *Energies* **5**(9), 3425–3449.

**URL:** <http://www.mdpi.com/1996-1073/5/9/3425>

SEAI (2008), 'Tidal & current energy resources in Ireland'.

**URL:** [http://www.seai.ie/Publications/Renewables\\_Publications\\_/Ocean/Tidal\\_Current\\_Energy\\_Re](http://www.seai.ie/Publications/Renewables_Publications_/Ocean/Tidal_Current_Energy_Re)

SEI (2004), *Tidal and Current Energy Resources in Ireland*, Sustainable Energy Ireland.

Shen, W. Z., Mikkelsen, R., Sørensen, J. N. & Bak, C. (2005), 'Tip loss corrections for wind turbine computations', *Wind Energy* **8**, 457–475.

Shives, M. & Crawford, C. (2014), 'Turbulence Modelling for Accurate Wake Prediction in Tidal Turbine Arrays', *Int. Conf. Ocean Energy* .

Shives, M. & Crawford, C. (2016), 'Adapted two-equation turbulence closures for actuator disk RANS simulations of wind & tidal turbine wakes', *Renew. Energy* **92**, 273–292.

**URL:** <https://linkinghub.elsevier.com/retrieve/pii/S0960148116301276>

- Sleiti, A. K. (2017), 'Tidal power technology review with potential applications in gulf stream'.
- Sodja, J. (2007), 'Turbulence models in CFD', *Univ. Ljubljana* (March), 1–18.  
**URL:** [http://mafija.fmf.uni-lj.si/seminar/files/2006\\_2007/Turbulence\\_models\\_in\\_CFD.pdf](http://mafija.fmf.uni-lj.si/seminar/files/2006_2007/Turbulence_models_in_CFD.pdf)
- Song, Y. & Perot, J. B. (2015), 'Cfd simulation of the nrel phase vi rotor', *Wind Engineering* **39**.
- Sørensen, J. (2011), Wind turbine wakes and wind farm aerodynamics, in 'Wind Energy Syst.', Elsevier, pp. 112–e131.  
**URL:** <https://linkinghub.elsevier.com/retrieve/pii/B9781845695804500041>
- Stallard, T., Collings, R., Feng, T. & Whelan, J. (2013), 'Interactions between tidal turbine wakes: Experimental study of a group of three-bladed rotors', *Philos. Trans. R. Soc. A Math. Phys. Eng. Sci.* **371**(1985).
- Stallard, T., Feng, T. & Stansby, P. K. (2015), 'Experimental study of the mean wake of a tidal stream rotor in a shallow turbulent flow', *J. Fluids Struct.* **54**, 235–246.  
**URL:** <http://dx.doi.org/10.1016/j.jfluidstructs.2014.10.017>
- Sufian, S. F., Li, M. & O'Connor, B. A. (2017), '3D modelling of impacts from waves on tidal turbine wake characteristics and energy output', *Renew. Energy* **114**, 308–322.
- Sun, X., Chick, J. P. & Bryden, I. G. (2008), 'Laboratory-scale simulation of energy extraction from tidal currents', *Renew. Energy* **33**(6), 1267–1274.
- Sun, Z., Chen, J., Shen, W. Z. & Zhu, W. J. (2016), 'Improved blade element momentum theory for wind turbine aerodynamic computations', *Renewable Energy* **96**, 824–831.
- Sun, Z., Shen, W. Z., Chen, J. & Zhu, W. J. (2017), 'Improved fixed point iterative method for blade element momentum computations', *Wind Energy* **20**, 1585–1600.
- Tarfaoui, M., Nachtane, M., Shah, O. & Boudounit, H. (2019), 'Numerical study of the structural static and fatigue strength of wind turbine blades', *Materials Today: Proceedings* **13**, 1215–1223.

- Tedds, S. C. (2014), Scale Model Testing of Tidal Stream Turbines : Wake Characterisation in Realistic Flow Conditions, PhD thesis, University of Liverpool.
- Thiébot, J., Bailly du Bois, P. & Guillou, S. (2015), 'Numerical modeling of the effect of tidal stream turbines on the hydrodynamics and the sediment transport - Application to the Alderney Race (Raz Blanchard), France', *Renew. Energy* **75**, 356–365.
- Tollmien, W., Schlichting, H., Görtler, H. & Riegels, F. W. (1961), *Applications of modern hydrodynamics to aeronautics*, Springer Berlin Heidelberg, pp. 433–515.
- Touimi, K., Benbouzid, M. & Tavner, P. (2018), 'Tidal stream turbines: With or without a gearbox?', *Ocean Engineering* **170**, 74–88.
- Turner, M. J., Clough, R. W., Martin, H. C. & Topp, L. J. (1956), 'Stiffness and deflection analysis of complex structures', *Journal of the Aeronautical Sciences* **23**, 805–823.
- Turnock, S. R., Phillips, A. B., Banks, J. & Nicholls-Lee, R. (2011), 'Modelling tidal current turbine wakes using a coupled RANS-BEMT approach as a tool for analysing power capture of arrays of turbines', *Ocean Eng.* **38**(11-12), 1300–1307.  
**URL:** <http://dx.doi.org/10.1016/j.oceaneng.2011.05.018>
- Verdant Power (2010), 'Roosevelt Island Tidal Energy Project'.  
**URL:** <https://tethys.pnnl.gov/project-sites/roosevelt-island-tidal-energy-rite-project-pilot>
- Vogel, C. R. & Willden, R. H. J. (2020), 'Investigation of wind turbine wake superposition models using Reynolds-averaged Navier-Stokes simulations', *Wind Energy* **23**(3), 593–607.  
**URL:** <https://onlinelibrary.wiley.com/doi/abs/10.1002/we.2444>
- Wang, Z. J. & Wang, Z. W. (2019), 'A review on tidal power utilization and operation optimization', *IOP Conf. Ser. Earth Environ. Sci.* **240**(5).
- Ward, S. L., Robins, P. E., Lewis, M. J., Iglesias, G., Hashemi, M. R. & Neill, S. P. (2018), 'Tidal stream resource characterisation in progressive versus standing wave systems', *Appl. Energy* **220**, 274–285.  
**URL:** <https://linkinghub.elsevier.com/retrieve/pii/S0306261918303970>

- White, F. (2009), *Fluid Mechanics*, sixth edition edn, McGraw-Hill.
- Wilcox, D. C. (1988), 'Reassessment of the scale-determining equation for advanced turbulence models', *AIAA J.* **26**(11), 1299–1310.  
**URL:** <https://arc.aiaa.org/doi/10.2514/3.10041>
- Wilcox, D. C. (1994), *Turbulence Modeling for CFD*, DCW Industries,.
- Wimshurst, A., Vogel, C. & Willden, R. (2018), 'Cavitation limits on tidal turbine performance', *Ocean Eng.* **152**, 223–233.  
**URL:** <https://linkinghub.elsevier.com/retrieve/pii/S002980181830060X>
- Wolff, G. (2007), 'Oceanography - a View of The Earth (4th Edition), edited by M. Grant Gross, Prentice-Hall International Editions, 1987. No. of pages: 406. Price: £17.95 (paperback).', *Geol. J.* **24**(2), 173–177.  
**URL:** <https://onlinelibrary.wiley.com/doi/10.1002/gj.3350240209>
- Wuβow, S., Sitzki, L. & Hahm, T. (2007), '3d-simulation of the turbulent wake behind a wind turbine', *Journal of Physics: Conference Series* **75**, 012033.
- Xue, M.-A. & Lin, P. (2011), 'Numerical study of ring baffle effects on reducing violent liquid sloshing', *Comput. Fluids* **52**, 116–129.  
**URL:** <https://linkinghub.elsevier.com/retrieve/pii/S0045793011002921>
- Yeo, E. J., Kennedy, D. M. & O'Rourke, F. (2022), 'Tidal current turbine blade optimisation with improved blade element momentum theory and a non-dominated sorting genetic algorithm', *Energy* **250**.
- Zang, W., Zheng, Y., Zhang, Y., Zhang, J. & Fernandez-Rodriguez, E. (2019), 'Experiments on the mean and integral characteristics of tidal turbine wake in the linear waves propagating with the current', *Ocean Eng.* **173**, 1–11.  
**URL:** <https://linkinghub.elsevier.com/retrieve/pii/S0029801818312113>
- Zhang, C. (2018), 'Reliability-based fatigue damage assessment and optimum maintenance strategy of offshore horizontal wind turbine blades'.  
**URL:** <https://www.researchgate.net/publication/334492552>
- Zhang, D., Guo, P., Hu, Q. & Li, J. (2022), 'Parametric study and multi-objective optimization of a ductless archimedes screw hydrokinetic turbine: Experimental and numerical investigation', *Energy Conversion and Management* **273**, 116423.



- Zhang, Y., Fernandez-Rodriguez, E., Zheng, J., Zheng, Y., Zhang, J., Gu, H., Zang, W. & Lin, X. (2020), 'A Review on Numerical Development of Tidal Stream Turbine Performance and Wake Prediction', *IEEE Access* **8**, 79325–79337.
- Zhang, Y., Zhang, J., Zheng, Y., Yang, C., Zang, W. & Fernandez-Rodriguez, E. (2017), 'Experimental analysis and evaluation of the numerical prediction of wake characteristics of tidal stream turbine', *Energies* **10**(12).
- Zhong, W., Shen, W., Wang, T. & Li, Y. (2020), 'A tip loss correction model for wind turbine aerodynamic performance prediction', *Renewable Energy* **147**, 223–238.
- Zhou, Z., Benbouzid, M., Charpentier, J.-F., Scuiller, F. & Tang, T. (2017), 'Developments in large marine current turbine technologies – a review', *Renewable and Sustainable Energy Reviews* **71**, 852–858.